

Primjena vlastitih oscilacija u vođenju i upravljanju plovilima

Mišković, Nikola

Doctoral thesis / Disertacija

2010

Degree Grantor / Ustanova koja je dodijelila akademski / stručni stupanj: **University of Zagreb, Faculty of Electrical Engineering and Computing / Sveučilište u Zagrebu, Fakultet elektrotehnike i računarstva**

Permanent link / Trajna poveznica: <https://urn.nsk.hr/urn:nbn:hr:168:682779>

Rights / Prava: [In copyright](#) / [Zaštićeno autorskim pravom.](#)

Download date / Datum preuzimanja: **2025-03-31**



Repository / Repozitorij:

[FER Repository - University of Zagreb Faculty of Electrical Engineering and Computing repository](#)



UNIVERSITY OF ZAGREB
FACULTY OF ELECTRICAL ENGINEERING AND COMPUTING
SVEUČILIŠTE U ZAGREBU
FAKULTET ELEKTROTEHNIKE I RAČUNARSTVA

Nikola Mišković

**USE OF SELF-OSCILLATIONS IN
GUIDANCE AND CONTROL OF MARINE
VESSELS**

**PRIMJENA VLASTITIH OSCILACIJA U
VOĐENJU I UPRAVLJANJU PLOVILIMA**

DOCTORAL THESIS
DOKTORSKA DISERTACIJA

Zagreb, 2010

DOCTORAL THESIS is written at the Department of Control and Computer Engineering, Faculty of Electrical Engineering and Computing
University of Zagreb

Supervisor: Professor Zoran Vukić

DOCTORAL THESIS has 189 pages. Dissertation No.

The dissertation evaluation committee:

1. Professor Vesna Županović, Ph.D.,
Faculty of Electrical Engineering and Computing, University of Zagreb
2. Professor Zoran Vukić, Ph.D.,
Faculty of Electrical Engineering and Computing, University of Zagreb
3. Professor Vladimir Koroman, Ph.D.,
Brodarski Institute, Zagreb

The dissertation defense committee:

1. Professor Vesna Županović, Ph.D.,
Faculty of Electrical Engineering and Computing, University of Zagreb
2. Professor Zoran Vukić, Ph.D.,
Faculty of Electrical Engineering and Computing, University of Zagreb
3. Professor Ivan Petrović, Ph.D.,
Faculty of Electrical Engineering and Computing, University of Zagreb
4. Associate Professor Antonio Pascoal, Ph.D.,
Institute Superior Tecnico, Institute for Systems and Robotics, Lisbon, Portugal
5. Professor Dario Matika, Ph.D.,
Croatian Ministry of Defence, Zagreb

Date of dissertation defense: 16th April, 2010

Mami, Tati i Seki.

Svesci knjiga ne bi bili dovoljni za iskazati zahvalnost svim osobama koje su mi pomogle i odigrale nezamjenjivu ulogu u studentskom razdoblju života koje zaključujem ovom disertacijom. Njih spominjem tek u nekoliko odlomaka koji slijede, a u mojim su mislima bili čitavim putem.

Na prvome mjestu zahvaljujem Mami, Tati i Seki kojima je disertacija posvećena i bez kojih ovo istraživanje nikako ne bi bilo moguće. Njihova bezuvjetna ljubav, tolerancija i podrška su neprocjenjivo blago, a osjećaj sigurnosti koji mi pružaju je bio, i ostat će, moj vječni pokretač u životu. Hvala vam na toplini i, često nezasluženoj, požrtvornosti. Zahvaljujem i cijeloj porodici koja je moje istraživanje i rezultate pratila pažljivo, te je bila uz mene u svim situacijama pa čak i na vrhu drva šljive.

Zahvaljujem se svome mentoru prof. dr. sc. Zoranu Vukiću koji me je uveo u području pomorske robotike. Njegovi savjeti i riječi podrške su mi uvelike pomogli u trenucima kada bih se našao pred inspirativnim zidom, a dugogodišnje iskustvo i zavidna količina znanja su mi utirali put k zadanim ciljevima. Zahvaljujući slobodi u odabiru istraživačkih tema, i tek rijetkim prigovorima zbog neurednog radnog stola, moj je ulazak u svijet znanosti prošao bezbolno i uvijek će ostati u prekrasnom sjećanju.

Stvaranje kreativnog nereda u sobi C09-09 je počelo zahvaljujući prof. dr. sc. Ljubomiru Kuljači koji me je velikodušno primio kao cimera. Između ostalog, profesoru Kuljači mogu zahvaliti na brojnim životnim mudrostima koje neizmerno cijenim, te na stručnom znanju koje je s lakoćom prenosio na mene. Zahvaljujem se i najbližim suradnicima iz Laboratorija za podvodne sustave i tehnologije Matku Barišiću, Đuli Nađu i Antoniu Vasiljeviću koji su uvijek bili tu kada je trebala pomoć. Uz njih su brojni tereni bili ugodno druženje.

Veliko hvala upućujem i ekipi s Brodarskog instituta a posebno Marinu Stipanovu čije bi (ponekad ekstravagantne) ideje zagolicala um i najkonzervativnijih istraživača. Imao sam neizmjernu sreću raditi na Zavodu za automatiku i računalno inženjerstvo čijim sam profesorima zahvalan za svo znanje koje sam stekao iz raznih područja automatike. Njima, znanstvenim novacima i ostalim zaposlenicima zahvaljujem na ugodnom društvu, zabavnim i poučnim razgovorima, korisnim savjetima te obiteljskoj atmosferi na radnom mjestu. Posebno se zahvaljujem Mati Jelaviću na nerijetkim trenucima smijeha i Mariji Đakulović na opuštajućim razgovorima. Hvala i studentima koji su me kao nastavnog asistenta poticali na proširivanje znanja i motivirali u nastavnom radu.

Ulogu menotra i savjetnika za vrijeme istraživanja provedenog u Consiglio Nazionale delle Ricerche u Genovi, preuzeo je Massimo Caccia kojemu se ovim putem zahvaljujem na srdačnom gostoprimstvu, korisnim savjetima i pažnji koju je posvetio momu radu. Nikako ne smijem zaboraviti Marca Bibulija kojem zahvaljujem na zajedničkom istraživanju i uvođenju u društveni život Genove.

Posljednji, ali nikako manje važni, na red dolaze moji najbolji životni prijatelji. Bez njih niti jedan uspjeh ne bi bio tako sladak, niti jedan pad tako mekan, niti jedan odmor tako ugodan, niti jedan trenutak tako dragocjen.

Nikola Mišković,
Zagreb, 20. travnja 2010.

1	Introduction	1
2	Mathematical Modeling of Marine Vehicles	8
2.1	Actuators	10
2.2	Actuator Allocation	14
2.3	Kinematic Model	16
2.4	Dynamic Model	16
2.5	Model Simplifications	19
2.5.1	Coupled model in the horizontal plane	20
2.5.2	Uncoupled model for underwater vehicles	20
2.5.3	Practical model for small surface vessels	22
2.6	Distance Keeping Model	24
2.7	Line Following	26
2.8	Conclusion	27
3	Systems	28
3.1	VideoRay ROV	28
3.2	AutoMarine AUV	31
3.3	Charlie USV	34
3.4	Vision-Based Laser Distance Module	36
3.5	Vision-Based Data Acquisition	40
3.5.1	Laboratory Apparatus	40
3.5.2	Data Acquisition	42
3.6	Conclusion	45
4	Conventional Identification Techniques for Marine Vehicles	46
4.1	Actuator Mapping	47
4.2	Least-Squares Identification	47
4.3	Identification Based on Open Loop Step Response	51
4.4	Zig-Zag Manoeuvre	56
4.5	Conclusion	59
5	Self-Oscillations	60
5.1	Describing Function	60
5.2	Symmetric Self-Oscillations	64
5.3	Asymmetric Self-Oscillations	69
5.4	On the Existence of Self-Oscillations	70
5.5	Conclusion	70

6	Identification by Use of Self–Oscillations (IS–O)	72
6.1	General Formulation	74
6.2	General Matrix Algorithm Formulation for Linear Static Processes	75
6.3	Modification for Type k Systems	78
6.4	Modification for Systems with Delays	80
6.5	Modification for Discrete–Time Systems	82
6.6	Application to Marine Vehicles	84
6.6.1	Identifying Yaw DOF	87
6.6.2	Identifying Surge DOF	88
6.6.3	Identifying Heave DOF	89
6.6.4	Identifying Heading Closed Loop	89
6.7	Software Implementation	91
6.8	Conclusion	94
7	Experimental Results for Different Identification Methods	95
7.1	Deciding on the Appropriate Model	95
7.2	Model Validation Techniques	98
7.3	Identifying Yaw DOF – VideoRay ROV	101
7.3.1	Least–Squares Results	102
7.3.2	IS–O Results	104
7.3.3	Model Validation and Comparison of IS–O and L–S Identification Methods	106
7.4	Identifying Yaw DOF – AutoMarine AUV	110
7.4.1	Results from Step Responses	110
7.4.2	IS–O Results	111
7.4.3	Model Validation and Comparison of IS–O and Step Response Identification Methods	113
7.5	Identifying Yaw DOF – Charlie USV	118
7.5.1	Least–Squares Results	119
7.5.2	IS–O Results	120
7.5.3	Model Validation and Comparison of IS–O and L–S Identification Methods	123
7.6	Identifying Surge DOF – VideoRay ROV	128
7.7	Identifying Heading Closed Loop – Charlie ASV	131
7.8	Conclusion	133
8	Control and Guidance of Marine Vehicles Using IS–O Experiments	135
8.1	Low–Level Control Design	136
8.1.1	Controller Structure	137
8.1.2	Stability Analysis	139
8.1.3	Antiwindup	143
8.1.4	Simulation Results	145

8.1.5	Experimental Results	147
8.1.6	Other Control Algorithms	149
8.2	Distance Keeping Control System	150
8.2.1	Kalman Filter Design	150
8.2.2	Distance Keeping Controller	153
8.2.3	Experimental Results	155
8.3	Line Following	157
8.3.1	Direct Actuator Control (Method 1)	157
8.3.2	Indirect Actuator Control (Method 2)	160
8.3.3	Monotonous Approach	163
8.3.4	Experimental Results	167
8.3.5	On Choosing the Model Transfer Function	170
9	Conclusion	172
	Bibliography	175
	Nomenclature	182
	Abstract	186
	Sažetak	187
	Curriculum Vitae	188
	Životopis	189

Introduction

Marine vessels (or vehicles) is a common name for all moving objects that operate fully or partially in the water. Based on the medium which surrounds them, they are divided into underwater vehicles (UVs) and surface vehicles (SVs). Further on, regarding the onboard crew, they are divided into manned and unmanned¹ vessels. Based on mode of operation, unmanned vessels are divided into remotely operated vehicles (ROVs) and autonomous underwater vehicles (AUVs). These abbreviations are usually used in literature for unmanned underwater vehicles (UUVs), unlike unmanned surface vehicles (USVs) or autonomous surface vehicles (ASV).

The main difference between remotely operated and autonomous vessels is that the first are connected with a tether to a central command centre, while the latter do not have direct link to the centre, but they operate as autonomous systems. In surface vehicles, the connecting link can be achieved either through a tether or via wireless electromagnetic link (which is more common). UVs in shallow waters have the capability to communicate via acoustic or electromagnetic signals. In deep waters only acoustic signals can be used but with short range. Acoustic signals require a lot of energy for longer range and they have low bandwidth which makes direct control and live video feed impossible. In other words, if live feed from an underwater vehicle to the surface is needed, the vehicle should be equipped with a physical link (tether). This may get quite inconvenient if the vehicle is supposed to operate at larger depths or greater distances from the base station – the tether length may increase to the level where it is impossible to control the vehicle. Autonomous vehicles do not experience this problem. On the other hand, physical link, common in ROVs, may also serve as an energy link, making remotely operated vehicles independent on the limited battery capacity which is inevitable in autonomous vehicles. One way of coping with this problem in autonomous vehicles is to ensure battery charging using the solar energy. Unfortunately, this is not possible underwater. Limited tether length is the main reason why ROVs are used for "point-to-point" inspections, where the vehicle is submerged in the vicinity of the area

¹Sometimes referred to as uninhabited

of interest. AUVs are usually used for searching larger areas. A short list of advantages and disadvantages of remotely operated and autonomous vessels is given in Table 1.1.

Table 1.1. *A short list of basic advantages and disadvantages of remotely operated and autonomous vessels.*

	REMOTELY OPERATED	AUTONOMOUS
ADVANTAGES	<ul style="list-style-type: none"> • unlimited power supply • real-time signal transmission and reception to surface station • decreased need for safety algorithms because of the human in the loop 	<ul style="list-style-type: none"> • possibility of performing tedious, long lasting missions without wasting manpower • area of operation limited only by the amount of available power • possibility of covert operation
DISADVANTAGES	<ul style="list-style-type: none"> • small area of operation due to limited communication link ("point-to-point" search) • each vessel must have at least one operator assigned to it at all times during mission 	<ul style="list-style-type: none"> • limited power supply • live video feed not possible underwater • need for complex algorithms which ensure full autonomy (solutions to unexpected problems)

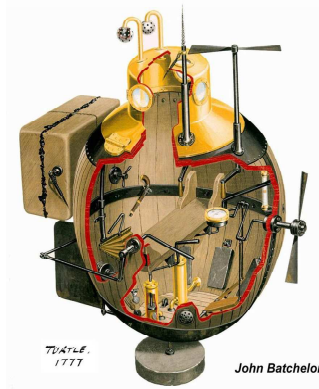
The first mention of automatically steered ships goes way back in history when fishermen used to bind the tiller or rudder of their boats in order to ensure optimal course, which increased the manpower used for releasing and recovering of nets. The concept of automation was first accepted during the industrial revolution, and the first autopilots appeared only in the first part of the twentieth century. First autopilots would mimic experienced helmsmen. It turned out this was in fact a proportional derivative controller, [72]. One of key figures in control theory is Minorski whose main contribution was the introduction of the proportional integral and derivative controller for ship steering, [49].

However, unmanned surface vessels do not appear in history until 1718. It was then that a former English Captain, now an infamous pirate, Charles Vane decided to escape a blockage imposed by Captain Woodes Rogers, by setting a brigantine without a crew on fire and directing it towards Rogers's warships. Once the brigantine approached, the cannons fired and the Royal Navy ships were forced to take evasive action, leaving a clear way for Vane to continue his piracy. He was captured three years later. After World War two, many projects involving radio controlled unmanned surface vehicles were initiated. In 1970, a number of European navies started developing radio controlled vessels as a new generation mine countermeasure systems. Multiple vessels were controlled of a manned mine countermeasure ships hence increasing the security of the crew and search area.

Great mathematicians through history were distinguished by their ideas which were



(a)



(b)

Figure 1.1. A short history view to the times of first submarines: (a) The demonstration of Drebbel's submarine with rows, and (b) the first one-man submarine *Turtle* used in military action.

far advanced for their contemporaries. One such was William Bourne who we have to thank for the first concept of a submarine in 1578. However, it was not until 1776 that a Dutchman Cornelius Drebbel used this concept to give a demonstration to King James I of the first oar based submersible which was able to cruise at depths 4 to 5 meters (see Fig. 1.1(a)). Not even the fact that James I took a ride in this leather coated vessel with a wooden frame was enough to track enough attention from the Admiralty – it was never used in combat. It was not until the American War of Independence that a submarine took part in naval operations. A Yale graduate and a great inventor David Bushnell, built in 1776 the *Turtle*, a hand-powered egg-shaped submarine with a single crew member (see Fig. 1.1(b)). The historic mission took place in the same year September 7, when Sergeant Ezra Lee² of Old Lyme, Connecticut had the honour to use the vessel to attach a mine to the bottom of the HMS *Eagle*, which was blocking the New York harbour. After two attempts, this ingenious plan failed. Ezra claimed the ship's copper sheathing could not have been penetrated. Since the British warships were not sheathed, the conclusion is raised that Ezra was exhausted due to increasing amount of carbon dioxide, setting the initial impetus for the search for unmanned underwater vehicles, [71].

An ancestor of a modern UUV could be considered a floating device, controlled from land, for destroying ships. It was developed by Captain Giovanni Luppis, member of the Austrian Navy born in Rijeka, Croatia³. After giving a successful presentation of the device he called *Salvacoste*⁴ to the emperor Franz Joseph in 1860, the naval

²At first, Ezra's namesake, David's brother, was supposed to carry out the mission.

³At that time Rijeka was called Fiume (Italian name) and was a part of the Austro-Hungarian empire. The Luppis family name derived from the Italian version de Lupis. Latin word for "wolf" is *lupus*, in Croatian it is "vuk", hence the Slavic form of the family name is Vukić.

⁴Italian for *Coast saver*

commission refused to accept it without better propulsion and control systems. It was then that he signed a contract with a British machine engineer Robert Whitehead who redesigned the torpedo to go under the waterline, making it more effective.

Even though the design of cable controlled underwater recovery vehicles was started by the US Navy in 1958, leading to successful recoveries of USS *Thresher* in 1963 and US Navy hydrogen bomb lost off the coast of Palomares, Spain in 1966, it was not until the discovery of offshore oil and gas supplies in the North Sea that commercial potential of UUVs, specifically ROVs, was recognized.

Marine vehicles can roughly be divided into three groups according to application: military, commercial and research vessels. As it was already mentioned, military UVs were the first UVs which appeared. Military applications include mine countermeasures, port security and harbour, anti-terrorism protection, force protection, surveillance and attack. Unmanned military applications nowadays refer mainly to surveillance and harbour protection (SAIC/Navtec Owl I and Owl II programmes which investigated the role of a small USV in the late 1990s) and recently anti-terrorism protection, force protection, shallow water anti-submarine warfare, shallow water mine countermeasures, covert surveillance and surface attack (US Spartan USV programme which focused on adaptation of standard 7 m and 11 m RIBs⁵ and a similar Israeli Protector USV with a stabilised machine gun onboard), [71]. However, torpedoes have been used for naval attack missions long before.

Commercial applications refer mainly to manned surface vessels which are used for transportation of merchandize around the world such as tankers, Ro-Ro⁶ boats, container ships, cruisers, ferries, etc. Even though this application is present since the first trading contacts of the old world with newly discovered territories, it is interesting that tanker ships were first developed during the Israeli Egyptian war in 1971 when Suez canal was closed down and classical trade routes were jammed. Transportation underwater vessels are not common, mainly due to safety reasons. This category also includes fishermen boats as well as boats used for tourists purposes. Tourist submarines are becoming more and more popular nowadays. They are usually not completely submerged, but are partially above water line, hence can be categorized as semi-submerged vessels. This category does not appear in an unmanned form, because of safety reasons, also. In addition to all mentioned, this category includes off-shore vessels.

Research vessels are usually unmanned vessels used for performing experiments in navigation, guidance and control, testing algorithms, familiarizing with the existing and the development of new technologies. In addition to that, these vessels are often used in research related to marine biology, underwater archeology, hydrography, oceanography, aquaculture, etc. Some autonomous surface research platforms which have been developed around the world are listed in the thesis, [10].

During the last two decades, MIT have developed the family of autonomous ves-

⁵Rigid inflatable boat

⁶Roll on – roll off

sels for education and civil applications, consisting of the fishing trawler-like vehicle ARTEMIS, the catamarans ACES⁷ and Auto-Cat, and the kayak SCOUT⁸, [23, 46, 47]. These USVs were used for testing automatic heading control, DGPS-based navigation, collecting hydrographic data, mission planning and for distributed acoustic underwater navigation (with the MIT Odyssey class AUVs). Some European projects in this field are the Measuring Dolphin MESSIN (developed and designed at the University of Rostock, Germany), [45]; the autonomous catamaran Delfim developed by the DSOR lab of Lisbon IST-ISR as a communication relay for a companion AUV; the autonomous catamaran Charlie by CNR-ISSIA Genova, Italy, [13], originally designed, developed and exploited for the collection of sea surface microlayer, and then upgraded for robotic research on autonomous vessels; the autonomous catamaran ROAZ (developed by the Autonomous Systems Laboratory at ISEP-Institute of Engineering of Porto), [48]; the autonomous catamaran Springer (developed by the University of Plymouth, UK, for tracing pollutants), [83].

Fig. 1.2 schematically describes different types of marine vessels grouped with regard to the medium in which they operate (surface, underwater), application (military, commercial, research) and crew (manned and unmanned). Unmanned vessels are divided according to mode of operation (remotely operated and autonomous). Red dots in the figure indicate that this type of vehicle is common in practice. This thesis will deal with unmanned marine vessels.

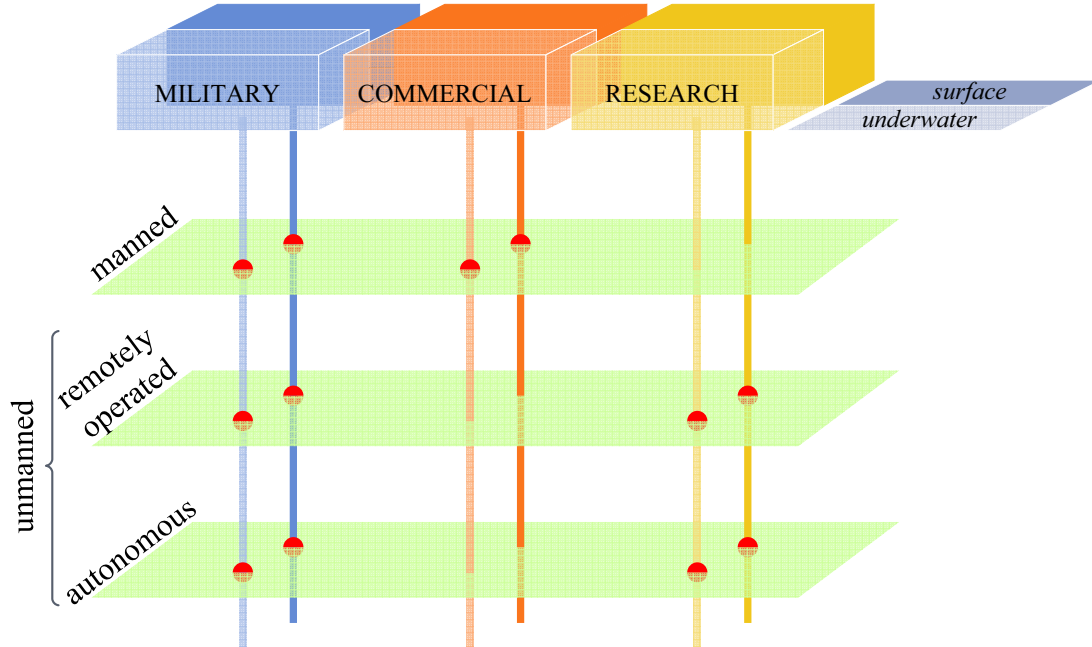


Figure 1.2. Marine vehicles according to medium of operation, application and crew.

⁷Autonomous Coastal Exploration System

⁸Surface Craft for Oceanographic and Undersea Testing

From the control point of view, autonomous vehicles require much more effort in control design and fail safe operation. In general, control structures for marine vehicles can be divided into three levels. The low level is responsible for control of the vehicles' speeds (surge, yaw rate, etc.), positions (depth, dynamic positioning, etc.) and orientations (heading, tilt angle, etc.), [16, 31]. Mid level of control is responsible for path following, trajectory tracking and it generates commands to the low level, [18]. High level of control is dedicated to mission management, mission planning (path and trajectory planning) and to safety issues (collision avoidance, fault tolerance, etc.), [65]. For a higher level to function properly, low levels have to be designed and they must work reliably. In order to design the low level control structure, UV mathematical model parameters have to be identified.

Many identification procedures applicable to marine vehicles can be found in the literature, and only few will be mentioned here. In order to identify mathematical model parameters of an underwater vehicle, different sensors can be used, such as inertial measurement units (IMUs), Doppler velocity loggers (DVLs), ultra-short baseline positioning systems (USBLs), etc., [17]. In research community, vision-based techniques are widely used, probably due to low cost. The position of an UV can be determined using a camera, and this data is then processed further to calculate higher order derivatives and consequently dynamic model parameters.

The above mentioned methodologies and apparatus allow application of classical process identification methods, [42]. These methods require time consuming experiments, great number of collected data and computations of high complexity, and can be quite tedious and impractical in situations where sensor suite of the ROV changes. The parameters of the mathematical model of the vehicle also change significantly and, unless this model was identified previously, heading and depth controllers will not behave in a satisfactory manner. Different payloads can be mounted on an UV (CTD probes, side-scan sonars, acoustic modems, etc.), depending on the application, and every time the model parameters will change. Performing conventional identification methods is tedious in these cases, and the need for a quick, feasible in the field, easily implementable method is required.

One of such methods has been used for ships and is called the "zig-zag" manoeuvre. It was first developed for evaluation of the ship manoeuvrability capabilities, and only later it was used to determine unknown parameters of the linear model of the ship. This thesis focuses on a method which uses similar oscillating data as in the "zig-zag" test, to determine linear and nonlinear model parameters of vessels. The proposed methodology enables quick and reliable parameter estimation in field conditions. The method has been proven to be applicable for controller design.

The thesis is organized as follows. Chapter 2 describes general mathematical models for marine vehicles. Each component of the control loop is described and detailed models are presented. Simplified models are derived which are appropriate for control design. Mathematical models for distance keeping and line following are presented since

these control systems will be designed later.

Chapter 3 describes marine vehicles and measuring devices which have been used in the thesis. The aim was to prove the functionality of the self-oscillation method on a vast range of marine systems – therefore an autonomous and a remotely controlled underwater vessel are described here together with an autonomous surface catamaran. In addition to that, two systems for data collection and distance keeping which are based on image processing are described.

Conventional identification techniques are described in Chapter 4. The focus has been placed on the classical least-squares identification and the previously mentioned "zig-zag" manoeuvre. An open loop step response technique, which is applicable in laboratory conditions is also presented.

Self-oscillations are introduced in Chapter 5. This section gives proof of theorems on the existence of self-oscillations and their characteristics. The conclusions raised from these theorems are used in the following chapter.

Chapter 6 describes the identification by use of self-oscillations method. Along with the generalized methodology for nonlinear systems, a convenient matrix-based algorithm, which is used for identification of static processes, is presented. This algorithm has then been modified for astatic systems, discrete-time systems and systems with delays. A detailed application of the proposed method to marine vehicles is given, and finally some implementation issues are addressed.

Chapter 7 presents extensive experimental results obtained from the laboratory and field experiments. The concept of identification by use of self-oscillations is tested and detailed validations have been presented. The proposed method is compared to conventional identification methods, and discussion on the results is given.

Chapter 8 is dedicated to control design. Control architecture which is common in marine vehicles is described and control methodology is presented. Experimental results which are obtained from the real vehicles are presented. These experiments are based on low-level algorithms, distance keeping and line following controllers. All the presented control algorithms have been designed on the basis of parameters identified by the method based on the identification by use of self-oscillations.

The thesis is concluded with Chapter 9 where a concise list of scientific contributions of this dissertation is given.

Mathematical Modeling of Marine Vehicles

In order to define the full mathematical model of a general marine vehicle, the terminology adopted from [25] will be used. First of all, two coordinate frames should be defined: an *Earth-fixed coordinate system* $\{E\}$ which is considered a steady, immobile coordinate frame, sometimes called the inertial coordinate system; and a *body-fixed coordinate system* $\{B\}$ which is usually attached to the centre of gravity (CG) of the vehicle whose model is to be defined. Variables that are included in the mathematical model of marine vehicles are linear and angular velocities, positions and orientations, and forces that excite the vehicle, as it is shown in Fig. 2.1. These are listed in Table 2.1 together with their names which are common in marine applications, according to SNAME¹ notation, [64].

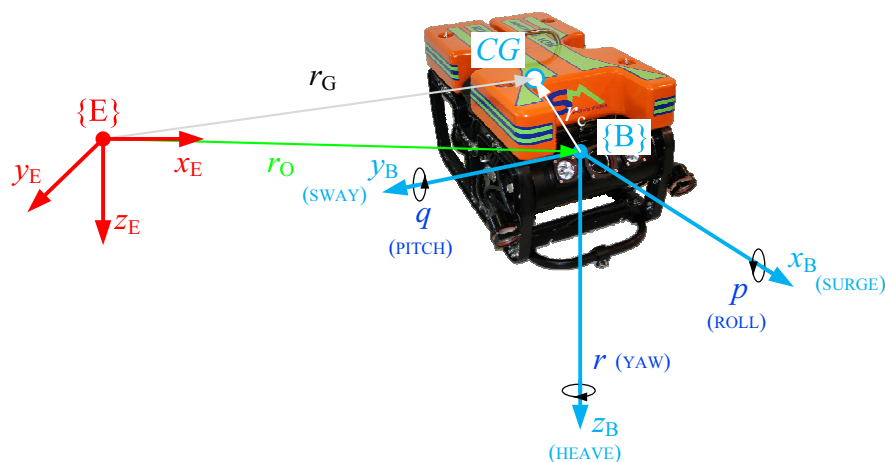


Figure 2.1. *Body-fixed and Earth-fixed coordinate frames.*

¹The Society of Naval Architects and Marine Engineers

Table 2.1. Notation used for marine vehicles

DOF	surge	sway	heave	roll	pitch	yaw	defined in
velocities	u	v	w	p	q	r	{B}
positions & angles	x	y	z	ϕ	θ	ψ	{E}
exciting forces & moments	X	Y	Z	K	M	N	{B}

Surge, sway and heave are defined as translational motion in the x -, y - and z -direction of {B} coordinate system, respectively, while roll, pitch and yaw are defined as rotation about x -, y - and z -axis in {B} coordinate system, respectively.

Earth-fixed coordinate system {E} is used to define vehicle's positions η_1 and orientations η_2 , forming a six element vector η .

$$\left. \begin{array}{l} \eta_1 = \begin{bmatrix} x & y & z \end{bmatrix}^T \\ \eta_2 = \begin{bmatrix} \phi & \theta & \psi \end{bmatrix}^T \end{array} \right\} \eta = \begin{bmatrix} \eta_1^T & \eta_2^T \end{bmatrix}^T \quad (2.1)$$

In the same manner, body-fixed coordinate frame is used to define vector \mathbf{v}_1 of linear velocities (surge, sway and heave), vector \mathbf{v}_2 of rotational velocities (roll, pitch and yaw) forming a six element vector \mathbf{v} .

$$\left. \begin{array}{l} \mathbf{v}_1 = \begin{bmatrix} u & v & w \end{bmatrix}^T \\ \mathbf{v}_2 = \begin{bmatrix} p & q & r \end{bmatrix}^T \end{array} \right\} \mathbf{v} = \begin{bmatrix} \mathbf{v}_1^T & \mathbf{v}_2^T \end{bmatrix}^T \quad (2.2)$$

Motion of the vehicle is achieved by applying external forces and moments. Three forces (each in the direction of one body-fixed frame axis) and three moments (defined as rotation about each body-fixed frame axis) form a six element vector of external forces as moments in the form

$$\boldsymbol{\tau} = \begin{bmatrix} X & Y & Z & K & M & N \end{bmatrix}^T. \quad (2.3)$$

External forces are exerted by actuators. Let τ^i denote commanded thrusts for each actuator ($i = 1, \dots, m$ where m is the number of actuators). These thrusts form a generalized vector $\boldsymbol{\tau}^i$ of size m . Let n^i denote commanded input for the i -th actuator (rotation speed of the propeller, rudder deflection, etc.). These inputs form a generalized vector \mathbf{n}^i of size m . Based on Fig. 2.2 and using the described notation, block diagram of a marine vehicle can be divided into 4 elementary parts:

1. Kinematic model which gives relations between positions and orientations η defined in {E} and speeds \mathbf{v} defined in {B},
2. Dynamic model which gives relations between the forces that act on the vessel $\boldsymbol{\tau}$ and the speeds \mathbf{v} exhibited by the vessel,

3. Actuator allocation which gives relations between forces exerted by actuators τ^i and forces that act on the vessel τ , and
4. Actuators which models the thrust exerted by actuators τ^i with regard to commanded input \mathbf{n}^i of each actuator.

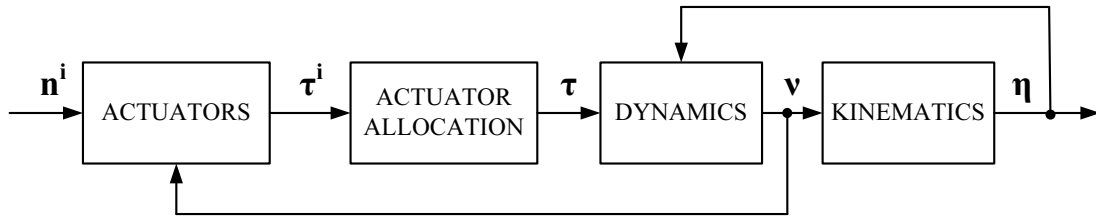


Figure 2.2. Block diagram of marine vehicle.

The following sections describe all parts of the model in more detail.

2.1 Actuators

Actuators in all technical systems are actuating devices that perform desired action on the system. In marine vehicles the same actuators can be found in underwater and surface vehicles. These can be divided roughly into

- thrusters (propulsors, propellers),
- control surfaces (rudders, fins, etc.) and
- mass.

Thrusters exist in many forms (bow thrusters, azimuth thrusters, etc.) and are based on a rotating propeller motion. They are most commonly used in marine vehicles and therefore will be described in detail in the following paragraph. Control surfaces are usually rudders and fins. While fins are mostly used for roll stabilization, rudders are used to control heave (indirectly via pitch) and yaw motion. Both are used since they ensure smooth motions of vehicles. Vehicles whose motion is controlled by moving the center of mass are called gliders, [40]. Changing the centre of mass causes the change in pitch which, given a surge speed, changes the depth of the vehicle. Gliders are slow moving underwater vehicles which are used for ocean sampling in specified water columns. It is worth mentioning a somewhat novel type of actuator which is based on a combination of propellers and rudders – the Voith–Schneider thruster. The rotating part has small rudders attached to it. Each of them rotates in such a way that a thrust vector is formed in the plane of rotation of the main part. This vector can be positioned arbitrarily in the plane making the vehicle controlled more efficiently than in the case of classical thrusters.

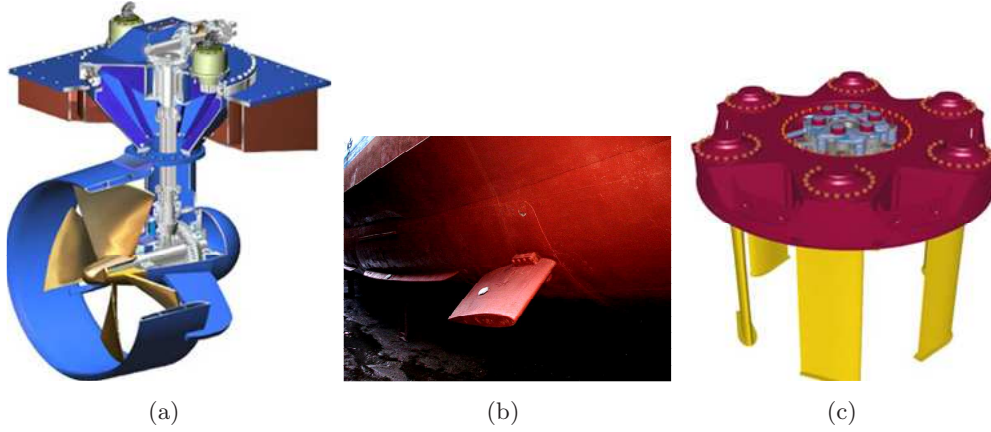


Figure 2.3. Some examples of actuators. (a) Azimuth thrusters which can rotate around the vertical axis therefore improving vessels manoeuvring capabilities (photo taken from www.thrustmastertexas.com). (b) Roll stabilizing fins mounted on a ship (photo taken from www.wikipedia.org). (c) Perspective view of the Voith–Schneider thruster (photo taken from www.marinelog.com).

In the following part a more detailed mathematical model of thrusters (propulsors) and rudders will be described.

Thrusters

In this thesis the discussion will be limited to classical thrusters (propulsors) since they are the most common in practice. As the thruster i rotates, it exerts thrust τ^i and torque q^i which can be described with

$$\begin{aligned}\tau^i &= T_{n|n} n^i |n^i| - T_{|n|u_a} |n^i| u_a \\ q^i &= Q_{n|n} n^i |n^i| - Q_{|n|u_a} |n^i| u_a\end{aligned}\quad (2.4)$$

where n^i (commanded input) is propeller revolution rate and $T_{n|n}$, $T_{|n|u_a}$, $Q_{n|n}$ and $Q_{|n|u_a}$ positive coefficients given by the propeller characteristics. This model is also known as the *bilinear thruster model*, [25]. Parameter u_a is sometimes called the ambient water velocity, [2, 65], and can be expressed with

$$u_a = (1 - u_{wake})U, \quad (2.5)$$

where u_{wake} is the so-called wake speed and U is the vessel's absolute speed given with

$$U = \sqrt{u^2 + v^2}. \quad (2.6)$$

The higher the ambient water velocity u_a , the smaller the exerted thrust will be. This means that if the vehicle is moving at a certain forward speed, the exerted thrust will be smaller than in the case when the vehicle is moving at smaller speed (given the

same propeller revolution rate). A simpler model given with (2.7) can be derived if ambient water speed u_a is neglected, where $a_{thruster}$ and $b_{thruster}$ are constant thruster parameters:

$$\tau^i = a_{thruster} |n^i| n^i + b_{thruster} n^i. \quad (2.7)$$

This model is more applicable in practice especially at low speeds. Further simplification gives that linear part of the model can also be neglected, i.e. $b_{thruster} = 0$, giving the so-called *affine model*.

However, the force exerted by thrusters is rarely the same when the propeller is rotating clockwise and counterclockwise. This is why a more complex model given with (2.8) should be used, [55], where subindices f and b denote 'forward' and 'backward'. An example of thrusters with identified characteristic as in (2.8) can be found in Chapter 4.1.

$$\tau^i = \begin{cases} a_f |n^i| n^i + b_f n^i, & n^i \geq 0 \\ a_b |n^i| n^i + b_b n^i, & n^i < 0 \end{cases} \quad (2.8)$$

Depending on the design of the thruster, 'positive' thrust can be exerted while the propeller rotates in clockwise or counterclockwise direction. The direction of the generated torque q^i is determined in both cases by the right-hand rule (curled fingers of the right hand point in the direction of rotation while the thumb points in the direction of the generated torque). Having this in mind, if a vehicle is equipped with two thruster positioned side-by-side (port and starboard thruster) and if both of them have the same 'positive' spin direction as shown in Fig. 2.4(a), generated torque from both thrusters is $q = q^1 + q^2$ causing the vehicle to perform unwanted rotation about the x - axes. This effect can be avoided if counter-rotating propellers are used, as shown in Fig. 2.4(b), so that the generated torque is $q = q^1 - q^2$ under the assumption that the propellers are the same.

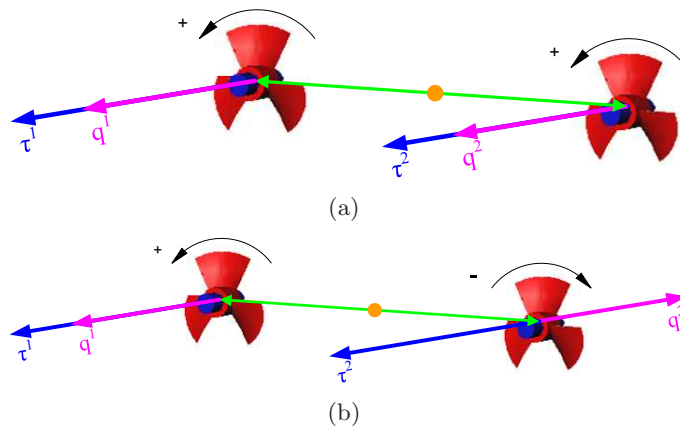


Figure 2.4. Propeller spin direction and exerted thrusts and torque for the case of a) the same and b) counter-rotating propellers.

Rudder

In this section, a rudder model given in [15] and [67] will be presented. This model assumes that the total resultant force generated by the rudder is normal to the central plane of the rudder. In order to generate a turning force to the vessel, some sort of water flow around the rudder is needed. This flow is usually generated with a thruster that is positioned in front of the rudder. The force achieved by the rudder acts from the centre of pressure (CP) as shown in Fig. 2.5 and can be described with

$$\tau^i = \begin{cases} c_F v_{av}^2 \sin\left(\frac{\pi}{2} \frac{\delta_a}{\delta_s}\right), & |\delta_a| < \delta_s \\ c_F v_{av}^2 \sin \delta_a, & |\delta_a| \geq \delta_s \end{cases}, \quad (2.9)$$

where δ is rudder angle, δ_a is the relative degree between the rudder and the flow (attack angle), δ_f is the angle of the flow in the body-fixed reference frame, and c_F is the rudder coefficient.

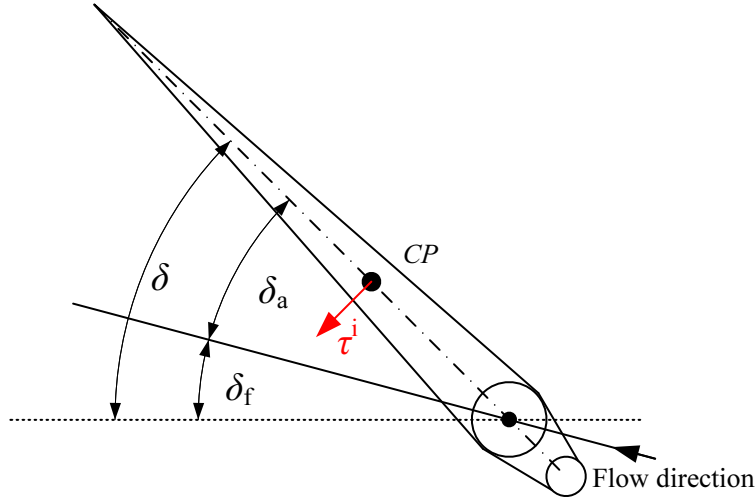


Figure 2.5. Rudder angles definition.

Stall angle is denoted with δ_s in (2.9) so the angle of attack can be computed as

$$\delta_a = \delta - \delta_f = \delta - \arctan\left(\frac{v + Lr}{u}\right)$$

where L is the distance from the rudder to the centre of mass of the vehicle in the x -direction. Parameter v_{av} is the average flow passing through the rudder and can, according to [67], be modeled with

$$v_{av}^2 = u_a^2 + C_T \tau \quad (2.10)$$

where τ is thrust generated by the propeller, u_a is ambient water velocity given with (2.5) and C_T is a constant parameter.

In the case when sway speed v is negligible and yaw rate r is small, the angle of attack can be approximated by the rudder angle δ . Having this in mind, the thrust exerted by the thruster can be written as

$$\tau^i = c_F v_{av}^2 \sin\left(\frac{\pi}{2\delta_s}\delta\right) \approx c_F v_{av}^2 \frac{\pi}{2\delta_s}\delta = k_F v_{av}^2 \delta \quad (2.11)$$

in the case where $|\delta_a| \approx |\delta| < \delta_s$ and the approximation $\sin \alpha \approx \alpha$ is assumed. By inserting a simplified version of (2.7) where $b_{thruster} = 0$ and (2.5) into (2.11), the equation (2.12) is obtained:

$$\tau^i = k_{r1} U^2 \delta + k_{r2} n |n| \delta \quad (2.12)$$

where k_{r1} and k_{r2} are constant parameters.

2.2 Actuator Allocation

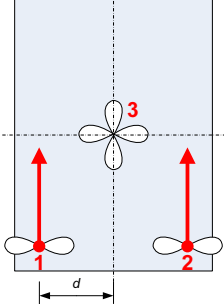
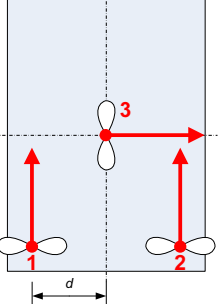
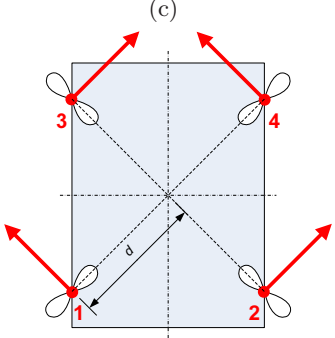
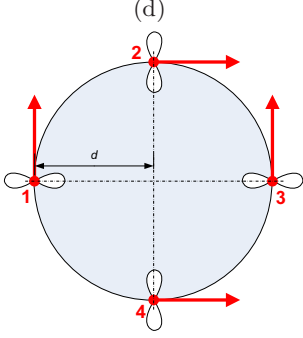
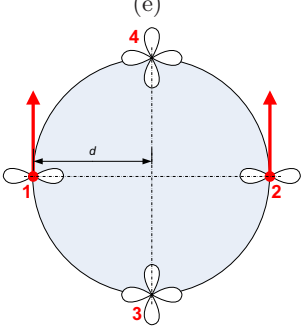
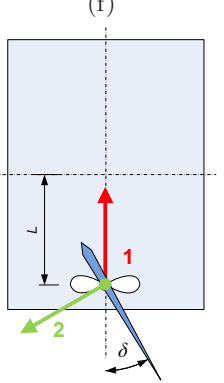
Actuator allocation is a connection between the space of actuator forces (described with vector τ^i) and the space of forces and moments (described with vector τ) in the body-fixed frame. The matrix which describes this link is called the *allocation matrix* and it depends on the number of available actuators and their topology. Table 2.2 gives some topologies and actuator allocations which can be found in practice on various vehicles (both surface and underwater).

The simplest and most common actuator topology is given with Table 2.2(a) (e.g. VideoRay ROV). The two horizontal thrusters can be placed anywhere on the sides of the vehicle. By adding generated port and starboard thrust, surge thrust X is obtained. The difference between the two thrusts generates a moment N which causes the vehicle to rotate about the z -axis. If a vertical thruster is available (in UVs), it ensures three degrees of freedom – surge, heave and yaw (allocation matrix has full rank 3).

The topology shown in Table 2.2(b) also has three DOF – surge, sway and yaw. Previously mentioned topologies and the one shown in Table 2.2(e) have as many degrees of freedom as there are thrusters. It is possible to ensure redundancy as it is shown in Table 2.2(c) and Table 2.2(d). In these cases four actuators are used to control three degrees of freedom. This is convenient in systems where fault tolerance is demanded – if one of the thrusters is faulty, the vehicle still remains with the same number of degrees of freedom, [65].

Topology shown in Table 2.2(f) represents the case when the vehicle is actuated with one thruster (to ensure surge motion) and a rudder (to ensure yaw motion). The thrust exerted by the rudder can be decomposed into the part which acts perpendicular to the x -axis, $\tau^2 \cos \delta$, and the one aligned with the x -axis, $\tau^2 \sin \delta$. The latter opposes the thrust generated by the thruster. It should be stressed that the force exerted by the rudder is dependent on δ as it is shown in (2.12).

Table 2.2. Some actuator configurations found in practice.

<p>(a)</p>  $\begin{bmatrix} X \\ Z \\ N \end{bmatrix} = \begin{bmatrix} 1 & 1 & 0 \\ 0 & 0 & 1 \\ d & -d & 0 \end{bmatrix} \begin{bmatrix} \tau^1 \\ \tau^2 \\ \tau^3 \end{bmatrix}$	<p>(b)</p>  $\begin{bmatrix} X \\ Y \\ N \end{bmatrix} = \begin{bmatrix} 1 & 1 & 0 \\ 0 & 0 & 1 \\ d & -d & 0 \end{bmatrix} \begin{bmatrix} \tau^1 \\ \tau^2 \\ \tau^3 \end{bmatrix}$
<p>(c)</p>  $\begin{bmatrix} X \\ Y \\ N \end{bmatrix} = \begin{bmatrix} a & a & a & a \\ -a & a & a & -a \\ d & -d & -d & d \end{bmatrix} \begin{bmatrix} \tau^1 \\ \tau^2 \\ \tau^3 \\ \tau^4 \end{bmatrix}$ <p style="text-align: center;">$a = \sin \frac{\pi}{4}$</p>	<p>(d)</p>  $\begin{bmatrix} X \\ Y \\ N \end{bmatrix} = \begin{bmatrix} 1 & 0 & 1 & 0 \\ 0 & 1 & 0 & 1 \\ d & d & -d & -d \end{bmatrix} \begin{bmatrix} \tau^1 \\ \tau^2 \\ \tau^3 \\ \tau^4 \end{bmatrix}$
<p>(e)</p>  $\begin{bmatrix} X \\ Z \\ M \\ N \end{bmatrix} = \begin{bmatrix} 1 & 1 & 0 & 0 \\ 0 & 0 & 1 & 1 \\ 0 & 0 & -d & d \\ d & -d & 0 & 0 \end{bmatrix} \begin{bmatrix} \tau^1 \\ \tau^2 \\ \tau^3 \\ \tau^4 \end{bmatrix}$	<p>(f)</p>  $\begin{bmatrix} X \\ Y \\ N \end{bmatrix} = \begin{bmatrix} 1 & -\sin \delta \\ 0 & -\cos \delta \\ 0 & L \cos \delta \end{bmatrix} \begin{bmatrix} \tau^1 \\ \tau^2(\delta) \end{bmatrix}$

2.3 Kinematic Model

Kinematic model gives the relation between the speeds \mathbf{v} in a body-fixed coordinate frame $\{B\}$ and first derivative of positions and angles $\boldsymbol{\eta}$ in an Earth-fixed coordinate system $\{E\}$. A full set of kinematic equations is given with (2.13), [25]:

$$\begin{bmatrix} \dot{\boldsymbol{\eta}}_1 \\ \dot{\boldsymbol{\eta}}_2 \end{bmatrix} = \begin{bmatrix} \mathbf{J}_1(\boldsymbol{\eta}_2) & \mathbf{0}_{3 \times 3} \\ \mathbf{0}_{3 \times 3} & \mathbf{J}_2(\boldsymbol{\eta}_2) \end{bmatrix} \begin{bmatrix} \mathbf{v}_1 \\ \mathbf{v}_2 \end{bmatrix} \Leftrightarrow \dot{\boldsymbol{\eta}} = \mathbf{J}(\boldsymbol{\eta})\mathbf{v} \quad (2.13)$$

where $\mathbf{0}_{3 \times 3}$ denotes a 3 by 3 null matrix,

$$\mathbf{J}_1(\boldsymbol{\eta}_2) = \begin{bmatrix} c\psi c\theta & -s\psi c\phi + c\psi s\theta s\phi & s\psi s\phi + c\psi s\theta c\phi \\ s\psi c\theta & c\psi c\phi + s\psi s\theta s\phi & -c\psi s\phi + s\psi s\theta c\phi \\ -s\theta & c\theta s\phi & c\theta c\phi \end{bmatrix}$$

and

$$\mathbf{J}_2(\boldsymbol{\eta}_2) = \begin{bmatrix} 1 & s\phi t\theta & c\phi t\theta \\ 0 & c\theta & s\phi \\ 0 & s\phi c^{-1}\theta & c\phi c^{-1}\theta \end{bmatrix}.$$

For the sake of brevity, c denotes cosine, s sine, t tangent and exponent -1 is the reciprocal function.

2.4 Dynamic Model

Dynamic model of a marine vehicle is nonlinear and coupled. For the sake of generality, let us assume that the centre of gravity (CG) does not coincide with the origin of the body-fixed coordinate system (O). In that case the dynamic equation which gives connection between velocities and accelerations of the rigid body and forces that act on it can be written in a form, [25]

$$\mathbf{M}_{RB}\dot{\mathbf{v}} + \mathbf{C}_{RB}(\mathbf{v})\mathbf{v} = \boldsymbol{\tau}_{RB}. \quad (2.14)$$

\mathbf{M}_{RB} is a rigid-body inertia matrix described with

$$\begin{aligned} \mathbf{M}_{RB} &= \begin{bmatrix} m\mathbf{I}_{3 \times 3} & -m\mathbf{S}(\mathbf{r}_G) \\ m\mathbf{S}(\mathbf{r}_G) & \mathbf{I}_0 \end{bmatrix} = \\ &= \begin{bmatrix} m & 0 & 0 & 0 & mz_G & -my_G \\ 0 & m & 0 & -mz_G & 0 & mx_G \\ 0 & 0 & m & my_G & -mx_G & 0 \\ 0 & -mz_G & my_G & I_x & -I_{xy} & -I_{xz} \\ mz_G & 0 & -mx_G & -I_{yx} & I_y & -I_{yz} \\ -my_G & mx_G & 0 & -I_{zx} & I_{zy} & I_z \end{bmatrix} \end{aligned} \quad (2.15)$$

where m is mass of the vehicle, \mathbf{r}_G is centre of gravity with respect to $\{B\}$

$$\mathbf{r}_G = \begin{bmatrix} x_G \\ y_G \\ z_G \end{bmatrix}, \quad (2.16)$$

\mathbf{I}_0 is inertia tensor with respect to $\{B\}$

$$\mathbf{I}_0 = \begin{bmatrix} I_x & -I_{xy} & -I_{xz} \\ -I_{yx} & I_y & -I_{yz} \\ -I_{zx} & -I_{zy} & I_z \end{bmatrix} \quad (2.17)$$

with I_x , I_y and I_z being moments of inertia about respective axes in the body-fixed frame

$$\begin{aligned} I_x &= \int_V (y^2 + z^2) \rho_A dV \\ I_y &= \int_V (x^2 + z^2) \rho_A dV, \\ I_z &= \int_V (x^2 + y^2) \rho_A dV \end{aligned} \quad (2.18)$$

$I_{xy} = I_{yx}$, $I_{xz} = I_{zx}$ and $I_{yz} = I_{zy}$ being products of inertia

$$\begin{aligned} I_{xy} &= \int_V xy \rho_A dV \\ I_{xz} &= \int_V xz \rho_A dV \\ I_{yz} &= \int_V yz \rho_A dV \end{aligned} \quad (2.19)$$

where ρ_A is the mass density of the body. It is worth noting that the rigid-body inertia matrix has the following properties: $\mathbf{M}_{RB} = \mathbf{M}_{RB}^T > 0$ and $\frac{d}{dt} \mathbf{M}_{RB} = 0$.

\mathbf{C}_{RB} is the rigid-body Coriolis and centripetal matrix described with

$$\begin{aligned} \mathbf{C}_{RB} &= \begin{bmatrix} \mathbf{0}_{3 \times 3} & -m\mathbf{S}(\mathbf{v}_1) - m\mathbf{S}(\mathbf{S}(\mathbf{v}_2)\mathbf{r}_G) \\ -m\mathbf{S}(\mathbf{v}_1) - m\mathbf{S}(\mathbf{S}(\mathbf{v}_2)\mathbf{r}_G) & m\mathbf{S}(\mathbf{S}(\mathbf{v}_1)\mathbf{r}_G) - \mathbf{S}(\mathbf{I}_0\mathbf{v}_2) \end{bmatrix} = \\ &= \begin{bmatrix} 0 & 0 & 0 & \cdots \\ 0 & 0 & 0 & \cdots \\ 0 & 0 & 0 & \cdots \\ -m(y_G q + z_G r) & m(y_G p + w) & m(z_G p - w) & \cdots \\ m(x_G q - w) & -m(z_G r + x_G p) & m(z_G q + u) & \cdots \\ m(x_G r + v) & m(y_G r - u) & -m(x_G p + y_G q) & \cdots \\ \cdots & m(y_G q + z_G r) & -m(x_G q - w) & m(x_G r + v) \\ \cdots & -m(y_G p + w) & m(z_G r + x_G p) & -m(y_G r - u) \\ \cdots & -m(z_G p - w) & -m(z_G q + u) & m(x_G p + y_G q) \\ \cdots & 0 & -I_{yz} q - I_{xz} p + I_z r & I_{yz} r + I_{xy} p - I_y q \\ \cdots & I_{yz} q + I_{xz} p - I_z r & 0 & -I_{xz} r - I_{xy} q + I_x p \\ \cdots & -I_{yz} r - I_{xy} p + I_y q & I_{xz} r + I_{xy} q - I_x p & 0 \end{bmatrix} \end{aligned} \quad (2.20)$$

$\boldsymbol{\tau}_{RB}$ is a generalized vector of forces and moments. It includes the following forces and moments:

1. Hydrodynamic rigid-body-like added mass forces and moments $-\mathbf{M}_A\dot{\mathbf{v}}$,
2. Hydrodynamic Coriolis-like added mass forces and moments $-\mathbf{C}_A(\mathbf{v})\mathbf{v}$,
3. Hydrodynamic damping and lift forces and moments $-\mathbf{D}(\mathbf{v})\mathbf{v}$,
4. Restoring (gravitational and buoyant) forces and moments $-\mathbf{g}(\boldsymbol{\eta})$,
5. Environmental forces and moments $\boldsymbol{\tau}_E$ and
6. Propulsion forces and moments (generated by the actuators) $\boldsymbol{\tau}$.

These elements form the rigid-body forces and moments equation, [25]

$$\boldsymbol{\tau}_{RB} = \boldsymbol{\tau}_E + \boldsymbol{\tau} - \mathbf{M}_A\dot{\mathbf{v}} - \mathbf{C}_A(\mathbf{v})\mathbf{v} - \mathbf{D}(\mathbf{v})\mathbf{v} - \mathbf{g}(\boldsymbol{\eta}). \quad (2.21)$$

Added-mass matrix \mathbf{M}_A and added-mass Coriolis and centripetal matrix $\mathbf{C}_A(\mathbf{v})$ are parameters which represent the effects that occur while moving through a fluid. Added (virtual) mass should be understood as pressure-induced forces and moments due to a forced harmonic motion of the body, which are proportional to the acceleration of the body, [2, 25, 63]. Consequently, the added mass forces and the acceleration will be 180° out of phase to the forced harmonic motion. If the ROV moves at low speed and has (almost) three planes of symmetry, then the following expressions for \mathbf{M}_A and $\mathbf{C}_A(\mathbf{v})$ are obtained:

$$\mathbf{M}_A = -diag\{X_{\dot{u}}, Y_{\dot{v}}, Z_{\dot{w}}, K_{\dot{p}}, M_{\dot{q}}, N_{\dot{r}}\} \quad (2.22)$$

$$\mathbf{C}_A = \begin{bmatrix} 0 & 0 & 0 & 0 & -Z_{\dot{w}}w & Y_{\dot{v}}v \\ 0 & 0 & 0 & Z_{\dot{w}}w & 0 & -X_{\dot{u}}u \\ 0 & 0 & 0 & -Y_{\dot{v}}v & X_{\dot{u}}u & 0 \\ 0 & -Z_{\dot{w}}w & Y_{\dot{v}}v & 0 & -N_{\dot{r}}r & M_{\dot{q}}q \\ Z_{\dot{w}}w & 0 & -X_{\dot{u}}u & N_{\dot{r}}r & 0 & K_{\dot{p}}p \\ -Y_{\dot{v}}v & X_{\dot{u}}u & 0 & -M_{\dot{q}}q & -K_{\dot{p}}p & 0 \end{bmatrix} \quad (2.23)$$

The notation of SNAME, [64], is used in expressions (2.22) and (2.23). For instance, the hydrodynamic added mass force Y_A along the y -axis due to an acceleration \dot{u} in the x -direction is written as $Y_A = Y_{\dot{u}}\dot{u}$ where $Y_{\dot{u}} \triangleq \frac{\partial Y}{\partial \dot{u}}$.

Total hydrodynamic damping matrix $\mathbf{D}(\mathbf{v})$ is highly complex and has nonlinear dependence to the speed of the vehicle. However, this matrix can be approximated with a diagonal structure with only linear and quadratic damping terms.

$$\mathbf{D}(\mathbf{v}) = -diag\{X_u + X_{|u|}|u|, Y_v + Y_{|v|}|v|, Z_w + Z_{|w|}|w|, K_p + K_{|p|}|p|, M_q + M_{|q|}|q|, N_r + N_{|r|}|r|\} \quad (2.24)$$

Restoring forces $\mathbf{g}(\boldsymbol{\eta})$ consist of a gravitational force and a buoyant force. Gravitational force is induced by weight W of the vehicle and acts through the centre of gravity $\mathbf{r}_G = \begin{bmatrix} x_G & y_G & z_G \end{bmatrix}^T$ of the vehicle. Buoyant force is induced by buoyancy

B and elevates the vehicle to the surface. It acts through the centre of buoyancy $\mathbf{r}_B = [x_B \ y_B \ z_B]^T$ which need not necessarily be at the same place as the centre of gravity (CG). Restoring forces are defined in the body-fixed frame $\{B\}$ and have the following form:

$$\mathbf{g}(\boldsymbol{\eta}) = \begin{bmatrix} (W - B) \sin \theta \\ -(W - B) \cos \theta \sin \varphi \\ -(W - B) \cos \theta \cos \varphi \\ -(y_G W - y_B B) \cos \theta \cos \varphi + (z_G W - z_B B) \cos \theta \sin \varphi \\ (z_G W - z_B B) \sin \theta + (x_G W - x_B B) \cos \theta \cos \varphi \\ -(x_G W - x_B B) \cos \theta \sin \varphi - (y_G W - y_B B) \sin \theta \end{bmatrix}. \quad (2.25)$$

Environmental forces and moments $\boldsymbol{\tau}_E$ are forces which act as the disturbance on the vehicle. These forces cannot be easily modeled and control systems are designed in such a way that these effects are attenuated. The main environmental forces to be considered for marine vehicles are surface waves, wind and ocean currents.

Actuation forces and moments $\boldsymbol{\tau}$ are forces exerted by actuators. More details on these forces can be found in Chapter 2.1.

Now that all the forces have been described, a full dynamic equation of forces acting on marine vehicles can be written as

$$\underbrace{(\mathbf{M}_{RB} + \mathbf{M}_A)}_{\mathbf{M}} \dot{\mathbf{v}} + \underbrace{(\mathbf{C}_{RB}(\mathbf{v}) + \mathbf{C}_A(\mathbf{v}))}_{\mathbf{C}(\mathbf{v})} \mathbf{v} + \mathbf{D}(\mathbf{v})\mathbf{v} + \mathbf{g}(\boldsymbol{\eta}) = \boldsymbol{\tau} + \boldsymbol{\tau}_E, \quad (2.26)$$

leaving only actuation and environmental forces on the right-hand side, [25].

2.5 Model Simplifications

In the previous section, a full mathematical model which describes behavior of marine vessels has been described. It was shown that this model is highly complex, with many parameters, couplings and nonlinear dynamics. These effects come as a consequence the six DOF motion and hydrodynamic effects. These mathematical models are usually implemented in simulators where it is highly important to include, as realistically as possible, all effect which may occur.

However, the situation is somewhat different when designing control systems for marine vessels. These mathematical models are often simplified for this purpose. Two simplifications that will be described in the following sections include limiting 6 DOF to 3 DOF in the horizontal plane and decoupling of motions. The first simplification is usual for surface vessels and underwater vehicles that operate at constant depth. The second simplification is used for vessels that move at low speed which causes Coriolis and centripetal effects to be negligible. In addition to that, a practical model, suitable for control design of small surface vessels is presented.

2.5.1 Coupled model in the horizontal plane

Often, for underwater applications, vehicles are trimmed in such a way that motions in horizontal plane are decoupled from heave motion. This is usually accomplished by appropriate positioning of ballast weights. Roll and pitch motions are often not controllable in underwater vehicles. They are considered as self-stabilizing degrees of freedom. This is the case due to restoring forces that exist here and also due to design of the vehicles. In surface marine vehicles, roll and pitch can be passively controlled (using fins) or actively controlled mainly to avoid parametric resonance using active fins, rudder or by other means, [27].

Because of these reasons, the complex dynamic model can be simplified if the above mentioned degrees of freedom are set to 0 ($w = \phi = \theta = 0$) and if motion in horizontal plane only is observed. This reduces the six-degree of freedom model (2.26) to only three degrees of freedom: surge (u), sway (v) and yaw (ψ). This way the kinematic model (2.13) is reduced to

$$\begin{bmatrix} \dot{x} \\ \dot{y} \\ \dot{\psi} \end{bmatrix} = \begin{bmatrix} \cos \psi & -\sin \psi & 0 \\ \sin \psi & \cos \psi & 0 \\ 0 & 0 & 1 \end{bmatrix} \begin{bmatrix} u \\ v \\ r \end{bmatrix} \quad (2.27)$$

while the full dynamic model given with (2.26) is reduced to

$$\begin{aligned} & \underbrace{\begin{bmatrix} m - X_{\dot{u}} & -X_{\dot{v}} & -my_G \\ -X_{\dot{v}} & m - Y_{\dot{v}} & mx_G \\ -my_G & mx_G & I_z - N_{\dot{r}} \end{bmatrix}}_{\mathbf{M}_{RB} + \mathbf{M}_A} \begin{bmatrix} \dot{u} \\ \dot{v} \\ \dot{r} \end{bmatrix} + \\ & \underbrace{\begin{bmatrix} 0 & 0 & -m(x_{Gr} + v) + Y_{\dot{v}}v \\ 0 & 0 & -m(y_{Gr} - u) - X_{\dot{u}}u \\ m(x_{Gr} + v) - Y_{\dot{v}}v & m(y_{Gr} - u) + X_{\dot{u}}u & 0 \end{bmatrix}}_{\mathbf{C}_{RB}(\nu) + \mathbf{C}_A(\nu)} \begin{bmatrix} u \\ v \\ r \end{bmatrix} \\ & - \underbrace{\begin{bmatrix} X_u + X_{u|u}|u| & 0 & 0 \\ 0 & Y_v + Y_{v|v}|v| & 0 \\ 0 & 0 & N_r + N_{r|r}|r| \end{bmatrix}}_{\mathbf{D}(\nu)} \begin{bmatrix} u \\ v \\ r \end{bmatrix} = \begin{bmatrix} X \\ Y \\ N \end{bmatrix} + \begin{bmatrix} \tau_{XE} \\ \tau_{YE} \\ \tau_{NE} \end{bmatrix} \end{aligned} \quad (2.28)$$

2.5.2 Uncoupled model for underwater vehicles

Coupling effects in (2.28) appear for the following reasons:

- existence of coupled terms in the added mass matrix ($X_{\dot{v}}$),
- existence of Coriolis and centripetal forces and

- difference between the centre of gravity and the origin of the body-fixed coordinate frame (vector \mathbf{r}_G not being null vector).

The first reason is almost always neglected because the term $X_{\dot{v}}$ has insignificant influence on the behavior of the vehicle, [25]. If it is assumed that the vehicle is moving at slow speed, the effect of Coriolis and centripetal forces can also be neglected. This simplification is almost always performed in modeling underwater vehicles, [70]. Incoincidence of the centre of gravity and the origin of the body-fixed coordinate system can be neglected in underwater vehicles of smaller dimensions [51].

The simplifications which are introduced in order to obtain an uncoupled model for underwater vehicles are:

- coupled added mass terms are negligible,
- centre of gravity (*CG*) coincides with the origin of the body-fixed coordinate frame $\{B\}$, i.e. $\mathbf{r}_G = \mathbf{0}$,
- pitch and roll motion difference between the centre of gravity and the origin of the body-fixed coordinate frame,
- roll and pitch motion are negligible, i.e. $\varphi = \theta = p = q = 0$.

As a consequence of these simplifications

- total mass matrix $\mathbf{M}_{RB} + \mathbf{M}_A$ is diagonal,
- the total Coriolis and the centripetal matrix $\mathbf{C}_{RB}(\nu) + \mathbf{C}_A(\nu)$ vanishes, and
- restoring forces influence only the heave degree of freedom.

These simplifications lead to the following uncoupled, nonlinear dynamic equations for

- surge DOF

$$(m - X_{\dot{u}}) \dot{u} - (X_u + X_{u|u}|u|) u = X + \tau_{XE} \quad (2.29)$$

- sway DOF

$$(m - Y_{\dot{v}}) \dot{v} - (Y_v + Y_{v|v}|v|) v = Y + \tau_{YE} \quad (2.30)$$

- heave DOF

$$(m - Z_{\dot{w}}) \dot{w} - (Z_w + Z_{w|w}|w|) w - (W - B) = Z + \tau_{ZE} \quad (2.31)$$

- yaw DOF

$$(I_z - N_{\dot{r}}) \dot{r} - (N_r + N_{r|r}|r|) r = N + \tau_{NE}. \quad (2.32)$$

Equations (2.29)–(2.32) can be represented with a single equation:

$$\boxed{\alpha_\nu \dot{\nu}(t) + \beta(\nu) \cdot \nu(t) = \Delta + \tau(t)} \quad (2.33)$$

where parameters $\nu(t)$, $\tau(t)$, Δ , α_ν and $\beta(\nu(t))$ are interpreted in Table 2.3 for each degree of freedom.

Table 2.3. Parameters in (2.33) depending on the DOF.

DOF	$\nu(t)$	α_ν	$-\beta(\nu)$	Δ	$\tau(t)$
surge	u	$m - X_{\dot{u}}$	$X_u + X_{u u} u $	τ_{XE}	X
sway	v	$m - Y_{\dot{v}}$	$Y_v + Y_{v v} v $	τ_{YE}	Y
heave	w	$m - Z_{\dot{w}}$	$Z_w + Z_{w w} w $	$\tau_{ZE} + W - B$	Z
yaw	r	$I_r - N_{\dot{r}}$	$N_r + N_{r r} r $	τ_{NE}	N

Further simplification includes the dominance of constant or linear drag only. It has been shown in literature that usually for small speed constant, drag can be approximated with a constant while at higher speeds linear drag better describes the dynamics of the vehicle, [25]. In other words, general drag $\beta(\nu)$ can obtain one of the two values:

$$\beta(\nu) = \begin{cases} \beta_\nu & \text{for constant drag} \\ \beta_{\nu\nu} |\nu| & \text{for linear drag} \end{cases}. \quad (2.34)$$

2.5.3 Practical model for small surface vessels

This model is derived for the actuator configuration which is found on Charlie catamaran, [14, 15], which is described in detail in Chapter 3.3. Charlie USV² is a small catamaran equipped with two stern thrusters. Each of the thrusters has a small rudder used for steering. The actuator configuration on Charlie is shown in Fig. 2.6 and is similar to the one in Table 2.2(f). Dynamic equations which describe behavior of Charlie ASV are (2.30) for surge, (2.32) for yaw and (2.30) for sway DOF. Actuator forces that act on the vehicle can be expressed with

$$\begin{aligned} X &= \underbrace{\tau^{p1} + \tau^{p2}}_{X_p(n,\cdot)} - \underbrace{(\tau^{r1} + \tau^{r2}) \sin \delta}_{X_r(\delta,\cdot)} \\ Y &= -(\tau^{r1} + \tau^{r2}) \cos \delta \\ N &= \underbrace{d(\tau^{p1} - \tau^{p2}) + \Delta(\tau^{p1} + \tau^{p2})}_{N_p(n,\cdot)} + \underbrace{(\tau^{r1} + \tau^{r2}) L \cos \delta + [(d - \Delta)\tau^{r2} - (d + \Delta)\tau^{r1}] \sin \delta}_{N_r(\delta,\cdot)}, \end{aligned} \quad (2.35)$$

where

²Unmanned surface vessel

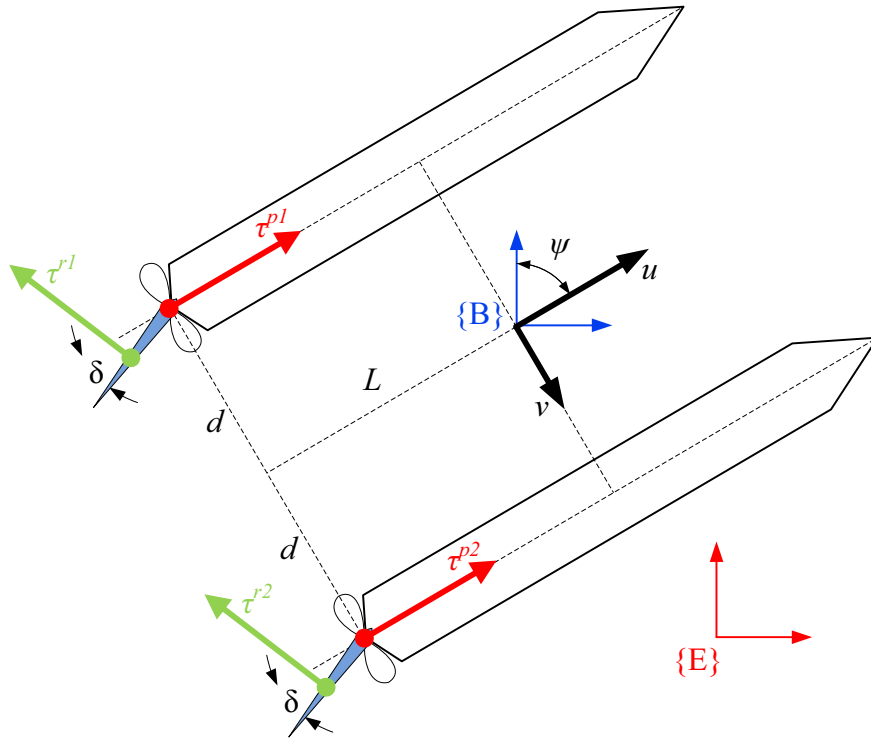


Figure 2.6. Small catamaran Charlie configuration.

- $X_p(n, \cdot)$ is thruster induced surge force,
- $X_r(\delta, \cdot)$ is resistance force induced by the rudder in surge direction,
- $N_p(n, \cdot)$ is thruster induced yaw moment with Δ_d being a possible small displacement of the centre of the mass with respect to the longitudinal axis of the vessel, and
- $N_r(\delta, \cdot)$ is yaw moment induced by rudder action.

External disturbances are omitted for the sake of clarity.

Charlie does not use thrusters to perform yaw motion. This is why the same control action is applied to both thrusters all the time, i.e. $\tau^{p1} = \tau^{p2} = \tau^p$. In addition to that, for the sake of simplicity, both rudders are also always commanded the same deflection angles, i.e. $\tau^{r1} = \tau^{r2} = \tau^r$. The term due to small displacement is neglected since $\Delta_d \delta \ll L$. Having this in mind and by making a valid assumption that $\sin \delta \approx \delta$ and

$\cos \delta \approx 1$ for small δ , (2.35) can be rewritten as

$$\begin{aligned} X &= \underbrace{2\tau^p}_{X_p(n,\cdot)} \underbrace{-2\tau^r \delta}_{X_r(\delta,\cdot)} \\ Y &= -2\tau^r \\ N &= \underbrace{2\Delta_d \tau^p}_{N_p(n,\cdot)} + \underbrace{2(L - \Delta_d \delta) \tau^r}_{N_r(\delta,\cdot)} \simeq \underbrace{2\Delta_d \tau^p}_{N_p(n,\cdot)} + \underbrace{2L\tau^r}_{N_r(\delta,\cdot)} \end{aligned} \quad (2.36)$$

Using expression (2.8) for τ^p (with $b_{thruster} = 0$) and (2.12) for τ^r , the following mathematical model which uses control inputs n and δ can be written:

$$\begin{aligned} X &= 2a |n| n - 2k_{r1} U^2 \delta^2 - 2k_{r2} |n| n \delta^2 \\ Y &= -2k_{r1} U^2 \delta - 2k_{r2} |n| n \delta \\ N &= 2\Delta_d a |n| n + 2Lk_{r1} U^2 \delta + 2Lk_{r2} |n| n \delta \end{aligned} \quad (2.37)$$

In cases when the vessel speed is negligible, from (2.6) it follows that $U = u$. By combining (2.37), (2.29) and (2.32) a set of equations is obtained³ which can be given with the following form:

$$\boxed{\begin{aligned} \alpha_u \dot{u} - (\beta_u + \beta_{uu} |u|) u &= -\hat{k}_{u^2 \delta^2} u^2 \delta^2 - \hat{k}_{n^2 \delta^2} n^2 \delta^2 + n^2 \\ \alpha_r \dot{r} - (\beta_r + \beta_{rr} |r|) r &= \hat{k}_{u^2 \delta} u^2 \delta + \hat{k}_{n^2} n^2 + n^2 \delta^2 \end{aligned}} \quad (2.38)$$

It should be noted that in (2.38) parameters α_u , β_u , β_{uu} , α_r , β_r , β_{rr} are not real added mass (inertia) and drag parameters, but normalized values. For the sake of simplicity, the same notation will be used for the normalized values.

2.6 Distance Keeping Model

The main task of distance keeping algorithms is to ensure that the vehicle keeps either a predefined distance from a fixed object (during inspections) or follows a moving object keeping a safe distance. For this purpose, a mathematical model which gives relation between vehicle behavior and distance and angle with regard to the surface has to be developed.

The mathematical model of distance keeping is derived based on Fig. 2.7 and is given in the following part. Using (2.33), the dynamic part of the model can be written with equations (2.39) and (2.40). Parameters $\beta(u)$ and $\beta(r)$ can be constant or linear, according to (2.34), which results in a linear or nonlinear dynamic model respectively:

$$\dot{u} = -\frac{\beta(u)}{\alpha_u} u + \frac{1}{\alpha_u} X \quad (2.39)$$

$$\dot{r} = -\frac{\beta(r)}{\alpha_r} r + \frac{1}{\alpha_r} N. \quad (2.40)$$

³After normalization so that control action n^2 and $n^2 \delta$ has unitary coefficient.

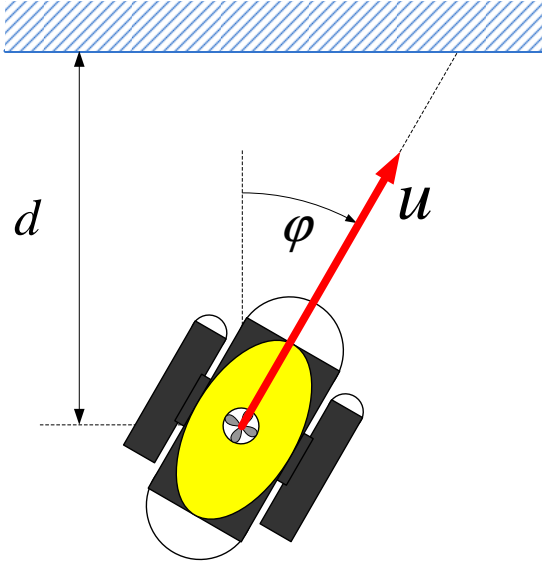


Figure 2.7. Variables used for determining the distance keeping mathematical model.

Parameter φ is the angle of the vessel's coordinate system with respect to the plane-like surface. Kinematic models for ψ and φ are the same and can be expressed with

$$\dot{\varphi} = r + v_{\varphi} \quad (2.41)$$

$$\dot{\psi} = r + v_{\varphi}, \quad (2.42)$$

where the variable v_{φ} is the disturbance that may act on the yaw degree of freedom of the vessel. The kinematic equation which describes distance d of the vessel with respect to the plane-like surface is given with

$$\dot{d} = -u \cos \varphi + v_d, \quad (2.43)$$

where the variable v_d represents disturbance that may act on the surge degree of freedom of the vessel.

For the sake of simplicity, disturbances v_{φ} and v_d are assumed to be constant, so the model can be augmented with two additional equations (2.44) and (2.45). These two states can also be interpreted as terms which include all the unknown dynamics of the system:

$$\dot{v}_{\varphi} = 0 \quad (2.44)$$

$$\dot{v}_d = 0. \quad (2.45)$$

Equations (2.39)–(2.45) give the full distance keeping model for marine vessels.

If angle φ is small enough, i.e. $\varphi \approx 0$, the vessel is almost perpendicular to the

surface and (2.43) can be simplified and written as (2.46), which approximates this kinematic equation with a linear one and makes control system design easier:

$$\dot{d} = -u + v_d. \quad (2.46)$$

Distance keeping control design is described in detail in Chapter 8.2.

2.7 Line Following

Line following is a mission which is based on setting a straight line which a vehicle has to follow. The line can be described by using two points and the orientation of the line, or one point, and an oriented vector.

The line following approach is graphicly described in Fig. 2.8. The main assumption is that the vessel is moving at a constant surge speed u_r . The aim is to steer the vehicle in such a way that its path converges to the desired straight line. In Fig. 2.8, γ denotes the orientation of the straight line that should be followed. A new parameter $\varphi = \psi - \gamma$, which is the vessel's orientation relative to the line, is defined.

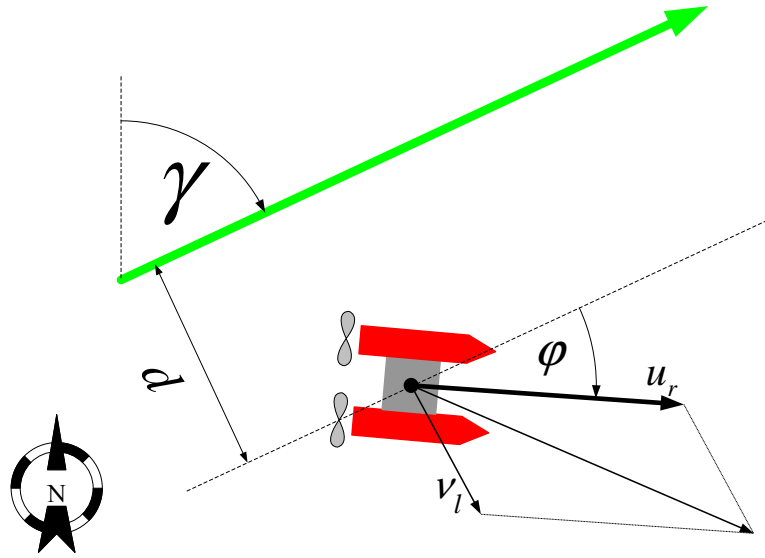


Figure 2.8. Line following scheme.

Using (2.33), the dynamic part of the yaw degree of freedom model can be written with (2.47), where parameter $\beta(r)$ can be constant or linear, according to (2.34).

$$\dot{r} = -\frac{\beta(r)}{\alpha_r}r + \frac{1}{\alpha_r}N \quad (2.47)$$

$$\dot{\psi} = r \quad (2.48)$$

$$\dot{\varphi} = r \quad (2.49)$$

$$\dot{d} = u_r \sin \varphi + v_l \quad (2.50)$$

The kinematic equation which describes distance d of the vessel with respect to the line is given with (2.50), where ν_l is the external disturbance which is assumed to be perpendicular to line.

The nonlinearities of the line-following model can appear in (2.47) and are inherent to (2.50). The first one can be eliminated by introducing a yaw rate or heading feedback, which will be described later. The second nonlinear equation can be linearized if angle φ is assumed to be small, i.e. $\varphi \approx 0$. In this case, (2.50) can be simplified and written with (2.51) what approximates this kinematic equation with a linear one and makes control system design easier:

$$\dot{d} = u_r \varphi + \nu_l. \quad (2.51)$$

An extensive control design procedure for line following is given in Chapter 8.3.

2.8 Conclusion

This chapter presented detailed mathematical models for marine vessels. The initial step was to define two coordinate systems which were then used to derive motion equations. A general modeling scheme which consists of actuators, actuator allocation, kinematic and dynamic model is given. All four elements are described giving equations which can be used to describe thrusters, rudders, actuator allocation, and full kinematic and dynamic behavior of marine vessels. Model simplifications which were introduced are based on the need to develop simpler models for control design. That is why models in horizontal plane and uncoupled models have been presented. The main conclusion from these models is that surface and underwater vehicles can be described using practically the same sets of equations.

In addition to that, mathematical models for distance keeping and line following have been developed. Both models include dynamic behavior which cannot be neglected in marine applications. The models that have been described here will be used later on for the purpose of control design.

Systems

This chapter will give descriptions of three marine vehicles that have been used for experiments, and two sensors that were developed primarily for the purpose of performing identification and control experiments.

The vehicles that were used are VideoRay ROV, AutoMarine AUV and Charlie USV. The first is a remotely operated vehicle by VideoRay, LLC., Phoenixville, USA. The control system for this ROV was developed at the University of Zagreb, Faculty of Electrical Engineering and Computing, Laboratory for Underwater Systems and Technologies (UNIZG-FER, LabUST), Croatia. AutoMarine AUV is in fact a module developed at the UNIZG-FER, LabUST for the purpose of autonomization of VideoRay ROV. Charlie USV is a small surface catamaran developed at Consiglio Nazionale delle Ricerche, Istituto di Studi sui Sistemi Intelligenti per l'Automazione (CNR-ISSIA), Genoa, Italy.

In addition to this, description of the vision-based laser distance module and a vision-based data acquisition apparatus, both of which developed in LabUST, will be presented.

3.1 VideoRay ROV

VideoRay ROV is a vehicle used for underwater inspection missions. It is shown in Fig. 3.1(a). Its dimensions are 355mm x 228mm x 215mm and it weighs 3.5kg. Heading sensor is a magnetic compass with 2° quantization. In addition to that, it is equipped with a pressure-based depth sensor. The vehicle is actuated using a port, starboard and vertical thruster. The schematic representation of thruster allocation is shown in Fig. 3.1(b) from where it follows that the thruster allocation matrix (see Chapter 2.2)

can be written using (3.1):

$$\begin{bmatrix} X \\ Z \\ N \end{bmatrix} = \begin{bmatrix} 1 & 1 & 0 \\ 0 & 0 & 1 \\ d & -d & 0 \end{bmatrix} \begin{bmatrix} \tau^1 \\ \tau^2 \\ \tau^3 \end{bmatrix}. \quad (3.1)$$

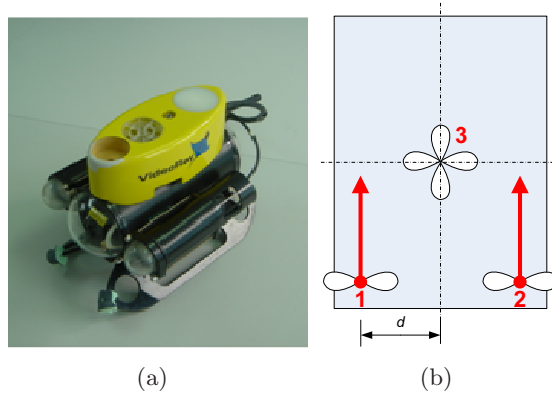


Figure 3.1. a) VideoRay ROV and b) thruster allocation.

The ROV is connected to the surface computer via tether as it is shown in Fig. 3.2. All the control algorithms are calculated and executed on the surface and sent to the ROV using the RS-232 interface.

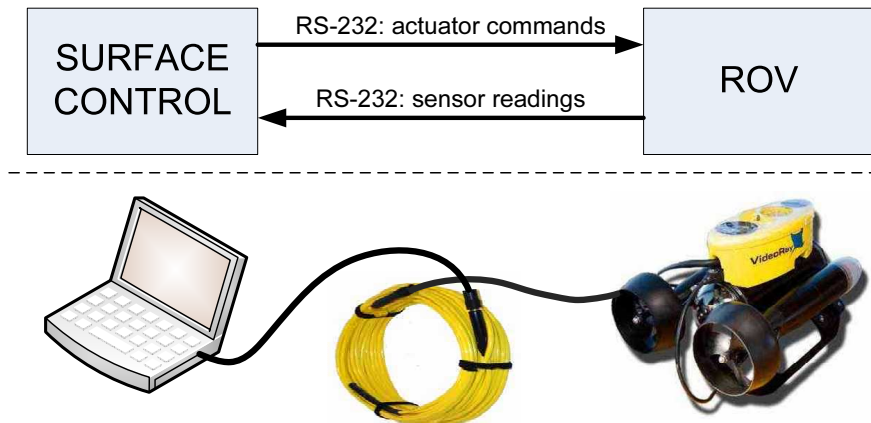


Figure 3.2. Connection of the ROV to the surface control unit.

The schematic representation of the complete system that best describes full mathematical model of the vessel is shown in Fig. 3.3. Yellow blocks represent the communication with the ROV. *COMM 1* is communication from the surface computer towards the vehicle and is modeled as one discretization step delay ($T_s = 0.1s$). Block *COMM*

2 is modeled in the same manner and it represents the communication delay from the ROV towards the surface where the heading and pressure data is acquired. The blue block entitled "VideoRay ROV" represents the vehicle itself. The signals inside this block are virtual and are marked with a hash symbol. The unknown parameters of the vehicle, the ones that are subject to change due to payload, are the parameters of the dynamic model of the vehicle.

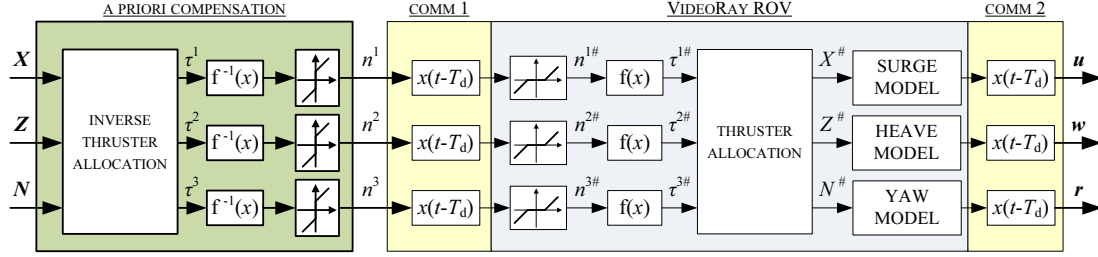


Figure 3.3. Schematic representation of the complete model.

The vehicle demonstrates some static nonlinear behaviors such as nonlinear thruster characteristic and dead zone due to friction in propellers. These nonlinearities can be detected before any method for identifying dynamic model parameters is applied. Nonlinear thruster characteristic is the relation between the thruster input voltage (n^i) and exerted thrust itself (τ^i). This relation has been described in Chapter 2.1 and is schematically represented as $f(x)$ in Fig. 3.3. The *thruster allocation* block is given with (3.1). It has been noted that small voltage applied to the thrusters will not cause them to rotate, mainly because of friction. This effect has been modeled using the dead zone blocks.

Now that these static nonlinearities and allocations have been defined, they can be compensated for before the identification procedure is initiated. The green a priori compensation block has the purpose to compensate for as many nonlinearities in the system as possible. The dead zone inherent to thrusters is avoided by adding a constant signal so that the thrusters are rotating even at small input voltages. The nonlinear thruster characteristic can easily be compensated by applying the inverse of identified characteristic, $f^{-1}(x)$. In order to control the vehicle by sending individual degree of freedom force and moments commands (τ), inverse thruster allocation has to be performed. This block presents the matrix inversion of (3.1).

In other words, the complete system, from the input force or moment (X , Z or N) through the output value (u , w or r , respectively) can be modeled with uncoupled equations for each controllable degree of freedom by using (3.2)–(3.4), in concordance to (2.33). For

- surge DOF

$$\alpha_u \dot{u} + \beta(u)u = X(t - 2T_d) + \tau_{XE}, \quad (3.2)$$

- heave DOF

$$\alpha_w \dot{w} + \beta(w)w = Z(t - 2T_d) + \tau_{ZE} + W - B \quad (3.3)$$

and

- yaw DOF

$$\alpha_r \dot{r} + \beta(r)r = N(t - 2T_d) + \tau_{NE}, \quad (3.4)$$

where τ_{XE} and τ_{NE} represent the external disturbance which is mainly caused by the tether. The variable τ_{ZE} includes, in addition to the disturbance term, the difference between the weight and the buoyancy. All three parameters are assumed to be constant, for the sake of simplicity, and have to be estimated during the identification process. As it was assumed in Chapter 2.5, drag terms $\beta(u)$, $\beta(w)$ and $\beta(r)$ are either dominantly constant or dominantly linear, and can therefore be described with (2.34). Since it is not known a priori what kind of model best describes the VideoRay ROV, a methodology for determining which of these models suits the vehicle best has to be developed.

3.2 AutoMarine AUV

Remotely operated vehicles (ROVs) are usually operated via a tether which serves as energy as well as a communication link with surface. The tether, however, presents a great disturbance for the vehicle¹, especially when the vehicle is operated at greater depths. This is one of the main reasons why autonomous underwater vehicles (AUVs) are slowly replacing tether-controlled ROVs. However, AUV systems require not only low-level control algorithms to be robust and fault-tolerant, but that trajectory and mission planning be carefully designed in order to avoid catastrophic situations.

The AutoMarine Module has been developed for the purpose of transforming VideoRay ROV into an AUV, with minimal development cost and time, for underwater system control research purposes at the University of Zagreb, Laboratory for Underwater Systems and Technologies, [74]. The AutoMarine Module is a system enclosed in a waterproof hull which can be attached to the bottom of the submersible. It controls and powers the submersible over its standard communication/power socket as shown in Fig. 3.4. This way, simple switching between the autonomous and remote mode of operation is achieved, and, most importantly, the interior of the original submersible stays intact.

Hardware choice for the autonomization module is focused on upgradeability, modularity and ease of reprogramming. These demands arise from the underwater system research purpose. For the module to be completely modular in design, it is necessary to use already developed components available on the market. This way, development time and cost is greatly reduced. For the module to be easily reprogrammable it is

¹Influence of the tether can be described using a complex mathematical model. This is crucial when working with towed marine systems, [24].

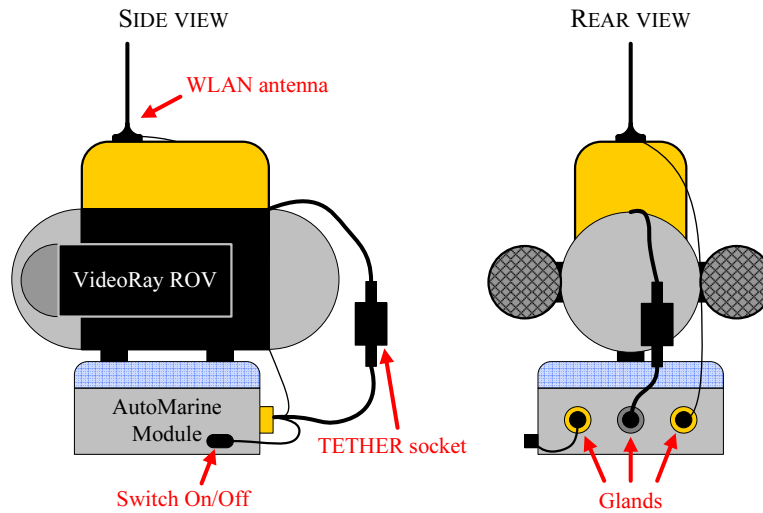


Figure 3.4. *The AutoMarine Module installation.*

best to use an embedded computer which supports one of popular computer operating systems. This way, the use of popular programming languages (for example NI LabVIEW like in this occasion) is made possible in an easy and cost effective way, instead of using specially designed integrated circuits which would require a lot more development time and costly equipment. Since Universal Serial Bus (USB) is a fast serial bus and there is a vast variety of products with support for it, one of the embedded computers with support for USB is the best solution for the task. This kind of design will result in inferior power efficiency and bigger size of the designed module, in comparison with an integrated circuit version. This is a small price to pay since the resulting module will endorse about 1.5 hours of autonomy for the resulting AUV, which is enough for laboratory use. A two wire differential Controller Area Network (CAN) is used for communication between the VideoRay submersible and its console. Therefore it is best to use a CAN to RS-232 converter, since an RS-232 port is available on the chosen embedded computer. The CAN232 converter supports CAN bit rates up to $1 \frac{\text{Mbit}}{\text{s}}$, which is more than enough since the CAN bus installed on the VideoRay Pro II operates at a very unusual speed of $138.24 \frac{\text{kbit}}{\text{s}}$. The chosen embedded computer is the Wafer LX-800 single board computer powered by a 500MHz low power processor which does not require active cooling. This is essential for the given purpose. Wafer LX-800 also supports a variety of standard busses and interfaces (USB, RS-232, LPT, PC-104, IDE, etc.). The computer is equipped with 1GB of Random Access Memory (RAM) and 80GB Hard Disk Drive (HDD) to satisfy any given operation. Large memory and powerful processor support even most demanding operating systems which simplify software development and component communication. An USB2.0 video grabber is used for digitalizing the video signal from the submersible (PAL² format, see Fig.

²Phase alternating line

3.5). The digitalized video is stored on the 80GB HDD.

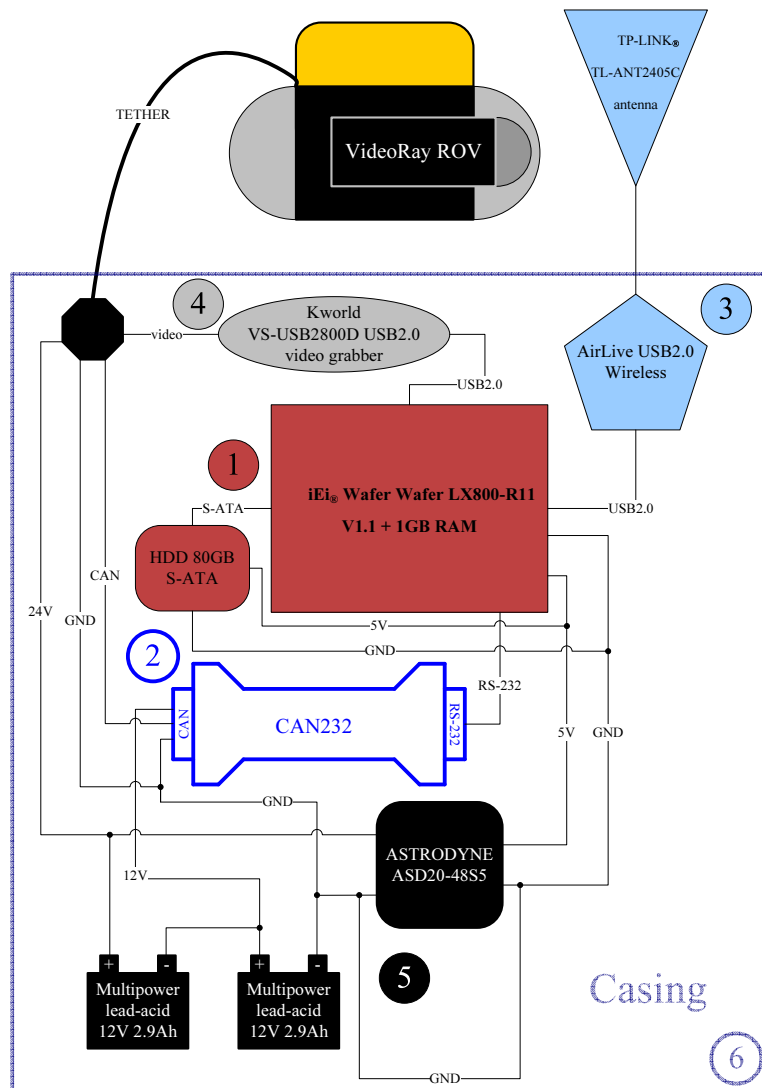


Figure 3.5. The AutoMarine Module wiring.

The VideoRay ROV requires 48V for operation. This voltage is only used for lights and thrusters. The circuitry in the submersible is powered over a DC/DC switching power supply (input range 18 – 75V DC) integrated in the submersible, which lowers the input voltage to 5V. Therefore any input voltage above 18V keeps the submersible operational. Knowing that, there is no need to secure a 48V source in the AutoMarine Module. To obtain a 48V power source, it would take four 12V batteries, but instead it is enough to secure 24V for the submersible (only two 12V batteries). This configuration uses much less space at the cost of submersible's thrust and lights intensity being 4 times weaker. That does not present a problem since the module is designed for laboratory testing. This way, the resulting AutoMarine Module is much smaller, since lead-acid

12V 2.9Ah batteries are used which are pretty big in size. These batteries were chosen due to their market availability. In an outdoor version of the AutoMarine Module, different batteries would be used, with a much better capacity/size ratio (like Li-Ion batteries). A separate DC/DC switching power supply with a 5V output is used in the AutoMarine Module for powering the installed hardware. Details on hardware components can be found in [73] and references within.

As seen in Fig. 3.4, the user communicates with the AutoMarine Module over a Wireless Local Area Network (WLAN). For this purpose, a USB2.0 Wireless LAN adapter is installed on the chosen embedded computer. The USB2.0 WLAN adapter uses an external dipole antenna which is put on top of the submersible for communication. Wireless communication is possible only when the AUV is surfaced. A server application continuously runs on the AUV itself, while a client application can be run from any surface computer. When the wireless connection to the server is detected, clients immediately start receiving data and sending control signals.

The mathematical model of AutoMarine AUV can be described in the same way as shown in Fig. 3.3 only that communications delay should be omitted, since there is no tether and all communication is performed onboard the vehicle. This leads to the conclusion that the same set of equations as for VideoRay ROV can be used to describe dynamic behavior of AutoMarine AUV.

3.3 Charlie USV



Figure 3.6. *Unmanned surface vehicle Charlie.*

The Charlie USV (see Fig. 3.6) is a small catamaran-like shape prototype vehicle originally developed by the CNR-ISSIA for the sampling of the sea surface microlayer

and immediate subsurface for the study of the sea–air interaction, [13]. Charlie is 2.40 m long, 1.70 m wide and weighs about 300 kg in air. The propulsion system of the vehicle is composed of a couple of DC motors (300 W @ 48 V). The vehicle is equipped with a rudder–based steering system, where two rigidly connected rudders, positioned behind the thrusters, are actuated by a brushless DC motor. The navigation instrumentation set consists of a GPS Ashtech GG24C integrated with compass KVH Azimuth Gyrotrac able to compute the True North. Electrical power supply is provided by four 12 V @ 40 Ah lead batteries integrated with four 32 W triple junction flexible solar panels. The on–board real–time control system, developed in C++, is based on GNU/Linux and run on a Single Board Computer (SBC), which supports serial and Ethernet communications and PC–104 modules for digital and analog I/O.

Charlie can be controlled from a ground station using a wireless connection. This link is used only to send mission commands and full missions to Charlie. All control algorithms are performed onboard Charlie. When the vessel is within the wireless link range, telemetry data can be observed on the ground station. Once the mission is complete, the same link is used to download all the mission telemetry to the ground station computer.

The mathematical model which can be used to describe Charlie is derived in details in Chapter 2.5.3 and given with (2.38). For the sake of simplicity, only yaw degree of freedom will be observed here, and it is given with

$$\alpha_r \dot{r} - (\beta_r + \beta_{r|r}|r|) r = \hat{k}_{u^2\delta} u^2 \delta + \hat{k}_{n^2} n^2 + n^2 \delta^2. \quad (3.5)$$

This model depends on the forward speed of the vessel as well as the applied torque (rudder angle δ). The vehicle is usually driven in such a way that forward speed is kept constant. For different forward speeds, different mathematical models can be identified. In addition to this, the general yaw model assumes that drag can be described as an affine function. This drag model can be simplified by assuming only linear or constant drag model.

Charlie’s sensors have a sample time of 0.5 s. This is not satisfactory enough for control purposes, therefore Kalman filtering is applied to estimate measurements at a higher frequency of 10Hz. In order to design the Kalman filter, dynamic model parameters are needed. This is the reason why identification procedures are performed at the sampling rate of 0.5s.

Having said that, Charlie yaw model (3.5) can be written in a simpler form

$$\alpha_r (n^2) \dot{r} + \beta(r, n^2) r = N(t - T_d) + \tau_{NE}, \quad (3.6)$$

where τ_{NE} represents disturbance which includes all external disturbances (wind, currents) and possible asymmetries in the vehicle. This parameter is assumed to be constant. The drag parameter $\beta(r, n^2)$ is either dominantly constant or dominantly linear, and can therefore be described with (2.34). This parameter will depend on the speed

of the vehicle (i.e. on the applied voltage n to the thrusters), and therefore has to be identified for every constant n^2 separately. The inertia parameter $\alpha_r(n^2)$ also depends on n^2 . If this type of model as adopted, input yaw moment N is proportional to the rudder deflection δ , according to (2.38). A detailed yaw model parameter identification procedure and results for Charlie USV are presented in Chapter 8.1.5.

3.4 Vision-Based Laser Distance Module

Distance keeping of underwater vehicles has important application in practice, especially during inspection missions. Distance modules can be of great help for the operator while performing an inspection mission (dams, ship hulls, etc.) and control systems which use these modules as sensors for distance keeping applications are essential in fully autonomous applications. In addition to that, distance modules can be used as an obstacle avoidance modules.

Distance modules (sensors) which can be found in underwater technologies are usually sonars, distance lasers and normal lasers. The greatest advantage of sonars is that they provide accurate and detailed information on the shape as well as the position of an obstacle. However, their cost might be a problem especially if low-cost solutions are needed. Distance lasers give direct distance measurement to the obstacle in front and are somewhat more appropriate cost-wise. However, the measurements provided are not as reliable. Normal lasers are the cheapest option (even though at least two are necessary) but their reliability is the poorest. Also, they are commonly used with the vision-based algorithms in order to determine the distance from an object. The latter type of sensor was developed at the Laboratory for Underwater Systems and Technologies, Zagreb and was mounted on VideoRay ROV, as shown in Fig. 3.7. The results shown in this thesis were obtained using the combination of these two systems.



Figure 3.7. *VideoRay ROV with vision-based laser distance module.*

Some prior implementations of similar technology can be found in [11, 31, 32]. Due to low reliability of laser sensors and the fact that inevitable image processing can be time-consuming, Kalman filtering is an essential addition to these systems, [59].

Image processing

The vision-based laser distance module has been developed for underwater vehicles for the purpose of calculating current distance from the plane-like surface. It is placed below the vehicle and is projecting two laser dots on the surface as shown in Fig 3.8, where L_L and L_R are the distances that the left and the right laser beams, respectively, have to travel to reach the plane, and d_{DM} is the distance between these two lasers. The forward distance D of the vessel to the plane and the angle Φ of the vessel with

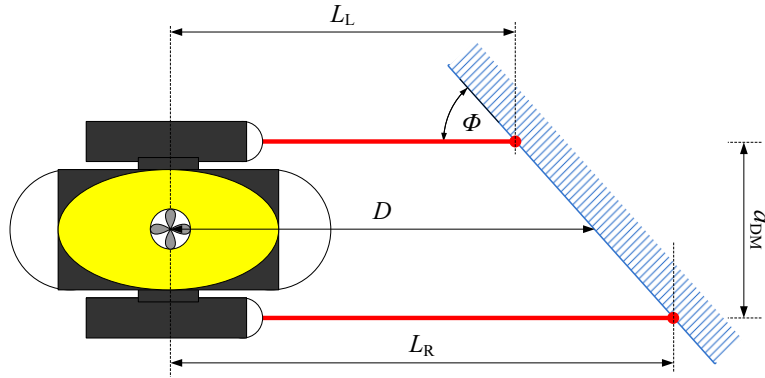


Figure 3.8. The schematic representation of the distance keeping module laser projections.

regard to the plane can easily be calculated by using (3.7) and (3.8):

$$\Phi = \arctan \frac{d_{DM}}{L_R(x_R) - L_L(x_L)} \quad (3.7)$$

$$D = \frac{L_R(x_R) + L_L(x_L)}{2} \quad (3.8)$$

The variables L_R and L_L are determined by image processing from the onboard camera. When there is a plane (obstacle) in front of the vessel, the image will contain two laser dots projected from the lasers. As the vessel approaches the plane, two laser dots become more distanced one from another. When the vessel moves away from the plane, two laser dots approach each other. In addition to the fact that the relative distance of the laser dots is changing, the distance of each of the dots with respect to the central vertex of the image (x_R and x_L for the right and the left dot respectively) changes also. If the vessel is perpendicular to the plane in front, theoretically $x_R = x_L$. As the angle of the vessel Φ changes, x_R and x_L will become more different in value.

Distance module calibration

Since the image processing gives distances of the laser dots from the central vertex within the acquired image (x_R and x_L), and values L_R and L_L are required, system

calibration is necessary to find relations $L_R = f(x_R)$ and $L_L = f(x_L)$.

The calibration was performed so that the vessel was kept perpendicular to the flat surface so that $D = L_L = L_R$. Then the vessel was moved from distances $D = 10\text{cm}$ to $D = 100\text{cm}$ at the steps of 5 cm. For each distance, x_R and x_L were noted and the results are shown in Fig. 3.9 (green dots represent measurements for L_L and red for L_R).

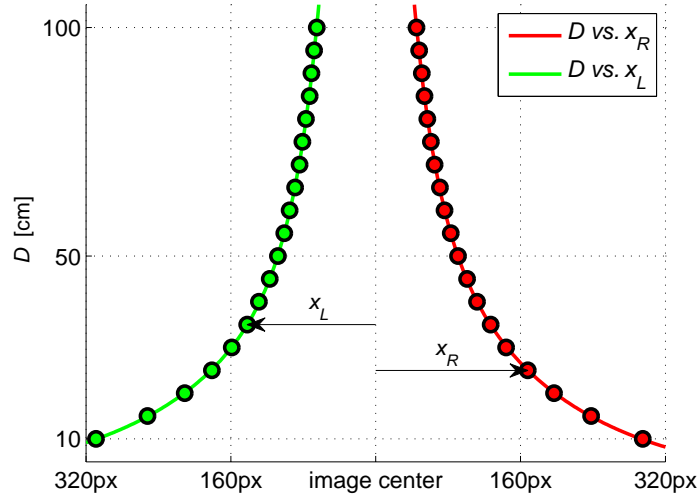


Figure 3.9. Calibration results for the vision-based laser distance module.

The measurements for each laser were interpolated by function

$$L_{R,L} = a_{calib}e^{b_{calib}x_{R,L}} + c_{calib}e^{d_{calib}x_{R,L}} \quad (3.9)$$

and the obtained parameters are shown in Table 3.4. In Fig 3.9 red line shows the interpolated curve for the right laser and green line for the left laser.

Table 3.1. Parameters of the interpolated curves given with (3.9).

LASER	a_{calib} [cm]	b_{calib} [cm ⁻¹]	c_{calib} [cm]	d_{calib} [cm ⁻¹]
RIGHT	230.2	-0.03876	83.3	-0.007234
LEFT	507.7	-0.03745	88.71	-0.007085

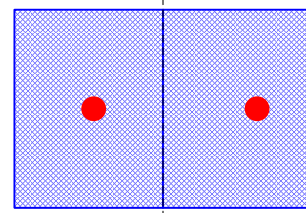
Improved image processing algorithm

The process of finding the two dots within the onboard camera image can be a computationally challenging task, especially if high resolution image ($n \times m$ pixels) is obtained.

This is the reason why an algorithm for finding the two laser dots which does not depend on the acquired image dimensions was developed. It is based on searching only a limited area of the image (dimensions $n^* \times m^*$ pixels where $n^* < n$ and $m^* < m$) around the dots which have been found in the previous step. This significantly reduces the time required for image analysis compared with other algorithms that search the whole image obtained from the integrated camera at each step. Detailed description is given in Algorithm 3.1 where blue areas represent the current search area within the acquired image.

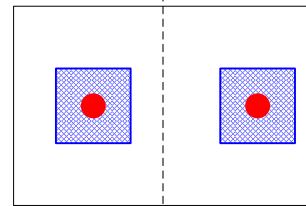
Algorithm 3.1. Improved image processing algorithm.

- I. Search the whole image ($n \times m$ pixels) and find two laser dots.

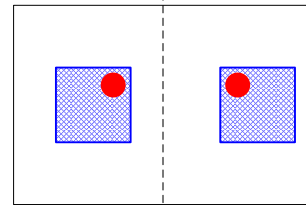


- II. Calculate D and Φ using (3.8) and (3.7).

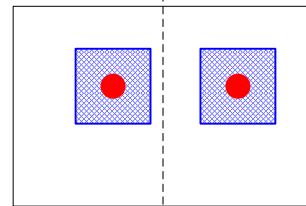
- III. Set two square search areas ($n^* \times m^*$ pixels, $n^* < n$, $m^* < m$) around each laser dot.



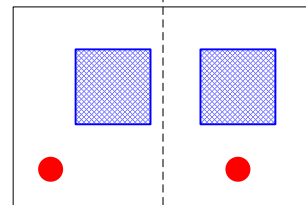
- IV. Search the two rectangles ($n^* \times m^*$ pixels) and find two laser dots.



- V. If laser dots are found, go to step 2.



- VI. If laser dots are not found, go to step 1.



■

The square search areas are sized in such a way that under normal conditions (normal vehicle speeds) the dots will not disappear between two searching steps. If the dots disappear, the vehicle is either moving too fast (the square search areas should be larger) or something occludes laser dots and they are not visible any more. In these cases, algorithm speed decreases until the laser dots are retrieved.

As it was mentioned in Chapter 3.1, the VideoRay ROV data are obtained at the frequency of 10 Hz. The same frequency is used to control the vehicle. However, the vision-based laser module operates at frequency 2 Hz mainly because of the image processing. In order to achieve control at 10 Hz, signals from the vision-based laser module have to be estimated in time instances when measurements are not available. This is done by the use of the extended Kalman filter, [39].

3.5 Vision-Based Data Acquisition

Many identification procedures applicable to marine vehicles can be found in the literature. In order to identify mathematical model parameters of an underwater vehicle, different sensors can be used, such as inertial measurement units (IMUs), Doppler velocity loggers (DVLs), ultra-short baseline positioning systems (USBLs), etc., [17]. In research community, vision-based techniques are widely used, probably due to the low cost. These techniques determine the position of an UV using a camera, and this data is then further processed to calculate higher order derivatives and thus dynamic model parameters.

3.5.1 Laboratory Apparatus

An interesting vision-based laboratory apparatus used for UV parameter identification was introduced in [70]. It was based on using a floor pattern at the bottom of the laboratory pool. The apparatus was used with URIS underwater vehicle, which is equipped with a down facing camera. It was placed in a swimming pool with a specifically coded floor pattern as shown in Fig. 3.10. Using the image analysis on the frames obtained from the onboard camera, the vehicle position can be uniquely determined.

The pattern consists of black and grey dots on a white surface. Places without dots are surrounded with global marks. Each global mark is unique and can be decoded based on the combination of the black and grey dots marked with P . In addition to that, dots marked with O are used to determine the orientation of the vehicle. After using the decoding algorithm, vehicle's position within the laboratory pool can be determined. This data is then used for determining the dynamic model of the vehicle. For details on the method, the reader is referred to [70] and references within. Even though this method is innovative, the downside is the complexity of the algorithm used for determining the position of the vehicle.

Another approach is to use an external camera placed next to the pool. This way the vehicle can be detected within subsequent frames and its model can be determined.

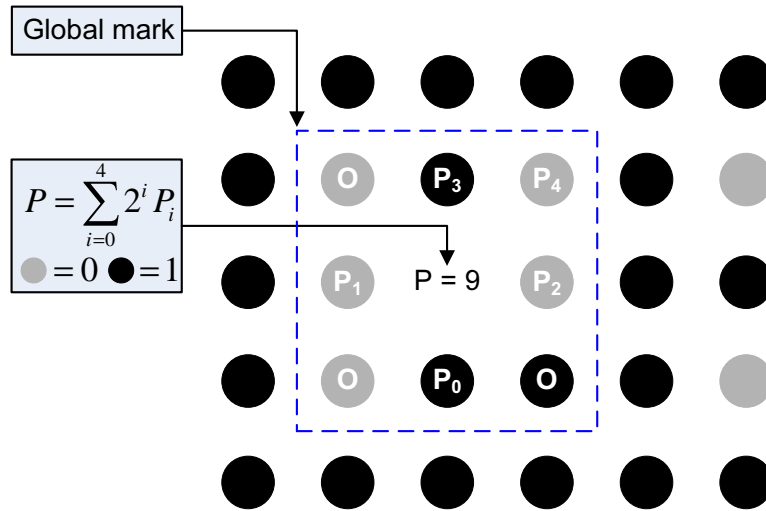


Figure 3.10. Floor pattern used in [70] for URIS UV identification.

In [20] the method that is used is based on placing a camera in such a way that the perspective view of the pool is obtained. The schematic representation is shown in Fig. 3.11 where points A, B, C and D mark the edges of a frame and the coordinate system (with (x, y) points) is view of the pool within the frame. In order to get the

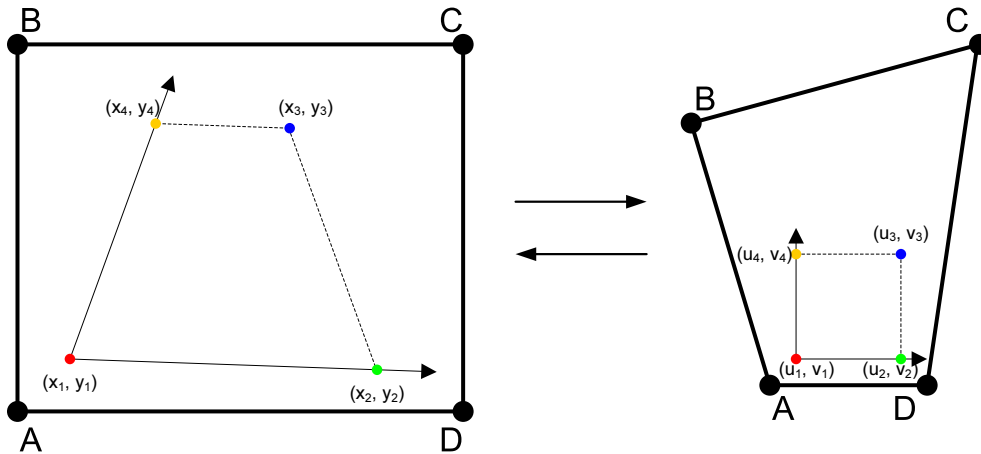


Figure 3.11. Mapping of the swimming pool from a perspective to orthogonal view used in [20].

orthogonal projection of the pool (such that the coordinate system is orthogonal) a linear transformation has to be performed – points (x_i, y_i) have to be translated into points (u_i, v_i) . This operation will distort the frame so the "upper" part of the pool has worse resolution than the "lower" part. In order to obtain satisfactory identification results, the camera should be placed in such a way that the frame segment with the

worst resolution provides good results.

The method that was implemented in the Laboratory for Underwater Systems and Technologies at the University of Zagreb is based on placing a camera directly above the swimming pool like in Fig. 3.12(a), [51]. This way the orthogonalization of the pool view



Figure 3.12. a) Laboratory setup for marine vehicle model identification and b) an acquired image from the camera placed above the pool.

is avoided and the algorithm itself is simpler. It should be mentioned that this method can be used for identification of mathematical models of surface marine vessels and underwater vehicles. In order to ensure easier detection of a vehicle within the camera view, a marker is placed on top of the ROV so that its position and orientation within the camera frame could easily be extracted from the acquired image (Fig. 3.12(b)). Since the depth cannot be detected with a camera positioned like this, the identification procedure can be performed only in the horizontal plane considering surge, yaw and sway.

3.5.2 Data Acquisition

The scheme of data acquisition system is shown in Fig. 3.13. It has been implemented in MATLAB as well as in LabVIEW. The principles of implementation in both software packages is the same and is described in the following part. The implementation itself somewhat differs given the fact that LabVIEW has many image processing functions already developed. The *Synchronization* block is used to ensure that a frame is recorded and that control signals are sent once every sample time ($T_s = 0.1s$). Once the synchronization is achieved, Algorithm 3.2 can be implemented.

Algorithm 3.2. Vision-based data acquisition.

- I. Acquire an RGB image from the camera (Fig. 3.12(b)) and separate it to a red, green and blue component.
- II. Convert the components to binary equivalents where detection of the specific color results in a logical 1 (white) and everything else results in a logical 0 (black) as it

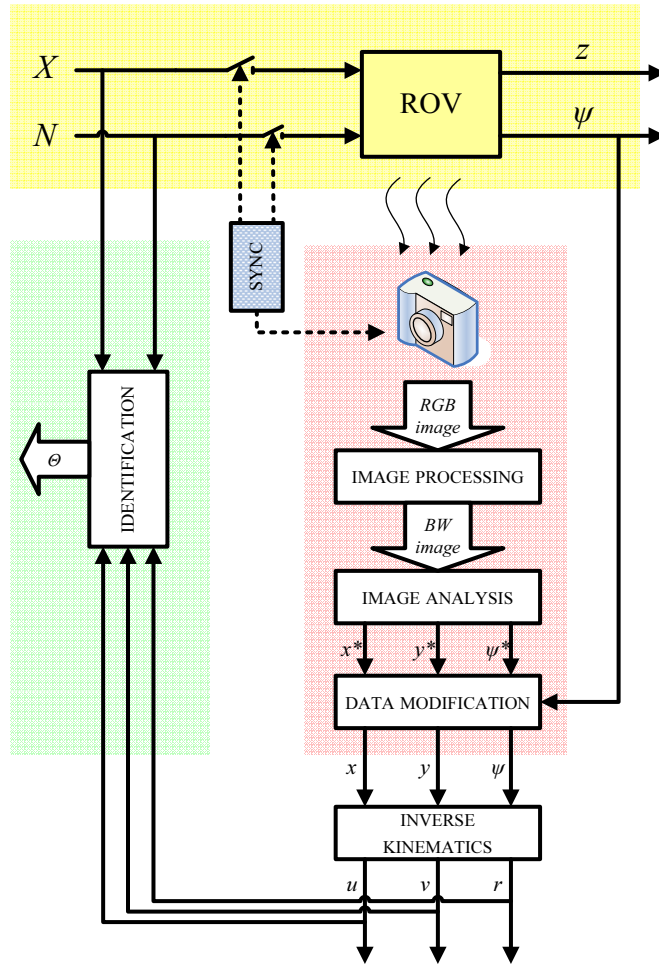


Figure 3.13. Vision-based data acquisition scheme.

is shown in Fig. 3.14. A threshold should be set when this conversion is performed in order to avoid noisy results.

III. Perform a logical operation

$$R \wedge \bar{B} \wedge \bar{G} \tag{3.10}$$

over the images shown in Fig. 3.14 where the \wedge symbol above the letter denotes logical AND and $\bar{}$ denotes logical negation. The result of this operation is shown in Fig. 3.15(a).

IV. Perform additional image processing to avoid scattered pixels in the image. Operations which are suggested are morphing and dilatation. *Morphing* will remove most of secluded pixels while dilatation will process the remaining areas from the inside with a circle of a specified radius, leaving the remaining group of pixels smooth.

- V. Find the centroid of the group of white pixels which represents the position of the ROV within the camera frame, and the orientation of the group of white pixels which represents the orientation of the ROV within the camera frame. The result of this analysis is shown in Fig. 3.15(b) where the original camera image is augmented with ROV's position (green circle) and orientation (blue line).
- VI. Perform inverse kinematics on the data to obtain linear and angular speeds that are required for model identification.

■

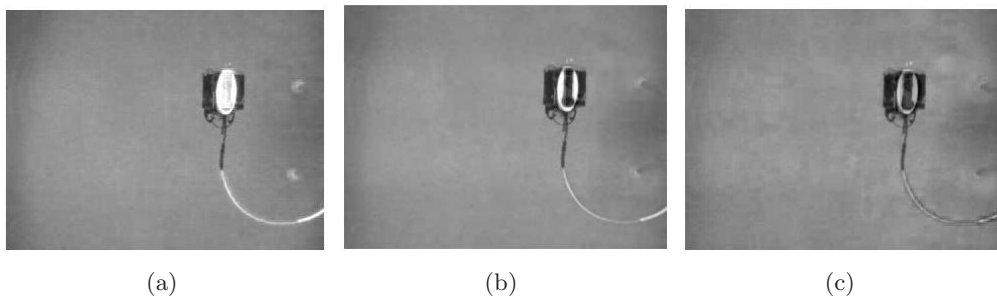


Figure 3.14. *a) Red, b) green and c) blue component of the acquired image shown in Fig. 3.12(b).*

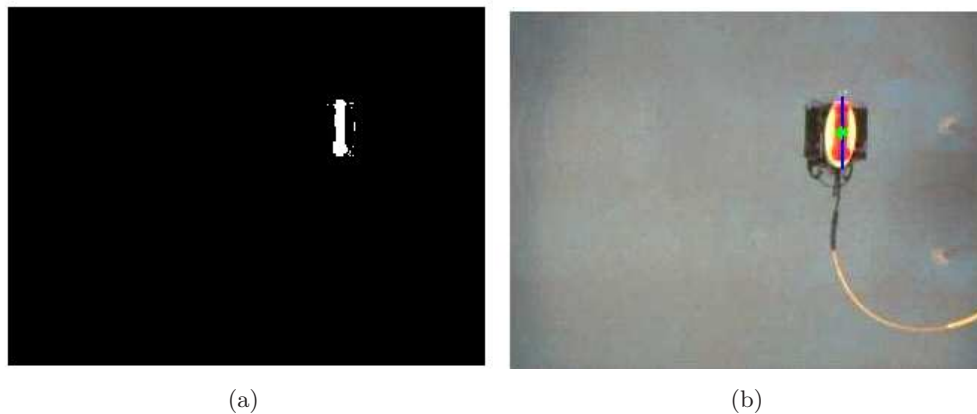


Figure 3.15. *(a) Binary equivalent as a result of logical operation (3.10) and (b) original image augmented with the calculated position and orientation of the vehicle.*

An example of obtained surge, sway and yaw velocities using the described procedure is shown in Fig. 3.16. Raw data from camera are naturally noisy, therefore they should be filtered. In the case in Fig. 3.16 a Savitzky–Golay filter was used. This data can now be used for identification purposes as it is schematically shown in Fig. 3.13.

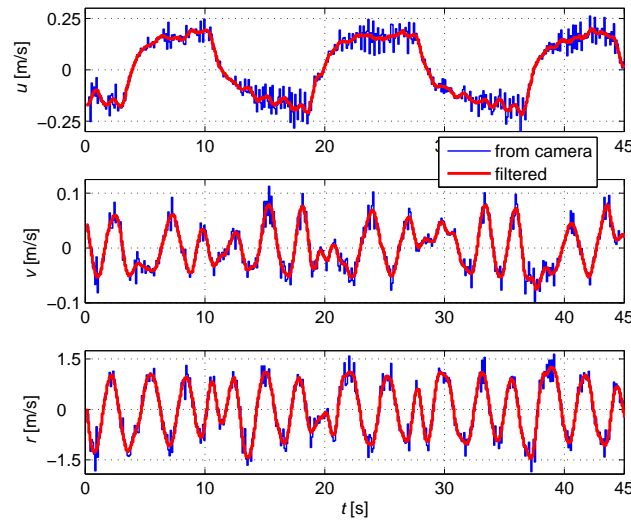


Figure 3.16. Example of speeds obtained using Algorithm 3.2.

3.6 Conclusion

In this chapter three marine vessels which were used as experimental platforms in this thesis are described: remotely operated underwater vehicle VideoRay, autonomous underwater vehicle AutoMarine Module and autonomous surface catamaran Charlie. Hardware construction as well as software and communication have been described for the three systems. The VideoRay ROV exhibits time delay due to communication via tether. All three systems can be described using the same mathematical model.

Further on, two measuring systems which were developed at the LabUST are described: vision-based laser distance module and vision-based data acquisition system. The laser distance module projects two laser dots on a flat surface in front of the vehicle. A description of the algorithm which is used to determine the distance to the surface is given. The speed of performance of this algorithm does not depend on the size of the image obtained from the onboard camera.

The vision-based data acquisition module which has proven to be easy to use and implement in laboratory conditions. By performing image analysis from the camera placed above the laboratory pool, positions and higher derivatives of the vessel can be obtained. The developed apparatus has a down side – it can only be used to determine mathematical models in the horizontal plane. In this chapter, a detailed analysis of image processing for the purpose of identification is given.

Conventional Identification Techniques for Marine Vehicles

The interest in marine vehicles has involved a great number of control engineers mostly due to the challenge of controlling such a complex system. Six degrees of freedom along with coupled and nonlinear behavior makes them difficult to control and model. In order to implement any type of advanced control algorithms, appropriate mathematical model of the system has to be identified.

Researchers who are involved in navigation and guidance of underwater vehicles use different methods to identify their system's dynamics. This should be the first step towards designing a complex navigation system. Indeed, control of different degrees of freedom can be accomplished by tuning the controller parameters heuristically, but in order to implement e.g. optimal controllers, the mathematical model is necessary. Some interesting aspects on identification of underwater vehicles by P. Ridao et al., [69, 70], and on surface vehicles by M. Caccia et al., [16, 17], can be found in the literature. While Caccia uses classical measured data and some estimations to obtain the model of Charlie USV, Ridao designed a uniquely patterned bottom of a laboratory test pool¹ in order to localize Uris (unmanned underwater vehicle) and thus calculate the speeds which are necessary for model identification. However, both authors identify only uncoupled models of their vehicles. Nevertheless, both provide crucial proof of negligible system parameters and propose improved methods for identifying marine systems' dynamics. Some additional methods have been published in [54].

This chapter deals with conventional identification methods applied on marine vehicles which can be found in the literature (least-squares identification, zig-zag manoeuvre) and an open-loop identification method which is applicable in laboratory conditions. First, a method for actuator mapping is presented, with experimental results. Least-squares identification is the most widely used identification method and its basics are described together with a so-called "zig-zag" manoeuvre which is only

¹More details on this can be found in Chapter 3.5

used in marine applications. The open loop step response method is described with mathematical derivations of identification formulae.

4.1 Actuator Mapping

Determining the static characteristic of a thruster, i.e. the relation between the exerted thrust and the thruster control signal is called *thruster mapping*. The procedure consists in inducing vehicle motion in such a way that the pull-force of the vehicle can be recorded by a dynamometer, as shown in Fig. 4.1(a). An example of thruster mapping results is shown in Fig. 4.1(b) where a VideoRay ROV (two horizontal thrusters and one vertical) is used as a case study. In Fig. 4.1(b) dots represent measured values and the full line gives the approximated curve.

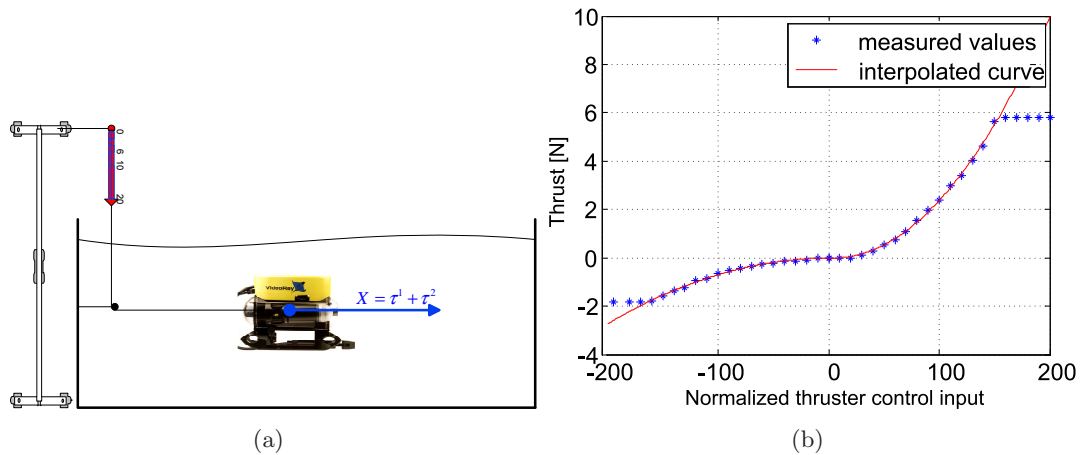


Figure 4.1. Thruster mapping a) experiment and b) results for VideoRay ROV.

4.2 Least-Squares Identification

The least-squares identification (L-S) is the most common identification method for all technical systems. This section will not describe the method in detail, but only a few guidelines for its application in marine systems will be presented.

L-S method is applied to discrete time systems, i.e. measurements at time instances are needed in order to determine system parameters. Let us say that a discrete time input-output model of a process can be written as

$$A(q^{-1})y(k) = B(q^{-1})u(k) + e(k) \quad (4.1)$$

where $y(k)$ is process output, $u(k)$ process input, $e(k)$ disturbance signal (white noise),

q^{-1} backward discrete operator, and $A(q^{-1})$ and $B(q^{-1})$ are

$$\begin{aligned} A(q^{-1}) &= 1 + a_1q^{-1} + a_2q^{-2} + \dots + a_nq^{-n} \\ B(q^{-1}) &= b_0q^{-d} + b_1q^{-d-1} + b_2q^{-d-2} + \dots + b_mq^{-d-m}. \end{aligned} \quad (4.2)$$

For the purpose of L-S identification, the process should be rewritten in a regression form, [42]

$$y(k) = \boldsymbol{\theta}^T(k-1) \boldsymbol{\varphi}(k) + e(k) \quad (4.3)$$

where $\boldsymbol{\varphi}(k)$ is the regression vector

$$\boldsymbol{\varphi}^T(k) = \begin{bmatrix} -y(k-1) & \dots & -y(k-n) & u(k-d) & \dots & u(k-d-m) \end{bmatrix}, \quad (4.4)$$

and $\boldsymbol{\theta}(k)$ is the vector of unknown parameters

$$\boldsymbol{\theta}^T(k) = \begin{bmatrix} a_1 & \dots & a_n & b_0 & \dots & b_m \end{bmatrix}. \quad (4.5)$$

The prediction of process output can be written as (4.6) since the disturbance is not known.

$$\hat{y}(k|\boldsymbol{\theta}) = \boldsymbol{\theta}^T(k-1) \boldsymbol{\varphi}(k) \quad (4.6)$$

From here follows that the prediction error is

$$\varepsilon(k) = y(k) - \hat{y}(k|\boldsymbol{\theta}). \quad (4.7)$$

If (4.3) generates true system outputs, and measurements $y(k)$ and $u(k)$ are available, model (4.8) can be used to determine vector of unknown parameters

$$y(k) = \boldsymbol{\varphi}^T(k) \hat{\boldsymbol{\theta}} + \hat{\varepsilon}(k) \quad (4.8)$$

where $\hat{\boldsymbol{\theta}}$ is vector of unknown parameters and $\hat{\varepsilon}(k)$ is fitting error at time k . The aim is to select $\hat{\boldsymbol{\theta}}$ so that the overall fitting error $\hat{\varepsilon}(k)$ is minimized in some sense.

Assume that the process has been running for a sufficient time to form data vectors of size N , where $N > n$. The data obtained in this way allows the model (4.8) to be expressed in a matrix form

$$\begin{bmatrix} y(1) \\ y(2) \\ \vdots \\ y(N) \end{bmatrix} = \begin{bmatrix} \boldsymbol{\varphi}^T(1) \\ \boldsymbol{\varphi}^T(2) \\ \vdots \\ \boldsymbol{\varphi}^T(N) \end{bmatrix} \hat{\boldsymbol{\theta}} + \begin{bmatrix} \hat{\varepsilon}(1) \\ \hat{\varepsilon}(2) \\ \vdots \\ \hat{\varepsilon}(N) \end{bmatrix}. \quad (4.9)$$

Rewriting (4.9) in a stacked form gives

$$\mathbf{Y} = \boldsymbol{\Phi} \hat{\boldsymbol{\theta}} + \hat{\mathbf{E}} \quad (4.10)$$

where

$$\begin{aligned}\mathbf{Y} &= \begin{bmatrix} y(1) & y(2) & \cdots & y(N) \end{bmatrix}^T \\ \mathbf{\Phi} &= \begin{bmatrix} \boldsymbol{\varphi}^T(1) & \boldsymbol{\varphi}^T(2) & \cdots & \boldsymbol{\varphi}^T(N) \end{bmatrix}^T \\ \hat{\mathbf{E}} &= \begin{bmatrix} \hat{\varepsilon}(1) & \hat{\varepsilon}(2) & \cdots & \hat{\varepsilon}(N) \end{bmatrix}^T\end{aligned}\quad (4.11)$$

By rearranging (4.10) in terms of the vector $\hat{\mathbf{E}}$ the following is obtained:

$$\hat{\mathbf{E}} = \mathbf{\Phi}\hat{\boldsymbol{\theta}} - \mathbf{Y}. \quad (4.12)$$

The least square principle says that the unknown parameters of a model should be chosen in such a way that the sum of squares of the differences between the actually observed data \mathbf{Y} and computed values of data $\hat{\mathbf{Y}} = \mathbf{\Phi}\hat{\boldsymbol{\theta}}$ is minimal, [76], i.e. the L-S criterion function (4.13) is minimal:

$$\begin{aligned}J(\hat{\boldsymbol{\theta}}) &= \frac{1}{2} \sum_{i=1}^N \hat{\varepsilon}_i^2(k) = \frac{1}{2} \hat{\mathbf{E}}^T \hat{\mathbf{E}} = \\ &= (\mathbf{Y} - \mathbf{\Phi}\hat{\boldsymbol{\theta}})^T (\mathbf{Y} - \mathbf{\Phi}\hat{\boldsymbol{\theta}}).\end{aligned}\quad (4.13)$$

In other words,

$$\frac{\partial J(\hat{\boldsymbol{\theta}})}{\partial \hat{\boldsymbol{\theta}}} = \mathbf{\Phi}^T \mathbf{\Phi} \hat{\boldsymbol{\theta}} - \mathbf{\Phi}^T \mathbf{Y} = \mathbf{0} \quad (4.14)$$

will give $\hat{\boldsymbol{\theta}}$ for which criterion (4.13) is minimal if the Hessian of $J(\hat{\boldsymbol{\theta}})$ is positive semidefinite, i.e. $\left| \frac{\partial^2 J(\hat{\boldsymbol{\theta}})}{\partial \hat{\boldsymbol{\theta}}^2} \right| \geq 0$. The Hessian $\frac{\partial^2 J(\hat{\boldsymbol{\theta}})}{\partial \hat{\boldsymbol{\theta}}^2} = \mathbf{\Phi}^T \mathbf{\Phi}$ will be positive semidefinite if $\mathbf{\Phi}$ has full rank.

The least squares parameter estimation follows from (4.14) as

$$\boxed{\hat{\boldsymbol{\theta}}_{LS} = (\mathbf{\Phi}^T \mathbf{\Phi})^{-1} \mathbf{\Phi}^T \mathbf{Y}}. \quad (4.15)$$

Definition 4.1. Matrix pseudoinverse. The pseudoinverse \mathbf{A}^\dagger of matrix \mathbf{A} (also referred to as Moore–Penrose pseudoinverse) is defined as

$$\mathbf{A}^\dagger = (\mathbf{A}^T \mathbf{A})^{-1} \mathbf{A}^T. \quad (4.16)$$

■

Using the described procedure, in the following part regressor forms are used for identification of a coupled model in the horizontal plane, and a decoupled model is given.

Coupled model in the horizontal plane

Coupled model of marine vessels in the horizontal plane is given in Chapter 2.5 with equation (2.28). Further simplifications that are introduced are that parameter $X_{\dot{v}}$ from added mass matrix is negligible, and $x_G = y_G = 0$. In other words, the added mass matrix is diagonal. These two assumptions have proven to be true for micro-ROVs, [51]. Having this in mind, three individual equations for each degree of freedom can be written:

$$\begin{aligned} \dot{u} &= \underbrace{\frac{X_u}{m - X_{\dot{u}}}}_{\alpha_{u1}} u + \underbrace{\frac{m - Y_{\dot{v}}}{m - X_{\dot{u}}}}_{\alpha_{u2}} rv + \underbrace{\frac{1}{m - X_{\dot{u}}}}_{\alpha_{u3}} X \\ \dot{v} &= \underbrace{\frac{Y_v}{m - Y_{\dot{v}}}}_{\alpha_{v1}} v - \underbrace{\frac{m - X_{\dot{u}}}{m - Y_{\dot{v}}}}_{\alpha_{v2}} ur \\ \dot{r} &= \underbrace{\frac{N_r}{I_z - N_{\dot{r}}}}_{\alpha_{r1}} r + \underbrace{-\frac{X_{\dot{u}} - Y_{\dot{v}}}{I_z - N_{\dot{r}}}}_{\alpha_{r2}} uv + \underbrace{\frac{1}{I_z - N_{\dot{r}}}}_{\alpha_{r3}} N. \end{aligned} \quad (4.17)$$

The assumption is that the vehicle is controllable only in surge and yaw. Sway motion may occur due to couplings or external disturbance.

In concordance to the derived models, the regression vectors used to fit input-output data are augmented with a constant δ_x in order to exclude all possible model uncertainties and external disturbances from influencing real model parameters, as in [70]. The matrix form (4.9) can now be written as

$$\underbrace{\frac{1}{T} \begin{bmatrix} x(1) - x(0) \\ x(2) - x(1) \\ \vdots \\ x(N) - x(N-1) \end{bmatrix}}_{\mathbf{Y}} = \underbrace{\begin{bmatrix} x(0) & x_2(0) & x_3(0) & F(0) & 1 \\ x(1) & x_2(1) & x_3(1) & F(1) & 1 \\ \vdots & \vdots & \vdots & \vdots & \vdots \\ x(N) & x_2(N) & x_3(N) & F(N) & 1 \end{bmatrix}}_{\mathbf{\Phi}} \underbrace{\begin{bmatrix} \alpha_{x1} \\ \alpha_{x2} \\ \alpha_{x3} \\ \delta_x \end{bmatrix}}_{\hat{\theta}} \quad (4.18)$$

where derivative has been approximated using Euler forward difference method². If (4.18) is used for surge than $x = u$, $x_2 = r$, $x_3 = v$ and $F = X$; for sway $x = v$, $x_2 = u$, $x_3 = r$ and $F = 0$; and for yaw $x = r$, $x_2 = u$, $x_3 = v$. It should be noted that α_{u2} and α_{v2} are reciprocal and with opposite signs. This fact can be taken into account during identification procedure, or it can just serve as an indicator of quality of identification, [51].

Uncoupled model

According to (2.33) and (2.34) general linear equation for uncoupled motions can be written as

$$\dot{\nu}(t) = \frac{\beta_{\nu}}{\alpha_{\nu}} \nu(t) + \frac{1}{\alpha_{\nu}} \tau(t) + \Delta^* \quad (4.19)$$

²Euler forward method: $s \approx \frac{z-1}{T}$

from where the matrix regression model used for L-S algorithm is generated (Euler forward difference method is again used to approximate the derivative):

$$\frac{1}{T} \underbrace{\begin{bmatrix} \nu(1) - \nu(0) \\ \nu(2) - \nu(1) \\ \vdots \\ \nu(N) - \nu(N-1) \end{bmatrix}}_{\mathbf{Y}} = \underbrace{\begin{bmatrix} -\nu(0) & \tau(0) & 1 \\ -\nu(1) & \tau(1) & 1 \\ \vdots & \vdots & \vdots \\ -\nu(N) & \tau(N) & 1 \end{bmatrix}}_{\mathbf{\Phi}} \underbrace{\begin{bmatrix} \frac{\beta_{\nu\nu}}{\alpha_{\nu}} \\ \frac{1}{\alpha_{\nu}} \\ \Delta^* \end{bmatrix}}_{\hat{\theta}} \quad (4.20)$$

The nonlinear model becomes:

$$\dot{\nu}(t) = \frac{\beta_{\nu\nu}}{\alpha_{\nu}} |\nu(t)| \nu(t) + \frac{1}{\alpha_{\nu}} \tau(t) + \Delta^* \quad (4.21)$$

and the matrix regression model can be represented with (4.20).

$$\frac{1}{T} \underbrace{\begin{bmatrix} \nu(1) - \nu(0) \\ \nu(2) - \nu(1) \\ \vdots \\ \nu(N) - \nu(N-1) \end{bmatrix}}_{\mathbf{Y}} = \underbrace{\begin{bmatrix} -|\nu(0)|\nu(0) & \tau(0) & 1 \\ -|\nu(1)|\nu(1) & \tau(1) & 1 \\ \vdots & \vdots & \vdots \\ -|\nu(N)|\nu(N) & \tau(N) & 1 \end{bmatrix}}_{\mathbf{\Phi}} \underbrace{\begin{bmatrix} \frac{\beta_{\nu\nu}}{\alpha_{\nu}} \\ \frac{1}{\alpha_{\nu}} \\ \Delta^* \end{bmatrix}}_{\hat{\theta}} \quad (4.22)$$

These two regression models, linear (4.20) and nonlinear (4.22), will be used later in the thesis for identification of Charlie USV (Chapter 7.5) and VideoRay ROV (Chapter 7.3).

4.3 Identification Based on Open Loop Step Response

Open loop identification methods are suitable for laboratory purposes. They are often time consuming since a great number of experiments should be run in order to obtain satisfactory results. On the other hand, these experiments give precise model parameters – the more experiments, the more precise results. Let's assume that a system is given with (4.23) where in general α_{ν} is inertia, $\beta(\nu)$ is generalized drag and ν and η are process variables.

$$\begin{aligned} \alpha_{\nu} \dot{\nu} + \beta(\nu) \nu &= \tau \\ \dot{\eta} &= \nu \end{aligned} \quad (4.23)$$

The response of this system depends on the form of the generalized drag $\beta(\nu)$ and whether the observed variable is ν or η . With regard to the observed variable, two cases are possible:

Astatic (Type 1) system is a system for which the step response is constantly rising.

The observed variables are “positions”, marked with η , like heading ψ , depth z

etc. In this case the SISO system response has a form shown in Fig. 4.2(a) and the dynamic equation can be represented with

$$\alpha_\nu \ddot{\eta}(t) + \beta(\nu) \dot{\eta}(t) = \tau S(t). \quad (4.24)$$

Static (Type 0) system for which the response to step input ends up in a steady state (under the assumption that the system is stable). The observed variables are velocities, marked with ν , like heading rate r , heave speed w , etc. In this case the SISO system response has a form shown in Fig. 4.2(b) and the dynamic equation can be represented with

$$\alpha_\nu \dot{\nu}(t) + \beta(\nu) \nu(t) = \tau S(t). \quad (4.25)$$

With regard to the drag parameter $\beta(\nu)$, two cases are observed:

Constant drag, i.e.

$$\beta(\nu) = \beta_\nu = \text{const.} \quad (4.26)$$

which forms a linear equation (4.23), and

Linear drag, i.e.

$$\beta(\nu) = \beta_{\nu|\nu} |\nu| \quad (4.27)$$

which forms a nonlinear equation (4.23).

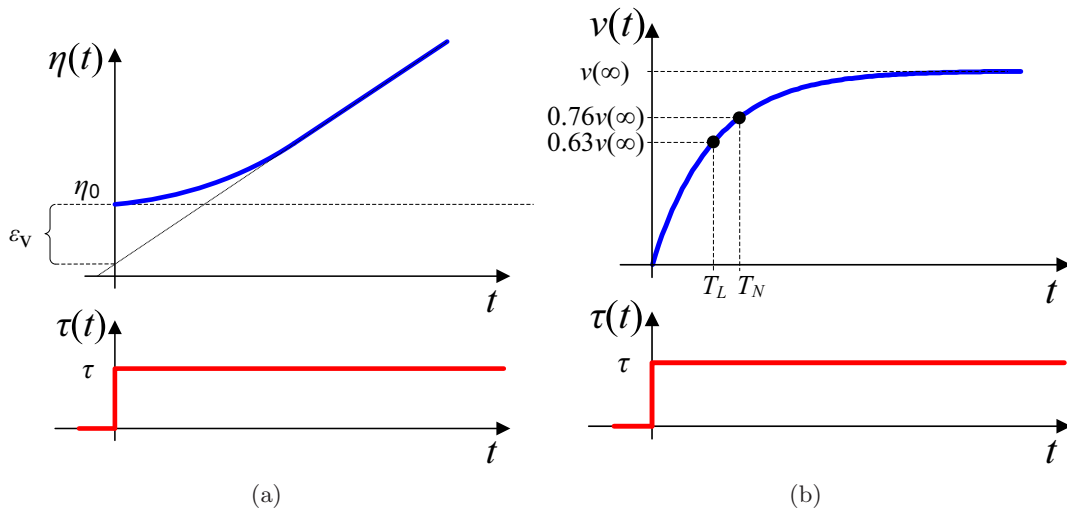


Figure 4.2. Open-loop step responses for a) astatic and b) static system.

Static (Type 0) system

For stable Type 0 systems the steady-state value of the step response given with (4.28) and some characteristic points of the response can be observed for the purpose of parameter identification.

$$K_{ss} = \lim_{t \rightarrow +\infty} \frac{d\nu(t)}{dt} \quad (4.28)$$

If a *linear model* (constant drag coefficient) is assumed, one degree of freedom of a marine vehicle can be described with (4.29) and the response is explicitly given with (4.30), [77].

$$\alpha_\nu \dot{\nu}(t) + \beta_\nu \nu(t) = \tau S(t) \quad (4.29)$$

$$\nu(t) = \frac{\tau}{\beta_\nu} \left(1 - e^{-\frac{\beta_\nu}{\alpha_\nu} t} \right) \quad (4.30)$$

The steady state value of the response is given with (4.31), from where, assuming enough experimental data, the drag can be determined as precisely as needed.

$$K_{ss} = \frac{\tau}{\beta_\nu} \quad (4.31)$$

For the calculation of inertia term α_ν a classical method for determining system's time constant can be used. Based on the fact that at the time instance

$$t = T_L = \frac{\alpha_\nu}{\beta_\nu} \quad (4.32)$$

system response achieves around 63% of the steady state value, i.e.

$$\nu(T_L) = \frac{\tau}{\beta_\nu} (1 - e^{-1}) = \nu(\infty) (1 - e^{-1}) \approx 0.63 \nu(\infty). \quad (4.33)$$

Therefore if T_L is determined, based on the known constant drag coefficient, inertia term can be easily calculated.

If the system is described as *nonlinear*, i.e. with linear drag, then the SISO equation is (4.34) and the response is somewhat more difficult to obtain.

$$\alpha \dot{\nu}(t) + \beta_{\nu\nu} |\nu(t)| \nu(t) = \tau S(t) \quad (4.34)$$

Under the assumption that $\text{sgn}(\tau) = \text{sgn}(\nu)$, (4.34) can be written as

$$\dot{\nu} = \text{sgn}(\tau) \left(-\frac{\beta_{\nu\nu}}{\alpha_\nu} \nu^2 + \frac{1}{\alpha_\nu} |\tau| \right)$$

from where by using the separation of variables the following equation can be obtained:

$$-\operatorname{sgn}(\tau) \frac{\alpha_\nu}{\beta_{\nu\nu}} \int_0^\nu \frac{d\nu}{\nu^2 - \frac{1}{\beta_{\nu\nu}} |\tau|} = \int_0^t dt.$$

For the sake of simplicity, it is assumed that $\nu_0 = \nu(0) = 0$. Since it is known that $\int \frac{a}{x^2 - a^2} dx = \tanh^{-1} \frac{x}{a}$, the step response of the system given by equation (4.34) is given with (4.35).

$$\nu(t) = \sqrt{\frac{|\tau|}{\beta_{\nu\nu}}} \tanh \left[\operatorname{sgn}(\tau) \frac{\sqrt{\beta_{\nu\nu} |\tau|}}{\alpha} t \right] \quad (4.35)$$

The steady state value of the response in this case is given with (4.36) and this term can be used to calculate the linear drag parameter $\beta_{\nu\nu}$.

$$K_{ss} = \operatorname{sgn}(\tau) \sqrt{\frac{|\tau|}{\beta_{\nu\nu}}} \quad (4.36)$$

Similarly as in the case with constant drag coefficient, at the time instance

$$t = T_N = \frac{\alpha}{\sqrt{\beta_{\nu\nu} |\tau|}} \quad (4.37)$$

the system response achieves around 76% of the steady state value, i.e.

$$r(T_N) = r(\infty) \tanh 1 \approx 0.761 r(\infty). \quad (4.38)$$

Astatic (Type 1) system

In this case the slope of the steady-state response (4.39) and velocity error (4.40) can be observed, [77].

$$k_{ss} = \lim_{t \rightarrow +\infty} \dot{\eta}(t) \quad (4.39)$$

$$\varepsilon_v = \lim_{t \rightarrow +\infty} [\eta(t) - k_{ss} t] \quad (4.40)$$

If a *linear model* given with (4.26) is assumed, one degree of freedom of a marine vehicle can be described with (4.41) where $S(t)$ is a Heaviside (step) function. The solution of this linear differential equation is given with (4.42), [77].

$$\alpha_\nu \ddot{\eta}(t) + \beta_\nu \dot{\eta}(t) = \tau S(t) \quad (4.41)$$

$$\eta(t) = \tau \frac{\alpha_\nu}{\beta_\nu^2} \left(e^{-\frac{\beta_\nu}{\alpha_\nu} t} - 1 \right) + \frac{\tau}{\beta_\nu} t + \psi_0 \quad (4.42)$$

The slope of the steady state response for this case is given with (4.43) and it can be determined from the identification experiments. Since the applied input τ is known,

constant drag can be precisely calculated using (4.43) depending on the number of experiments.

$$k_{ss} = \frac{\tau}{\beta_\nu} \quad (4.43)$$

The velocity error for this case is given with (4.44).

$$\varepsilon_v = \eta_0 - \frac{\alpha}{\beta_\nu^2} \tau \quad (4.44)$$

In other words, if the step input τ and the initial value η_0 are known a priori, drag coefficient can be determined from (4.43), and velocity error can be determined from the response making it easy to calculate the inertia α of the system.

If the system is described by *nonlinear* mathematical model, i.e. using linear drag (4.27), the input–output equation is given with (4.45) and the response is somewhat more difficult to calculate explicitly.

$$\alpha_\nu \ddot{\eta}(t) + \beta_{\nu\nu} |\dot{\eta}(t)| \dot{\eta}(t) = \tau S(t) \quad (4.45)$$

By integrating (4.35) once,

$$\begin{aligned} \eta(t) &= \int_{\eta_0}^{\eta} \sqrt{\frac{|\tau|}{\beta_{\nu\nu}}} \operatorname{tgh} \left(\operatorname{sgn}(\tau) \frac{\sqrt{\beta_{\nu\nu} |\tau|}}{\alpha_\nu} t \right) = \\ &= \sqrt{\frac{|\tau|}{\beta_{\nu\nu}}} \operatorname{sgn}(\tau) \frac{\alpha_\nu}{\sqrt{\beta_{\nu\nu} |\tau|}} \ln \left| \cosh \left(\operatorname{sgn}(\tau) \frac{\sqrt{\beta_{\nu\nu} |\tau|}}{\alpha_\nu} t \right) \right| + \eta_0 = \\ &= \operatorname{sgn}(\tau) \frac{\alpha_\nu}{\beta_{\nu\nu}} \ln \left| \cosh \left(\frac{\sqrt{\beta_{\nu\nu} |\tau|}}{\alpha_\nu} t \right) \right| + \eta_0 = \\ &= \operatorname{sgn}(\tau) \frac{\alpha_\nu}{\beta_{\nu\nu}} \ln \left| \frac{e^{t \frac{\sqrt{\beta_{\nu\nu} |\tau|}}{\alpha_\nu}} + e^{-t \frac{\sqrt{\beta_{\nu\nu} |\tau|}}{\alpha_\nu}}}{2} \right| + \eta_0 = \\ &= \operatorname{sgn}(\tau) \frac{\alpha_\nu}{\beta_{\nu\nu}} \left[-\ln 2 + \ln \left| e^{t \frac{\sqrt{\beta_{\nu\nu} |\tau|}}{\alpha_\nu}} \right| + \ln \left| 1 + e^{\ln e^{-t \frac{\sqrt{\beta_{\nu\nu} |\tau|}}{\alpha_\nu}} - \ln e^{t \frac{\sqrt{\beta_{\nu\nu} |\tau|}}{\alpha_\nu}}} \right| \right] + \eta_0, \end{aligned}$$

the solution is explicitly given with (4.46).

$$\eta(t) = \eta_0 + \operatorname{sgn}(\tau) \frac{\alpha_\nu}{\beta_{\nu\nu}} \left(-\ln 2 + t \frac{\sqrt{\beta_{\nu\nu} |\tau|}}{\alpha_\nu} + \ln \left| 1 + e^{-2t \frac{\sqrt{\beta_{\nu\nu} |\tau|}}{\alpha_\nu}} \right| \right) \quad (4.46)$$

The slope of the steady state response for this case is given with (4.47). Just as in the case before (see (4.43)), linear drag coefficient $\beta_{\nu\nu}$ can be calculated easily based

on the known parameters.

$$k_{ss} = \sqrt{\frac{\tau}{\beta_{vv}}} \quad (4.47)$$

The velocity error for this case is given with (4.48). The result is similar as in the case with constant drag coefficient (see (4.44)), but here constant multiplying term appears. Again, inertia term α can be calculated based on the parameters which are known from before.

$$\varepsilon_v = v_0 - \operatorname{sgn}(\tau) \frac{\alpha_v}{\beta_{vv}} \ln 2 \quad (4.48)$$

Therefore if T_N is determined, based on the known linear drag coefficient determined from (4.36), inertia term α_v can be easily calculated. Table 4.1 gives a short overview of equations for determining model parameters using the open loop experiments.

Table 4.1. An overview of equations for parameter identification based on open loop step responses.

	LINEAR MODEL		NONLINEAR MODEL	
ASTATIC (TYPE 1) MODEL	$\alpha_v = (\psi_0 - \varepsilon_v) \frac{\tau}{k_{ss}^2}$	$\beta_{vv} = \frac{\tau}{k_{ss}}$	$\alpha_v = \frac{1}{\ln 2} (\psi_0 - \varepsilon_v) \frac{\tau}{k_{ss}^2}$	$\beta_{vv} = \frac{\tau}{k_{ss}^2}$
STATIC (TYPE 0) MODEL	$\alpha_v = T_L \frac{\tau}{K_{ss}}$	$\beta_{vv} = \frac{\tau}{K_{ss}}$	$\alpha_v = T_N \frac{\tau}{K_{ss}}$	$\beta_{vv} = \frac{\tau}{K_{ss}^2}$

4.4 Zig–Zag Manoeuvre

When designing marine vessels, special attention has to be paid to its manoeuvring capabilities such as holding the course, performing turns, operating at a low speed and stopping in a satisfactory way, [1]. Standard ship manoeuvres which are used to test these abilities are turning circle, pull–out, zig–zag³ and direct and reverse spiral tests. A concise description of these tests can be found in [43] while detailed literature is [38]. The zig–zag manoeuvre can also be used to determine unknown parameters of the yaw mathematical model of the vessel. This aspect will be described in the following part.

In determining marine surface vehicles' dynamic behavior, zig–zag maneuvers are widely accepted and are obligatory for ships, according to IMO⁴. The zig–zag maneuver is used for determining manoeuvring capabilities of the ship and because of that is used when designing ship autopilots, i.e. determining yaw motion of a surface vessel, [43, 61]. The maneuver which is usually run for ships consists of the steps given with Algorithm 4.1, while the ship is sailing in advance at a predetermined speed.

³The zig–zag manoeuvre is also referred to in literature as Kempf's zig–zag manoeuvre.

⁴IMO – International Maritime Organisation

Algorithm 4.1. Zig-zag manoeuvre for $\pm 10^\circ$ rudder deflection⁵.

- I. Turn the rudder at the maximum speed to the starboard⁶ side at 10° (20°).
- II. When ships course changes by 10° from the initial course, turn the rudder to the opposite side (port⁷) at 10° . After a while, the ship will turn to port.
- III. When the ship course changes by 10° from the initial course on the opposite side, turn the rudder again to the starboard side at 10° .

■

This manoeuvre is usually performed on ships, hence the port and starboard side. The results of this test give us the manoeuvring capabilities, i.e. the capacity of the rudder to control the ship's heading. It is advised that the algorithm is performed at maximal as well as minimal forward speed, [1]. The heading ψ and the rudder position δ should be recorded all the time during the experiment. This algorithm can be simulated as shown in Fig. 4.3. The response of the zig-zag manoeuvre is shown in Fig. 4.4.

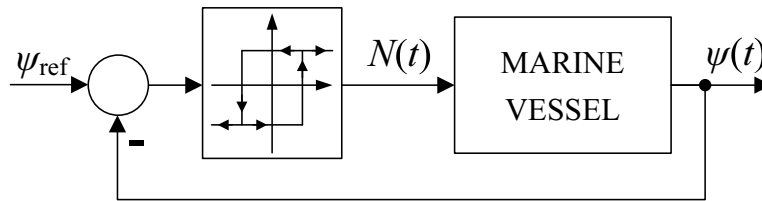


Figure 4.3. Simulation scheme for the zig-zag manoeuvre.

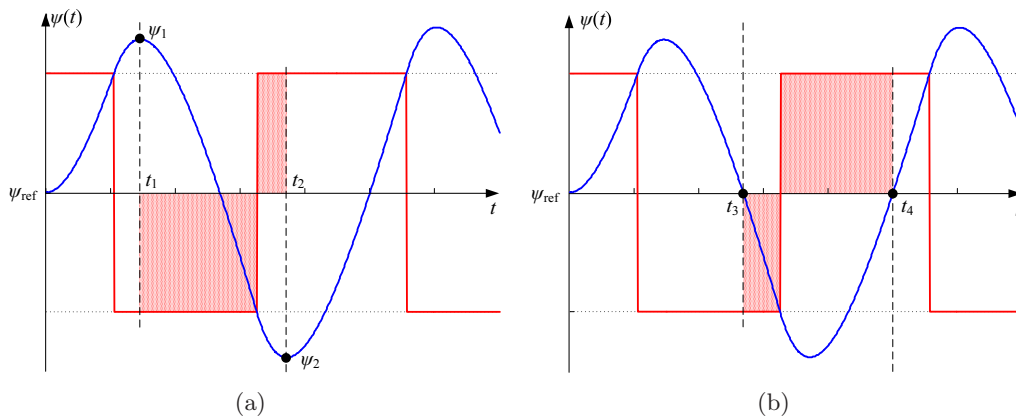


Figure 4.4. The zig-zag manoeuvre: integration area for determining (a) drag and (b) inertia.

⁵Zig-zag test is performed for $\pm 5^\circ$, $\pm 10^\circ$, $\pm 15^\circ$, $\pm 20^\circ$, $\pm 25^\circ$, etc. rudder deflection.

⁶Marine term for "left".

⁷Marine term for "right"

The initial assumption for application of the zig-zag manoeuvre for parameter identification is that the yaw motion can be described using a simple Nomoto model, [62], given with

$$\frac{\psi}{\delta} = \frac{K}{(Ts + 1)s} \quad (4.49)$$

where δ is the rudder deflection, ψ heading and K and T parameters which are to be determined. T and K are also known as the Nomoto time and gain constants, respectively. The same model can be applied to underwater vehicles linear yaw model (4.50) where the exciting force is the yaw moment.

$$\alpha_r \ddot{\psi} + \beta_r \dot{\psi} = N \quad (4.50)$$

In [22] and [30] it was shown that the first order Nomoto equation can be used to analyze the ship's behaviour during zig-zag manoeuvres, i.e. to find the values of K and T . The unknown parameters can be determined by pure integration of the Nomoto model, i.e. by integration of (4.50) which results in

$$\alpha_r \int_{t_1}^{t_2} \dot{r} dt + \beta_r \int_{t_1}^{t_2} r dt = \int_{t_1}^{t_2} N dt.$$

If the integration is performed between the first two time instances when extreme headings appear (the yaw rate at these points equals zero) as it is shown in Fig. 4.4(a), i.e.

$$\alpha_r r|_{t_1}^{t_2} + \beta_r \psi|_{t_1}^{t_2} = \int_{t_1}^{t_2} N dt, \quad (4.51)$$

equation (4.52) is obtained.

$$\beta_r = \frac{\int_{t_1}^{t_2} N dt}{\psi_2 - \psi_1} \quad (4.52)$$

If the integration is performed between two consequent zero crossing points of the heading response as it is shown in Fig. 4.4(b), equation (4.53) is obtained. In this case, yaw rate values $r(t_3)$ and $r(t_4)$ at the zero crossing points are needed.

$$\alpha_r = \frac{\int_{t_3}^{t_4} N dt}{r_4 - r_3} \quad (4.53)$$

It is obvious that in order to get the two parameters, integration of the control input has to be performed. In Fig. 4.4 the shaded areas are to be integrated in order to determine inertia and linear drag.

There are a few downsides to the described procedure:

- Zig-zag identification can be used only if linear Nomoto model describes the vessel's dynamic properly⁸. However, if nonlinear terms in the drag appear, the

⁸This assumption is valid only for small deflections of the rudder.

procedure cannot be used and they cannot be evaluated.

- If the external disturbance is acting, the equations for calculating unknown parameters and the external disturbance increase significantly in complexity, [30], and the resulting terms are implicit in the unknown parameters which makes their calculation complex.
- If the rudder dynamics is included into observation, i.e. the nonlinear element in the closed loop is more complex than the relay with hysteresis (see Fig. 4.3), the computation of unknown parameters has to be performed iteratively as shown in [30].

4.5 Conclusion

This chapter gave an overview of some identification procedure which are often applied for identification of marine vehicle parameters. The chapter starts with a simple description of thruster mapping procedure.

The least-squares method is also briefly described, as the most common method for system identification. Its application on linear and nonlinear models of marine vehicles is given. The main disadvantage of this method is that it requires great number of experimental data, which leads to multiple time-consuming experiments. On the other hand, this method can produce precise parameters if the model is accurate and enough data is gathered. A great advantage is that external disturbance can be taken into account which significantly improves the accuracy of the method.

The method which is based on open loop step response is suitable for laboratory purposes only since it does not take into account disturbances which may appear and moreover assumes stable processes. It was shown that it can be used to identify nonlinear marine models. The proposed methodology also requires a great number of experiments to be performed in order to ensure accuracy of the identified parameters.

The zig-zag manoeuvre was first developed for determining steering capabilities of ships and later the obtained data was used to determine vessel's parameters. This method gives exact parameters if the model is linear and external disturbances are not present. The greatest disadvantage of this approach is that the model of the vessel must be linear, and if the external disturbance is present, the procedure becomes complex, resulting in an iterative algorithm for calculation of unknown parameters.

The methods that were described here will be used in the following section of the thesis as a comparison to the novel method based on self-oscillations (IS-O method).

Self-Oscillations

One of the many possible behaviors that nonlinear systems can exhibit is called the limit cycle. During the limit cycle regime the closed-loop system state trajectories are in a closed form. In the time domain, this behavior is represented as oscillatory behavior. These oscillations are called self-oscillations. The self-oscillations are a stable behavior characteristic for nonlinear systems, [78], unlike oscillations that arise in linear time-invariant systems, [77].

The self-oscillations are often considered a malicious effect in control systems. In transmission systems gears, backlash is most often the cause of self-oscillations which can cause gears to wear out. Even in computer controlled systems quantizers (A/D and D/A converters) can cause unwanted oscillations. On the other hand, for some systems (such as airplanes, marine vessels, etc.) self-oscillations are a normal mode of operation.

It is beneficial to know under what circumstances self-oscillations appear, what are their properties and how they can be avoided. The answer to this question can be obtained from the harmonic linearization procedure. The following subsections will give insight to the describing function method which is an inevitable tool in harmonic linearization. Description of conditions for the existence of symmetric and asymmetric self-oscillations in control systems will also be given.

5.1 Describing Function

Harmonic linearization is a tool for obtaining an approximation of a nonlinear element in the cases when oscillations are present. The describing function is consequently an equivalent gain of a nonlinear element which is excited by periodic signals. Let us define a biased monoharmonic signal in a form

$$x(t) = x_0 + X_m \sin \omega t = x_0 + x^* \quad (5.1)$$

and let it be at the input of a nonlinear element whose output is in the form

$$y_N(t) = F(x) \quad (5.2)$$

where $F(x) = -F(-x)$ is symmetric. The output $y_N(t)$ of the nonlinear element $F(x)$ can be expressed by the Fourier series:

$$y_N(t) = Y_0 + \sum_{k=1}^{\infty} Y_{Pk} \sin(k\omega t) + \sum_{k=1}^{\infty} Y_{Qk} \cos(k\omega t) \quad (5.3)$$

where

$$\begin{aligned} Y_0 &= \frac{1}{2\pi} \int_0^{2\pi} F(x_0 + X_m \sin \omega t) d(\omega t) \\ Y_{Pk} &= \frac{1}{\pi} \int_0^{2\pi} F(x_0 + X_m \sin \omega t) \sin(k\omega t) d(\omega t) \\ Y_{Qk} &= \frac{1}{\pi} \int_0^{2\pi} F(x_0 + X_m \sin \omega t) \cos(k\omega t) d(\omega t). \end{aligned} \quad (5.4)$$

If only the first harmonic is taken into account, (5.3) can be simplified to

$$\begin{aligned} y_N(t) &\approx Y_0 + Y_{P1} \sin \omega t + Y_{Q1} \cos \omega t = \\ &= Y_0(x_0, X_m) + \left[\frac{Y_{P1}(x_0, X_m)}{X_m} + \frac{Y_{Q1}(x_0, X_m)}{X_m} \frac{p}{\omega} \right] x^* \end{aligned} \quad (5.5)$$

where $p = \frac{d}{dt}$ is the differential operator. The basic definition of the describing function is formed assuming symmetric input oscillations. Therefore, by using (5.5) the output of the nonlinear element can be written as

$$\begin{aligned} y_N(t) &= Y_{P1} \sin \omega t + Y_{Q1} \cos \omega t = \\ &= \left[\frac{Y_{P1}(X_m)}{X_m} + \frac{Y_{Q1}(X_m)}{X_m} \frac{p}{\omega} \right] x^* \end{aligned} \quad (5.6)$$

from where the following definition is stated.

Definition 5.1. Describing function. The describing function of a nonlinear element is defined as the ratio between the first harmonic of output and input signals of this nonlinear element expressed in complex form:

$$G_N(X_m) = P_N(X_m) + jQ_N(X_m) \quad (5.7)$$

where

$$\begin{aligned} P_N(X_m) &= \frac{Y_{P1}}{X_m} = \frac{1}{\pi X_m} \int_0^{2\pi} F(X_m \sin \omega t) \sin \omega t d(\omega t) \\ Q_N(X_m) &= \frac{Y_{Q1}}{X_m} = \frac{1}{\pi X_m} \int_0^{2\pi} F(X_m \sin \omega t) \cos \omega t d(\omega t) \end{aligned} \quad (5.8)$$

■

Similarly, the output of a nonlinear element with a biased harmonic input can then be written as

$$y_N(t) \approx Y_0(x_0, X_m) + \left[P_N(x_0, X_m) + Q_N(x_0, X_m) \frac{p}{\omega} \right] x^* \quad (5.9)$$

where

$$\begin{aligned} Y_0 &= \frac{1}{2\pi} \int_0^{2\pi} F(x_0 + X_m \sin \omega t) d(\omega t) \\ P_N &= \frac{1}{\pi} \int_0^{2\pi} F(x_0 + X_m \sin \omega t) \sin(\omega t) d(\omega t) \\ Q_N &= \frac{1}{\pi} \int_0^{2\pi} F(x_0 + X_m \sin \omega t) \cos(\omega t) d(\omega t). \end{aligned} \quad (5.10)$$

This definition allows us to define the describing function parameters of the asymmetrical relay. Equation set (5.10) is in fact a generalization of (5.8) – if $x_0 = 0$ is inserted in (5.10), (5.8) is obtained.

Example 5.1. A symmetric two position relay with hysteresis is given with its output value C and hysteresis width x_a . The input signal is in the form $x(t) = x_0 + X_m \sin \omega t$ and the output is shown in Fig. 5.1.

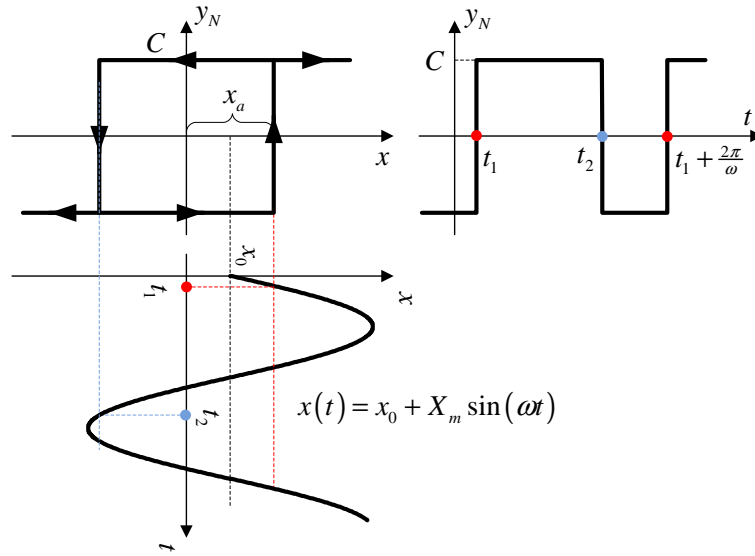


Figure 5.1. Symmetric two-position relay with hysteresis and its input and output signal forms.

If substitutions $\varphi_1 = \omega t_1$ and $\varphi_2 = \omega t_2 - \pi$ are made, the following equations give expressions for φ_1 and φ_2 .

$$\begin{aligned} x_0 + X_m \sin \varphi_1 &= x_a \Rightarrow \varphi_1 = \arcsin \frac{x_a - x_0}{X_m} \\ x_0 + X_m \sin \varphi_2 &= -x_a \Rightarrow \varphi_2 = \arcsin \frac{x_a + x_0}{X_m} \end{aligned}$$

Using (5.10), the describing function for the given nonlinear element when the input signal is biased is obtained.

$$\begin{aligned}
Y_0(x_0, X_m) &= \frac{1}{2\pi} \int_0^{2\pi} y_N d\varphi \\
&= \frac{1}{2\pi} \left(\int_{\varphi_1}^{\pi+\varphi_2} C d\varphi + \int_{\pi+\varphi_2}^{2\pi+\varphi_1} -C d\varphi \right) = \\
&= \frac{C}{2\pi} (\varphi_2 + \pi - \varphi_1 - 2\pi - \varphi_1 + \varphi_2 + \pi) = \\
&= \frac{C}{\pi} (\varphi_2 - \varphi_1) \\
Y_0(x_0, X_m) &= \frac{C}{\pi} \left(\arcsin \frac{x_a + x_0}{X_m} - \arcsin \frac{x_a - x_0}{X_m} \right) \tag{5.11}
\end{aligned}$$

The biased component can also be expressed as

$$\begin{aligned}
Y_0(x_0, X_m) &= \frac{C}{\pi} (\varphi_2 - \varphi_1) = \frac{C}{\pi} (\omega t_2 - \pi - \omega t_1) = \\
&= \frac{C}{\pi} (\omega t_2 - \pi - \omega t_1) = \frac{C}{\pi} \left(\omega t_2 - \frac{T_H + T_L}{2} \omega - \omega t_1 \right) = \\
&= \frac{C}{\pi} \omega \left(T_H - \frac{T_H + T_L}{2} \right) = \frac{C}{\pi} \frac{2\pi}{T_H + T_L} \frac{T_H - T_L}{2} = \\
&= C \frac{T_H - T_L}{T_H + T_L} \tag{5.12}
\end{aligned}$$

$$\begin{aligned}
P_N(x_0, X_m) &= \frac{1}{\pi X_m} \int_0^{2\pi} y_N \sin \varphi d\varphi = \\
&= \frac{1}{\pi X_m} \left(\int_{\varphi_1}^{\pi+\varphi_2} C \sin \varphi d\varphi + \int_{\pi+\varphi_2}^{2\pi+\varphi_1} -C \sin \varphi d\varphi \right) = \\
&= \frac{C}{\pi X_m} [-\cos(\varphi_2 + \pi) + \cos \varphi_1 + \cos(2\pi + \varphi_1) - \cos(\varphi_2 + \pi)] = \\
&= \frac{2C}{\pi X_m} [\cos \varphi_1 + \cos \varphi_2] \\
P_N &= \frac{2C}{\pi X_m} \left[\sqrt{1 - \left(\frac{x_a - x_0}{X_m} \right)^2} + \sqrt{1 - \left(\frac{x_a + x_0}{X_m} \right)^2} \right] \tag{5.13}
\end{aligned}$$

$$\begin{aligned}
Q_N(x_0, X_m) &= \frac{1}{\pi X_m} \int_0^{2\pi} y_N \cos \varphi d\varphi = \\
&= \frac{1}{\pi X_m} \left(\int_{\varphi_1}^{\pi+\varphi_2} C \cos \varphi d\varphi + \int_{\pi+\varphi_2}^{2\pi+\varphi_1} -C \cos \varphi d\varphi \right) = \\
&= \frac{C}{\pi X_m} [\sin(\varphi_2 + \pi) - \sin \varphi_1 - \sin(2\pi + \varphi_1) + \sin(\varphi_2 + \pi)] = \\
&= -\frac{2C}{\pi X_m} (\sin \varphi_1 + \sin \varphi_2) \\
Q_N(x_0, X_m) &= -\frac{4C x_a}{\pi X_m^2} \tag{5.14}
\end{aligned}$$

it is worth noting that the imaginary part of the describing function, $Q_N(x_0, X_m)$, is in fact not a function of x_0 . If the input signal to the relay is unbiased, $x(t) = X_m \sin \omega t$, it follows that $F_0(X_m) = 0$ and

$$\begin{aligned} Q_N(X_m) &= -\frac{4Cx_a}{\pi X_m^2} \\ P_N(X_m) &= \frac{4C}{\pi X_m} \sqrt{1 - \left(\frac{x_a}{X_m}\right)^2} \end{aligned} \quad (5.15)$$

forming the describing function $G_N(X_m) = P_N(X_m) + jQ_N(X_m)$. ■

Theorem 5.1 (On vanishing of even harmonics). *If a nonlinear element described with $y_N(t) = F(x)$ where $F(x) = -F(-x)$ (symmetrical nonlinear characteristic) is excited with an unbiased monoharmonic signal, $x(t) = X_m \sin(\omega t)$, then the output $y_N(t)$ consists of odd multiples of the principle harmonic, only.*

Proof. The simplest way of proving this theorem is to show that even multiples of the principle harmonic vanish. In other words, $Y_{P,2k}$ and $Y_{Q,2k}$ have to become equal to 0.

$$\begin{aligned} Y_{P,2k} &= \frac{1}{\pi} \int_0^{2\pi} F(x_0 + X_m \sin \omega t) \sin(2k\omega t) d(\omega t) = \\ &= \frac{1}{\pi} \int_0^{\pi} F(X_m \sin \omega t) \sin(2k\omega t) d(\omega t) \\ &\quad + \frac{1}{\pi} \int_{\pi}^{2\pi} F(X_m \sin(\omega t + \pi)) \sin(2k\omega t + 2k\pi) d(\omega t) = \\ &= \frac{1}{\pi} \int_0^{\pi} F(X_m \sin \omega t) \sin(2k\omega t) d(\omega t) \\ &\quad - \frac{1}{\pi} \int_0^{\pi} F(X_m \sin \omega t) \sin(2k\omega t) d(\omega t) = 0 \end{aligned}$$

In a similar manner the proof goes for $Y_{Q,2k}$. □

5.2 Symmetric Self-Oscillations

Symmetric oscillations in general are defined for a closed loop system where nonlinear and linear part can be separated as shown in Fig. 5.2. It is assumed that the system is not excited (r is zero). In addition to that, the linear part of the system G_L must attenuate higher multiples of the principle harmonic of self-oscillations. This is usually achieved when the linear system is a low-pass filter. Since all marine vehicles have low-pass properties, an assumption is made, from here on, that the higher harmonics are sufficiently attenuated.

Given a closed loop system as in Fig. 5.2 and under the assumption that the self-oscillations are symmetric, the input signal is zero $R(t) = 0$, the following closed loop

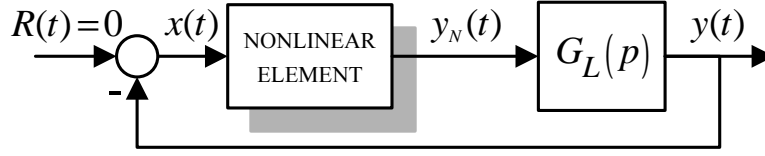


Figure 5.2. A closed loop consisting of a nonlinear element and a linear part $G_L(p)$ of the system.

equations for some frequency ω can be written:

$$\begin{aligned} x(p) &= -y(p) \\ y(j\omega) &= G_L(j\omega) y_N(j\omega) \\ y_N(j\omega) &= G_N(X_m) x(j\omega). \end{aligned} \quad (5.16)$$

These equations boil down to the closed loop equation which is used to calculate the magnitude X_m and frequency ω of self-oscillations:

$$G_N(X_m) G_L(j\omega) + 1 = 0. \quad (5.17)$$

Previously it was stated that the input to the closed loop system should be 0 for the self-oscillations to be symmetric. The following theorem will show that if the process in the closed loop is astatic (Type k , $k > 0$), be it linear or nonlinear, the induced self-oscillations will still be symmetric.

Lemma 5.1 (On symmetric nonlinearities). *Let the nonlinear element be described with $y_N(t) = F(x)$ where $F(x) = -F(-x)$ (symmetrical nonlinear characteristic) and let the odd derivatives at the origin $F^{(2n+1)}(0)$, $n \in \mathbb{N}_0$ be of the same sign. The bias component F_0 of the output vanishes if and only if the nonlinear element is excited with an unbiased monoharmonic signal, $x(t) = X_m \sin(\omega t)$.*

Proof. For the sake of generality, let the nonlinear function be divided into two parts

$$F(x) = \begin{cases} F_u(x), & \dot{x} \geq 0 \\ F_d(x), & \dot{x} < 0 \end{cases}, \quad (5.18)$$

where F_u and F_d are the analytic nonlinearities which effect the rising and the falling input signal, respectively. This definition is introduced to include the nonlinear elements with the hysteresis into observation. If $F(x)$ is (odd) symmetric, then the following is true:

$$\begin{aligned} F_u(x) &= -F_d(-x) \\ F_d(x) &= -F_u(-x) \end{aligned} \quad (5.19)$$

For the case of single-valued nonlinearities (without hysteresis), i.e. $F_u(x) = F_d(x)$, this condition boils down to $F(x) = -F(-x)$. What needs to be proven is that under

the given conditions

$$Y_0(x_0 + X_m \sin \omega t) = 0 \Leftrightarrow x_0 = 0. \quad (5.20)$$

Since the function $f(x) = \int_0^x F(x_0 + X_m \sin \varphi) d\varphi$ is periodic, it can be written that

$$\int_0^{2\pi} F(x_0 + X_m \sin \varphi) d\varphi = \int_{\alpha}^{2\pi+\alpha} F(x_0 + X_m \sin \varphi) d\varphi.$$

Further on, the output can be divided into two parts according to two ranges in which the input signal is rising and falling:

$$F(x_0 + X_m \sin \varphi) = \begin{cases} F_u(x_0 + X_m \sin \varphi), \varphi \in (-\frac{\pi}{2}, \frac{\pi}{2}) \\ F_d(x_0 + X_m \sin \varphi), \varphi \in (\frac{\pi}{2}, \frac{3\pi}{2}) \end{cases}.$$

From here follows that

$$\begin{aligned} Y_0 &= \int_0^{2\pi} F(x_0 + X_m \sin \varphi) d\varphi = \int_{-\frac{\pi}{2}}^{\frac{3\pi}{2}} F(x_0 + X_m \sin \varphi) d\varphi = \\ &= \int_{-\frac{\pi}{2}}^{\frac{\pi}{2}} F_u(x_0 + X_m \sin \varphi) d\varphi + \int_{\frac{\pi}{2}}^{\frac{3\pi}{2}} F_d(x_0 + X_m \sin \varphi) d\varphi = \\ &= \int_0^{\pi} F_u(x_0 + X_m \cos \varphi) d\varphi + \int_0^{\pi} F_d(x_0 - X_m \cos \varphi) d\varphi. \end{aligned}$$

Since $F(x)$ is analytic, $F_u(x)$ and $F_d(x)$ can be developed in the Taylor series around $x = 0$ as $F_u(x) = \sum_{n=0}^{\infty} a_{u,n} x^n$ and $F_d(x) = \sum_{n=0}^{\infty} a_{d,n} x^n$ where $a_{u,n} = \left. \frac{d^n F_u(x)}{dx^n} \right|_{x=0}$ and $a_{d,n} = \left. \frac{d^n F_d(x)}{dx^n} \right|_{x=0}$. The even and odd parts of these Taylor series can be separated resulting in the following equation:

$$\begin{aligned} F_0 &= \underbrace{\int_0^{\pi} \sum_{n=0}^{\infty} a_{u,2n} (x_0 + X_m \cos \varphi)^{2n} d\varphi}_{I_{u,2n}} + \underbrace{\int_0^{\pi} \sum_{n=0}^{\infty} a_{u,2n+1} (x_0 + X_m \cos \varphi)^{2n+1} d\varphi}_{I_{u,2n+1}} \\ &+ \underbrace{\int_0^{\pi} \sum_{n=0}^{\infty} a_{d,2n} (x_0 + X_m \cos \varphi)^{2n} d\varphi}_{I_{d,2n}} + \underbrace{\int_0^{\pi} \sum_{n=0}^{\infty} a_{d,2n+1} (x_0 + X_m \cos \varphi)^{2n+1} d\varphi}_{I_{d,2n+1}} = 0. \end{aligned} \quad (5.21)$$

By developing the term into the binomial series

$$(x_0 + X_m \cos \varphi)^n = \sum_{k=0}^n \binom{n}{k} x_0^k (X_m \cos \varphi)^{n-k}, \quad (5.22)$$

where the binomial coefficient for non-negative integers n and k is defined as

$$\binom{n}{k} = \begin{cases} \frac{n!}{k!(n-k)!}, & k \in \{0, 1, \dots, n\} \\ 0, & k > n \end{cases}, \quad (5.23)$$

the following is obtained

$$\begin{aligned} I_{u,2n} &= \int_0^\pi \sum_{n=0}^\infty a_{u,2n} \sum_{k=0}^n \binom{2n}{k} \left[x_0^k (X_m \cos \varphi)^{2n-k} \right] d\varphi = \\ &= \int_0^\pi \sum_{n=0}^\infty a_{u,2n} \sum_{k=0}^n \binom{2n}{2k} \left[x_0^{2k} (X_m \cos \varphi)^{2n-2k} \right] d\varphi \\ &+ \underbrace{\int_0^\pi \sum_{n=0}^\infty a_{u,2n} \sum_{k=0}^n \binom{2n}{2k+1} \left[x_0^{2k+1} (X_m \cos \varphi)^{2n-2k-1} \right] d\varphi}_{=0} \end{aligned} \quad (5.24)$$

$$\begin{aligned} I_{u,2n+1} &= \int_0^\pi \sum_{n=0}^\infty a_{u,2n+1} \sum_{k=0}^n \binom{2n+1}{k} \left[x_0^k (X_m \cos \varphi)^{2n+1-k} \right] d\varphi = \\ &= \int_0^\pi \sum_{n=0}^\infty a_{u,2n+1} \sum_{k=0}^n \binom{2n+1}{2k} \left[x_0^{2k} (X_m \cos \varphi)^{2n+1-2k} \right] d\varphi \\ &+ \underbrace{\int_0^\pi \sum_{n=0}^\infty a_{u,2n} \sum_{k=0}^n \binom{2n+1}{2k+1} \left[x_0^{2k+1} (X_m \cos \varphi)^{2n-2k} \right] d\varphi}_{=0} \end{aligned} \quad (5.25)$$

$$\begin{aligned} I_{d,2n} &= \int_0^\pi \sum_{n=0}^\infty a_{d,2n} \sum_{k=0}^n \binom{2n}{k} \left[x_0^k (X_m \cos \varphi)^{2n-k} \right] d\varphi = \\ &= \int_0^\pi \sum_{n=0}^\infty a_{d,2n} \sum_{k=0}^n \binom{2n}{2k} \left[x_0^{2k} (X_m \cos \varphi)^{2n-2k} \right] d\varphi \\ &+ \underbrace{\int_0^\pi \sum_{n=0}^\infty a_{d,2n} \sum_{k=0}^n \binom{2n}{2k+1} \left[x_0^{2k+1} (X_m \cos \varphi)^{2n-2k-1} \right] d\varphi}_{=0} \end{aligned} \quad (5.26)$$

$$\begin{aligned} I_{d,2n+1} &= \int_0^\pi \sum_{n=0}^\infty a_{d,2n+1} \sum_{k=0}^n \binom{2n+1}{k} \left[x_0^k (X_m \cos \varphi)^{2n+1-k} \right] d\varphi = \\ &= \int_0^\pi \sum_{n=0}^\infty a_{d,2n+1} \sum_{k=0}^n \binom{2n+1}{2k} \left[x_0^{2k} (X_m \cos \varphi)^{2n+1-2k} \right] d\varphi \\ &+ \underbrace{\int_0^\pi \sum_{n=0}^\infty a_{d,2n} \sum_{k=0}^n \binom{2n+1}{2k+1} \left[x_0^{2k+1} (X_m \cos \varphi)^{2n-2k} \right] d\varphi}_{=0} \end{aligned} \quad (5.27)$$

The integrals with even powers of the cosine term vanish (since the subintegral function is odd in the range of integration) and the result is as follows:

$$Y_0 = \int_0^\pi \sum_{n=0}^{\infty} \sum_{k=0}^n \binom{2n}{2k} (X_m \cos \varphi)^{2n-2k} x_0^{2k} [a_{u,2n} + a_{d,2n} + x_0 \frac{2n+1}{2k+1} (a_{u,2n+1} + a_{d,2n+1})] d\varphi \quad (5.28)$$

Since the nonlinear element is odd symmetric, from (5.19) it can be written that

$$\begin{aligned} \sum_{n=0}^{\infty} a_{u,n} x^n &= - \sum_{n=0}^{\infty} a_{d,n} (-x)^n \\ \sum_{n=0}^{\infty} a_{u,2n} x^{2n} + \sum_{n=0}^{\infty} a_{u,2n+1} x^{2n+1} &= - \sum_{n=0}^{\infty} a_{d,2n} x^{2n} - \sum_{n=0}^{\infty} (-1) a_{d,2n+1} x^{2n+1} \end{aligned} \quad (5.29)$$

from where it follows that

$$\begin{aligned} a_{u,2n} &= -a_{d,2n} \\ a_{u,2n+1} &= a_{d,2n+1}. \end{aligned} \quad (5.30)$$

Since the assumption is that $a_{u,2n+1}$ and $a_{d,2n+1}$ are of the same sign, (5.28) is valid if and only if $x_0 = 0$, i.e. (5.20) is satisfied. \square

Theorem 5.2 (On symmetric oscillations with constant input signal). *Let the closed loop consist of a symmetric nonlinear element $y_N = F(x)$ where $F^{(2n+1)}(0)$ is of the same sign for all $n \in \mathbb{N}_0$ and a linear time invariant process with $k > 0$ integrators (Type k process), and let there be a constant input $R_0 \neq 0$ to the closed loop system. If the self-oscillations are induced, then they are symmetric, regardless of the constant input.*

Proof. Let us say that the process in general is nonlinear and therefore can be joined to the nonlinear part of the system forming a nonlinearity given with $y_N = F_N(u, \dot{u}, \ddot{u}, \dots, \dot{y}_N, \ddot{y}_N, \dots)$ leaving only the k integrators as the linear process as shown in Fig. 5.3.

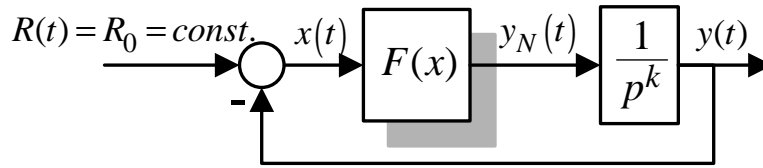


Figure 5.3. Closed loop system for proving symmetry of self-oscillations with constant input and astatic process.

Let us assume that the input to the nonlinear part is biased, i.e. that the self-oscillations are asymmetric, $x(t) = x_0 + x^*$. The output of the nonlinear element is then

$$y_N(t) = Y_0 + \left[P_N(x_0, X_m, \omega) + \frac{Q_N(x_0, X_m, \omega)}{\omega} p \right] x^* \quad (5.31)$$

where the describing function is dependent on the frequency of self-oscillations ω also. The aim is to prove that under the given conditions, $x_0 = 0$. This is important since usually the described constantly excited systems exhibit asymmetric self-oscillations. The closed loop equations give

$$\begin{aligned} x &= R_0 - y \\ \frac{1}{p^k} y_N &= y \\ y_N &= F(x). \end{aligned} \quad (5.32)$$

Under the assumption that $x(t)$ is biased causing the output of the nonlinear element to be (5.31), the following equation is obtained:

$$x_0 + x^* = R_0 - \frac{1}{p^k} \left[Y_0 + \left(P_N + \frac{Q_N}{\omega} p \right) x^* \right]. \quad (5.33)$$

The static part of the equation gives that $p^k (x_0 - R_0) = -Y_0$. Since x_0 and R_0 are constant, it follows that $Y_0 = 0$. From Lemma 5.1 follows that $x_0 = 0$, what proves the theorem. \square

5.3 Asymmetric Self-Oscillations

Asymmetric self-oscillations in general can be a result of a constant input to the system (Theorem 5.2 proves that this is not the case with any type of closed loop system) or asymmetry in the nonlinear element. The following theorem will show that for astatic systems, self-oscillations can be symmetric if and only if the nonlinear element is asymmetric.

Theorem 5.3 (On asymmetric self-oscillations of astatic systems). *Let the closed loop consist of a symmetric nonlinear element $y_N = F(x)$ where $F^{(2n+1)}(0)$ is of the same sign for all $n \in \mathbb{N}_0$ and a linear time invariant process with $k > 0$ integrators (Type k process), and let there be a constant input $R_0 \neq 0$ to the closed loop system. The induced self-oscillations are asymmetric if and only if there exists an additive signal $\Delta \neq 0$ at the output of the nonlinear element.*

Proof. As it was shown in the proof of Theorem 5.2, the closed loop equation is in the form given with (5.33). Let's assume there is an additive signal Δ at the output of the nonlinear element. Then the closed loop equation is in the form

$$x_0 + x^* = R_0 - \frac{1}{p^k} \left[Y_0 + \Delta + \left(P_N + \frac{Q_N}{\omega} p \right) x^* \right]. \quad (5.34)$$

From here follows that $Y_0 = -\Delta$. If the self-oscillations are asymmetric, $x_0 \neq 0$ then by negating Lemma 5.1 follows that $Y_0 \neq 0$ which is the case when $\Delta \neq 0$. This proves one direction of the theorem. If there exists $\Delta \neq 0$, then $Y_0 \neq 0$ which again from the

negation of Lemma 5.1. This proves the other direction of the theorem. \square

Remark 5.1. *Theorem 5.3 is important in order to understand why self-oscillations may be asymmetric in astatic systems with symmetric nonlinear elements. Basically, it states that only the presence of the external disturbance δ may cause the oscillations to be asymmetric. In that case, the disturbance Δ can be added to the nonlinear element, forming a new nonlinearity $y_N = F(x) + \Delta$ which is now asymmetric.*

5.4 On the Existence of Self-Oscillations

Not every nonlinear element can cause self-oscillations in the closed loop systems. Also, if one closed loop system operates in self-oscillations regime, it does not mean that the same nonlinear element will cause self-oscillations with a different process in the closed loop.

The existence of solution of the closed loop equation (5.17) implies the existence of self-oscillations. However, the solution of this equation can be impossible to find analytically, and very difficult to find using numerical methods. This is why grapho-analytical methods have been developed to alleviate the problem of determining the existence of self-oscillations. One such method is called the Goldfarb method, [78]. By rearranging (5.17) into (5.35) a graphical procedure for determining self-oscillation parameters can be obtained.

$$G_L(j\omega) = -\frac{1}{G_N(X_m)} \quad (5.35)$$

By drawing $G_L(j\omega)$ (Nyquist plot of the linear part of the system) and the inverse negative describing function (as a function of X_m), the intersection point is obtained if solution exists. This intersection point is characterized by the magnitude X_m and the frequency ω of self-oscillations. Also, if and only if there is an intersection between the two curves, self-oscillations will exist. For example, an inverse negative describing function of the two-position relay without hysteresis is a line which coincides with the negative real axis in the Nyquist plane. Further on, a second order system, has a Nyquist curve which does not intersect with the negative real axis in the Nyquist plane, leading to the conclusion that self-oscillations will not be induced for this combination of elements.

5.5 Conclusion

The previous chapter gave a basic description of the harmonic linearization method with the description of the describing function. In addition to that, three theorems and two lemmas were stated and proved. It is proved that symmetric nonlinear elements

with unbiased input signal can have only odd multiples of the principle harmonic, which is an important property of symmetric nonlinear element.

A proof that symmetric nonlinear element will not have biased output if and only if the input signal is unbiased was used in the theorem which stated that the closed loop systems with symmetric nonlinearities, the astatic process and a constant input signal will produce symmetric self-oscillations. This fact will be used throughout the thesis, and it proves that in yaw motion (which is astatic if heading is taken into account) the induced self-oscillations will have the same parameters regardless of the heading ψ_{ref} around which they are induced.

Another important theorem, which is proved, is that in a closed loop system with astatic systems and a nonlinearity, self-oscillations can be asymmetric if and only if the nonlinear element is asymmetric. The consequence of this theorem is that if self-oscillations in experiments with marine vehicles (which are described later) are asymmetric, this is due to asymmetric nonlinear element which is such due to disturbance which acts on the vessel, i.e. output of the nonlinear element.

Identification by Use of Self-Oscillations (IS-O)

Self-oscillations are very common and sometimes unwanted in control systems. However, self-oscillations can be used to determine systems's parameters. In these cases, nonlinear elements are intentionally introduced in the closed loop in order to induce self-oscillations.

Identification of process parameters in open-loop is often tedious and time consuming. If process' parameters change in time (due to time-variant payload, disturbances, environment, etc.), classical identification methods are simply not convenient. In field conditions, it is simply not practical to perform series of tests which will give satisfactory set of parameters based on which controllers might be tuned. This was the main motivation for research in the field of identification by use of self-oscillations and its application to marine vehicles. This method, unlike conventional identification methods, is time-parsimonious, easily implementable and applicable in field conditions by non-experts.

The concept of identification by use of self-oscillations was introduced about 25 years ago when Åström and Hägglund in [4] derived a so called ATV¹ method used for system identification and automatic tuning of regulators. The method was presented as simple one and quite appropriate for in situ identification. The method is based on using a relay-feedback to bring the system to self-oscillations. Then Luyben in [44] used this method in chemical industry to identify a transfer function of extremely nonlinear systems (distillation columns). Since then, inducing self-oscillations proved to be an efficient tool for controller tuning in processes and for process identification, [19, 41], especially in pharmaceutical industry.

Many modifications of the original autotuning method have been made in order to apply it to different types of processes. The main objection to this method is that only one frequency is taken into consideration (the frequency of self-oscillations). That is

¹Auto-tuning variation

why some authors used an additional time delay in series with a relay to insert a phase delay which will rotate the Nyquist curve and therefore obtain different oscillation frequencies, [8, 75]. Another approach for determining process' characteristics at different frequencies was to place an integrator in a cascade to a relay element, [34]. As this area of research expanded, more complex methods have been developed using a similar concept. Great improvement was achieved in using transient response of the relay feedback system response to tune controllers and identify systems, [28, 81]. Wang et al. used a switching technique between a relay and a relay with an integrator to obtain sufficient information about the process, [79]. Another modification of a relay experiment is using a biased relay to identify system's parameters, [33, 80]. This method is very accurate when used to determine open loop gain of the process.

All of these methods were used primarily for static processes (Type 0). However, a number of processes are not open loop stable, and there are not many references regarding this problem. First publications that used this method for identification of Type 1 (one integrator) systems included a derivator in series with a relay element to compensate for the influence of the integrator. This method is more of a theoretical value than a practical one, due to non-causality of an ideal derivator. Another, implementable, approach that uses a liner feedback which ensures the static behavior of the process was presented by Kwak et al. in [36]. References that address the use of this method for Type k processes² were not found in the available literature.

There are no records of this methodology being used for marine vehicles apart from the work from the authors. The first published work was [56] and it included some heuristical recommendations for underwater vehicle autopilot tuning based on self-oscillation experiments. Since then, many papers have been published with a topic of application of the proposed method on marine underwater and surface vehicles.

This chapter gives detailed description of the identification by use of self-oscillations (IS-O). A general formulation applicable to any type of system is presented. From there, a general matrix algorithm is derived. This algorithm enables the IS-O method to be easily applied to linear astatic processes of any order. The presented algorithm is augmented to Type k systems, systems with delays and discrete-time systems. Moreover, software implementation issues are addresses and finally the application of the algorithm to a class of nonlinear systems which are used to describe marine vehicles is described.

²Processes with k integrators

6.1 General Formulation

Let a general nonlinear process with a relative degree³ greater than zero be described with

$$f(a_i, x^{(n)}, x^{(n-1)}, \dots, x, u^{(m)}, u^{(m-1)}, \dots, u) = u + \Delta \quad (6.1)$$

where a_i are process' parameters, x is the process output, u the process input and δ constant term at the input. It is worth stressing that this process is static by definition. However, modifications for astatic processes will be made in further sections of the thesis. If self-oscillations are induced by introducing a nonlinear element, the input to the nonlinear element can be written as $-x(t) = x_0 + X_m \sin(\omega t)$ where X_m and ω are magnitude and frequency of the established self-oscillations, respectively, and x_0 is the biased component caused by δ . Without the loss of generality, the closed loop reference is assumed $x_{ref} = 0$. The derivatives of the process' output are

$$\begin{aligned} x &= x_0 + X_m \sin(\omega t) \\ \dot{x} &= X_m j\omega \sin(\omega t) \\ &\vdots \\ x^{(k)} &= X_m (j\omega)^k \sin(\omega t) \end{aligned} \quad (6.2)$$

and the process can be developed into a Fourier series. Keeping only the first harmonic, (6.1) can be written as

$$\begin{aligned} f_0(a_i, x_0, X_m, \omega) + [f_R(a_i, x_0, X_m, \omega) + j f_I(a_i, x_0, X_m, \omega)] x^* &= \\ = u(t) + \Delta(t). \end{aligned} \quad (6.3)$$

where $f_0(\cdot) = \frac{1}{2\pi} \int_0^{2\pi} f(\cdot) d(\omega t)$, $f_R(\cdot) = \frac{1}{\pi} \int_0^{2\pi} f(\cdot) \sin(\omega t) d(\omega t)$ and

$$f_I(\cdot) = \frac{1}{\pi} \int_0^{2\pi} f(\cdot) \cos(\omega t) d(\omega t).$$

Unity feedback implies that

$$u(t) = -Y_0(x_0, X_m) - G_N(x_0, X_m) \cdot x^*(t) \quad (6.4)$$

where $F_0(x_0, X_m)$, and $G_N(x_0, X_m) = P_N(x_0, X_m) + jQ_N(x_0, X_m)$ are parameters of the describing function of the nonlinear element and they do not depend on frequency of self-oscillations if the nonlinearity is static, [78]. Combining (6.3) with (6.4) the following equation is obtained

$$\begin{aligned} f_0(a_i, x_0, X_m, \omega) + [f_R(a_i, x_0, X_m, \omega) + j f_I(a_i, x_0, X_m, \omega)] x^* &= \\ = -Y_0(x_0, X_m) - G_N(x_0, X_m) \cdot x^*(t) + \Delta(t). \end{aligned} \quad (6.5)$$

³Relative degree in linear systems is the pole excess of the system, difference between the number of poles n and finite zeros m , [50]. This means that for linear systems this condition boils down to $n > m$

Equation (6.5) can be separated to an oscillatory component and static component forming a set of two equations given with (6.6).

$$\begin{aligned} f_R(a_i, x_0, X_m, \omega) + jf_I(a_i, x_0, X_m, \omega) &= -P_N(x_0, X_m) - jQ_N(x_0, X_m) \\ f_0(a_i, x_0, X_m, \omega) &= -Y_0(x_0, X_m) + \Delta \end{aligned} \quad (6.6)$$

This set of equations represents the generalized procedure for parameter identification. By solving this set of equations, the vector of unknown parameters (a_i) can be determined if all other parameters are known (X_m , ω , x_0 and the describing function parameters P_N , Q_N). If multiple parameters are to be identified, a number of self-oscillating experiments should be conducted thus obtaining X_{m1} , X_{m2} , ..., ω_1 , ω_2 , ..., P_{N1} , P_{N2} , ... and Q_{N1} , Q_{N2} , ...

6.2 General Matrix Algorithm Formulation for Linear Static Processes

A linear time invariant process can be described by a transfer function (6.7) where n is the degree of the denominator (number of non-zero poles), m degree of the nominator (number of finite zeros) and the process is strictly proper ($n > m$):

$$G_L(s) = \frac{\sum_{i=0}^m b_i s^i}{\sum_{i=0}^n a_i s^i}. \quad (6.7)$$

Let us suppose that the closed loop system is as in Fig. 5.2. Using the Goldfarb method given with (5.35) a general equation in the frequency domain that gives relation between oscillation parameters (magnitude X_m and frequency ω) and process' parameters can be obtained. The process transfer function transferred to frequency domain has the following form:

$$\begin{aligned} G_L(j\omega) &= \frac{\sum_{i=0}^m b_i (j\omega)^i}{\sum_{i=0}^n a_i (j\omega)^i} = \\ &= \frac{\left[\sum_{i=0}^{\lfloor n/4 \rfloor} b_{4i} \omega^{4i} - \sum_{i=0}^{\lfloor n/4 \rfloor} b_{4i+2} \omega^{4i+2} \right] + j \left[\sum_{i=0}^{\lfloor n/4 \rfloor} b_{4i+1} \omega^{4i+1} - \sum_{i=0}^{\lfloor n/4 \rfloor} b_{4i+3} \omega^{4i+3} \right]}{\left[\sum_{i=0}^{\lfloor n/4 \rfloor} a_{4i} \omega^{4i} - \sum_{i=0}^{\lfloor n/4 \rfloor} a_{4i+2} \omega^{4i+2} \right] + j \left[\sum_{i=0}^{\lfloor n/4 \rfloor} a_{4i+1} \omega^{4i+1} - \sum_{i=0}^{\lfloor n/4 \rfloor} a_{4i+3} \omega^{4i+3} \right]} \end{aligned} \quad (6.8)$$

After combining (5.35) and (6.8), and equating imaginary and real parts, the following equations are obtained:

$$\begin{aligned} \left[\sum_{i=0}^{\lfloor n/4 \rfloor} a_{4i} \omega^{4i} - \sum_{i=0}^{\lfloor n/4 \rfloor} a_{4i+2} \omega^{4i+2} \right] = & - P_N \left[\sum_{i=0}^{\lfloor n/4 \rfloor} b_{4i} \omega^{4i} - \sum_{i=0}^{\lfloor n/4 \rfloor} b_{4i+2} \omega^{4i+2} \right] + \\ & + Q_N \left[\sum_{i=0}^{\lfloor n/4 \rfloor} b_{4i+1} \omega^{4i+1} - \sum_{i=0}^{\lfloor n/4 \rfloor} b_{4i+3} \omega^{4i+3} \right] \end{aligned} \quad (6.9)$$

$$\begin{aligned} \left[\sum_{i=0}^{\lfloor n/4 \rfloor} a_{4i+1} \omega^{4i+1} - \sum_{i=0}^{\lfloor n/4 \rfloor} a_{4i+3} \omega^{4i+3} \right] = & - Q_N \left[\sum_{i=0}^{\lfloor n/4 \rfloor} b_{4i} \omega^{4i} - \sum_{i=0}^{\lfloor n/4 \rfloor} b_{4i+2} \omega^{4i+2} \right] - \\ & - P_N \left[\sum_{i=0}^{\lfloor n/4 \rfloor} b_{4i+1} \omega^{4i+1} - \sum_{i=0}^{\lfloor n/4 \rfloor} b_{4i+3} \omega^{4i+3} \right] \end{aligned} \quad (6.10)$$

From this the conclusion is made that one self-oscillation based experiment gives two equations that can be used for identification. If enough self-oscillation based experiments are performed so that all unknown parameters can be determined, the latter two equations can be expressed in a matrix form. In order to obtain a unique solution of the matrix equation, one of the unknown parameters should be fixed. Fixing $a_0 = 1$ comes as a natural choice. The number of the experiments that need to be run in order to identify all the parameters of process (6.7) with $a_0 = 1$ is

$$\varepsilon = \left\lceil \frac{n+m+1}{2} \right\rceil. \quad (6.11)$$

Let us define three vectors of measurements

$$\boldsymbol{\omega} = \left[\omega_1 \quad \cdots \quad \omega_\varepsilon \right]^T \quad (6.12)$$

$$\mathbf{P} = \left[P_{N1} \quad \cdots \quad P_{N\varepsilon} \right]^T \quad (6.13)$$

$$\mathbf{Q} = \left[Q_{N1} \quad \cdots \quad Q_{N\varepsilon} \right]^T \quad (6.14)$$

where elements P_{Ni} and Q_{Ni} are functions of the experimentally obtained magnitude of self-oscillations and nonlinear elements parameters, and ω_i frequency of the self-oscillations obtained in the i -th experiment. The vector of unknown parameters is defined as

$$\boldsymbol{\Theta} = \left[\boldsymbol{\Theta}_a \quad \boldsymbol{\Theta}_b \right]^T = \left[a_1 \quad \cdots \quad a_n \quad b_0 \quad \cdots \quad b_m \right]^T. \quad (6.15)$$

From the above definitions of vectors, matrix equation (6.16) can be written where $\boldsymbol{\Omega}_a$ and $\boldsymbol{\Omega}_b$ are given with (6.17) and (6.18), respectively, where \mathbf{I}_ε is the identity matrix of dimensions $\varepsilon \times \varepsilon$, $\underline{\mathbf{I}} = \left[1 \quad \cdots \quad 1 \right]^T$ of size ε , $\mathbf{0}_\varepsilon$ is the zero matrix of dimensions $\varepsilon \times \varepsilon$, $\underline{\mathbf{0}} = \left[0 \quad \cdots \quad 0 \right]^T$ of size ε .

$$\underbrace{\begin{bmatrix} \Omega_a & \Omega_b \end{bmatrix}}_{\Omega} \Theta = \underbrace{\begin{bmatrix} -I \\ \underline{0} \end{bmatrix}}_{\mathbf{Y}} \quad (6.16)$$

$$\omega_a = \begin{bmatrix} \mathbf{0}_\varepsilon & -\mathbf{I}_\varepsilon & \mathbf{0}_\varepsilon & \mathbf{I}_\varepsilon \\ \mathbf{I}_\varepsilon & \mathbf{0}_\varepsilon & -\mathbf{I}_\varepsilon & \mathbf{0}_\varepsilon \end{bmatrix} \underbrace{\begin{bmatrix} \omega.^1 & \underline{0} & \underline{0} & \underline{0} & \omega.^5 & \underline{0} & \dots \\ \underline{0} & \omega.^2 & \underline{0} & \underline{0} & \underline{0} & \omega.^6 & \dots \\ \underline{0} & \underline{0} & \omega.^3 & \underline{0} & \underline{0} & \underline{0} & \dots \\ \underline{0} & \underline{0} & \underline{0} & \omega.^4 & \underline{0} & \underline{0} & \dots \end{bmatrix}}_n \quad (6.17)$$

$$\Omega_b = \begin{bmatrix} \mathbf{P}^T & \mathbf{Q}^T \\ \mathbf{Q}^T & -\mathbf{P}^T \end{bmatrix} \begin{bmatrix} \mathbf{I}_\varepsilon & \mathbf{0}_\varepsilon & -\mathbf{I}_\varepsilon & \mathbf{0}_\varepsilon \\ \mathbf{0}_\varepsilon & -\mathbf{I}_\varepsilon & \mathbf{0}_\varepsilon & \mathbf{I}_\varepsilon \end{bmatrix} \cdot \underbrace{\begin{bmatrix} \omega.^0 & \underline{0} & \underline{0} & \underline{0} & \omega.^4 & \underline{0} & \dots \\ \underline{0} & \omega.^1 & \underline{0} & \underline{0} & \underline{0} & \omega.^5 & \dots \\ \underline{0} & \underline{0} & \omega.^2 & \underline{0} & \underline{0} & \underline{0} & \dots \\ \underline{0} & \underline{0} & \underline{0} & \omega.^3 & \underline{0} & \underline{0} & \dots \end{bmatrix}}_{m+1} \quad (6.18)$$

The dot symbol (\cdot^k) denotes the element-wise exponent. The parameter vector Θ can be found by using the formula $\Theta = \Omega^{-1}\mathbf{Y}$ only if there is an even number of unknown parameters. If there is an odd number of parameters, matrix Ω will have one row more than there are parameters. In this case, the last row can simply be omitted, or the pseudo-inversion (6.19) can be used to determine the solution,

$$\Theta = (\Omega^T \Omega)^{-1} \Omega^T \mathbf{Y}. \quad (6.19)$$

Example 6.1. The following example will describe the algorithm development for the second order process: $n = 2$; $m = 0$. According to (6.11), $\varepsilon = 2$. Partial measurement matrices Ω_a and Ω_b are obtained as

$$\Omega_a = \begin{bmatrix} \mathbf{0}_2 & -\mathbf{I}_2 & \mathbf{0}_2 & \mathbf{I}_2 \\ \mathbf{I}_2 & \mathbf{0}_2 & -\mathbf{I}_2 & \mathbf{0}_2 \end{bmatrix} \begin{bmatrix} \omega.^1 & \underline{0} \\ \underline{0} & \omega.^2 \\ \underline{0} & \underline{0} \\ \underline{0} & \underline{0} \end{bmatrix} = \begin{bmatrix} 0 & -\omega_1^2 \\ 0 & -\omega_2^2 \\ \omega_1 & 0 \\ \omega_2 & 0 \end{bmatrix}$$

$$\begin{aligned}\Omega_b &= \begin{bmatrix} \mathbf{P}^T \mathbf{I}_2 & -\mathbf{Q}^T \mathbf{I}_2 & -\mathbf{P}^T \mathbf{I}_2 & \mathbf{Q}^T \mathbf{I}_2 \\ \mathbf{Q}^T \mathbf{I}_2 & \mathbf{P}^T \mathbf{I}_2 & -\mathbf{Q}^T \mathbf{I}_2 & -\mathbf{P}^T \mathbf{I}_2 \end{bmatrix} \begin{bmatrix} \omega^0 \\ 0 \\ 0 \\ 0 \end{bmatrix} = \\ &= \begin{bmatrix} \begin{bmatrix} P_{N1} & 0 \\ 0 & P_{N2} \end{bmatrix} \begin{bmatrix} \omega_1^0 \\ \omega_2^0 \end{bmatrix} \\ \begin{bmatrix} Q_{N1} & 0 \\ 0 & Q_{N2} \end{bmatrix} \begin{bmatrix} \omega_1^0 \\ \omega_2^0 \end{bmatrix} \end{bmatrix} = \begin{bmatrix} P_{N1} \\ P_{N2} \\ Q_{N1} \\ Q_{N2} \end{bmatrix}.\end{aligned}$$

Full matrices in (6.19) are

$$\begin{aligned}\Omega &= \begin{bmatrix} 0 & -\omega_1^2 & P_{N1} \\ 0 & -\omega_2^2 & P_{N2} \\ \omega_1 & 0 & Q_{N1} \\ \omega_2 & 0 & Q_{N2} \end{bmatrix} \\ \Theta &= \begin{bmatrix} a_1 & a_2 & b_0 \end{bmatrix}^T \\ \mathbf{Y} &= \begin{bmatrix} -1 & -1 & 0 & 0 \end{bmatrix}^T\end{aligned}$$

From here, equation (6.16) gives the process' parameters. ■

The algorithm described so far was generalized for static processes of any order. The modifications presented in the following subsections will enable the use of the general algorithm for astatic, discrete-time and processes with delay without changing its appropriate matrix formulation.

6.3 Modification for Type k Systems

Let us suppose that the general nonlinear process (6.1) has k integrators at the input

$$u(t) + \Delta(t) \doteq \underbrace{\int_0^t \cdots \int_0^t}_{k} [u(t) + \Delta(t)] dt = \frac{1}{p^k} [u(t) + \Delta(t)]. \quad (6.20)$$

These integrators can be added to the unity feedback equation (6.4) which is now rewritten as

$$\frac{1}{p^k} u(t) = -\frac{1}{p^k} Y_0(x_0, X_m) - \frac{1}{p^k} G_N(x_0, X_m) \cdot x^*(t), \quad (6.21)$$

under the assumption that Δ , i.e. $Y_0(x_0, X_m)$, is constant at all times. According to (6.3), the closed loop equation is now

$$\begin{aligned} f_0(a_i, x_0, X_m, \omega) + [f_R(a_i, x_0, X_m, \omega) + jf_I(a_i, x_0, X_m, \omega)]x^* &= \\ &= \frac{1}{p^k} [u(t) + \Delta(t)]. \end{aligned} \quad (6.22)$$

Equation (6.22) can be separated into an oscillatory component and static component forming a set of two equations

$$\begin{aligned} f_R(a_i, x_0, X_m, \omega) + jf_I(a_i, x_0, X_m, \omega) &= -[P_N(x_0, X_m) + jQ_N(x_0, X_m)](j\omega)^{-k} \\ p^k f_0(a_i, x_0, X_m, \omega) &= -Y_0(x_0, X_m) + \Delta \end{aligned} \quad (6.23)$$

under the assumption that F_0 , Δ and f_0 are constant, since the derivative p^k of a constant is 0, (6.23) boils down to

$$\begin{aligned} f_R(a_i, x_0, X_m, \omega) + jf_I(a_i, x_0, X_m, \omega) &= -[P_N(x_0, X_m) + jQ_N(x_0, X_m)](j\omega)^{-k} \\ Y_0(x_0, X_m) &= \Delta. \end{aligned} \quad (6.24)$$

This modification can be observed from another point of view: the astatic part of the process is in fact joined to the nonlinear part, thus converting the original nonlinear element into an inertial nonlinear element that depends upon the frequency of oscillations. This leads to the conclusion that in fact the original describing function vector $P_N + jQ_N$ is rotated by 90° and multiplied by ω^{-1} for each integrator, obtaining the modified describing function parameters P_N^* and Q_N^* given with (6.25). Since the modification for each experimentally obtained describing function parameter has to be performed, subscript i which stands for the experiment number is introduced:

$$\boxed{\begin{bmatrix} P_{Ni}^* \\ Q_{Ni}^* \end{bmatrix}} = \begin{bmatrix} 0 & \omega_i^{-1} \\ -\omega_i^{-1} & 0 \end{bmatrix}^k \begin{bmatrix} P_{Ni} \\ Q_{Ni} \end{bmatrix}. \quad (6.25)$$

This approach is practical, because the original IS-O algorithm developed for static systems can easily be modified for Type k systems. The only parameters that have to be changed are P_{Ni} and Q_{Ni} , i.e. the describing function vector.

Remark 6.1 (Modification for linear Type k processes). *The same results may be easier to comprehend if a linear process is taken into consideration, as it is demonstrated in [52]. Let us suppose that a linear process described with transfer function $G_P(s)$ has k integrators,*

$$G_L^*(s) = G_L(s) \frac{1}{s^k}. \quad (6.26)$$

Applying the Goldfarb method to this type of process gives

$$\begin{aligned} \frac{1}{G_L(j\omega_i)} &= -(j\omega_i)^{-k} (P_{Ni} + jQ_{Ni}) = \\ &= -(P_{Ni}^* + jQ_{Ni}^*) \end{aligned}$$

which leads to the same modification as in (6.25).

6.4 Modification for Systems with Delays

Delays in systems have great influence on quality of control. They are often present and seldom negligible. Some research has been done on identifying of systems with time delays, but they were mostly based on inserting an additional time delay in order to shift the system in phase and therefore obtain different frequency points for identification. In this thesis, time delay is treated as a known part of the system, and its influence has to be compensated for. The influence of time delays is rather obvious in systems forced into self-oscillations. Systems with delays have greater magnitude and smaller frequency of oscillations. If the system with a delay is to be identified, the delay should be taken into account.

Let us suppose that the general nonlinear process (6.1) has a time delay T_d at the input

$$u(t) + \Delta(t) \doteq u(t - T_d) + \Delta(t - T_d). \quad (6.27)$$

This time delay can be added to the unity feedback equation (6.4) which is now rewritten as

$$u(t - T_d) = -Y_0(x_0, X_m) - G_N(x_0, X_m) \cdot x^*(t - T_d); \quad (6.28)$$

under the assumption that Δ , i.e. $Y_0(x_0, X_m)$, is constant at all times. The closed loop equation is now

$$\begin{aligned} f_0(a_i, x_0, X_m, \omega) + [f_R(a_i, x_0, X_m, \omega) + j f_I(a_i, x_0, X_m, \omega)] x^* = \\ = u(t - T_d) + \Delta(t - T_d). \end{aligned} \quad (6.29)$$

Equation (6.29) can be separated to an oscillatory component and static component forming a set of two equations

$$\begin{aligned} f_R(a_i, x_0, X_m, \omega) + j f_I(a_i, x_0, X_m, \omega) &= -[P_N(x_0, X_m) + j Q_N(x_0, X_m)] e^{-j\omega T_d} \\ f_0(a_i, x_0, X_m, \omega) &= -Y_0(x_0, X_m) + \Delta \end{aligned} \quad (6.30)$$

under the assumption that $\Delta(t) = \Delta(t - T_d)$ and $Y_0(x_0, X_m, t) = Y_0(x_0, X_m, t - T_d)$.

This modification can be observed as rotation of the original vector of the describing function $P_N + jQ_N$ by an angle $-\omega T_d$. In other words, same equations as for the system without process delay can be used, only the modified describing function parameters P_N^* and Q_N^* have to be calculated using (6.31). Since the modification for each experimentally obtained describing function parameter has to be performed, subscript i which stands for the experiment number is introduced:

$$\boxed{\begin{bmatrix} P_{Ni}^* \\ Q_{Ni}^* \end{bmatrix}} = \begin{bmatrix} \cos \omega_i T_d & \sin \omega_i T_d \\ -\sin \omega_i T_d & \cos \omega_i T_d \end{bmatrix} \begin{bmatrix} P_{Ni} \\ Q_{Ni} \end{bmatrix}. \quad (6.31)$$

The approach of combining the known time delay with the nonlinear element is elegant and does not require great intervention with the general algorithm. The case when time delay exists within the system is similar to the case with k integrators – it can be viewed as rotation of the nonlinear describing function vector, as shown in Fig 6.1.

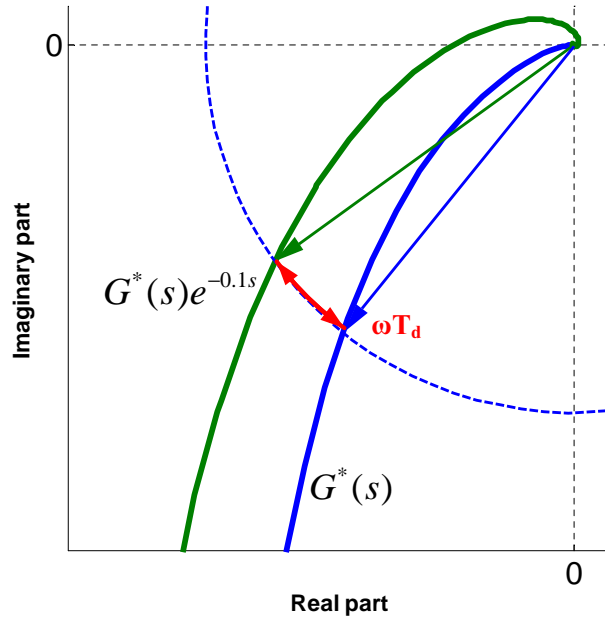


Figure 6.1. Rotation of the Nyquist plot due to the presence of the delay.

Unlike the case with integrators, this transformation does not change the magnitude of describing function, but only its angle. In this case, the describing function can achieve all possible angles, based on the time delay.

Remark 6.2 (Modification for linear processes with delays). *The same results may be easier to comprehend if a linear process is taken into consideration, as it is demonstrated in [52]. Let us suppose that a linear process described with transfer function $G_P(s)$ has a time delay,*

$$G_L^*(s) = G_L(s)e^{-sT_d}. \quad (6.32)$$

Applying the Goldfarb method to this type of process gives

$$\begin{aligned} \frac{1}{G_L(j\omega)} &= -e^{-j\omega T_d} (P_N + jQ_N) = \\ &= -(P_N^* + jQ_N^*) \end{aligned}$$

which leads to the same modification as in (6.31).

Example 6.2. Take a system given with $G(s) = \frac{50}{s(0.3s+1)}e^{-0.1s}$. The simulation was run with relay with hysteresis nonlinearity ($x_a = 10$ and $C = 1$). The obtained oscillations have the magnitude $X_m = 24.47$ and a period $T = 2.8$. As it is seen from

Table 6.1, the errors that occurred when the time delay was ignored are enormous. Once the algorithm was modified using the proposed method, the results were much more accurate.

Table 6.1. Comparison of results with and without the proposed modification for systems with delay.

MODIFICATION	NO	YES
rotation matrix	$\begin{bmatrix} 1 & 0 \\ 0 & 1 \end{bmatrix}$	$\begin{bmatrix} 0.964 & 0.266 \\ -0.266 & 0.964 \end{bmatrix}$
K (relative error)	76.98 (+156.6%)	55.14 (+10.28%)
T (relative error)	0.6037 (+101.23%)	0.346 (+15.33%)

■

6.5 Modification for Discrete-Time Systems

What type of modification is needed when dealing with the discrete-time systems will be shown in the following example. When the identification by use of self-oscillations is used in practice, the process is usually computer controlled. Therefore a slight modification of the procedure has to be done.

Let us say that the nonlinear element which caused the self-oscillations in the system is a relay with hysteresis with $x_a = 3$. This means that it should switch when the input signal has value 3. It could happen that at some time step k the input is 2.15 and at the following time step $k + 1$ it is 6.57, as shown in Fig. 6.2.

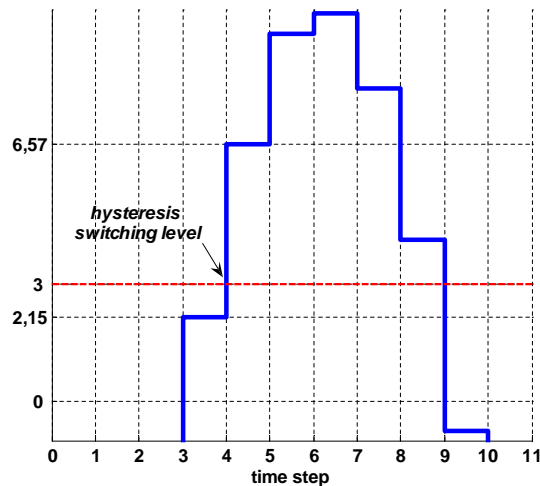


Figure 6.2. Illustration of false switching in discrete-time systems.

Since at the moment k the input to the relay has not yet reached the switching value, it will switch at the moment $k + 1$. In other words, this is equivalent to hysteresis

parameter x_a having the value 6.57, which is more than double the assumed value, therefore false results can be expected. It can also happen that the switching occurs exactly at the desired moment, resulting in accurate identification. Since it cannot be known a priori whether the chosen hysteresis parameters will give satisfactory results, the only way is to perform the correction of the hysteresis width, after the experiment has been performed. The described procedure is also described in [52].

To conclude, the following procedure is proposed when dealing with discrete-time systems:

- perform the IS-O test with the relay width x_a ,
- after acquiring the self-oscillations, determine the exact points in which the switching occurred (i.e. determine the new x_a^*),
- use the general algorithm with the corrected x_a^* parameter.

The following simulation example will demonstrate the improvement of the identification when the proposed procedure is used.

Example 6.3. The example process is $G(s) = \frac{50}{s(0.3s+1)}$ with sample time $T_s = 0.1$ s. When the hysteresis width x_a is chosen to be 16, the same oscillations (magnitude $X_m = 24.47$ and period $T = 2.8$) are obtained as in the case when the width is 20 (see Table 6.2). In the first case the identification is far from exact values, while in the second case it is much better. If the proposed algorithm modification is applied, it is clear that the relay switching occurs at the moments when hysteresis input is 20.28. When this hysteresis parameter is used in the identification algorithm, the identified parameters are the closest to real values.

Table 6.2. Comparison of results with and without the proposed modification for a discrete-time system.

Modification	NO		YES
x_a	16	20	20.28
K (relative error)	67.43 (+34.86%)	53.94 (+7.88%)	53.2 (+6.4%)
T (relative error)	0.526 (+75.33%)	0.325 (+8.33%)	0.311 (+3.67%)

Fig. 6.3(a) shows results of simulations for hysteresis widths x_a from 5 to 20 with sample time 0.1 s. Void circles present percent parameter errors for the cases when hysteresis width was not modified. Full circles are positioned at the modified hysteresis widths and show percent parameter errors. It is self-evident that the results are much better when relay hysteresis is modified. For the hysteresis widths positioned between full circles, the magnitude and frequency of self-oscillations remain constant. It is obvious that with greater sampling time, one has more chance of choosing such hysteresis width so that the real switching moment does not coincide with the assumed one.

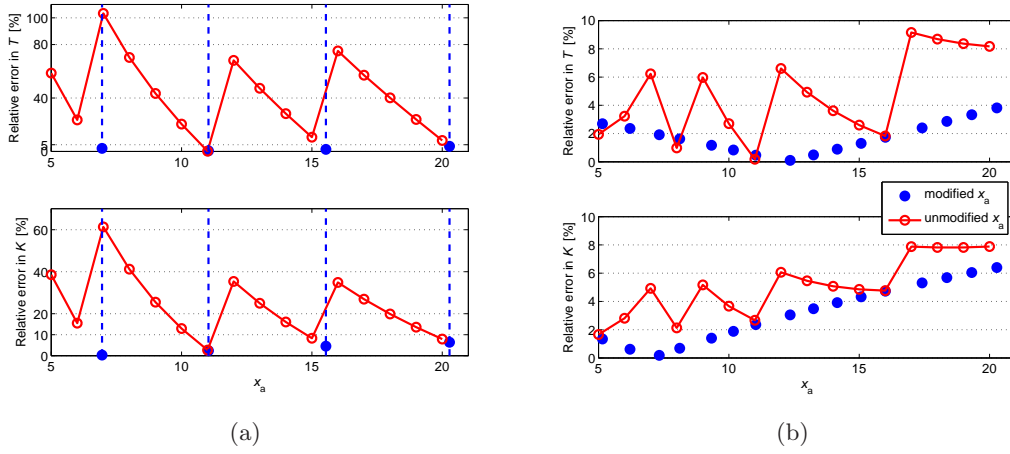


Figure 6.3. Simulation example of improved identification with the proposed modification for discrete-time systems. Sample time is a) 0.1 s and b) 0.01 s.

In the case when the sampling time is much smaller, i.e. $T_s = 0.01$ s as in Fig. 6.3(b), it is clearly visible that the cases where hysteresis width was modified also give better results. However, the results without modification give satisfactory errors (below 10%). This is expected, because as sampling time gets smaller, the chances of relay to switch at a significantly different input value are much smaller, hence the error is smaller. ■

6.6 Application to Marine Vehicles

In Chapter 2.5 it was concluded that different degrees of freedom of underwater vehicles can be represented with a generalized model in a form given with (6.33). In addition to this, the drag parameter $\beta(\nu)$ is often approximated with a constant or a linear term, as shown with (6.34).

$$\alpha_\nu \dot{\nu}(t) + \beta(\nu) \cdot \nu(t) = \Delta + \tau(t) \quad (6.33)$$

$$\beta(\nu) = \begin{cases} \beta_\nu & \text{for constant drag} \\ \beta_{\nu\nu} |\nu| & \text{for linear drag} \end{cases} . \quad (6.34)$$

A simplification which will be introduced is given with:

$$\dot{\eta} = \nu. \quad (6.35)$$

This is a standard equation for yaw degree of freedom where $r = \dot{\psi}$, and heave degree of freedom where $w = \dot{z}$. These are in fact simplified kinematic models which assume

that pitch and roll angles are 0. These simplifications are introduced in order to obtain identification procedure for determining dynamic model parameters for marine vessels.

This section will show how the proposed identification by use of self-oscillations method can be applied for identifying yaw, surge and heave degree of freedom of marine vessels, under the assumption that their dynamics are described using (6.33).

Linear model (constant drag)

If a simplification given with (6.35) is applied, (6.33) can be rewritten as (6.36) under the assumption that drag is constant, i.e. $\beta(\nu) = \beta_\nu$. This case study will also be referred to as the "constant damping" or the "constant drag" case.

$$\alpha_\nu \ddot{\eta} + \beta_\nu \dot{\eta} = \tau + \Delta \quad (6.36)$$

The linear model can be written as a transfer function describing the output ν with regard to the input τ given with (6.37).

$$\frac{\psi(s)}{\tau(s)} = \frac{\frac{1}{\beta_\nu}}{s \left(\frac{\alpha_\nu}{\beta_\nu} s + 1 \right)} = \frac{b_0}{s(a_1 s + 1)} \quad (6.37)$$

By following the generalized procedure described in Chapter 6.2 and (6.11), only one self-oscillation experiment has to be conducted in order to obtain two unknown parameters. From (6.17) and (6.18) follows that

$$\Omega_a = \begin{bmatrix} 0 \\ \omega \end{bmatrix}$$

and

$$\Omega_b = \begin{bmatrix} P_N \\ Q_N \end{bmatrix}.$$

Since the system has one integrator, according to (6.25) the following modification has to be made upon the describing function vector:

$$\begin{bmatrix} P_N^* \\ Q_N^* \end{bmatrix} = \begin{bmatrix} 0 & \omega^{-1} \\ -\omega^{-1} & 0 \end{bmatrix} \begin{bmatrix} P_N \\ Q_N \end{bmatrix} = \begin{bmatrix} \frac{Q_N}{\omega} \\ -\frac{P_N}{\omega} \end{bmatrix}.$$

By inserting the obtained values in (6.16), the following matrix equation is obtained

$$\begin{bmatrix} 0 & \frac{Q_N}{\omega} \\ \omega & -\frac{P_N}{\omega} \end{bmatrix} \begin{bmatrix} a_1 \\ b_0 \end{bmatrix} = \begin{bmatrix} -1 \\ 0 \end{bmatrix},$$

which yields the following linear equation parameters:

$$\alpha_\nu = \frac{P_N(x_0, X_m)}{\omega^2} \quad (6.38)$$

$$\beta_\nu = -\frac{Q_N(x_0, X_m)}{\omega} \quad (6.39)$$

The biased term δ which is not included in the transfer function can be determined as the bias term in the describing function, i.e.

$$\Delta = Y_0(x_0, X_m). \quad (6.40)$$

It should be mentioned that these equations can be derived using the methodology developed for nonlinear systems, described in Chapter 6.1. However, the proposed matrix formulation for linear systems is convenient and can easily be applied in this case.

Nonlinear model (linear drag)

If a simplification given with (6.35) is applied, (6.33) can be rewritten as (6.41) under the assumption that drag is linear, i.e. $\beta(\nu) = \beta_\nu \cdot |\nu|$. This case study will also be referred to as the "linear damping" or the "linear drag" case.

$$\alpha_\nu \ddot{\eta} + \beta_{\nu\nu} |\dot{\eta}| \dot{\eta} = \tau + \Delta \quad (6.41)$$

By following the generalized procedure described in Chapter 6.1, specifically by substituting (6.2) into (6.36) gives the following equation

$$\begin{aligned} \alpha_\nu X_m (j\omega)^2 \sin(\omega t) + j\beta_{\nu\nu} X_m^2 \omega^2 |\sin(\omega t)| \sin(\omega t) = \\ = \Delta + [-Y_0 - (P_N + jQ_N) X_m \sin(\omega t)] \end{aligned}$$

with $Y_0 = Y_0(x_0, X_m)$, $P_N = P_N(x_0, X_m)$ and $Q_N = Q_N(x_0, X_m)$. Further development of the nonlinear term to the Fourier series gives

$$|\sin(\omega t)| \sin(\omega t) \approx \frac{3\pi}{8} \sin(\omega t),$$

and finally, three equations that describe the unknown parameters can be written:

$$\alpha = \frac{P_N(x_0, X_m)}{\omega^2} \quad (6.42)$$

$$\beta_{\nu\nu} = -\frac{3\pi}{8} \frac{Q_N(x_0, X_m)}{X_m \omega} \quad (6.43)$$

$$\Delta = Y_0(x_0, X_m) \quad (6.44)$$

If the mathematical model of a specific degree of freedom has a time delay, then modification given with (6.31) should be applied. In most cases, the nonlinear element which will be used for identification purposes will be relay with hysteresis, whose describing function parameters $P_N(x_0, X_m)$, $Q_N(x_0, X_m)$ and $Y_0(x_0)$ are derived in Chapter 5.1. Here only final formulae are given with (6.45), (6.46) and (6.47).

$$P_N(x_0, X_m) = \frac{2C}{\pi X_m} \left[\sqrt{1 - \left(\frac{x_a - x_0}{X_m} \right)^2} + \sqrt{1 - \left(\frac{x_a + x_0}{X_m} \right)^2} \right] \quad (6.45)$$

$$Q_N(x_0, X_m) = -\frac{4Cx_a}{\pi X_m^2} \quad (6.46)$$

$$Y_0 = C \frac{T_H - T_L}{T_H + T_L} \quad (6.47)$$

To sum up, the terms for identifying unknown parameters of the two case studies when the nonlinear element is in the closed loop, can be found in Table 6.3.

Table 6.3. Formulae for determining unknown parameters using IS-O method with relay with hysteresis

LINEAR MODEL (CONSTANT DRAG)	NONLINEAR MODEL (LINEAR DRAG)
$\alpha_\nu = \frac{P_N(x_0, X_m)}{\omega^2} = \frac{2C}{\pi} \frac{1}{\omega^2 X_m} \left[\sqrt{1 - \left(\frac{x_a - x_0}{X_m} \right)^2} + \sqrt{1 - \left(\frac{x_a + x_0}{X_m} \right)^2} \right]$	
$\beta_\nu = -\frac{Q_N(X_m)}{\omega} = \frac{4Cx_a}{\pi} \frac{1}{\omega X_m^2} \quad \beta_{\nu\nu} = -\frac{3\pi}{8} \frac{Q_N(X_m)}{X_m \omega^2} = \frac{3Cx_a}{2} \frac{1}{\omega^2 X_m^3}$	
$\Delta = C \frac{T_H - T_L}{T_H + T_L}$	

The following sections will give detailed description on how to apply the proposed procedure on yaw, surge and heave degree of freedom of marine vehicles. In addition to this, the proposed method will be applied for identification of unknown parameters of the heading closed loop system. Finally, the software implementation is presented. Some of these application have been published in [53] and [54].

6.6.1 Identifying Yaw DOF

The identification of yaw degree of freedom using the IS-O method requires only the use of an onboard compass. This means that yaw rate measurements are not necessary, which significantly simplifies the procedure. The schematic approach to conducting the IS-O experiment for yaw degree of freedom is shown in Fig. 6.4. Once the experimental data has been obtained, formulae in Table 6.3 can be applied (by substituting $\nu =$

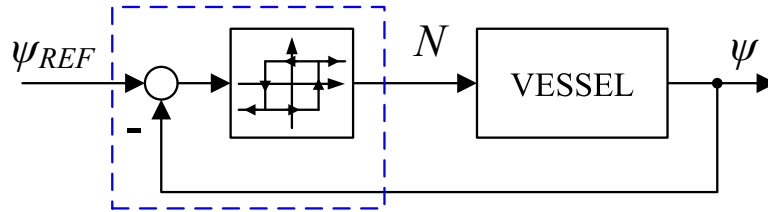


Figure 6.4. Application of IS-O method to yaw degree of freedom.

r) to determine the unknown model parameters. Experimental results of the IS-O method applied on VideoRay ROV, AutoMarine AUV and Charlie ASC are presented in Chapters 7.3, 7.4 and 7.5, respectively.

6.6.2 Identifying Surge DOF

The procedure for determining the surge model depends on the sensors that are available onboard. If a Doppler velocity logger (DVL) is available, direct measurements of surge speed is available. DVL also gives speeds in all other directions. This means that the model to be identified would be of the first order without an integrator. However, the same procedure as in yaw case can be applied if the integral of measured surge speed $u^\diamond = \int u dt$ is introduced to the relay input, as it is shown in Fig. 6.5. Then the surge model can be described with (6.48) where $\beta(u^\diamond)$ can be either β_u or $\beta_{uu} |u^\diamond|$, just like in the yaw case. Introducing an extra integrator ensures symmetric self-oscillations around any u_{REF} (where usually $u_{REF} = 0$).

$$\alpha_u \ddot{u}^\diamond + \beta(u^\diamond) \cdot \dot{u}^\diamond = X(t - 2T_d) + \tau_{XE} \quad (6.48)$$

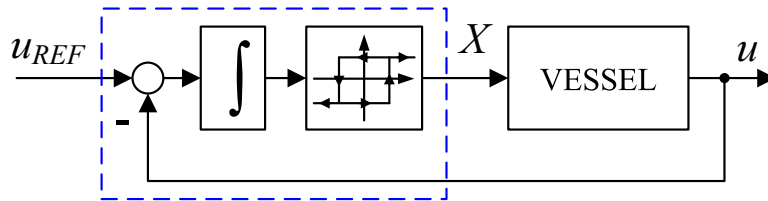


Figure 6.5. Application of IS-O method to surge degree of freedom – Approach 1.

Another approach is to use a measurement of a distance d with regard to a flat surface. The distance keeping model is described in detail in Chapter 2.6. In that model, d is distance to a flat surface, φ is the angle of the vessel with regard to the surface, and $\dot{d} = -u \cos(\varphi)$. If it is ensured that $\varphi \approx 0$, the approximation $\dot{d} \approx -u$ can be made. Having this in mind, value $d_{REF}(t) - d(t)$ can be used as input to the relay during the experiment and there is no need for introducing an extra integrator – only small angle with respect to surface has to be maintained. This angle is maintained by using an angle controller with $\varphi_{ref} = 0$ as it is shown in Fig. 6.6.

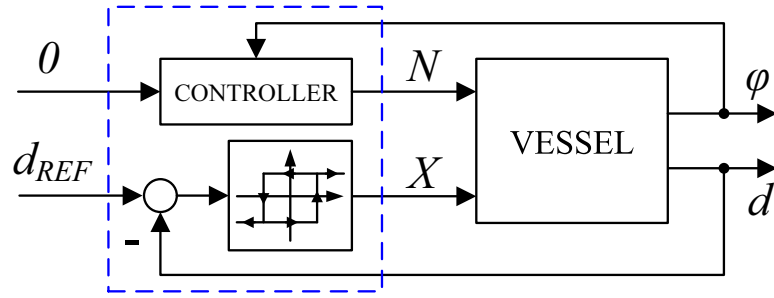


Figure 6.6. Application of IS-O method to surge degree of freedom – Approach 2.

For both approaches the output of the nonlinear element is desired surge force X . Once the experimental data has been obtained, formulae in Table 6.3 can be applied (by substituting $\nu = u$) to determine the unknown model parameters.

Experimental results of the IS-O method using the second approach applied on VideoRay ROV with a vision-based distance sensor are presented in Chapter 7.6.

6.6.3 Identifying Heave DOF

Determining heave degree of freedom makes sense for underwater vehicles only. In order to conduct the procedure, depth sensor has to be available onboard. The schematic approach to conducting the IS-O experiment for yaw degree of freedom is shown in Fig. 6.4.

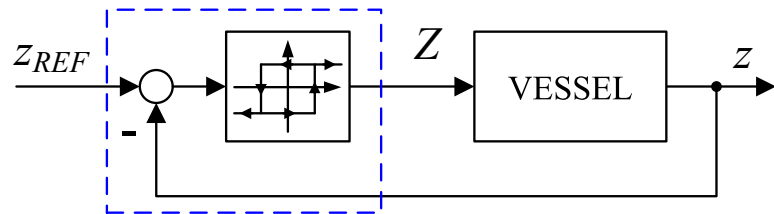


Figure 6.7. Application of IS-O method to heave degree of freedom.

It should be stressed here that heave degree of freedom has dominant influence of the difference between the buoyancy and weight of the vehicle. Because of this, the self-oscillation data will be asymmetric as it is shown in Fig. 6.8 where the data have been obtained from a simulation model. Once the experimental data has been obtained, formulae in Table 6.3 can be applied (by substituting $\nu = w$) to determine the unknown model parameters, where Δ will dominantly represent the difference between the buoyancy and weight of the underwater vehicle.

6.6.4 Identifying Heading Closed Loop

The heading closed loop might have to be identified for the purpose of designing a higher level of control (see Chapter 8.3 for details). The schematic approach to conducting

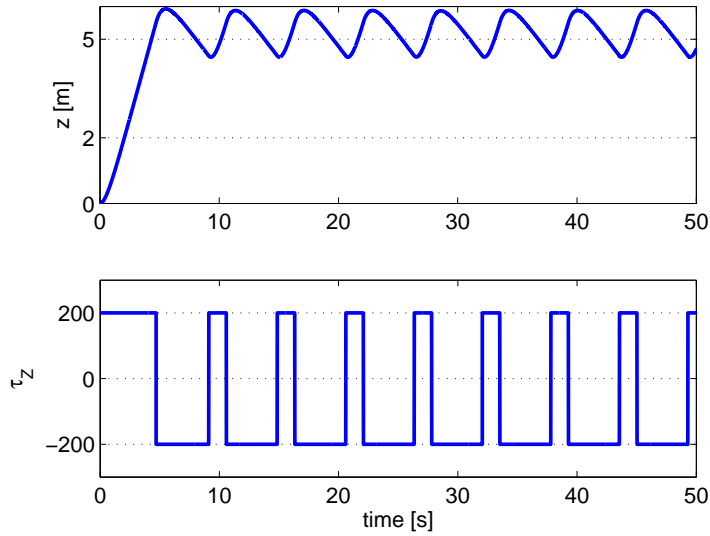


Figure 6.8. IS-O experiment responses for determining heave model (simulation example).

the IS-O experiment for heading closed loop identification is shown in Fig. 6.9. The reference heading ψ_{REF}^* is the value around which the oscillations will take place. The value ψ_{REF} is the relay output, i.e. the commanded heading for the heading closed loop.

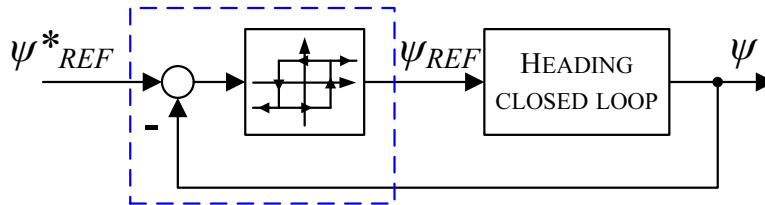


Figure 6.9. Application of IS-O method to heading closed loop.

Here an assumption is made that the heading closed loop transfer function can be expressed with (6.49). Later on in Chapter 8.3 this assumption will be elaborated in more detail.

$$\frac{\psi}{\psi_{ref}} = \frac{b_1\psi s + 1}{a_3\psi s^3 + a_2\psi s^2 + a_1\psi s + 1} \quad (6.49)$$

According to the general matrix algorithm for identification by use of self-oscillations presented in Chapter 6.2, the derivation of equations is as follows. According to (6.11), the number of experiments that have to be conducted is $\varepsilon = 3$, since systems order is $n = 3$ and number of finite zeros is $m = 1$. Using (6.16), the matrix equation is given

with (6.50).

$$\begin{bmatrix} 0 & -\omega_1^2 & 0 & P_{N1} & -\omega_1 Q_{N1} \\ 0 & -\omega_2^2 & 0 & P_{N2} & -\omega_2 Q_{N2} \\ 0 & -\omega_3^2 & 0 & P_{N3} & -\omega_3 Q_{N3} \\ \omega_1 & 0 & \omega_1^3 & Q_{N1} & \omega_1 P_{N1} \\ \omega_2 & 0 & \omega_2^3 & Q_{N2} & \omega_2 P_{N2} \\ \omega_3 & 0 & \omega_3^3 & Q_{N3} & \omega_3 P_{N3} \end{bmatrix} \begin{bmatrix} a_{1\psi} \\ a_{2\psi} \\ a_{3\psi} \\ b_{0\psi} \\ b_{1\psi} \end{bmatrix} = \begin{bmatrix} -1 \\ -1 \\ -1 \\ 0 \\ 0 \\ 0 \end{bmatrix}. \quad (6.50)$$

With an assumption that heading closed loop gain is 1, i.e. $b_0 = 1$, equation (6.50) can be rewritten as

$$\begin{bmatrix} 0 & -\omega_1^2 & 0 & -\omega_1 Q_{N1} \\ 0 & -\omega_2^2 & 0 & -\omega_2 Q_{N2} \\ 0 & -\omega_3^2 & 0 & -\omega_3 Q_{N3} \\ \omega_1 & 0 & \omega_1^3 & \omega_1 P_{N1} \\ \omega_2 & 0 & \omega_2^3 & \omega_2 P_{N2} \\ \omega_3 & 0 & \omega_3^3 & \omega_3 P_{N3} \end{bmatrix} \begin{bmatrix} a_{1\psi} \\ a_{2\psi} \\ a_{3\psi} \\ b_{1\psi} \end{bmatrix} = \begin{bmatrix} -1 - P_{N1} \\ -1 - P_{N2} \\ -1 - P_{N3} \\ -Q_{N1} \\ -Q_{N2} \\ -Q_{N3} \end{bmatrix}. \quad (6.51)$$

Two equations can be omitted – the ones obtained from the third experiment are a reasonable choice, leaving equation (6.52) which is applied for identification purposes. The unknown parameters are easily obtained by solving the matrix equation.

$$\begin{bmatrix} 0 & -\omega_1^2 & 0 & -\omega_1 Q_{N1} \\ 0 & -\omega_2^2 & 0 & -\omega_2 Q_{N2} \\ \omega_1 & 0 & \omega_1^3 & \omega_1 P_{N1} \\ \omega_2 & 0 & \omega_2^3 & \omega_2 P_{N2} \end{bmatrix} \begin{bmatrix} a_{1\psi} \\ a_{2\psi} \\ a_{3\psi} \\ b_{1\psi} \end{bmatrix} = \begin{bmatrix} -1 - P_{N1} \\ -1 - P_{N2} \\ -Q_{N1} \\ -Q_{N2} \end{bmatrix} \quad (6.52)$$

In this case, it is assumed that the external disturbance is attenuated by the inner closed loop therefore Δ parameter is not calculated separately.

Experimental results of the IS-O method applied for identification of the heading closed loop of Charlie ASV are presented in Chapter 7.7. Two experiments with different autopilot structures are given.

6.7 Software Implementation

One of the biggest advantages of the proposed identification by use of self-oscillations is that it is easy to implement and automate apart from the fact that it is time parsimonious.

The schematic representation of the subsystem for automated performing of IS-O experiments and the controller is shown in Fig. 6.10. The subsystem drawn with blue lines is called *The Monitoring and Identification System*. It is in charge of making decisions on when the self-oscillation experiment has finished. Its inputs are relay

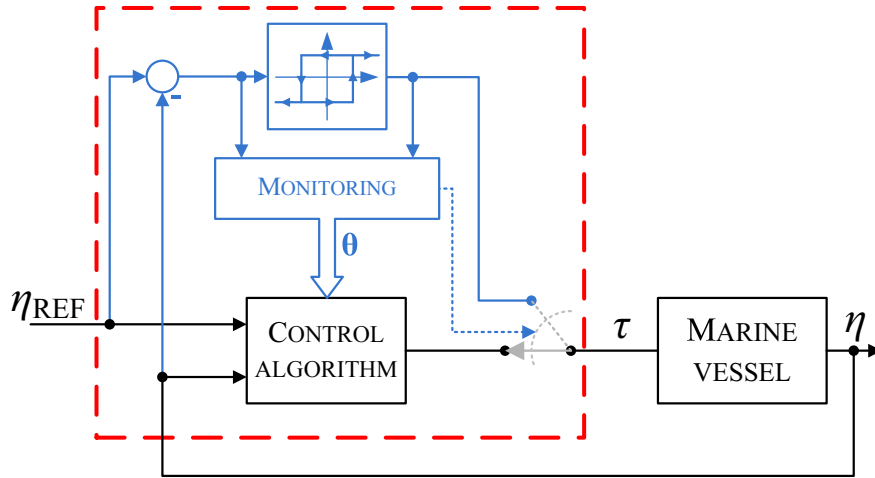


Figure 6.10. Schematic representation of a closed loop system with a monitoring and identification subsystem and a controller.

output (commanded force or moment) and relay input (heading, depth, etc.), and outputs are identified system parameters and switching signal.

The complete algorithm is shown in Fig. 6.11. The identification process is usually initiated by user. The rest of the procedure is performed automatically. The initiation phase is in fact inserting the nonlinear element (relay with hysteresis) in the closed loop, which initiates data collection.

Relay input and output are acquired at every time step. Based on the relay output data, every time $t_{switch}(i)$ the relay output changes, the duration of the previous "half-period" determined with $t_{switch}(i) - t_{switch}(i - 1)$ is recorded, and the extremal value during that time is logged. If the extremal value is minimum, the period $t_{switch}(i) - t_{switch}(i - 1)$ is the time the relay was in low position (T_L), and if it is maximum the period is the time the relay was in high position (T_H). It should be noted that mentioned "half-period" need not be exactly one half of the period of oscillations, which is the case when external disturbance is present.

When x_a , x_0 and X_m from each oscillation are obtained, the condition $x_a + |x_0| < X_m$ is checked. If it is fulfilled, that means that the self-oscillations are proper, i.e. the describing function of the relay with hysteresis can be calculated. If at least one oscillation does not satisfy this condition, the shift registers are cleared and the procedure begins from the start. This increases the robustness of the algorithm.

This procedure is performed until a predefined number of measurements has a standard deviation less than a predefined value. The variables in Fig. 6.11 that are in bold blue are FILO⁴ shift registers of the size the same as the number of oscillations that are to be taken into account. The green variables are scalar variables. In this thesis, the standard deviation of five consecutive maximal and five consecutive minimal values of

⁴They are filled and emptied on the first in last out principle.

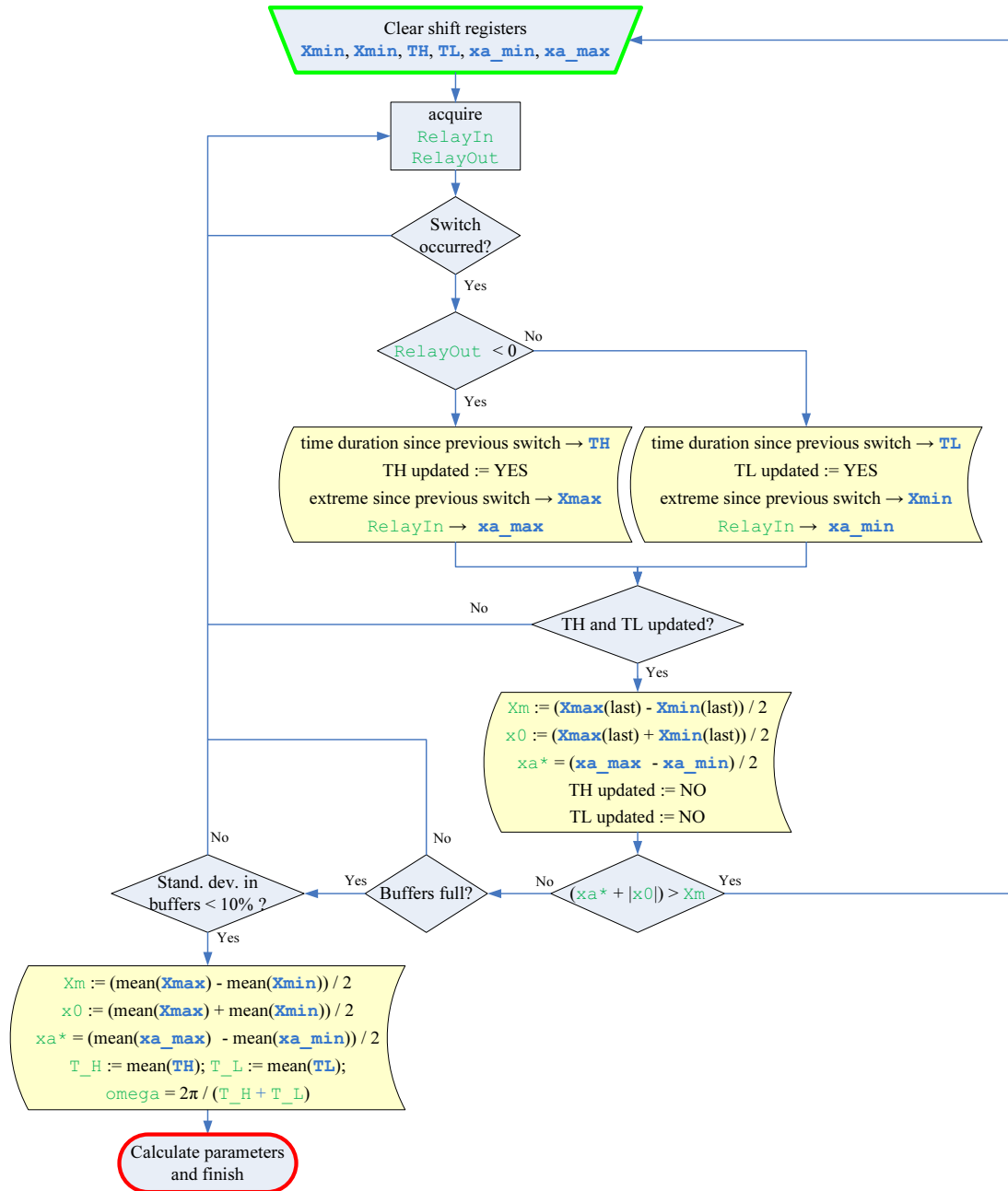


Figure 6.11. Algorithm for implementation of the IS-O method.

self-oscillations (five consecutive periods) was required to be within 10%. This means that the obtained data is reliable and can be used for identification procedure. This leads the algorithm to the phase in which the system parameters are calculated and the controller with the new parameters is inserted in the closed loop.

The procedure described here is the implementation for identification of controllable degrees of freedom for marine vessels. Similar procedure can be applied for identification

of the heading closed loop. It is expected in this case that $x_0 = 0$ for the reasons explained before.

6.8 Conclusion

The chapter begins with an overview of identification methods based on self-oscillations which can be found in literature. It is shown that autotuning is widely used in process industry for tuning controllers for linear (or at least linearized processes).

This is why a generalized procedure has been developed for identification by use of self-oscillations. This procedure was that limited to linear static processes of arbitrary order, resulting in a matrix algorithm for calculating the unknown parameters. Further on, the method was augmented to Type k systems. The only modification that has to be done for this case is change the describing function of the nonlinear element, i.e. simply multiply the describing function vector with a matrix. Similarly, a modification is needed if the process has time delay. In order to determine parameters of a process with time delay, the delay has to be known. This way its influence can be computationally compensated for. Since most of processes are computer controlled, an effect which occurs in that case is described and a methodology for minimizing it is presented. A couple of descriptive examples are given to clearly depict the proposed methodology.

Since the goal of this thesis is to develop a methodology for determining parameters of marine vessels, the described method for nonlinear systems is then focused on determining parameters of nonlinear differential equations that describe marine vessel motion. In addition to that, the general matrix IS-O equation is used to determine parameters of a heading closed loop transfer function. This will be used later on the thesis for tuning higher level controllers.

Finally, the chapter finishes with some software implementation issues. The completely automated system for IS-O performing consists of *The Monitoring and Identification Subsystem* which is in charge for automated completion of the IS-O experiment. A block diagram with detail description of this subsystem is given and described thoroughly.

Experimental Results for Different Identification Methods

Previous chapters are mostly engaged in description of the mathematical models and identification procedures. This chapter will present experimental results obtained with two underwater vehicles (VideoRay ROV and AutoMarine AUV) and one autonomous surface vehicle (catamaran) Charlie. The IS–O method that was introduced in this thesis will be compared to conventional methods, and comparative analysis and detailed results will be presented.

The chapter begins with a description of the methodology on how to decide on the appropriate model when using IS–O method. Then validation methods are presented. The following part, gives results for yaw identification of the three marine vessels and for identification of surge degree of freedom of VideoRay ROV. The latter is performed with the help of the vision based laser module described in Chapter 3.4. Finally, experimental results for identification of the closed loop system of Charlie USV are given. In order to prove the applicability of the method, two different low–level control structures were used during the experiments.

7.1 Deciding on the Appropriate Model

As is the case with identification methods, once the data have been collected, the first step is to determine which model fits the data best. With conventional identification methods such as the least–squares algorithm (L–S), the usual procedure is to perform a correlation function between the input and the output data to determine which parameters in the regression model are the most dominant, i.e. most contributing to the vehicle behavior, [51].

Another approach for the least–squares method is to fit the data to all the models that are considered. Once this is done, standard deviation can be calculated over sets of estimated parameters. The set of model parameters with the smallest standard deviation will than which is the model that best fits the collected data. This approach

has been applied in the thesis.

However, while performing IS–O experiments, a set of data is obtained and unknown parameters of different models can be calculated. It is obvious that the conclusion on which model is more appropriate cannot be made from only one IS–O experiment. That is why an additional experiment, with different relay parameters should be conducted, giving us two sets of estimated model parameters. The methodology on how to determine which model structure is more appropriate is described in the continuing part.

Let us say that from the first experiment α_{x1} , β_{x1} , β_{xx1} are calculated, and from the second α_{x2} , β_{x2} , β_{xx2} . Having this in mind, standard deviations between α_{x1} and α_{x2} , β_{x1} and β_{x2} , and β_{xx1} and β_{xx2} can be calculated as

$$\begin{aligned}\sigma_{\alpha_x}\% &= \left| \frac{\alpha_{x1} - \alpha_{x2}}{\alpha_{x1} + \alpha_{x2}} \right| \cdot 100\% \\ \sigma_{\beta_x}\% &= \left| \frac{\beta_{x1} - \beta_{x2}}{\beta_{x1} + \beta_{x2}} \right| \cdot 100\% \\ \sigma_{\beta_{xx}}\% &= \left| \frac{\beta_{xx1} - \beta_{xx2}}{\beta_{xx1} + \beta_{xx2}} \right| \cdot 100\%.\end{aligned}\tag{7.1}$$

Theoretically, $\sigma_{\alpha_x}\%$ will be 0 because it is calculated through the same formula for both assumed models (see Table 6.3). In real experiments it will have some value, which can be interpreted as measurement uncertainty. The criterion which is proposed for determining which model best describes the vehicle is given with (7.2). In (7.2), λ is a parameter which determines the robustness of the decision making which model is more appropriate.

$$\sigma_{\beta_x}\% - \sigma_{\beta_{xx}}\% \begin{cases} > \lambda & \Rightarrow \text{linear drag } (\beta_{xx}) \\ < -\lambda & \Rightarrow \text{constant drag } (\beta_x) \\ \in [-\lambda, \lambda] & \Rightarrow \text{no decision} \end{cases}.\tag{7.2}$$

Depending on robustness parameter λ , four different criteria are tested:

1. $\lambda = 0$ is the least robust criterion ensuring that any pair of measurements will result in a decision on the model, even though the difference between standard deviations is small. This criterion may lead to wrong decisions.
2. $\lambda = \sigma_{\alpha_x}\%$ is a criterion which includes the measurement uncertainty described by the standard deviation of α_x . Robustness in this case is increased and there is a margin in which decision might not be made.
3. $\lambda = \sigma_{\alpha_x}\% + 5\%$ is a criterion with increased robustness. The margin of not making a decision is also increased.
4. $\lambda = \sigma_{\alpha_x}\% + 10\%$ is a criterion with increased robustness where it is demanded that the difference between standard deviations be significantly different. In this case the decision that is made can be considered correct, but the path to making a decision may require more measurements being taken.

Example 7.1. The normalized yaw simulation model parameters of the FALCON vehicle are shown in Table 7.1. The results of the two self-oscillation experiments that were performed for yaw degree of freedom are shown in Table 7.2. The calculated

Table 7.1. *FALCON ROV yaw simulation model parameters*

α_r	β_r	β_{rr}
80	300	10

Table 7.2. *Self-oscillation data for FALCON ROV yaw simulation model identification*

	$X_m[^\circ]$	$\omega[s^{-1}]$	$\tilde{\alpha}_r$	$\tilde{\beta}_r$	$\tilde{\beta}_{rr}$
$x_a = 10^\circ$ $C = 300$	14	3.722	78.97	298.48	385.66
$x_a = 20^\circ$ $C = 300$	24.4	2.547	79.29	288.3	312.97
$\sigma\%$			0.29%	2.45%	14.71%

standard deviation of $\tilde{\beta}_r$ is less than the one of $\tilde{\beta}_{rr}$ under all suggested criteria which leads to the conclusion that linear model describes the behavior of the system better. However, it should be noticed that the true simulated vehicle dynamics also include the β_{rr} term. ■

Example 7.2. The real heave model parameters of the FALCON vehicle are shown in Table 7.3. The results of the two self-oscillation experiments that were performed for heave are shown in Table 7.4. The calculated standard deviation of $\tilde{\beta}_w$ is less than the

Table 7.3. *FALCON ROV heave simulation model parameters*

α_w	β_w	β_{ww}	τ_{ZE}
130	200	20	10

one of $\tilde{\beta}_{ww}$ under all suggested criteria which leads to the conclusion that linear model describes the behavior of the system better. However, it should again be noticed that the true simulated vehicle dynamics also include a β_{ww} term. ■

Table 7.4. Self-oscillation data for FALCON ROV heave simulation model identification

	$X_m[^\circ]$	$\omega[s^{-1}]$	$\tilde{\alpha}_w$	$\tilde{\beta}_w$	$\tilde{\beta}_{ww}$
$x_a = 0.5m$ $C = 200$	0.664	1.405	127.79	205.75	259.94
$x_a = 0.5m$ $C = 100$	0.594	0.935	132.28	192.86	408.81
$\sigma\%$			1.73%	3.23%	22.26%

Example 7.3. The real heave model parameters of an underwater vehicle with dominant nonlinear behavior in yaw degree of freedom that were used in this simulation example are shown in Table 7.5. The results of the two self-oscillation experiments that were performed for yaw are shown in Table 7.6.

Table 7.5. Dominantly nonlinear yaw simulation model parameters

α_r	β_r	β_{rr}
1.018	0	1.257

Table 7.6. Self-oscillation data for the dominantly nonlinear yaw model identification

	$X_m[^\circ]$	$\omega[s^{-1}]$	$\tilde{\alpha}_r$	$\tilde{\beta}_r$	$\tilde{\beta}_{rr}$
$x_a = 20^\circ$ $C = 1$	35.12	1.32	0.98	0.896	1.305
$x_a = 20^\circ$ $C = 0.8$	35.32	1.18	0.984	0.795	1.292
$\sigma\%$			0.2%	5.97%	0.5%

■

7.2 Model Validation Techniques

Once a model has been chosen, and parameters have been identified, the usual approach is to validate the obtained model. This is performed on validation sets of data which should be different from the data set that was used for identification. One of common validation techniques is the *sum of absolute errors*. It is based on running the validation input data through the identified model. The output y_{valid} which is obtained through validation is then compared to the experimentally obtained output y , i.e. the differences

at the same time instances are calculated and their absolute values are summed up as shown with (7.3), where $e(k) = y_{valid}(k) - y(k)$.

$$J = \frac{1}{N} \sum_{k=1}^N |e(k)| \quad (7.3)$$

If a novel method (I–SO) is to be compared to a conventional identification method (e.g. least–squares), the results obtained from a conventional method should be considered exact, perfectly correct. In this case the parameters obtained by using the novel method are compared to those obtained by a conventional one.

Often, when the parameters are compared to parameters obtained from a conventional method, the difference in parameters can seem significantly large, but the responses do not seem to differ. This is usually the case with systems that have large quantization levels or sampling time of the same order of magnitude as dominant system dynamics.

Comparison of steady states

It is often much more convenient to compare the two obtained models by giving a comparison of steady–state values that both give. This way it is much easier to make conclusions on the similarity of the two models. In addition to this, systems with significant quantization levels may give different identification results when using two methods, but because of the quantization of the measured signal, better results cannot be obtained. An example of systems with large quantization levels is VideoRay ROV which has an onboard compass with quantization of 2° . This may not seem large, but when least–squares identification is performed, the output heading is differentiated in order to identify first order input yaw moment to yaw rate differential equation. When the output heading is differentiated, the resulting yaw rate will have a quantization level of $20^\circ/\text{s}$ (under the assumption the sample time is 0.1s). This is why the following comparison validation tests are suggested, where bullet (\bullet) superscript stands next to the variables regarding conventional method, and circle (\circ) marks the variables regarding a novel method.

For the *linear* astatic case, the step response is given with (4.30). From here it follows that the steady state value is given with (7.4) where, in the specific case of yaw identification, τ is applied yaw moment (N), $\nu_{SS} = r_{SS}$ and β_ν is constant drag.

$$\nu_{SS} = \nu(\infty) = \frac{|\tau|}{\beta_\nu} \quad (7.4)$$

The next step is to calculate the difference in steady states ($\Delta\nu_{SS}$) by using (7.5).

$$\Delta\nu_{SS} = |\nu_{SS}^\bullet - \nu_{SS}^\circ| = \left| \tau \left(\frac{1}{\beta_\nu^\bullet} - \frac{1}{\beta_\nu^\circ} \right) \right| \quad (7.5)$$

If this difference is within one quantization interval, the identified drag β_x° can be considered the same, i.e. due to the quantization error, the difference between the two estimated parameters is insignificant given the sensors which were used to perform the identification. The difference in steady states is a function of τ so the worst case scenario is calculated by substituting $\tau = \tau_{max}$, where τ_{max} is the maximal applied input during the identification experiments.

A similar approach can be used for the *nonlinear* astatic case, for which the response is given with (4.35). The steady state value is now given with (7.6) where again in the specific case of yaw identification, τ is applied yaw moment (N), $\nu_{SS} = r_{SS}$ and $\beta_{\nu\nu}$ is linear drag.

$$\nu_{SS} = \nu(\infty) = \sqrt{\frac{|\tau|}{\beta_{\nu\nu}}} \quad (7.6)$$

The difference in steady states ($\Delta\nu_{SS}$) is given with (7.7). After applying $\tau = \tau_{max}$ the same procedure can be followed as in the linear case.

$$\Delta\nu_{SS} = |\nu_{SS}^\bullet - \nu_{SS}^\circ| = \left| \sqrt{\tau} \left(\frac{1}{\sqrt{\beta_{\nu\nu}^\bullet}} - \frac{1}{\sqrt{\beta_{\nu\nu}^\circ}} \right) \right| \quad (7.7)$$

Comparison of equivalent time constants

Similar logic can be applied to validate the correctness of the identified inertia parameter for the linear and nonlinear models. Inertia identified using a novel method (IS-O) can differ substantially from the one obtained using a conventional identification method, and still step responses of the two models need not be that different. That is why the proposed validation technique is based on finding equivalent time constants of the system, and making a comparison between the two. For the *linear* astatic case, the step response is given with (4.30). From here it follows that the time constant T_L (which is defined as the time it takes for the step response to reach 63% of the steady state value) is given with (7.8) where, in the specific case of yaw identification, $\alpha_\nu = \alpha_r$ and $\beta_\nu = \beta_r$. It is worth noting that T_L does not depend on the input τ , i.e. the system will respond equally fast for any input signal.

$$T_L = \frac{\alpha_\nu}{\beta_\nu} \quad (7.8)$$

The next step is to calculate the difference in equivalent time constants ΔT_L by using the parameters obtained from a conventional and novel identification method, as it is shown with (7.9). It is worth noting that these time constants depend on the previously determined drag.

$$\Delta T_L = \left| \frac{\alpha_\nu^\bullet}{\beta_\nu^\bullet} - \frac{\alpha_\nu^\circ}{\beta_\nu^\circ} \right| \quad (7.9)$$

Using ΔT_L it can be determined how many time samples is the difference between the rise time of the two models. Based on this, the conclusion can be made on the quality of

the identified inertia α_ν° : the smaller the difference, the better the identification results.

Again a similar approach is used for *nonlinear* astatic case, for which the response is given with (4.35). The equivalent time constant T_N which has been defined in Chapter 4.3 as the time it takes the output to reach 73% of the steady state value is given with (7.10). It is worth noticing that this time *constant* is a function of input τ : the smaller the input, the longer it will take for the output to reach 73% of steady state, and vice versa.

$$T_N = \frac{\alpha_\nu}{\sqrt{\beta_{\nu\nu}} |\tau|} \quad (7.10)$$

The next step is to calculate the difference in equivalent time constants ΔT_N by using the parameters obtained from a conventional and novel identification method, as it is shown with (7.11). It is worth noting that these time constants depend on the previously determined drag.

$$\Delta T_N = \left| \frac{1}{\tau} \left(\frac{\alpha_\nu^\bullet}{\sqrt{\beta_{\nu\nu}^\bullet}} - \frac{\alpha_\nu^\circ}{\sqrt{\beta_{\nu\nu}^\circ}} \right) \right| \quad (7.11)$$

Since ΔT_N is a function of the input τ a similar approach is used as in the case with quantization levels. The worst case scenario implies substitution $\tau = \tau_{min}$. Theoretically, this means that τ_{min} should be chosen to be 0. Since that choice does not make much sense, τ_{min} can be chosen as the smallest input applied during the identification experiments. From here, just as in the linear case, ΔT_N can be used to determine how many time samples is the difference between the rise times of the two models, given some step input value τ . Based on this, the conclusion can be made on the quality of the identified inertia α_ν° : the smaller the difference, the better the identification results.

7.3 Identifying Yaw DOF – VideoRay ROV

The experimental data for the identification of the yaw degree of freedom have been obtained from experiments performed in the Laboratory for Underwater Systems and Technologies, Faculty of Electrical Engineering and Computing, University of Zagreb with the VideoRay ROV. The vehicle's technical characteristics, system architecture and mathematical models are described in Chapter 3.1. The Laboratory is equipped with a circular pool 1.5 m deep, which makes it impossible to conduct heave degree of freedom tests on the real vehicle. However, extensive experiments have been carried out on identifying the yaw degree of freedom.

The data have been collected by inducing the system into self-oscillations. An example of responses during one experiment is shown in Fig. 7.1. First plot gives the input to the relay, $\psi_{ref} - \psi$, while the second plot gives commanded yaw moment to the vehicle N , which is in fact output of the relay with $C = |N|$. Red circles represent maxima of the oscillations, green dots minima and yellow stars represent the moments

in which relay switching occurred.

For the experiment to be successful, self-oscillations have to be obtained. A condition which has to be fulfilled for this is given with (7.12). This comes as a direct consequence of the domain of real part of the describing function of the asymmetric relay with hysteresis. An example of the relay parameters set inappropriately is given in Fig. 7.2, where hysteresis width was chosen to be $x_a = 0$.

$$\frac{x_a^* + |x_0|}{X_m} < 1 \quad (7.12)$$

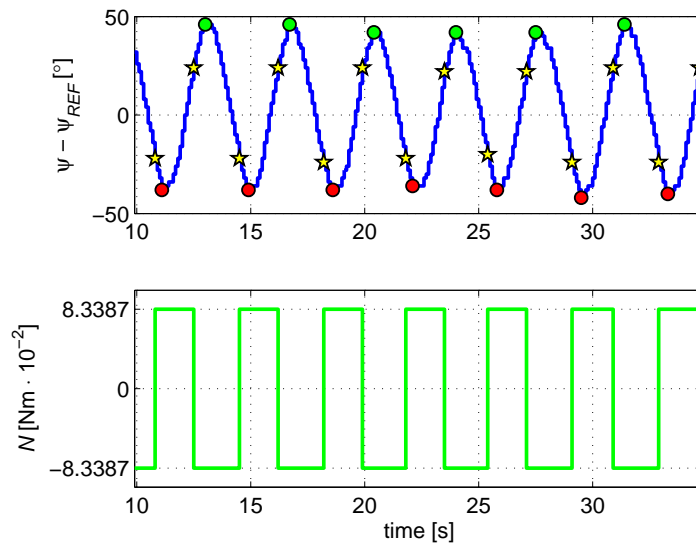


Figure 7.1. Example of responses during an IS-O experiment performed with VideoRay ROV for yaw degree of freedom.

All together, 15 data sets were obtained by changing relay hysteresis output N and width x_a . These experiments are considered to be informative enough to make a decision on the mathematical model parameters.

The obtained data is first used to fit a model by using the least-squares algorithm (L-S). Later on, the same data sets will be used to determine the model by using IS-O method.

7.3.1 Least-Squares Results

The least-squares method was applied on the data obtained from the self-oscillation experiments. For each data set a least-squares identification was performed. The assumed dynamic model of the yaw degree of freedom is given with (3.4) where drag β_r can be expressed as constant or linear as in (2.34). From here follow the linear

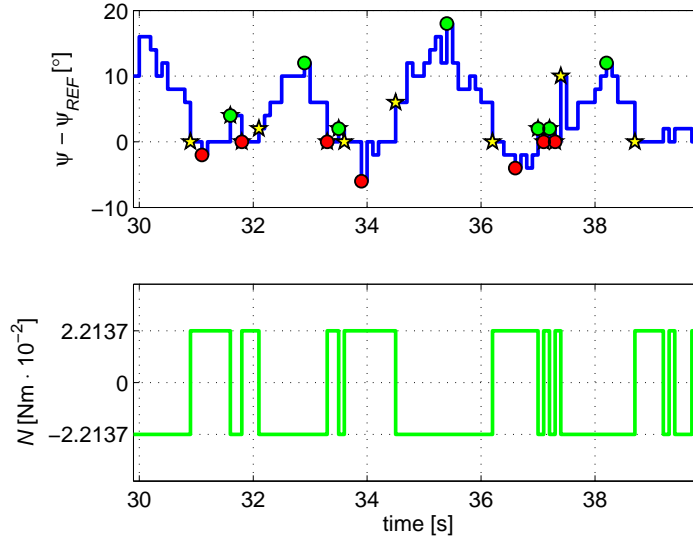


Figure 7.2. Example of responses during the IS–O method when conditions for inducing self-oscillations are not fulfilled ($x_a = 0$).

and nonlinear regression model used for performing least-squares identification. Least-squares identification is described in detail in Chapter 4.2, so it will be omitted here. In addition to that, linear and nonlinear regression models are given with (4.20) and (4.22), respectively ($\nu = r$ in this case).

The identified parameters of the linear and nonlinear model are shown separately in Tables 7.7 and 7.8. The conventional identification by use of the least-squares gives poor results at small input signals because of the big quantization level. It was shown that in these cases drag can be identified with sufficient accuracy, but inertia is difficult to determine due to rather large quantization levels. This is why measurements marked with a dagger (†) are not taken into account when calculating the mean value of the measurements.

From Tables 7.7 and 7.8 it is obvious that standard deviation of identified inertia α_r is higher than 30% for both linear and nonlinear case. This comes as a direct consequence of the compass quality. In addition to that, this data is not confident enough to make a conclusion on which model fits the data better. However, in the nonlinear case the standard deviation of the identified drag β_{rr} is much smaller (around 10%) than in the linear case where drag β_r was identified with standard deviation of about 32%. This leads to the conclusion that the nonlinear model better describes VideoRay ROV in the yaw degree of freedom, based on the discussion presented in Section 7.1.

Table 7.7. Experimental results for the Videoray ROV yaw DOF by applying least-squares identification – the linear model.

N [Nm · 10 ⁻²]	α_r [$\frac{\text{Nms}^2}{\text{deg}} \cdot 10^{-4}$]	$\bar{\alpha}_r$ [$\frac{\text{Nms}^2}{\text{deg}} \cdot 10^{-4}$]	β_r [$\frac{\text{Nms}}{\text{deg}} \cdot 10^{-4}$]	$\bar{\beta}_r$ [$\frac{\text{Nms}}{\text{deg}} \cdot 10^{-4}$]
2.21	3.36	3.36 †	8.66	8.66
	3.44		12.93	
3.96	3.17	3.01	11.99	11.90
	3.34		11.76	
	2.07		10.92	
	5.06		18.29	
	5.87		18.40	
8.34	4.52	5.30	16.77	17.44
	5.36		16.91	
	5.69		16.82	
12.71	7.27	7.27	18.98	18.98
	7.26		20.33	
17.09	6.72	7.30	20.11	20.11
	7.41		19.99	
	7.81		20.01	
\bar{x}		5.72		15.42
$\frac{\sigma_x}{\bar{x}} \cdot 100\%$		35.60		31.91

7.3.2 IS–O Results

From each of the 15 experiments, unknown parameters were identified using the identification by use of self-oscillations method. The results obtained from the experiments are shown in Table 7.9.

The results by using IS–O are consistent even at smaller applied moments, i.e. when oscillations have smaller amplitudes. This is one great advantage in comparison to the L–S method: there is no need to differentiate heading signal in order to obtain a second order model but only heading measurements are needed. This way the sensor’s bad properties are not exacerbated by differentiation.

Mean values for overall measurements shown in Table 7.9 are insignificant because IS–O method should give satisfactory parameters for *each* experiment. The table only has standard deviation as a parameter so that the consistency in determining inertia and drag can be noticed.

Inertia term α_r is calculated using the same formula for both linear and nonlinear model. Linear model has much greater standard deviation in the drag parameter β_r (around 28%) than the nonlinear model with 11.22% standard deviation in drag parameter β_{rr} . This again shows that the nonlinear model better describes the yaw de-

Table 7.8. Experimental results for the Videoray ROV yaw DOF by applying least-squares identification – the nonlinear model.

N [Nm · 10 ⁻²]	α_r [$\frac{\text{Nms}^2}{\text{deg}} \cdot 10^{-4}$]	$\bar{\alpha}_r$ [$\frac{\text{Nms}^2}{\text{deg}} \cdot 10^{-4}$]	β_{rr} [$\frac{\text{Nms}^2}{\text{deg}^2} \cdot 10^{-6}$]	$\bar{\beta}_{rr}$ [$\frac{\text{Nms}^2}{\text{deg}^2} \cdot 10^{-6}$]
2.21	3.17	3.17 †	23.53	23.53
	3.25		31.12	
3.96	3.21	2.99	26.01	26.38
	3.19		27.20	
	2.30		21.18	
	4.95		28.61	
	5.57		33.43	
8.34	4.18	4.87	25.62	28.97
	4.78		28.59	
	4.87		28.58	
12.71	6.53	6.53	26.31	26.31
	6.56		22.72	
17.09	6.15	6.63	22.22	22.15
	6.66		21.62	
	7.17		22.04	
\bar{x}		5.26		25.95
$\frac{\sigma_x}{\bar{x}} \cdot 100\%$		32.60		10.29

gree of freedom of VideoRay, but more importantly shows the consistency of parameter identification during a single experiment.

Deciding on the model

Based on the experiments which were performed, the conclusion is made that the model with linear drag (nonlinear model) describes system dynamics better than the one with constant drag (linear model). However, the point is not to have to perform numerous IS–O experiments to determine the suitable model, but only two as it is suggested in Section 7.1.

Among the 15 experiments, pairs were taken in such a way that each member of the pair must have different relay outputs N . This is not an uncommon demand, since the two experiments that are performed to decide on the model should be as different as possible. This condition leads to 83 different combinations of pairs. All four criteria listed in Section 7.1 have been tested and the results are shown in Fig. 7.3, where dark green represents the number of pairs when the conclusion was correctly made, light green the number of pairs when the conclusion was falsely made and in yellow the number of pairs where the conclusion could not be made.

Table 7.9. Experimental results for the Videoray ROV yaw DOF by applying identification by use of self-oscillations (I-SO).

N [Nm · 10 ⁻²]	x_a^* [deg]	X_m [deg]	ω [$\frac{\text{rad}}{\text{s}}$]	x_0 [deg]	α_r [$\frac{\text{Nms}^2 \cdot 10^{-4}}{\text{deg}}$]	β_r [$\frac{\text{Nms} \cdot 10^{-4}}{\text{deg}}$]	β_{rr} [$\frac{\text{Nms}^2 \cdot 10^{-6}}{\text{deg}^2}$]
2.21	10.29	20.60	1.47	2.00	4.26	6.75	26.17
3.96	11.00	26.17	1.64	1.17	5.16	8.10	22.20
	16.84	29.78	1.52	2.22	4.52	8.77	22.89
	21.20	35.25	1.35	1.25	4.75	8.38	20.69
	41.07	53.00	0.95	3.86	4.87	8.79	20.52
8.34	6.58	26.36	2.34	3.80	5.46	11.27	21.53
	12.21	30.69	1.95	1.62	6.29	12.69	24.92
	17.73	36.57	1.86	2.86	5.35	12.01	20.84
	22.37	41.08	1.71	2.62	5.38	12.01	20.21
12.71	31.29	47.17	1.47	1.50	5.43	13.02	22.10
	22.42	44.09	1.91	1.55	6.09	15.20	21.21
	12.00	38.67	2.60	2.33	5.57	16.03	18.78
17.09	17.83	44.40	2.38	4.40	5.38	15.92	17.72
	22.50	47.33	2.21	2.67	5.59	16.77	18.93
	34.00	60.33	1.79	2.67	6.46	16.45	17.94
\bar{x}							
$\frac{\sigma_{\bar{x}}}{\bar{x}} \cdot 100\%$					11.46	28.08	11.22

It is obvious from Fig. 7.3 that criterion 1 always caused the decision to be made, and in almost 90% of chosen pairs the conclusion was made correctly. In about 9 times less cases, the conclusion was false. When using criterion 2, the margin of no decision is introduced and for a number of experiments the decision could not be made (less than 20%). If a pair for which the conclusion cannot be made is chosen, additional experiments should be performed to make conclusion about the possible model. However, in this case, the number of correct decisions is 16 time bigger then wrong decisions. By increasing the margin of decision (criteria 3 and 4) the number of cases without decision increases, but the number of pairs with falsely made decision vanishes.

7.3.3 Model Validation and Comparison of IS-O and L-S Identification Methods

In this section, the parameters obtained by use of the least-squares method will be taken as correct ones, even though the standard deviations of the estimated parameters are significant. However, they will be used as a means of comparison to the model obtained by using the IS-O method, as it was described in Section 7.2. Fig. 7.4 shows the absolute value of the percentage error of each IS-O obtained inertia parameter α_r

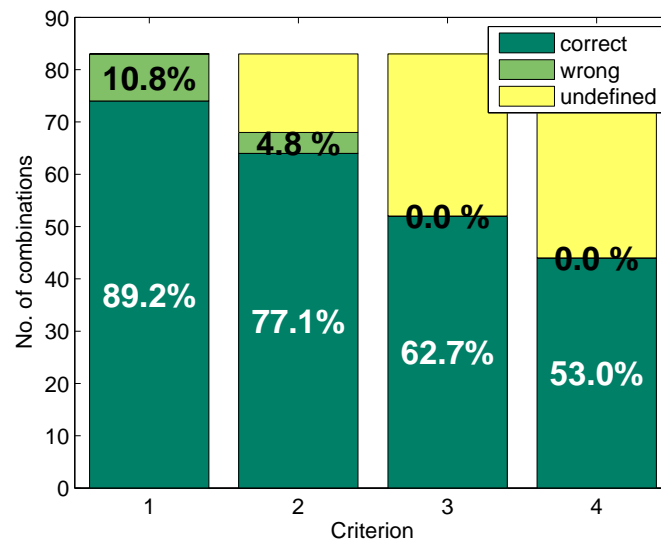


Figure 7.3. Number of cases when the conclusion was correct, false or undefined for VideoRay ROV.

with respect to the parameter obtained from the least-squares method with a nonlinear model. The error is always smaller than 25%. The same type of errors only for the obtained drag β_{rr} are shown in Fig. 7.5. From here it is seen that the errors can get significantly high, up to 30% or more for greater relay outputs, when comparing to the L-S identified parameters.

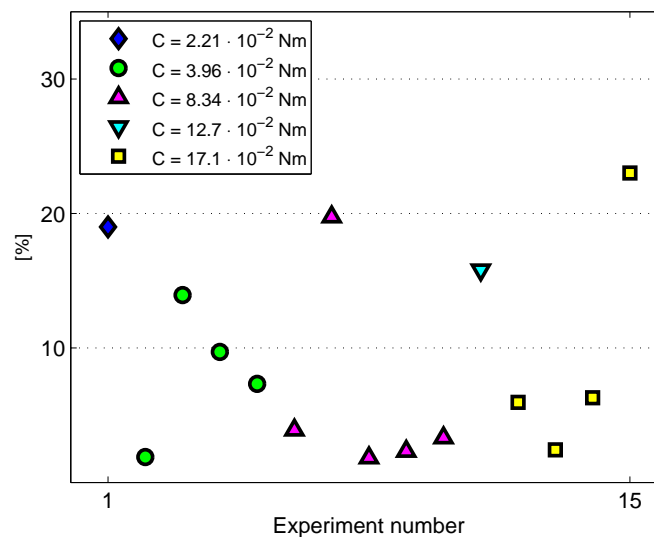


Figure 7.4. Relative errors of IS-O obtained inertia α_r with respect to the inertia obtained by LS method.

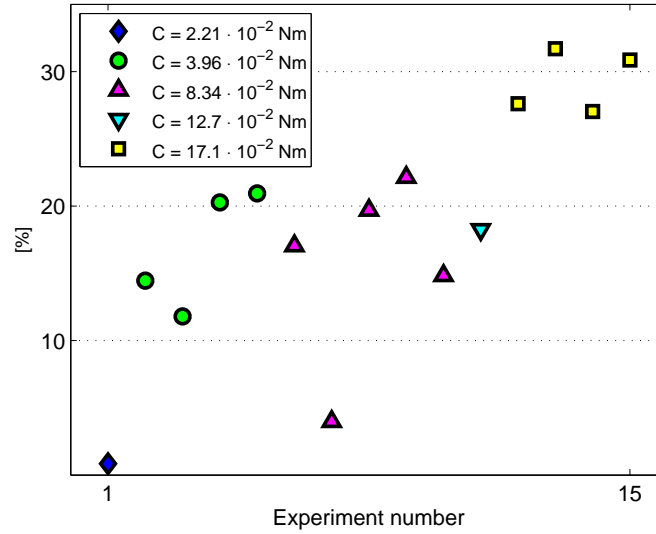


Figure 7.5. Relative errors of IS–O obtained drag β_{rr} with respect to the drag obtained by LS method.

Comparison of steady states

However, these results may be misleading. Using the methodology described in Section 7.2, the differences in achieved steady states of each IS–O model is compared to the L–S obtained model and Δr_{SS} is calculated by using (7.7). Since Δr_{SS} is a function of τ , the worst case scenario is when $\tau = C$ is the biggest. For this reason, the maximal C that was used in all experiments is taken into calculation ($C = 17.1 \text{ Nm} \cdot 10^{-2}$).

The results are shown in Fig. 7.6. From this point of view, Δr_{SS} is always smaller than $20^\circ/\text{s}$.

Comparison of equivalent time constants

The error which is included in the identified α_r should be observed from the point of view of equivalent time constant T_N as it was elaborated in Section 7.2. T_N is calculated for each of the identified IS–O models and compared to the L–S obtained model. ΔT_N is calculated using (7.11). Since ΔT_N is a function of τ , the worst case scenario is when $\tau = C$ is the smallest. For this reason, the minimal C that was used in all experiments is taken into calculation ($C = 2.21 \text{ Nm} \cdot 10^{-2}$).

The results are shown in Fig. 7.7 as numbers of time samples contained in each ΔT_N . From this point of view, it is much easier to comprehend what the difference between IS–O and L–S obtained models really is. It is obvious that in only one case the difference is greater than 3 sample times and all other cases it is smaller than 2 sample times, they will reflect as 2 sample times difference.

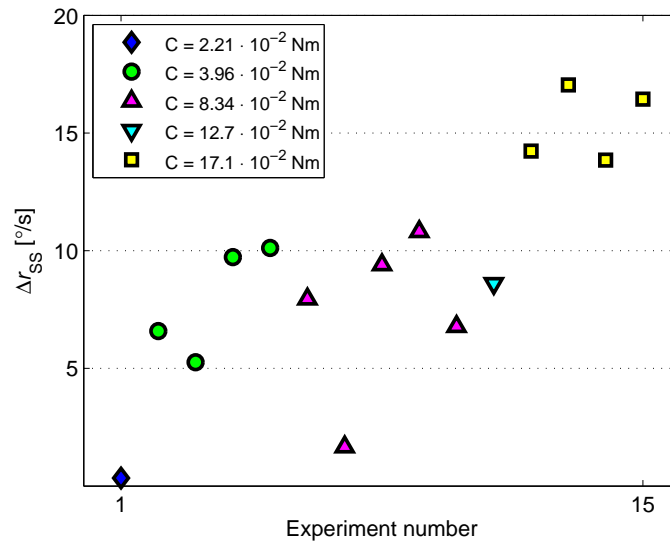


Figure 7.6. Relative errors of IS-O obtained drag β_{rr} with respect to the L-S obtained one observed from the steady state quantization point of view.

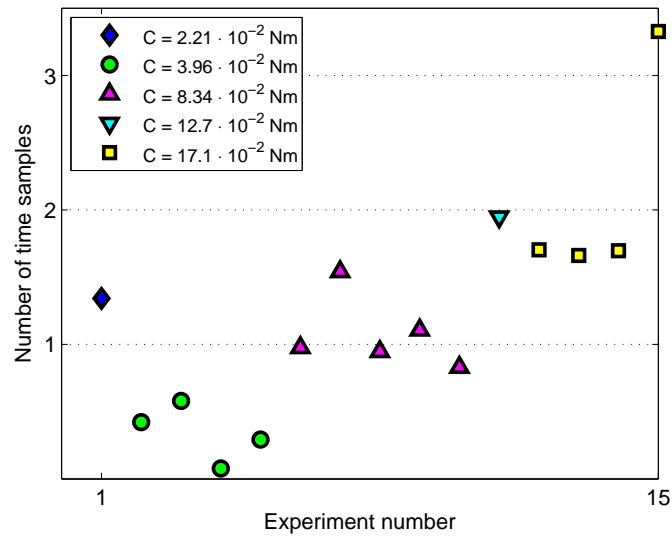


Figure 7.7. Relative errors of IS-O obtained inertia α_r with respect to the L-S obtained one observed from the rise time T_N point of view.

Sum of absolute errors

Finally, the rudimentary sum of absolute errors is performed for each obtained model. The model obtained using the least-squares method has been validated on all 15 data sets and the calculated average sum of absolute errors \bar{J}_{LS} was taken as reference. Each of the 15 models obtained using the IS-O method was also validated on all 15 data sets,

and for each model i an average sum of square errors $\bar{J}_{IS-O,i}$ was calculated. Fig. 7.8 shows the relative difference

$$\frac{\bar{J}_{IS-O,i} - \bar{J}_{LS}}{\bar{J}_{LS}} \quad (7.13)$$

for all experiments. It can be seen that the models obtained using the IS–O method give smaller sum of absolute errors in most cases. In other cases the increase in sum of absolute errors is acceptable with respect to the simplicity of performing the IS–O method. These results are the best demonstration of how IS–O method gives good identification results.

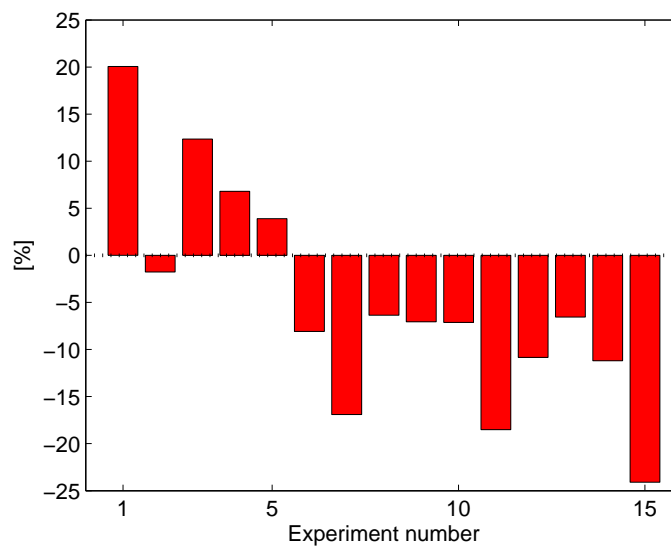


Figure 7.8. Comparison of sum of absolute errors obtained using IS–O obtained models with the L–S model.

7.4 Identifying Yaw DOF – AutoMarine AUV

The experimental data for the identification of the yaw degree of freedom have been obtained from experiments performed in the Laboratory for Underwater Systems and Technologies, Faculty of Electrical Engineering and Computing, University of Zagreb on the AutoMarine AUV. The vehicle’s technical characteristics, system architecture and mathematical models are described in Chapter 3.2.

7.4.1 Results from Step Responses

Conventional method that was used for this vehicle is the identification based on the open loop step response (SR method) which is described in detail in Chapter 4.3. The experiments were carried out on the AUV in such a way that each time a different

yaw moment ranging from -0.0515Nm to 0.0515Nm was applied, resulting in 24 SR experiments. The measurements that were made were based on the compass signal which implies that the identified system was astatic. From each experiment, the steady state was determined and the results are shown in Fig. 7.9 with green circles. From these results it is obvious that the model that fits the data better is the nonlinear model, with linear drag. By fitting the obtained steady state data to a linear drag model, using (4.47), the red line in Fig. 7.9 is obtained.

Next step was to determine the velocity errors ε_v from the experimental data sets. By using (4.48), the unknown inertia parameter α_r can be calculated for each experiment. These results are shown in Fig. 7.10 with green circles. The fitted constant value is shown with the red line.

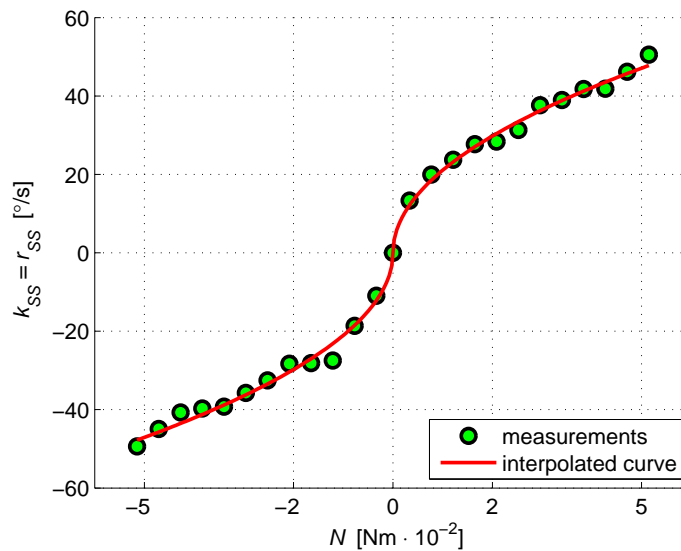


Figure 7.9. Steady-state yaw rate values obtained from step response (SR) experiments.

The experimental data are also shown in Table 7.10 showing the parameters of fitted curves as mean values from all experiments. It is also seen that standard deviations of measurements are satisfactory, which leads to the conclusion that the chosen model fits the data well.

7.4.2 IS–O Results

The IS–O method was applied on AutoMarine AUV and 32 experiments were performed with different relay outputs and hysteresis widths. The results are presented in Table 7.11.

Mean values for overall measurements shown in Table 7.11 are insignificant, just as in the case with VideoRay ROV, because IS–O method should give satisfactory parameters for EACH experiment. The standard deviation in determining inertia and

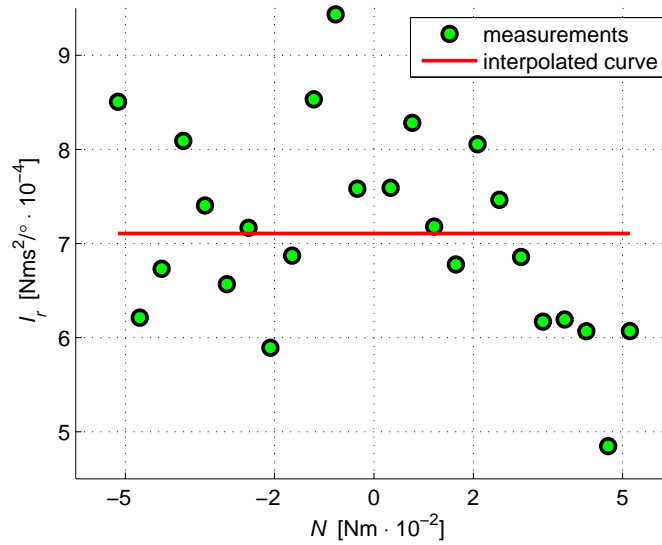


Figure 7.10. Parameter α_r obtained from step response (SR) experiments.

drag gives the measure of consistency of experimentally obtained parameters.

Inertia term α_r is calculated using the same formula for both linear and nonlinear model. Linear model has greater standard deviation in the drag parameter β_r (around 12.5%) than the nonlinear model with 8.55% standard deviation in drag parameter β_{rr} . This again shows that the nonlinear model better describes the yaw degree of freedom of AutoMarine AUV, but more importantly shows the consistency of parameter identification during a single experiment.

Deciding on the model

Based on the experiments which were performed, the conclusion is made that the model with linear drag (nonlinear model) describes system dynamics better than the one with constant drag (linear model). However, the same as in the case of VideoRay ROV, the point is not to have to perform numerous IS–O experiments to determine the suitable model, but only two as it is suggested in Chapter 7.1.

Among the 32 IS–O experiments, pairs were taken in such a way that each member of the pair must have different relay outputs N . This is not an uncommon demand, since the two experiments that are performed to decide on the model should be as different as possible. This condition leads to 347 different combinations of pairs. All four criteria listed in Chapter 7.1 have been tested and the results are shown in Fig. 7.11, where dark green represents the number of pairs when the conclusion was correctly made, light green the number of pairs when the conclusion was falsely made and in yellow the number of pairs where the conclusion could not be made.

Fig. 7.11 shows that criterion 1 always caused the decision to be made, and in about

Table 7.10. Experimental results obtained from the AutoMarine AUV yaw DOF using the step response (SR) method.

N [Nm · 10 ⁻²]	k_{ss} [$\frac{\text{deg}}{\text{s}}$]	ε_v [deg]	β_r [$\frac{\text{Nms}^2}{\text{deg}} \cdot 10^{-4}$]	β_{rr} [$\frac{\text{Nms}}{\text{deg}} \cdot 10^{-6}$]	α_r [$\frac{\text{Nms}^2}{\text{deg}^2} \cdot 10^{-4}$]
-5.15	-49.38	27.93	10.42	21.11	8.51
-4.71	-44.93	18.46	10.48	23.33	6.21
-4.27	-40.73	18.12	10.49	25.75	6.73
-3.83	-39.71	23.06	9.66	24.32	8.09
-3.40	-39.26	23.28	8.65	22.04	7.40
-2.96	-35.72	19.63	8.29	23.19	6.57
-2.52	-32.53	20.85	7.75	23.83	7.17
-2.08	-28.29	15.68	7.37	26.05	5.89
-1.65	-28.13	22.87	5.86	20.82	6.87
-1.21	-27.49	36.94	4.40	16.01	8.53
-0.77	-18.62	29.38	4.15	22.26	9.44
-0.34	-10.96	18.86	3.05	27.87	7.58
0.34	13.32	27.89	2.51	18.87	7.59
0.77	19.96	29.61	3.87	19.39	8.28
1.21	23.72	23.15	5.10	21.50	7.18
1.65	27.71	21.90	5.95	21.46	6.78
2.08	28.38	21.57	7.35	25.89	8.05
2.52	31.35	20.16	8.05	25.67	7.46
2.96	37.64	22.75	7.86	20.89	6.86
3.40	38.99	19.14	8.71	22.35	6.17
3.83	41.77	19.53	9.18	21.98	6.19
4.27	41.84	17.23	10.21	24.41	6.07
4.71	46.18	15.22	10.20	22.08	4.85
5.15	50.54	20.88	10.18	20.15	6.07
\bar{x}			7.49	22.55	7.11
$\frac{\sigma_x}{\bar{x}} \cdot 100\%$			34.00	11.84	14.75

63% of chosen pairs the conclusion was made correctly. Criteria 2, 3 and 4 significantly minimize the number of cases when the conclusion is made. If a pair for which the conclusion cannot be made is chosen, additional experiments should be performed to make conclusion about the model.

7.4.3 Model Validation and Comparison of IS–O and Step Response Identification Methods

In this section, the parameters obtained by use of the SR method will be taken as the correct ones. They will be used as a means of comparison to the model obtained by using the IS–O method, as it was described in Chapter 7.2. Fig. 7.12 shows the absolute

Table 7.11. Experimental results for the AutoMarine AUV yaw DOF by applying identification by use of self-oscillations (I-SO).

N [Nm · 10 ⁻²]	X_m [deg]	ω [s ⁻¹]	x_a^* [deg]	x_a [deg]	α_r [$\frac{\text{Nms}^2 \cdot 10^{-4}}{\text{deg}}$]	β_{rr} [$\frac{\text{Nms} \cdot 10^{-6}}{\text{deg}}$]	β_r [$\frac{\text{Nms}^2 \cdot 10^{-4}}{\text{deg}^2}$]
3.40	23.8	1.42	13.0	10	7.60	24.54	7.01
	23	1.68	11.2	10	7.32	20.90	6.85
	27.0	1.52	14.6	12	7.36	20.64	7.18
	28.4	1.45	16.8	14	7.30	22.22	7.79
	31.2	1.35	18.8	16	7.59	21.63	7.76
4.27	32.8	1.31	20.4	18	7.58	21.62	7.88
	34.6	1.30	23.0	20	6.97	21.12	8.05
	37.0	1.21	25.0	22	7.37	21.50	8.19
	39.4	1.17	27.6	24	7.17	21.04	8.25
	40.2	1.13	28.4	26	7.55	22.09	8.49
	41.8	1.11	30.2	28	7.35	21.65	8.50
	43.8	1.07	32.8	30	7.21	21.91	8.70
	47.0	1.00	35.4	32	7.61	21.83	8.71
	26.0	1.78	12.8	10	6.89	17.65	6.95
	28.4	1.63	14.8	12	7.43	18.83	7.39
5.15	30.0	1.52	17.6	14	7.61	21.64	8.40
	30.2	1.53	18.6	16	7.35	22.42	8.76
	31.8	1.45	20.4	18	7.54	23.37	9.13
	34.6	1.36	23.2	20	7.60	23.38	9.34
	37.2	1.25	25.0	22	8.39	24.13	9.50
	40.2	1.19	26.6	24	8.70	22.49	9.10
	30.8	1.59	14.8	10	9.21	19.30	8.05
	32.6	1.58	15.6	12	8.89	17.51	7.65
	33.4	1.55	16.8	14	8.89	18.24	8.00
	34.8	1.50	18.8	16	8.89	19.32	8.54
6.46	37.0	1.43	21.0	18	8.89	19.52	8.79
	37.6	1.38	22.6	20	9.21	21.70	9.54
	38.4	1.34	24.4	22	9.18	23.16	10.14
	42.2	1.26	27.4	24	9.39	22.37	10.07
	43.0	1.24	29.0	26	9.16	22.92	10.39
	44.6	1.20	30.6	28	9.33	23.25	10.55
	47.2	1.14	33.8	30	9.39	24.04	10.96
\bar{x}					8.06	21.50	8.58
$\frac{\sigma_x}{\bar{x}} \cdot 100\%$					10.66	8.55	12.53

value of the percentage error of each IS–O obtained inertia parameter α_r , with respect to the parameter obtained from the SR method with a nonlinear model. The error can

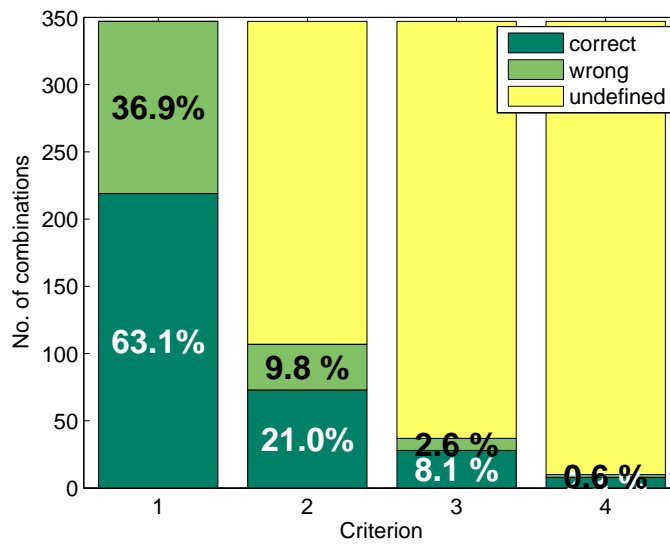


Figure 7.11. Number of cases when the conclusion was correct, false or undefined for AutoMarine AUV.

get around 30%. The same type of errors only for the obtained drag β_{rr} are shown in Fig. 7.13, from where it is obvious that the errors can get as high as to almost 25%.

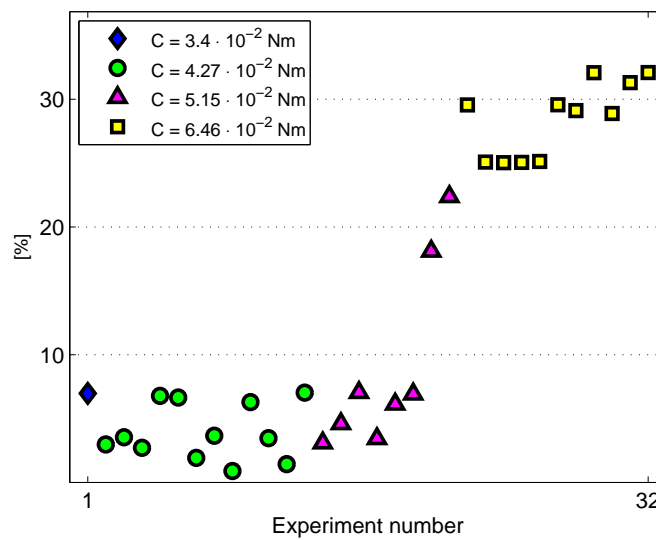


Figure 7.12. Relative errors of IS-O obtained inertia α_r with respect to the inertia obtained by the Step Response method.

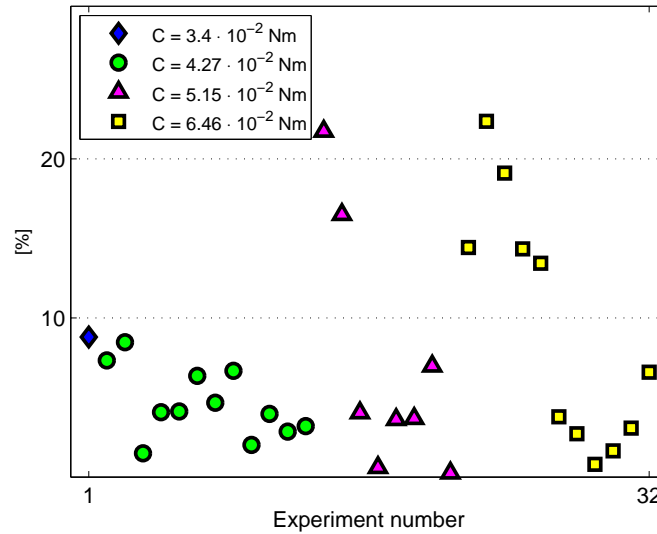


Figure 7.13. Relative errors of IS–O obtained drag β_{rr} with respect to the drag obtained by the Step Response method.

Comparison of steady states

Again, these results may be misleading since the model obtained by using the SR method is taken as the perfect model. Using the methodology described in Chapter 7.2, the differences in achieved steady states of each IS–O model is compared to the SR obtained model and Δr_{SS} is calculated by using (7.7). Since Δr_{SS} is a function of τ , the worst case scenario is when $\tau = C$ is the biggest. For this reason, the maximal C that was used in all experiments is taken into calculation ($C = 6.46 \text{ Nm} \cdot 10^{-2}$).

The results are shown in Fig. 7.14. From this point of view, it is seen that the system parameters have been identified well, since Δr_{SS} for each IS–O experiment is less than $8^\circ/\text{s}$.

Comparison of equivalent time constants

The error which is included in the identified α_r should be observed from the point of view of equivalent time constant T_N as it was elaborated in Chapter 7.2. T_N is calculated for each of the identified IS–O models and compared to the SR obtained model. ΔT_N is calculated using (7.11). Since ΔT_N is a function of τ , the worst case scenario is when $\tau = C$ is the smallest. For this reason, the minimal C that was used in all experiments is taken into calculation ($C = 3.4 \text{ Nm} \cdot 10^{-2}$).

The results are shown in Fig. 7.7. From this point of view, it is much easier to comprehend what the difference between IS–O and SR obtained models really is. It is obvious that only for the last set of experiments this difference gets higher than 0.2 s, but never above 0.35 s.

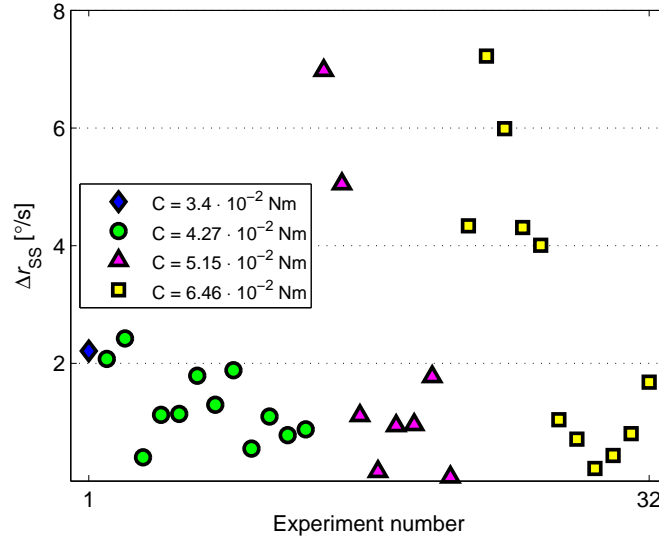


Figure 7.14. Relative errors of IS-O obtained drag β_{rr} with respect to the Step Response obtained one observed from the steady state quantization point of view.

Sum of absolute errors

Since the main assumption was that the SR obtained model is the perfect one, the best way of validating the IS-O obtained models is to calculate the sum of absolute errors validation data sets. All together, 35 different validation data sets were taken. One set is shown in Fig. 7.16 where blue line in the upper plot shows the experimentally obtained data, red line the simulated output of the nonlinear model, and green line simulated output if the linear model. This example once again shows how nonlinear model fits the data better. The lower plot gives the input yaw moment during the validation experiment.

In order to have better visual representation of the systems output, the experimentally obtained yaw rate was filtered by using the Golay filter. As a consequence of this, the original validation input was fed through the same filter producing filtered input which is than used for validating the models. This way the filtering of the real output was compensated for.

Based on these validation sets, the average sum of absolute errors \bar{J}_{SR} was calculated for the SR model. For each of the 32 obtained IS-O models, the average sum of absolute errors was also calculated resulting in $\bar{J}_{IS-O,i}$, where i is the model number. Fig. 7.17 shows the relative difference

$$\frac{\bar{J}_{IS-O,i} - \bar{J}_{SR}}{\bar{J}_{SR}} \quad (7.14)$$

for all experiments. It can be seen that the models obtained using the IS-O method give smaller sum of absolute errors in most cases. These results are again the best demonstration of how IS-O method is preferable to SR method.

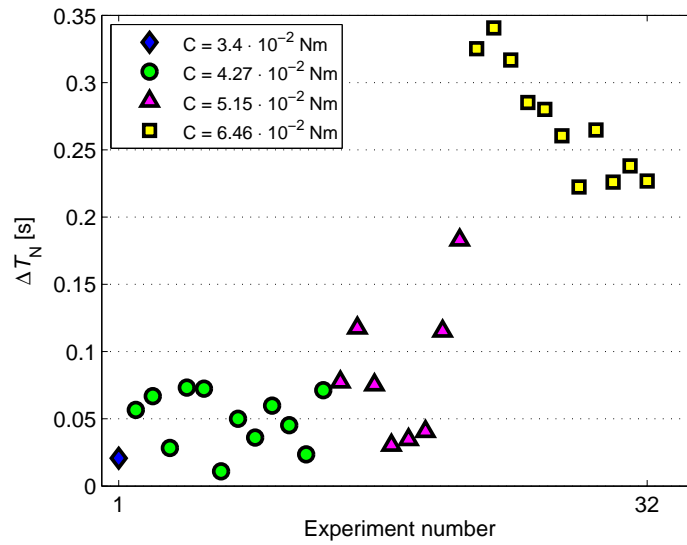


Figure 7.15. Relative errors of IS-O obtained inertia α_r with respect to the Step Response obtained one observed from the rise time T_N point of view.

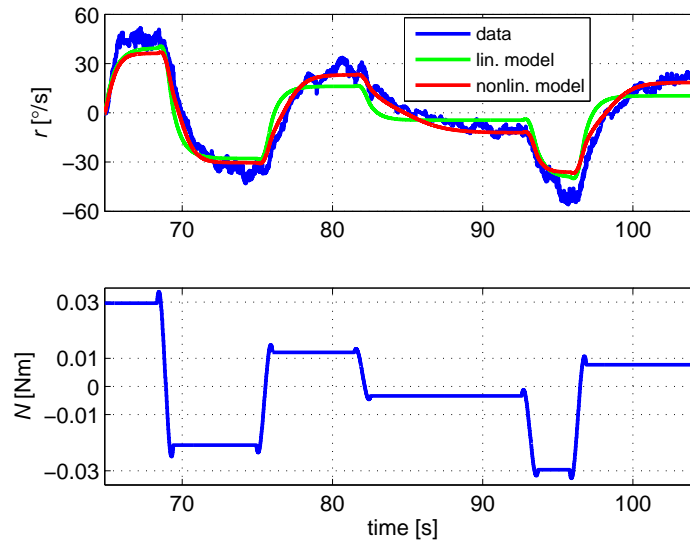


Figure 7.16. Relative errors of IS-O obtained inertia α_r with respect to the SR obtained one observed from the rise time T_N point of view.

7.5 Identifying Yaw DOF – Charlie USV

The experiments on the Charlie USV were carried out in Genoa Pra Harbour in Genoa, Italy during two day extensive trials. During Day 1 (25th September 2009) and Day 2 (29th September 2009) the same experimental procedures were performed. The forward speed was changed consecutively through the values of $n_i^2 = \{16, 25, 36, 49, 64\} [V^2]$. For

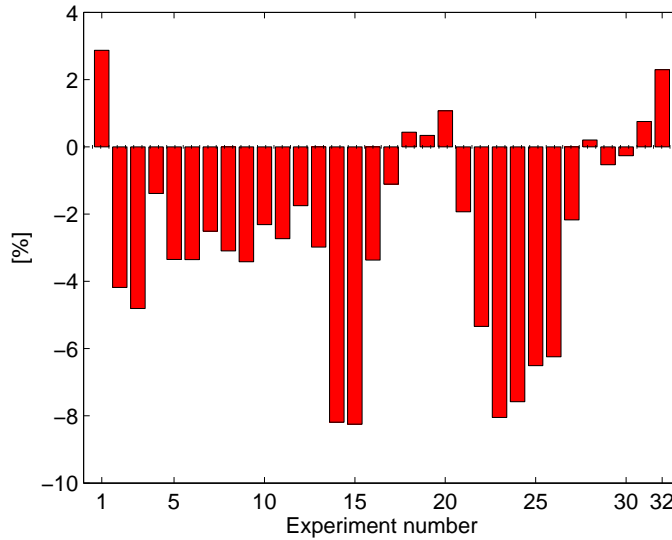


Figure 7.17. Comparison of sum of absolute errors obtained using IS–O obtained models with the SR model.

each speed the self-oscillating experiment was changed with the relay output parameter taking the values $C_i = \{10, 15, 20, 25\}$ [deg]. For each pair (n_i^2, C_i) the hysteresis width was changed between the values $x_{a,i} = \{5, 10, 15\}$ [deg]. In other words, each of two days (Day 1 and Day 2) had 5 *speed sets*, each of which had 4 different *relay output sets*, each of which had 3 different *relay switching sets*. This means that during one day, 60 different experiments were taken, resulting in all together 120 experiments.

The experiments were taken during two days so that the results could be compared under different environmental conditions. Charlie is equipped with an anemometer which gives wind speed and wind direction relative to the vehicle. The wind speed conditions during days 1 and 2 are shown in Fig. 7.18(a) and Fig. 7.18(b), respectively. Green circles denote average wind speeds during the whole day of experiments, at different angles relative to the vehicle. Blue dashed lines show the measurement standard deviation which shows how much the conditions changed during the day.

From Fig. 7.18(a) it is obvious that during Day 1 the wind was significantly stronger than during Day 2 (see Fig. 7.18(b)).

7.5.1 Least-Squares Results

The least-squares method was applied on the data obtained from the self-oscillation experiments. For each data set a least-squares identification was performed. The assumed dynamic model of the yaw degree of freedom is given with (3.5) where drag β_r can be expressed as constant or linear as in (2.34). From here follow the linear and nonlinear regression models used for performing least-squares identification. Least-squares identification is described in detail in Chapter 4.2, so it will be omitted here.

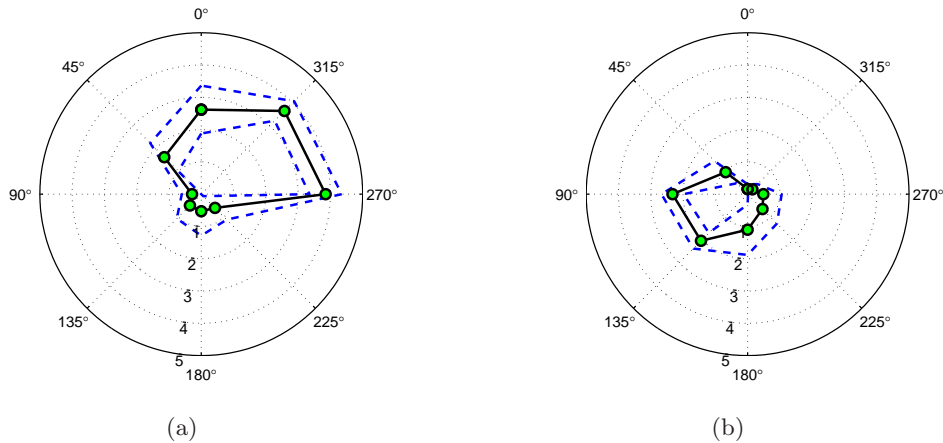


Figure 7.18. Average wind speed and direction during (a) Day 1 and (b) Day 2 measured in the Earth-fixed coordinate frame show significantly different environmental conditions during the two days.

In addition to that, linear and nonlinear regression models are given with (4.20) and (4.22), respectively ($\nu = r$ in this case).

Using the same regression models and the parameters estimated with the least-squared algorithm, evaluation of results was performed. Table 7.12 shows estimated drag coefficients for different surge speeds. For the sake of clarity, only drag coefficients are shown. These results can be used to determine whether a linear or nonlinear model described the vehicle behavior better. From the results shown in Table 7.12 it can be concluded that for speeds higher than $n^2 = 16V^2$, almost the same model parameters can be applied. It is also obvious that the results obtained from the two different days give practically the same identified parameters what leads to the conclusion that the identification method is consistent. In addition to that, the evaluation parameters e_{lin} and e_{nonlin} for the linear and nonlinear model, respectively, show that linear model describes the vehicle behavior in yaw degree of freedom better than the nonlinear model.

7.5.2 IS–O Results

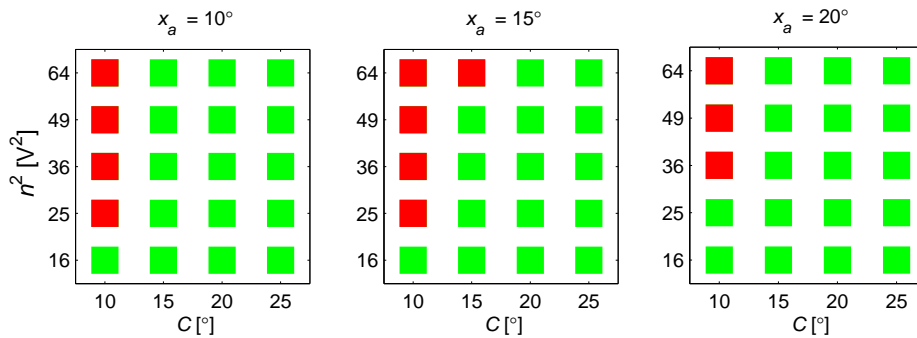
The self-oscillation experiments were taken in such a way that 5 consecutive oscillations have to be obtained to compute the unknown parameters. In order to have a successful self-oscillation experiment, condition (7.12) has to be fulfilled, just as described before. If any of the 5 consecutive oscillations does not fulfill condition (7.12), the experiment was discarded from the analysis.

During Day 1, all the obtained oscillations were self-oscillations (condition (7.12) is fulfilled) which lead to 60 valid self-oscillation experiments. During Day 2, not all oscillations were self-oscillations. Fig. 7.19 gives a schematic representation of the experiments which were not successful. Red squares present the experiments which

Table 7.12. Experimental results obtained from the Charlie USV yaw DOF using the L-S method.

	n^2 [V ²]	$\alpha_r(\text{lin})$ [$\frac{\text{Nms}^2}{\text{rad}}$]	β_r [$\frac{\text{Nms}^2}{\text{rad}}$]	e_{lin} [$\frac{\text{rad}}{\text{s}} \cdot 10^{-3}$]	$\alpha_r(\text{nelin})$ [$\frac{\text{Nms}^2}{\text{rad}}$]	β_{rr} [$\frac{\text{Nms}}{\text{rad}}$]	e_{nelin} [$\frac{\text{rad}}{\text{s}} \cdot 10^{-3}$]
Day 1	16	11.09	-3.42	16.02	11.95	-35.58	19.02
	25	8.55	-2.56	16.54	8.95	-22.14	23.88
	36	7.51	-2.39	17.30	7.79	-20.08	22.92
	49	7.89	-2.67	17.10	8.35	-24.41	22.78
	64	7.92	-2.66	17.48	8.44	-22.89	24.63
Day 2	16	10.50	-3.24	11.40	11.01	-34.28	14.71
	25	8.96	-2.71	13.96	9.32	-23.47	20.63
	36	8.89	-2.54	21.36	9.03	-21.01	29.81
	49	10.42	-2.82	23.15	10.84	-24.53	34.33
	64	9.47	-2.98	19.14	9.90	-24.10	29.46

were not successful, while green ones are the successful ones. It can be clearly seen that the majority of unsuccessful experiments were obtained while hysteresis output was $C = 10^\circ$. This is quite normal since greater output is needed to induce the self-oscillations. This leads to the conclusion that higher relay output should be applied in order to conduct a successful experiment.

**Figure 7.19.** Graphical representation of successful and unsuccessful IS-O experiments in relation to parameters of the relay with hysteresis.

After the unsuccessful experiments were discarded, 48 experiments from Day 2 were taken into consideration. All together, this resulted in 108 self-oscillation experiments.

An example of a successful self-oscillation experiment obtained on Charlie USV is shown in Fig. 7.20, where green circle marks the beginning and red square the end of the self-oscillation experiment (it has finished after 5 oscillations were recorded). During the experiment, the vessel was performing a path shown in Fig. 7.21 where green circle marks the beginning, red square the end of data recording and dotted line

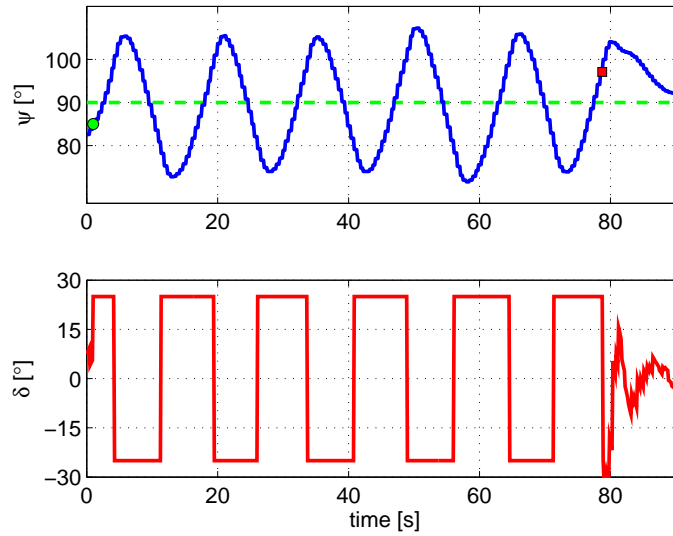


Figure 7.20. Charlie's heading and rudder angle during one of the self-oscillation experiments.

is the path before and after the experiment.

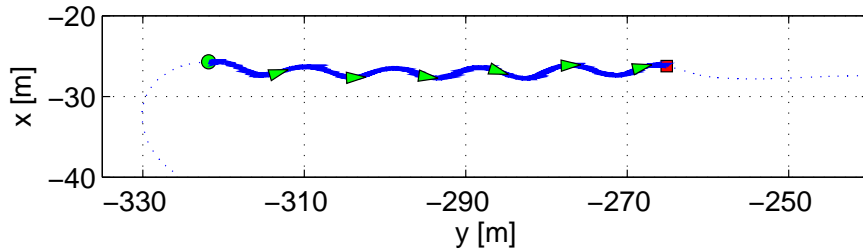


Figure 7.21. Charlie's path during one of the IS-O experiments.

The drag coefficient β_r obtained from the self-oscillation was compared to the drag coefficient obtained using the least-squares algorithm (see Table 7.12), and relative error was calculated using (7.15) where $k_{r,IS-O}$ is drag obtained from the self-oscillation experiment and $k_{r,LS}$ drag obtained from the least squares experiment.

$$\Delta k_r [\%] = \left| \frac{k_{r,IS-O} - k_{r,LS}}{k_{r,LS}} \right| \quad (7.15)$$

Tables with experimental results are omitted due to great number of experiments.

Deciding on the model

Based on the experiments which were performed, the conclusion is made that the model with constant drag (linear model) describes system dynamics better than the one with linear drag (nonlinear model). However, the point is not to have to perform numerous IS–O experiments to determine the suitable model, but only two as it is suggested in Chapter 7.1.

Among the experiments taken during one day, pairs were taken in such a way that each member of the pair must have different relay outputs N . This is not an uncommon demand, since the two experiments that are performed to decide on the model should be as different as possible. This condition leads to more than 1300 different combinations of pairs for Day 1, and more than 800 different combinations of pairs for Day 2. All four criteria listed in Section 7.1 have been tested and the results are shown in Fig. 7.22 and Fig. 7.23 for experiments taken during Day 1 and Day 2, respectively. Dark green colour represents the number of pairs when the conclusion was correctly made, light green the number of pairs when the conclusion was falsely made and in yellow the number of pairs where the conclusion could not be made.

From Fig. 7.22 and Fig. 7.23 it can be concluded that the criterion 1 always caused the decision to be made, and in about 90% of chosen pairs the conclusion on the most appropriate model was made correctly, during both days. When using criterion 2, the margin of no decision is introduced and for a number of experiments the decision could not be made. If a pair for which the conclusion cannot be made is chosen, additional experiments should be performed to make conclusion about the model. By increasing the margin of decision (criteria 3 and 4) the number of cases without decision increases, but the number of pairs with falsely made decision is extremely low, proving the robustness of the decision making algorithm. In addition to that, the decisions are made somewhat easier during Day 2, when the influence of external disturbances was smaller.

7.5.3 Model Validation and Comparison of IS–O and L–S Identification Methods

Since the model which described yaw degree of freedom is linear, the proposed comparison of steady state and comparison of equivalent time constants will give the same results as validation based on error in β_r and α_r . Having this in mind, the validation of the obtained models is performed by observing error in determined β_r and by comparing equivalent linear time constants.

In this section, the parameters obtained by use of the least–squares method will be taken as correct ones. However, they will be used as a means of comparison to the model obtained by using the IS–O method, as it was described in Section 7.2. Fig. 7.24 and Fig. 7.28 show the absolute value of the percentage error of each IS–O obtained inertia parameter β_r with respect to the parameter obtained from the least–squares

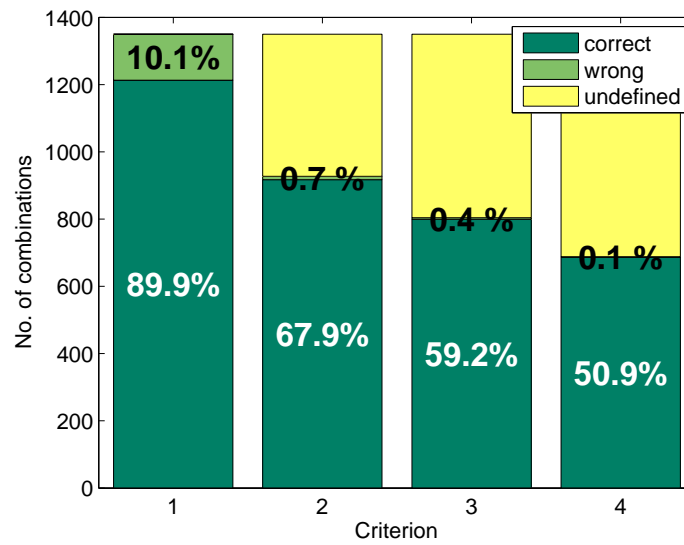


Figure 7.22. Number of cases when the conclusion was correct, false or undefined for Charlie USV during Day 1.

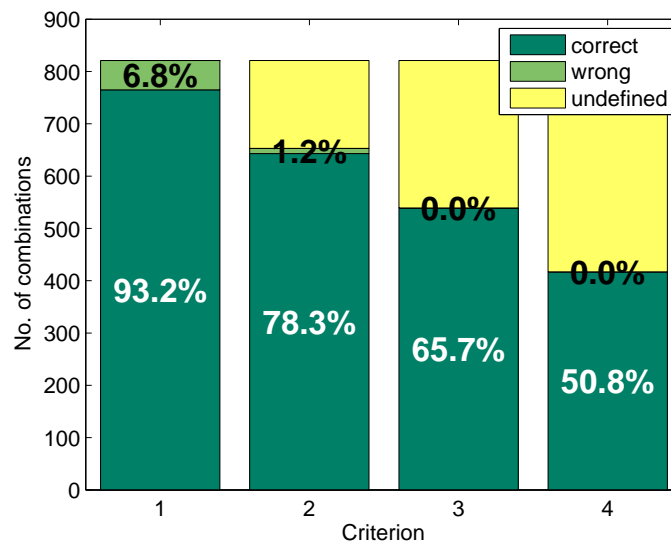


Figure 7.23. Number of cases when the conclusion was correct, false or undefined for Charlie USV during Day 2.

method with a linear model. The errors get as high as 22% during Day 1, while during Day 2 they are below 15%.

As it is shown in Fig. 7.26, a great majority (more than 90%) of experiments show the relative drag error smaller than 15%. During Day 2, when weather conditions were better, all experiments resulted in the identified drag relative error smaller than 15%.

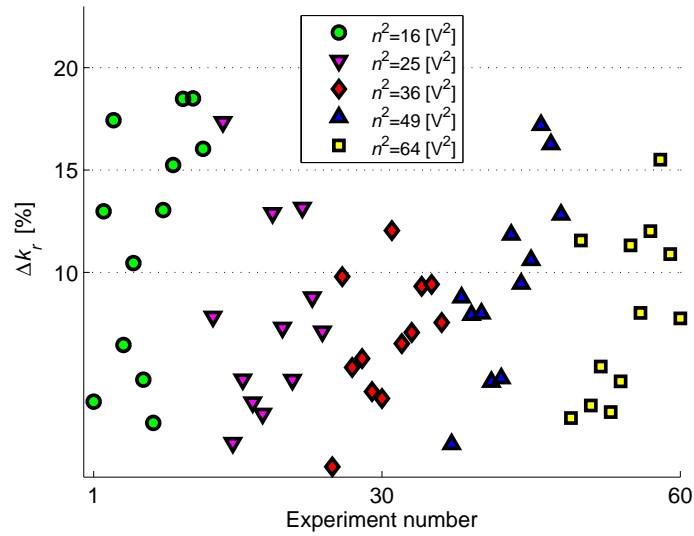


Figure 7.24. Relative drag error from experiments obtained during Day 1.

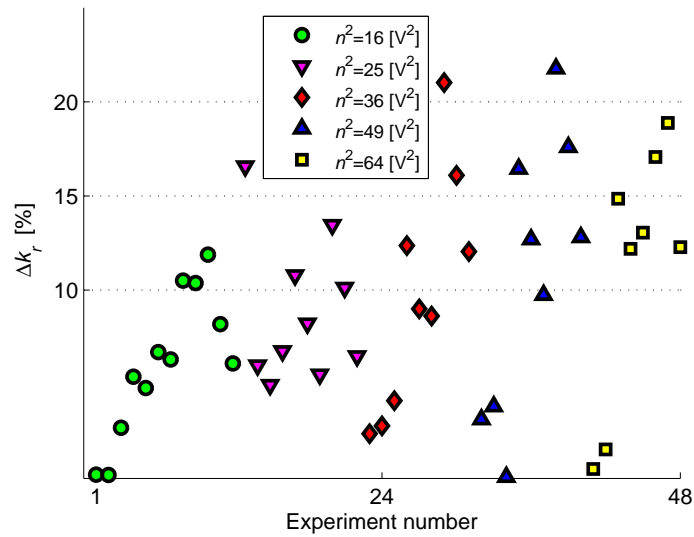


Figure 7.25. Relative drag error from experiments obtained during Day 2.

During Day 1, only 5 experiments resulted in relative error greater than 15% while the maximum error was about 22%.

The error which is included in the identified α_r should be observed from the point of view of equivalent linear time constant T_L as it was elaborated in Section 7.2. T_L is calculated for each of the identified IS–O models and compared to the L–S obtained model. ΔT_L is calculated using 7.11. In the case of linear model, ΔT_L is not a function of τ , i.e. the system will take T_L to achieve 63% of the steady state value, regardless of

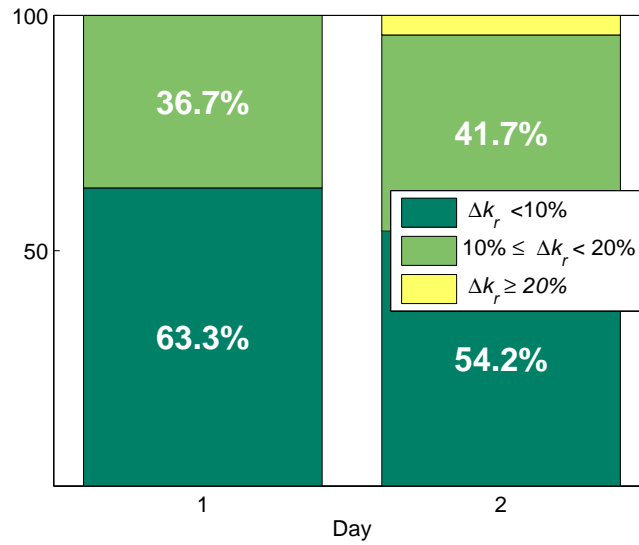


Figure 7.26. Percentual representation of IS-O method accuracy while identifying $k_r = \beta_r$.

the input signal. This, of course, is under the assumption that the system is completely linear.

The results are shown in Fig. 7.27 and Fig. 7.28 as numbers of time samples contained in each ΔT_L , for Day 1 and Day 2, respectively. From this point of view, it is much easier to comprehend what the difference between IS-O and L-S obtained models really is.

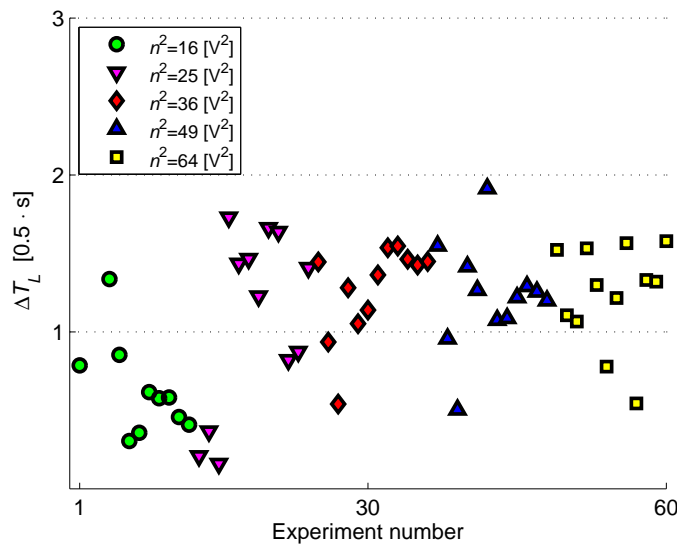


Figure 7.27. Relative errors of IS-O obtained inertia α_r with respect to the L-S obtained one observed from the rise time T_L point of view – Day 1.

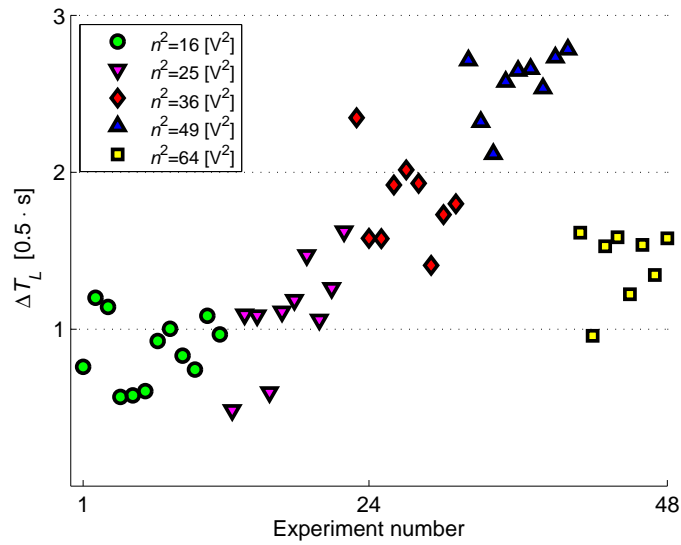


Figure 7.28. Relative errors of IS-O obtained inertia α_r with respect to the L-S obtained one observed from the rise time T_L point of view – Day 2.

The percentual analysis of these results is shown in Fig. 7.29 from where it is seen that always in more than 90% of cases the results fall within $2T_S$ difference. During Day 1, only one experiment resulted in the difference being above $2T_S$ but it was always under $3T_S$. During Day 2, the results were always under $3T_S$.

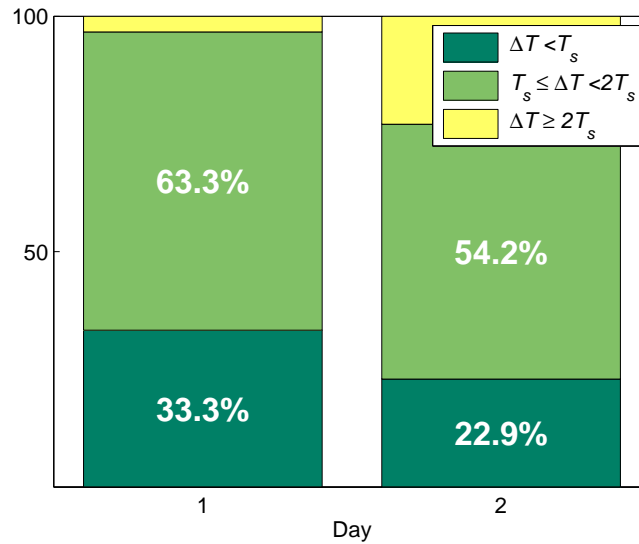


Figure 7.29. Percentual representation of IS-O method accuracy while determining equivalent time constant difference ΔT_L .

These results show that the identification by use of self-oscillations is a method

which gives confident results. Identified drag and inertia in all experiments fall within the boundaries of acceptable results. In addition to that, the results obtained under considerable wind are also confident which leads to the conclusion that this method is robust to external disturbances.

Sum of absolute errors

Finally, the rudimentary sum of absolute errors is performed for each obtained model. Each identification data set was used also as a validation set. The model obtained using the least-squares method has been validated on all data sets obtained with a specific forward speed. The calculated average sum of absolute errors \bar{J}_{LS} is taken as reference. Each IS-O model was also validated on these data sets, and for each model i an average sum of square errors $\bar{J}_{IS-O,i}$ was calculated.

Fig. 7.30 shows the relative difference

$$\frac{\bar{J}_{IS-O,i} - \bar{J}_{LS}}{\bar{J}_{LS}} \quad (7.16)$$

for experiments during Day 1, for different commanded forward speeds. The same results are shown for Day 2 in Fig. 7.31.

The results which were obtained using the IS-O method are somewhat worse than the ones obtained by L-S method, but still satisfactory. Given the time it takes to perform IS-O experiments, these results can be used in practice.

7.6 Identifying Surge DOF – VideoRay ROV

Surge degree of freedom has been identified for the purpose of designing the distance keeping controller. Distance keeping modeling has been described in detail in Chapter 2.6. For this application, VideoRay ROV was equipped with a vision-based laser system which is described in Chapter 3.4.

Due to the limited distance at which the vision-based laser system can operate, a great number of experiments could not have been performed. In addition to that, the sample rate of the vision-based laser system is 1s, therefore careful tuning of relay parameters had to be performed in order to obtain oscillations which can be used for identification purposes.

In order to identify surge degree of freedom using the available apparatus, angle with regard to the flat surface had to be kept at a small value. This way, the distance from the surface is in fact integral of the surge speed, as it can be seen from (2.43). This is why, firstly, the angle controller is set, and then surge degree of freedom can be identified.

The experimental results are shown in Fig. 7.32 with relay switching set to $x_a = 10\text{cm}$. The a posteriori analysis showed the modified relay switching is $x_a^* = 12.33\text{cm}$.

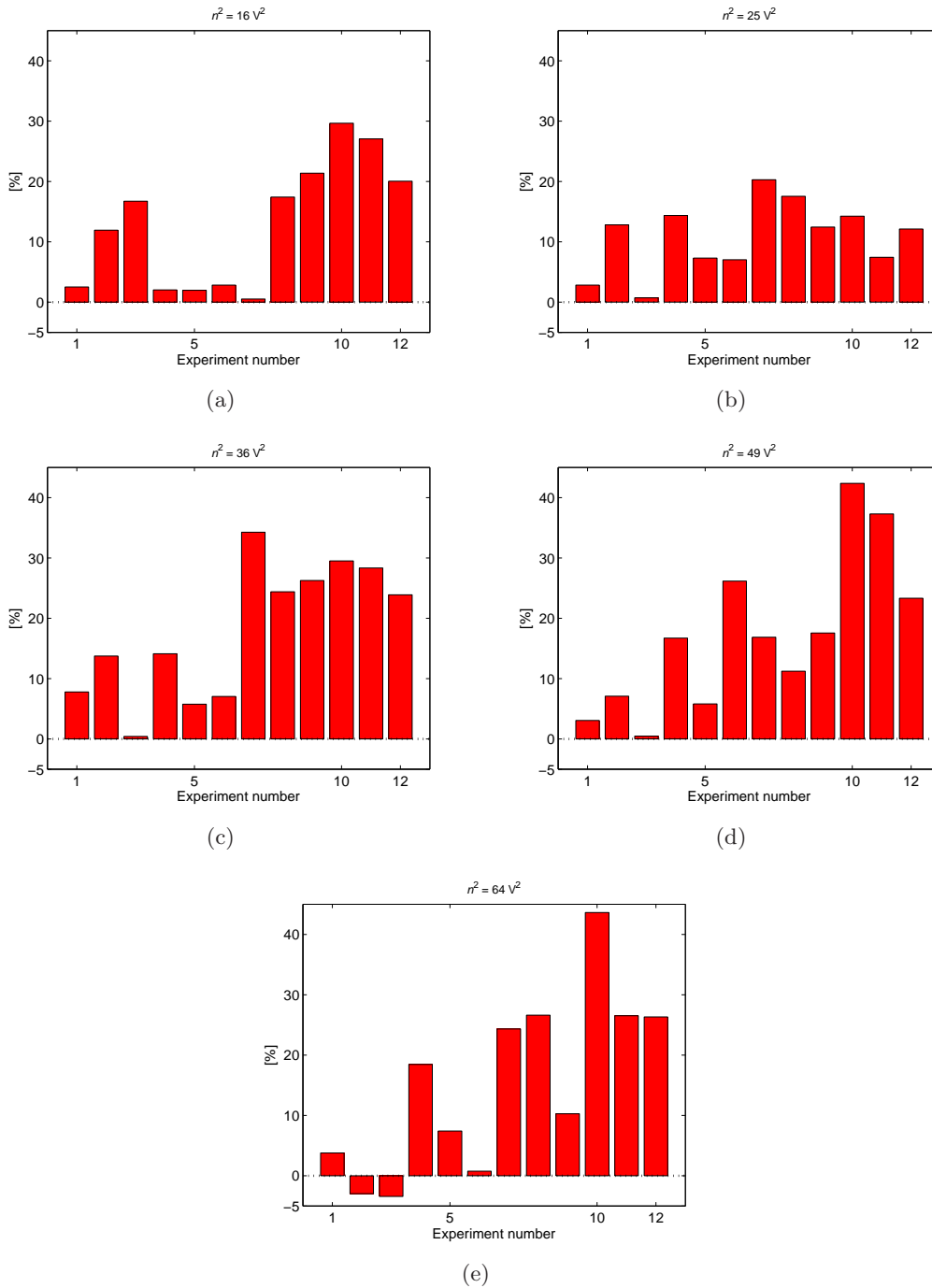


Figure 7.30. Comparison of sum of absolute errors obtained using IS-O obtained models with the L-S model – Day 1.

In this case, relay output is somewhat asymmetric which is a result of influence of the tether that presents significant disturbance. The self-oscillation parameters obtained

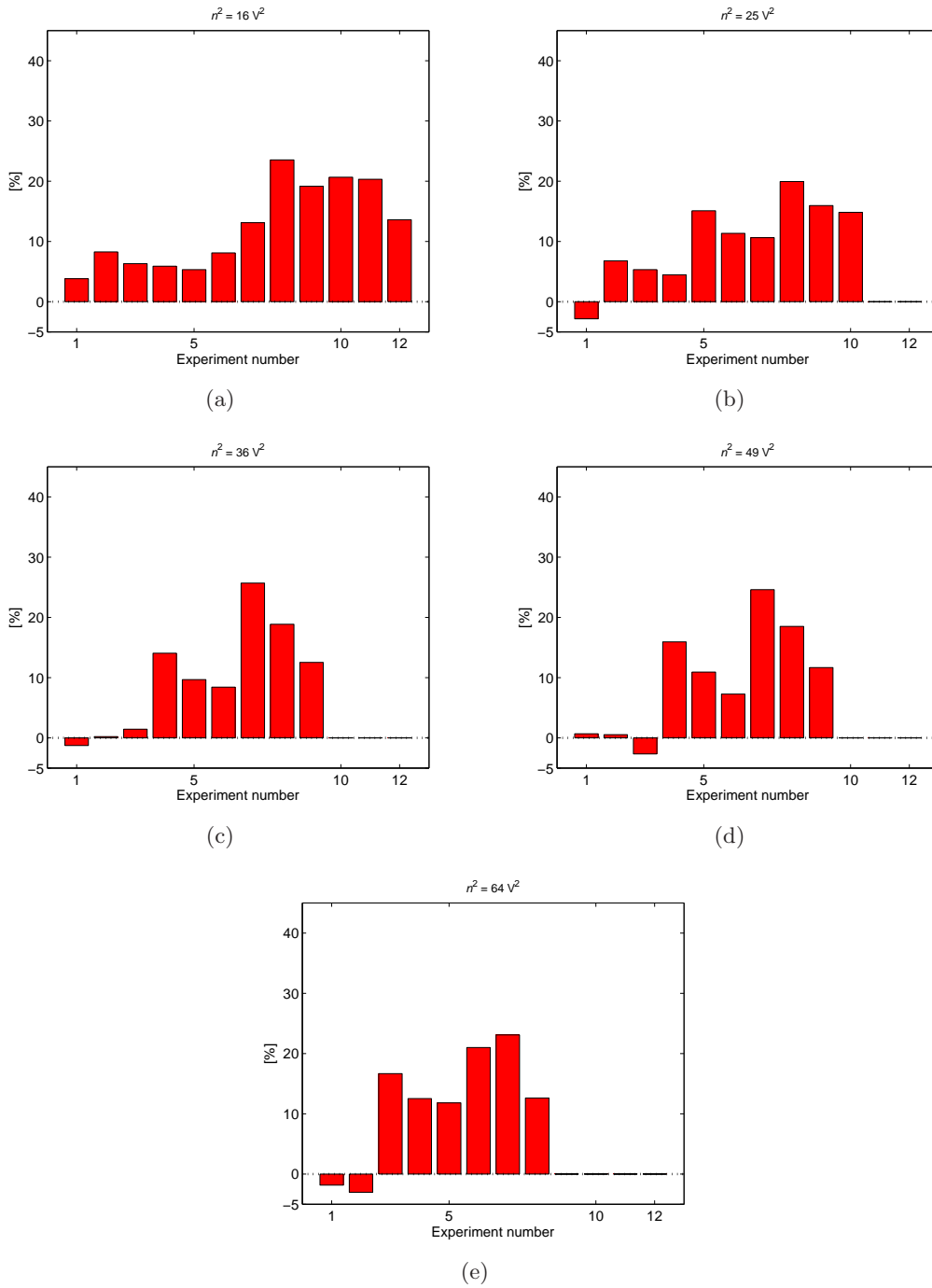


Figure 7.31. Comparison of sum of absolute errors obtained using IS-O obtained models with the L-S model – Day 2.

from the experiment are $X_m = 16.22\text{cm}$ and $\omega = 0.393\text{s}^{-1}$. While calculating the identified parameters, it was assumed that surge drag is linear, i.e. the surge model is

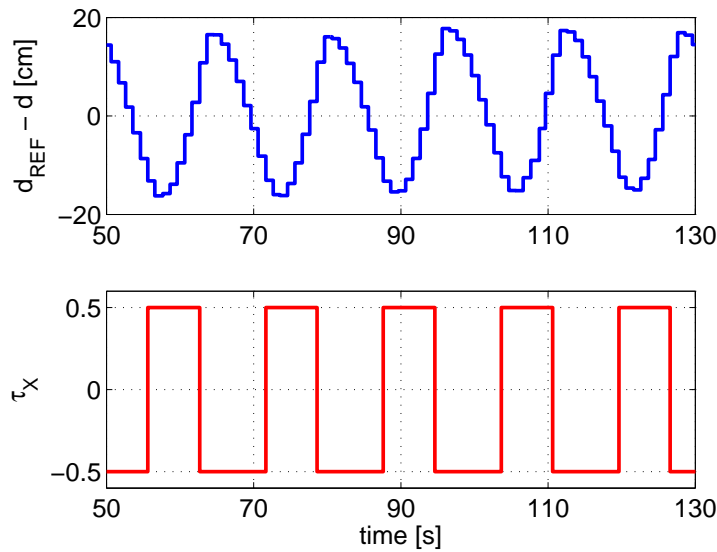


Figure 7.32. The self-oscillation experiment for identifying surge degree of freedom.

dominantly nonlinear.

7.7 Identifying Heading Closed Loop – Charlie ASV

The experiments for identification of heading closed loop transfer function were performed on a Charlie ASV. Two cases with different heading controllers, i.e. different closed loop structures were taken into account:

- Case 1 includes a P–D heading controller and
- Case 2 an I–PD heading controller.

These experiments were performed to test if the the proposed methodology works for various inner control loop structures. The relay parameters for both cases are listed in Table 7.13. Each case included two S–O experiments, since both are needed to determine the heading closed loop transfer function parameters (see Chapter 6.6.4). As it is shown in Fig. 6.9, relay output is commanded heading ψ_{ref} .

Table 7.13. Relay parameters for Cases 1 & 2.

CASE	IS–O EXPERIMENT #1	IS–O EXPERIMENT #2
1	$C = 20^\circ, x_a = 5^\circ$	$C = 15^\circ, x_a = 5^\circ$
2	$C = 10^\circ, x_a = 5^\circ$	$C = 30^\circ, x_a = 10^\circ$

Experiments for Case 1 are shown in Fig. 7.7 and for Case 2 in Fig. 7.7. In both cases, duration of the experiment is short and last 5 oscillations per experiment. The procedure for obtaining this data is the same as in the case of IS-O applied to yaw degree of freedom.

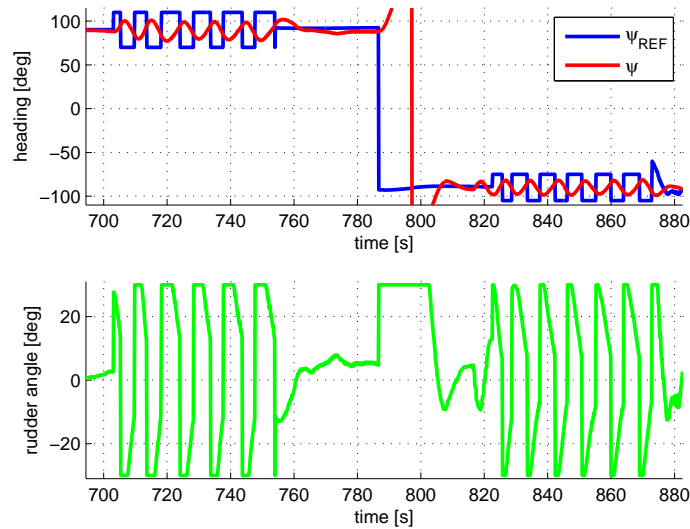


Figure 7.33. IS-O results for Case 1.

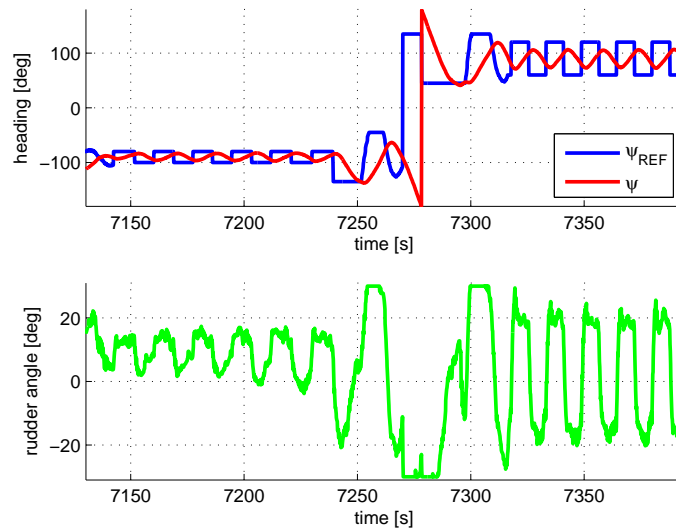


Figure 7.34. IS-O results for Case 2.

While performing the experiments, relay output can be chosen in such a way that the rudder of the vessel saturates. This is the case if relay output has high values.

Since the model which is to be identified is linear, these saturations should be avoided, i.e. during the experiment the vehicle should operate in the linear domain. Since it is not known a priori what the inner closed loop structure is, relay parameters have to be tuned during the experiment so that the saturation does not occur.

These self-oscillation data can be used to determine the heading closed loop transfer function parameters and tune high level controllers. These results are given in Chapter 8.3.2.

7.8 Conclusion

This chapter primarily deals with experimental results which prove the applicability of the IS-O method on real vessels. First, a method is described which can be used to determine which model better describes vessel dynamics. It's a simple approach that relies on performing an additional IS-O experiment. Based on the two sets of identified parameters, criteria are given which are later on used to determine validity of models. The proposed method has proven to give good results.

Once the parameters have been identified, the models should be validated and compared to some conventional identification methods. The validation which was engaged in this thesis is the classical sum of absolute errors and two methods based on steady state values and equivalent time constants. By comparing steady state values of the model obtained using a conventional method and the one using the IS-O method, a conclusion was made on the quality of identified drag parameter. This approach has proven to be suitable when significant quantization levels appear in the system. The second approach engages comparison of equivalent time constants of the two models, based on which a conclusion can be made on the quality of the identified inertia. For liner systems, the equivalent time constant is the time it takes the step response to reach 63% of steady state value. For nonlinear cases, it was shown that this constant should be time for step response to reach 73% of steady state value.

The experimental results were performed on three vehicles and comparisons between IS-O method and some conventional method: for VideoRay ROV it was IS-O vs. L-S, for AutoMarine AUV it was IS-O vs. open loop step response, and for Charlie ASC it was also IS-O vs. L-S.

L-S experiments on VideoRay first showed that nonlinear model describes the system better. This was also proved by using IS-O experiments and the procedure described in the chapter. These experiments also prove that IS-O gives even better results than the L-S method, especially when it comes to identification of yaw inertia. The sum of absolute errors validation tests show that IS-O obtained results are sometimes even better than the L-S obtained ones. An important conclusion, and an advantage of the IS-O method is that it does not require signal differentiation, compared with the case of L-S method. The parameters identified by the IS-O method have proven to be consistent.

The open loop step response method was applied on AutoMarine AUV and it showed that nonlinear model better describes the dynamics also. The validation results show that SR method gives good results and that it is applicable in laboratory conditions. In addition to that, results show that IS-O method gives satisfactory results. It is much simpler and faster than the SR method.

The methods which were applied to Charlie USV were L-S and IS-O identification. The results show that for forward speeds greater than $n^2 = 16V^2$ the model parameters practically do not depend on the forward speed. Experiments were performed during two days in order to show the robustness of the IS-O procedure with different environmental disturbances. Extensive experiment have demonstrated that IS-O method gives good results. This was shown with a thorough validation of the results.

Finally, the procedure for identifying heading closed loop was applied to Charlie ASC with two different inner loop structures. The experiments give satisfactory results what will best be seen when results if line following will be presented. An important thing in application is to make sure that the actuators do not saturate during the experiments since the main assumption which is made is that the inner closed loop is linear. The low level controller should make sure that this is true.

Control and Guidance of Marine Vehicles Using IS–O Experiments

The control architecture for marine vessels can roughly be divided into three levels of control as it is shown in Fig. 8.1. The highest control level is called *Planning* and it

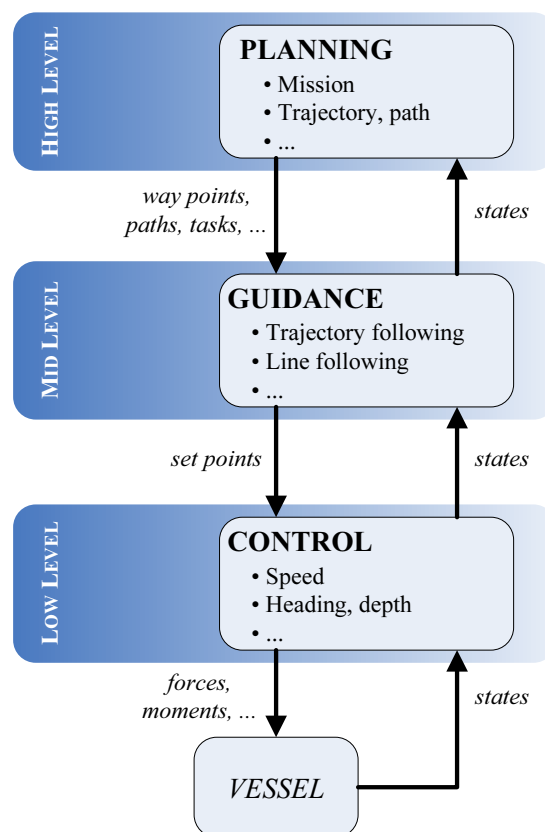


Figure 8.1. Marine vehicle control architecture.

includes mission planning, [5], path and trajectory planning, [3, 6, 35, 68], and way–

point generating. In a completely automated system, this level takes into account all the situational changes and makes sure that the planned path does not collide with other vessels' paths or with unmoving objects, [29]. On-line replanning is of high importance especially in the case of control of multiple vessels or moving obstacles, [7]. The inputs to this level of control are state variables based on which the conclusion is made on the state of the current mission. Using this information, high level will output planned paths, trajectories, way-points to the mid control level. If high control level does not exist, the control is not fully automated and the operator is in charge of mission planning.

The medium control level, also called *Guidance*, takes the planned paths, trajectories or way points from the high level (or the operator), [9, 12, 21, 37, 61, 66], and generates reference values for the low control level. The task of this control level is to ensure that individual path, trajectory or task, in general, commanded from the higher level is executed with a predefined accuracy. This level also includes performing tasks such as vessel parking within a certain area (dynamic positioning), keeping a predefined distance to an object, etc.

The low-level control is a rudimentary control level, called simply *Control*. It is in charge of compensating external disturbances and keeping elementary variables such as speeds or positions at a predefined, set value commanded by the mid control level. In surface marine vehicles, this level usually includes heading control (autopilots), forward speed control and roll control, [26, 27]. In underwater marine vehicles, this level is in charge of controlling all controllable speeds (usually yaw rate, surge and heave speeds), heading, depth, pitch, etc. Output of this level is directly connected to the vessels actuators, setting the desired forces and moments upon the vessel. Low level inputs are measured and/or estimated vessel states.

A simplified control hierarchy in this section was described starting from the high level and descending to the low control level. However, while designing individual control levels, low level is the first step. After that, higher control levels can be designed. In order to design low control level, mathematical model and parameters of the controlled vehicle have to be known, i.e. systems identification has to be performed.

This chapter will describe methods for designing low-level controllers, distance keeping controllers and line following controllers based on IS–O experiments, which have been published in [57, 59, 60]. After the theoretical background, experimental results are given.

8.1 Low-Level Control Design

In Chapter 2 a detailed description of mathematical models for marine vehicles is presented. It is stated that these models can be simplified for the purpose of controller design. The main nonlinearities which appear in these models are nonlinearities introduced by actuators (see Chapter 2.1) and by the nonlinear model of the vessel.

The basic low-level control structure is shown in Fig. 8.2. The mathematic model of a vessel is shown as the blue subsystem and it consists of all the elements described thoroughly in Chapter 2. Before control algorithms are developed, it is crucial to compensate for as many static nonlinearities in the system as possible. This is done in the *Control accommodation* block. The *Actuator nonlinearity compensation* block is in charge of compensating for the nonlinear characteristic of the actuators (an example of this is given in Chapter 4.1) which in the case of thrusters can be described with 2.4. This block in fact contains the inverse function of this nonlinearity, if it is static.

The *Control allocation* block is in fact the inverse function of the actuator allocation matrix described in Chapter 2.2. It ensures that commanded forces and moments vector τ , which acts on the rigid body, are mapped properly on each of the available thrusters on the vessel, forming the vector τ^i . If the actuator allocation matrix Φ is square, than this block implements its inverse Φ^{-1} . If it is not square, i.e. there is redundancy in the number of actuators, there are multiple solutions of how commanded forces and moments can be distributed to the thrusters. The simplest way is to perform a pseudoinversion $(\Phi^T \Phi)^{-1} \Phi^T$. Other approaches for distributing these forces and thrusts can be found in [65].

Once the control accommodation has been implemented, the controllers for controlling the dynamic part of the process have to be designed. These are given with the *Control* block in Fig. 8.2. The following part of this section deal with methods for designing these controllers (autopilots).

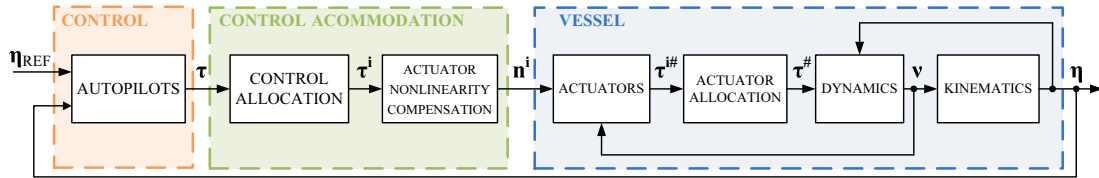


Figure 8.2. Low-level control structure.

8.1.1 Controller Structure

The controller which is developed in this section is designed based on a model function. Using the proposed controller, even a nonlinear process will give desired response. This will be achieved by compensating the nonlinearity which arises in the system itself.

Under the assumption that the process in general can be written using

$$\alpha_\nu \ddot{\eta}(t) + \beta(\nu) \dot{\eta}(t) = \tau(t) + \tau_E, \quad (8.1)$$

where

$$\beta(\nu) = \begin{cases} \beta_\nu & \text{for linear model} \\ \beta_{\nu\nu} |\nu| & \text{for nonlinear model} \end{cases},$$

the I–PD controller algorithm given with (8.2) is designed, [77].

$$\tau(t) = K_{I\eta} \int_0^t [\eta_{ref}(t) - \eta(t)] dt - K_{P\eta} \eta(t) - K_{D\eta} \dot{\eta}(t) - \tau_E \quad (8.2)$$

This controller is used since the control action never abruptly changes: step–like reference changes are driven only through the integral channel, i.e. they are not directly fed to the actuator. This is convenient in marine applications where abrupt actuator changes are not allowed. Using the proposed control algorithm given with (8.2), the closed loop equation is given with (8.3).

$$\frac{\eta}{\eta_{ref}} = \frac{1}{\frac{\alpha_\nu}{K_{I\eta}} s^3 + \frac{\beta(\nu) + K_{D\eta}}{K_{I\eta}} s^2 + \frac{K_{P\eta}}{K_{I\eta}} s + 1}. \quad (8.3)$$

The controller parameters are set so that the closed–loop transfer function is equal to the model function given with (8.4) which is stable.

$$G_m(s) = \frac{1}{a_{3\eta} s^3 + a_{2\eta} s^2 + a_{1\eta} s + 1}. \quad (8.4)$$

In that case, the controller parameters are as follows:

$$\begin{aligned} K_{I\eta} &= \frac{\alpha_\nu}{a_{3\eta}} \\ K_{P\eta} &= \frac{a_{1\eta}}{a_{3\eta}} \alpha_\nu \\ K_{D\eta} &= \frac{a_{2\eta}}{a_{3\eta}} \alpha_\nu - \beta(\nu). \end{aligned} \quad (8.5)$$

This controller can be used for controlling yaw and heave motion as well as other degrees of freedom.

Heading control

As it was mentioned before, yaw degree of freedom can be described by using (8.1) where $\eta = \psi$, $\tau = N$, $\alpha_\nu = \alpha_r$ and $\tau_E = 0$. If the model is linear, $\beta(\nu) = \beta_r$ and if it is nonlinear $\beta(\nu) = \beta_{rr}|r|$. The assumption is that only estimated model parameters are available, i.e. $\tilde{\alpha}_r$ and $\tilde{\beta}_r$ or $\tilde{\beta}_{rr}$, depending on the appropriate model. According to (8.5), parameters of the controller given with (8.2) are

$$\begin{aligned}
K_{I\psi} &= \frac{\tilde{\alpha}_r}{a_{3\psi}} \\
K_{P\psi} &= \frac{a_{1\psi}}{a_{3\psi}} \tilde{\alpha}_r \\
K_{D\psi} &= \frac{a_{2\psi}}{a_{3\psi}} \tilde{\alpha}_r - \beta(r).
\end{aligned} \tag{8.6}$$

It should be stressed that in the nonlinear case parameter $\beta(r)$ varies in time resulting in time-varying controller parameters.

Depth control

Just as in the case of the yaw motion control, the heave degree of freedom can be described by using (8.1) where $\eta = z$, $\tau = Z$, $\alpha_\nu = \alpha_w$. In this case there will exist a bias term τ_E which represents the difference between the weight and buoyancy of the vehicle. This term can be compensated by adding an estimated bias $\tilde{\tau}_E$ to the controller action. If the model is linear, $\beta(\nu) = \beta_w$ and if it is nonlinear $\beta(\nu) = \beta_{ww}|w|$. The assumption is that only estimated model parameters are available, i.e. $\tilde{\alpha}_w$ and $\tilde{\beta}_w$ or $\tilde{\beta}_{ww}$, depending on the appropriate model. According to (8.5), parameters of the controller given with (8.2) are

$$\begin{aligned}
K_{Iz} &= \frac{\tilde{\alpha}_w}{a_{3z}} \\
K_{Pz} &= \frac{a_{1z}}{a_{3z}} \tilde{\alpha}_w \\
K_{Dz} &= \frac{a_{2z}}{a_{3z}} \tilde{\alpha}_w - \beta(w).
\end{aligned} \tag{8.7}$$

Again, it should be stressed that in the nonlinear case parameter $\beta(w)$ varies in time resulting in time-varying controller parameters.

For both yaw and heave control cases, the controller can be presented with a general structure shown in Fig. 8.3, which will be explained after the robustness analysis.

8.1.2 Stability Analysis

Every identification method has a certain uncertainty in the identified parameters, [42]. The stability of the closed-loop system can be compromised if

- the identified parameters are not identical to real process parameters (robust stability), or
- if the process has a structure different than the one that is assumed (structural stability).

Because of the two reasons, the stability of the closed-loop system will be observed with regard to the following assumptions.

Assumption 8.1. Identified parameters $\tilde{\alpha}_\nu$ and $\tilde{\beta}(\nu)$ may differ from real parameters α_ν and $\beta(\nu)$ in value.

Assumption 8.2. The process may not have the structure which can be described with dominant constant or linear drag as shown with (8.1), but with a more general, affine equation (8.8).

$$\alpha_\nu \ddot{\eta}(t) + \beta_\nu \dot{\eta}(t) + \beta_{\nu\nu} |\dot{\eta}(t)| \dot{\eta}(t) = \tau(t) \quad (8.8)$$

Assumption 8.3. The controller is always designed under the assumption that the process structure can be described with constant or linear drag as shown with (8.1).

Because of Assumption 8.1, the controller parameters are written with estimated (denoted with a tilde) process parameters so that the closed loop equation can be described with (8.9) where α_ν and $\beta(\nu)$ are real process parameters.

$$\frac{\eta}{\eta_{ref}} = \frac{1}{\frac{\alpha_\nu}{\tilde{\alpha}_\nu} a_{3\eta} s^3 + \left[a_{2\eta} + a_{3\eta} \frac{\beta(\nu) - \tilde{\beta}(\nu)}{\alpha_\nu} \right] s^2 + a_{1\eta} s + 1} \quad (8.9)$$

It should be noticed that in the case of exact parameter identification for values $\tilde{\alpha}_\nu = \alpha_\nu$ and $\tilde{\beta}(\nu) = \beta(\nu)$ the model function itself is obtained.

From the characteristic equation of the system, stability of the closed loop can be determined by using the Jury criterion, [77], which results in conditions (8.10)–(8.13).

$$\frac{\alpha_\nu}{\tilde{\alpha}_\nu} a_{3\eta} > 0 \quad (8.10)$$

$$a_{1\eta} > 0 \quad (8.11)$$

$$a_{2\eta} + a_{3\eta} \frac{\beta(\nu) - \tilde{\beta}(\nu)}{\tilde{\alpha}_\nu} > 0 \quad (8.12)$$

$$\tilde{\beta}(\nu) - \beta(\nu) < \frac{a_{2\eta}}{a_{3\eta}} \tilde{\alpha}_\nu - \frac{1}{a_{1\eta}} \alpha_\nu. \quad (8.13)$$

Conditions (8.10) and (8.11) are always satisfied if the model function is stable. Condition (8.12) can be written in the form

$$\tilde{\beta}(\nu) - \beta(\nu) < \frac{a_{2\eta}}{a_{3\eta}} \tilde{\alpha}_\nu. \quad (8.14)$$

Since only conditions (8.13) and (8.14) are left, it should be determined which of these is stricter. By observing the sign of the right-hand side of (8.13), inequality (8.15) is obtained.

$$\frac{\tilde{\alpha}_\nu}{\alpha_\nu} > \frac{a_{3\eta}}{a_{2\eta} a_{1\eta}} \quad (8.15)$$

For example, third order Butterworth filter has a transfer function

$$G_{Butter}(s) = \frac{1}{s^3 + 2s^2 + 2s + 1}$$

which gives $\frac{\tilde{\alpha}_\nu}{\alpha_\nu} > 0.25$. The third order Bessel filter has a transfer function

$$G_{Bessel}(s) = \frac{1}{\frac{1}{15}s^3 + \frac{2}{15}s^2 + s + 1}$$

which gives $\frac{\tilde{\alpha}_\nu}{\alpha_\nu} > 0.1667$. Since the ratios between estimated and real parameters can never be so drastic, this implies that (8.15) is always satisfied. The conclusion is that condition (8.13) is stricter than condition (8.14) and therefore it will be used for determining stability. Further on, since

$$\frac{\alpha_\nu}{a_{1\eta}} < \frac{a_{3\eta}}{a_{2\eta}} \tilde{\alpha}_\nu, \quad (8.16)$$

the right-hand side of (8.13) is always greater than 0. From (8.13), if $\tilde{\beta}(\nu) - \beta(\nu) < 0$ the system is always stable. If $\tilde{\beta}(\nu) - \beta(\nu) > 0$ a constraint on the system stability given with (8.13) is obtained. For further calculus, ratios between the identified parameters and real parameters are defined as

$$p_{\alpha_\nu} = \frac{\tilde{\alpha}_\nu - \alpha_\nu}{\alpha_\nu} \quad (8.17)$$

$$p_{\beta(\nu)} = \frac{\tilde{\beta}(\nu) - \beta(\nu)}{\beta(\nu)} \quad (8.18)$$

from where it follows that

$$\alpha_\nu = \frac{\tilde{\alpha}_\nu}{p_{\alpha_\nu} + 1}, p_{\alpha_\nu} \in (-1, 1) \quad (8.19)$$

$$\beta(\nu) = \frac{\tilde{\beta}(\nu)}{p_{\beta(\nu)} + 1}, p_{\beta(\nu)} \in (-1, 1). \quad (8.20)$$

It was mentioned before that for $p_{\beta(\nu)} < 0$ the system is always stable, therefore the assumption for further analysis is that $p_{\beta(\nu)} > 0$.

From Assumption 8.2 and Assumption 8.3 follows that there exist four different cases: when the model is assumed to be linear and it is linear or affine, and when the model is assumed to be nonlinear and it is nonlinear or affine. These cases are observed in the following part.

Linear model & linear controller

For this case the model has $\beta(\nu) = \beta_\nu$ and the controller $\tilde{\beta}(\nu) = \tilde{\beta}_\nu$. From (8.13) follows that (8.21) has to be fulfilled in order to have stable closed-loop system.

$$1 < \frac{\frac{a_{2\eta}}{a_{3\eta}}\tilde{\alpha}_\nu - \frac{1}{a_{1\eta}}\alpha_\nu}{\tilde{\beta}_\nu - \beta_\nu} \quad (8.21)$$

Using the ratios, (8.22) is obtained.

$$\frac{\tilde{\beta}_\nu}{\tilde{\alpha}_\nu} \frac{p_{\beta_\nu}}{p_{\beta_\nu} + 1} - \frac{a_{2\eta}}{a_{3\eta}} < -\frac{1}{a_{1\eta}} \frac{1}{p_{\alpha_\nu} + 1} \quad (8.22)$$

This inequality gives an elegant method of determining stability of the closed system after the system parameters have been identified. With estimated errors of identification, bounds can be set on the model function in order to ensure stability. If it is assumed that the identification experiment is carried out in such a way that the absolute error in determining β_ν is definitely smaller than 20%, it can be written that $|p_{\beta_\nu}| < 0.2$. If this is the case, than parameter α_ν has an absolute error lower than 10%, i.e. $|p_{\alpha_\nu}| < 0.1$. The worst case for stability condition (8.22) is when $p_{\beta_\nu} = 0.2$ and $p_{\alpha_\nu} = -0.1$, which gives (8.23).

$$\frac{\tilde{\beta}_\nu}{\tilde{\alpha}_\nu} < \frac{2}{3} \frac{9a_{1\eta}a_{2\eta} - 10a_{3\eta}}{a_{1\eta}a_{3\eta}} \quad (8.23)$$

Affine model & linear controller

For this case the model has $\beta(\nu) = \beta_{\nu\nu} |\nu| + \beta_\nu$ and the controller $\tilde{\beta}(\nu) = \tilde{\beta}_\nu$. From (8.13) follows that (8.24) has to be fulfilled in order to have stable closed-loop system.

$$\tilde{\beta}_\nu - \beta_\nu < \frac{a_{2\eta}}{a_{3\eta}}\tilde{\alpha}_\nu - \frac{1}{a_{1\eta}}\alpha_\nu + \beta_{\nu\nu} |\nu| \quad (8.24)$$

By comparing (8.22) and (8.24) it can be seen that condition (8.22) is stricter – if the stability is ensured for the previous case, this case will also be stable. However, while designing the controller, one should bear in mind that the differences between the identified and real parameters might be greater.

Nonlinear model & nonlinear controller

For this case the model has $\beta(\nu) = \beta_{\nu\nu} |\nu|$ and the controller $\tilde{\beta}(\nu) = \tilde{\beta}_{\nu\nu} |\nu|$. From (8.13) follows that (8.25) has to be fulfilled in order to have stable closed-loop system.

$$|\nu| < \frac{\frac{a_{2\eta}}{a_{3\eta}}\tilde{\alpha}_\nu - \frac{1}{a_{1\eta}}\alpha_\nu}{\tilde{\beta}_{\nu\nu} - \beta_{\nu\nu}} \quad (8.25)$$

Using the ratios, (8.26) is obtained.

$$|\nu| < \frac{\tilde{\alpha}_\nu}{\tilde{\beta}_{\nu\nu}} \frac{p\beta_{\nu\nu} + 1}{p\beta_{\nu\nu}} \left(\frac{a_{2\eta}}{a_{3\eta}} - \frac{1}{a_{1\eta}} \frac{1}{p\alpha_\nu + 1} \right) \quad (8.26)$$

This inequality does not provide stability condition immediately after the parameters have been identified, but it can be used to set a limit to the derivative control action of the controller. This limitation in the controller will ensure the stability of the system. If the same identification errors as described before are assumed, i.e. $p\beta_\nu = 0.2$ and $p\alpha_\nu = -0.1$, the worst case scenario gives limitation (8.27).

$$|\nu| < \frac{2}{3} \frac{\tilde{\alpha}_\nu}{\tilde{\beta}_{\nu\nu}} \frac{9a_{1\eta}a_{2\eta} - 10a_{3\eta}}{a_{1\eta}a_{3\eta}} \quad (8.27)$$

Affine model & nonlinear controller

For this case the model has $\beta(\nu) = \beta_{\nu\nu} |\dot{x}| + \beta_\nu$ and the controller $\tilde{\beta}(\nu) = \tilde{\beta}_{\nu\nu} |\nu|$. From (8.13) follows that (8.28) has to be fulfilled in order to have stable closed-loop system.

$$|\nu| \left(\tilde{\beta}_{\nu\nu} - \beta_{\nu\nu} \right) < \frac{a_{2\eta}}{a_{3\eta}} \tilde{\alpha}_\nu - \frac{1}{a_{1\eta}} \alpha_\nu + \beta_\nu \quad (8.28)$$

By comparing (8.26) and (8.28) it can be seen that condition (8.26) is stricter, which means that false assumption on the process' structure will not cause instability. However, in this case one should be careful while limiting ν because the estimation errors may be larger than in the previous case.

After having defined the stability bounds for the closed-loop system, the general controller given in Fig. 8.3 can be described. Parameter $\tilde{K}_D^* = \frac{a_{2\eta}}{a_{3\eta}} \tilde{\alpha}_\nu$ is the part of \tilde{K}_D that does not change whether the controller is linear or nonlinear. Parameter $\tilde{\beta}_{\nu\nu}$ equals 0 if the controller is linear. The limiter which is in the derivation channel is here to ensure stability of the closed loop. If the process is linear the limiter does not have any function since this channel does not exist and stability is determined immediately after calculating the controller parameters. If the process is nonlinear, the lower limit to the saturation block is 0, while the upper limit is given with (8.26).

8.1.3 Antiwindup

Real processes are always subject to different constraints. One such constraint that is present in marine systems is input force (moment) saturation. For example, Charlie USV which is controlled by rudder has a constraint that maximum rudder deflection angle is 30° . Model based controllers such as the one described in previous section do not take these limits into consideration. However, they are present and can cause significant problems in system response.

If a process is controlled by a controller consisting of an integrating channel, the controller may give outputs which are not feasible. Specifically, integrator output may

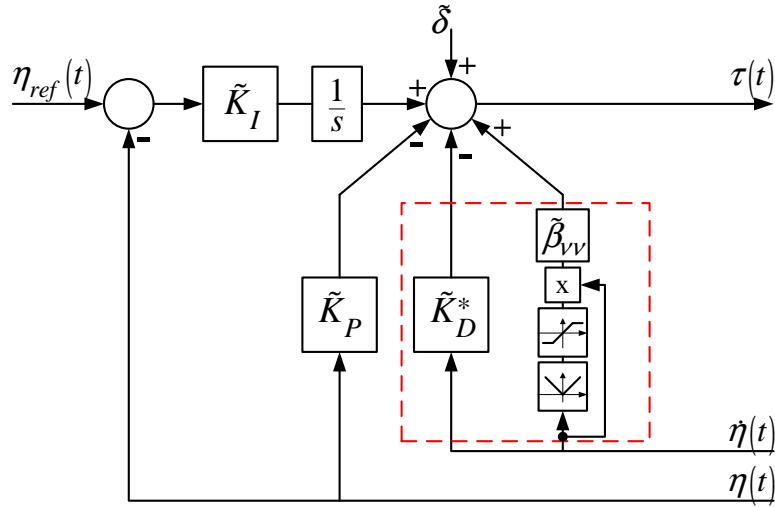


Figure 8.3. The I-PD controller structure

increase, even though the system cannot accept the change in the controller any more. The problem arises when the integrator starts "discharging": first it has to "discharge" all the output which was not accepted by the process, before the process starts reacting. This is why the output may have large overshoot and oscillations, as it is shown in Fig. 8.4. The effect which has been described is called integrator windup.

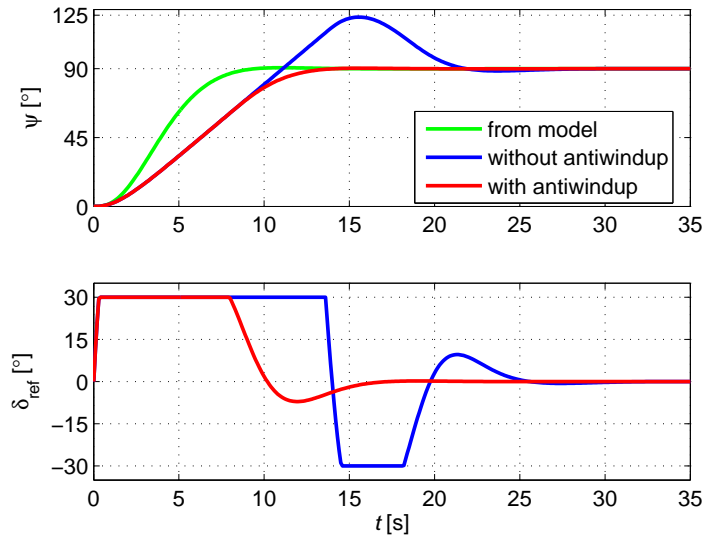


Figure 8.4. Closed loop responses with and without antiwindup.

In order to avoid this effect, the integrator should stop integrating when controller

output τ_c is greater than feasible action τ_{ref} . This procedure is called *antiwindup*. This procedure can be implemented as shown in Fig. 8.5 and the integral channel output in this case is

$$\tau_I = K_I \int_0^t (\eta_{ref} - \eta) dt - \int_0^t [\tau_c - sat(\tau_c, \tau_{min}, \tau_{max})] dt \quad (8.29)$$

where τ_{min} and τ_{max} are upper and lower saturation limit of the input signal to the vehicle.

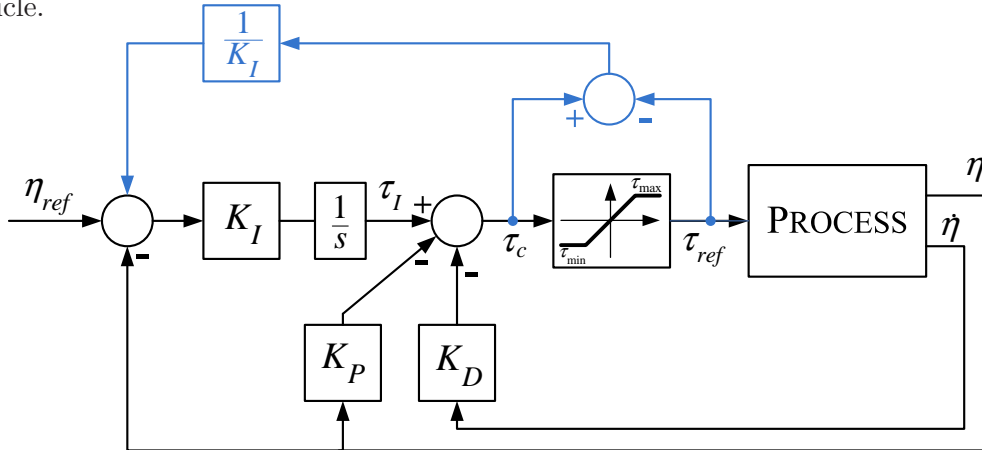


Figure 8.5. The antiwindup controller scheme.

When implementing the antiwindup scheme programmatically (in a microprocessor), the implementation is somewhat simpler since integration only has to be stopped when $\tau_c > \tau_{max}$. Fig. 8.4 also shows the responses when antiwindup is used. The model function is given in green colour while the red one is using the antiwindup. Of course, it cannot be expected for the system to be exactly like the model function because of the limiter, but the overshoot is almost the same as in the model function. Lower figure shows the realized controller output τ_{ref} for the cases with and without antiwindup.

8.1.4 Simulation Results

The simulation results were performed in such a way that the parameters of the vessel were identified using the identification by use of self-oscillation method as it is described in detail in Chapter 6.

Example 8.1. A simulation example of a dominantly linear system, FALCON ROV yaw model was used whose parameters are given in Table 7.1. Based on the procedure for determining the appropriate model given in Chapter 7.1, it was decided that the linear model describes the yaw degree of freedom better, and the identified parameters are given in Table 7.2. First set of identified parameters was used to tune controller parameters. However, it should be noticed that the real vehicle dynamics also include a β_{rr} term.

Based on these identification results, a linear I–PD controller with parameters according to (8.6) with $\beta(r) = \beta_r$ can be designed so that a 3rd order Bessel filter with characteristic frequency $\omega_0 = 1.5 \frac{\text{rad}}{\text{s}}$ behavior is achieved. This model function is chosen so that the vehicle could perform a 90° turn without the thrusters saturating. Using the stability condition (8.23), inequality $3.78 < 17.84$ is obtained which proves the stability of the designed closed loop. The simulation results are shown in Fig. 8.6.

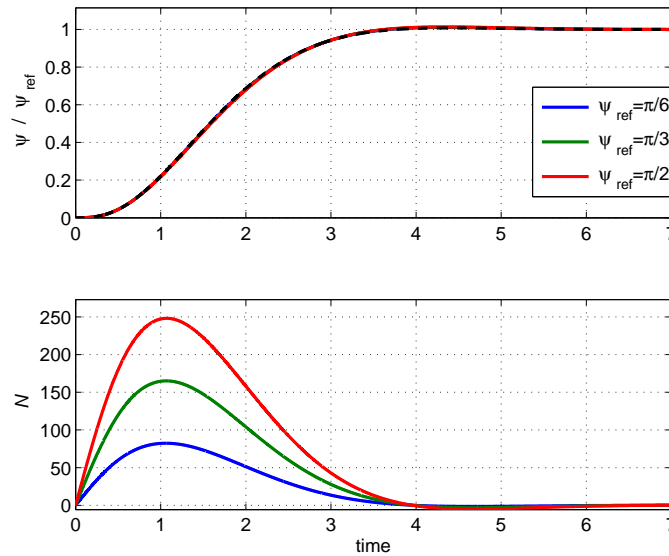


Figure 8.6. FALCON ROV heading response.

■

Example 8.2. A simulation example of a dominantly linear system with a biased component, FALCON ROV heave model was used whose parameters are given in Table 7.3. Based on the procedure for determining the appropriate model given in Chapter 7.1, it was decided that the linear model describes the heave degree of freedom better, and the identified parameters are given in Table 7.4. First set of identified parameters was used to tune controller parameters. However, it should be noticed that the real vehicle dynamics also include a β_{ww} term.

Based on these identification results, a linear I–PD controller with parameters according to (8.6) with $\beta(w) = \beta_w$ can be designed so that a 3rd order Bessel filter with characteristic frequency $\omega_0 = 0.8 \frac{\text{rad}}{\text{s}}$ behavior is achieved. This model function is chosen so that the vehicle could perform a 3m dive without the thrusters saturating. Using the stability condition (8.23), inequality $1.61 < 9.5153$ is obtained which proves the stability of the designed closed loop. The simulation results are shown in Fig. 8.7.

■

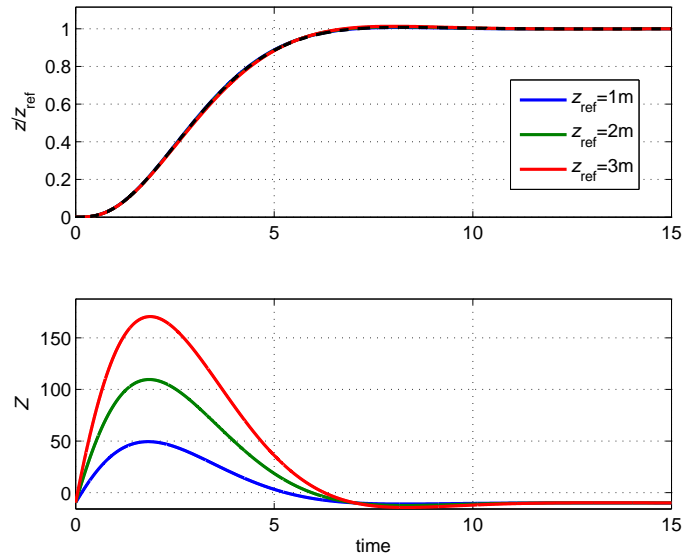


Figure 8.7. FALCON ROV depth response.

Example 8.3. A simulation example of a dominantly nonlinear system, yaw model was used whose parameters are given in Table 7.5. Based on the procedure for determining the appropriate model given in Chapter 7.1, it was decided that the nonlinear model describes the heave degree of freedom better, and the identified parameters are given in Table 7.6. First set of identified parameters was used to tune controller parameters.

Based on these identification results, an I-PD controller with parameters according to (8.6) with $\beta(r) = \beta_{rr}|r|$ can be designed so that a 3rd order Bessel filter with characteristic frequency $\omega_0 = 1.5 \frac{rad}{s}$ behavior is achieved. This model function is chosen so that the vehicle could perform a 90° turn without the thrusters saturating. Using the stability condition (8.27), the yaw rate should be limited to $|\dot{\psi}| < 13.4$. The simulation results are shown in Fig. 8.8 and in the third graph of the same figure it can be seen that $|\dot{\psi}|$ never passes the critical value, i.e. the limit in the controller in Fig. 8.3 is never reached. ■

8.1.5 Experimental Results

The experimental results which will be shown here are obtained on yaw degree of freedom of Charlie USV, and were performed in Genoa, Italy together with the team from Consiglio Nazionale delle Ricerche. The algorithm for controller tuning procedure using the self-oscillation identification experiment can be summarized as follows:

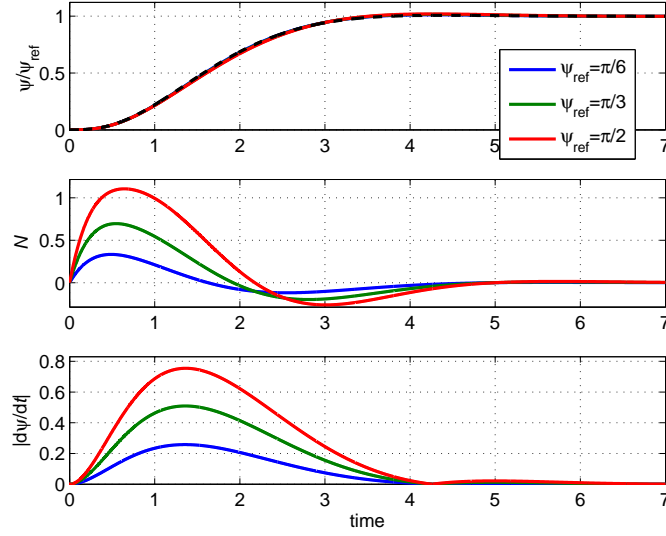


Figure 8.8. Heading response of the dominantly nonlinear yaw model.

Algorithm 8.4. Tuning the heading controller.

- I. Perform one self-oscillation experiment with the open loop steering system and determine magnitude X_m and frequency ω of self-oscillations.
- II. Calculate $\tilde{\alpha}_r$ and $\tilde{\beta}_r$ using formulae in Table 6.3.
- III. Define desired closed loop dynamics ($a_{3\psi}$, $a_{2\psi}$ and $a_{1\psi}$).
- IV. Calculate controller parameters using (8.6) and implement the controller using (8.2).

■

Extensive IS–O experiments for identifying Charlie USV are given in Chapter 7.5. Only one experiment has to be performed in order to tune heading controller for Charlie USV. Specifically in this case, the experiment consisted in setting relay output (rudder angle δ) to $C = 25^\circ$ and hysteresis width to $x_a = 10^\circ$. The experiment is shown in Fig. 7.20. The complete identification experiment finished after 5 oscillations which took about 80s. The I–PD controller given with was tuned so that the desired closed loop function is Bessel filter with characteristic frequency $0.45s^{-1}$, i.e. $G_{m\psi}(s) = \frac{1}{10.97s^3 + 12.01s^2 + 5.48s + 1}$. Heading responses are shown in Fig. 8.9. Heading response has small overshoot and the steady state error does not exist. Rudder activity in the steady state is low, which is one of the strongest specifications while designing the control system in order to minimize energy consumption and mechanical stress.

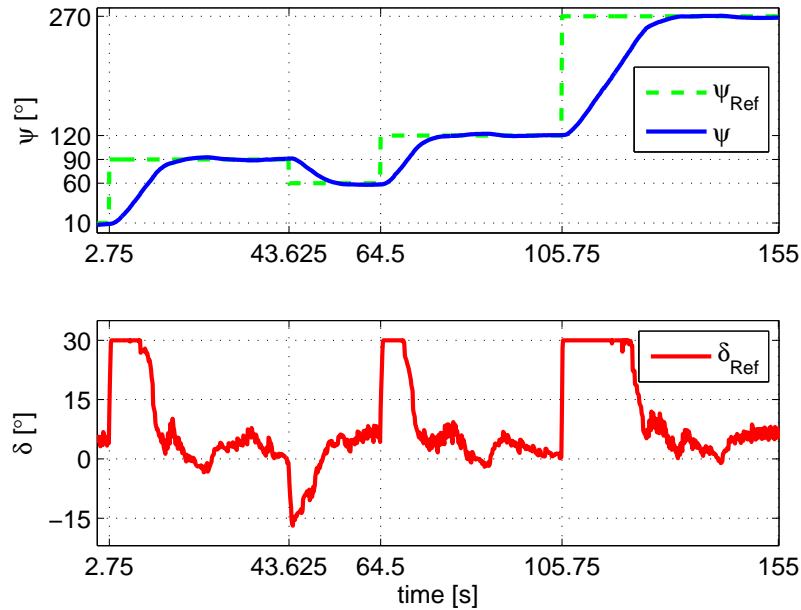


Figure 8.9. Heading and rudder angle response.

8.1.6 Other Control Algorithms

Other control algorithms will be derived only for the heading controller, for the sake of simplicity. Heading controllers can have different structures. Naturally, heading closed loops depend on these structures. For heading control it is rather important to have smooth control signals, especially if actuators cannot bear abrupt changes (e.g. rudders) which occur during step reference changes. This is why “-” controllers are often used, e.g. I-PD controller implies that the control difference is taken through the integration channel, while proportional and derivative channel are connected directly to heading, [77]. This can be quite convenient, especially if it is taken into account that the derivation channel connected to the heading signal is in fact the yaw rate measurement which is almost always available.

Table 8.1 shows heading closed loop transfer functions for numerous control algorithms under the assumption that the steering equation is described with a Nomoto model given in the form

$$\frac{\psi}{\psi_{ref}} = \frac{K}{s(Ts + 1)}. \quad (8.30)$$

This assumption does not limit the application of the proposed procedure since the control algorithm can be modified in such a way that the nonlinearity inherent to the steering equation can be compensated for, e.g. as described in the previous section and in [58]. All algorithms, except for classic PID, have at most three poles and one

Table 8.1. Heading closed loop transfer functions depending on the control algorithm ($e = \psi_{ref} - \psi$)

NAME	ALGORITHM	TRANSFER FUNCTION $\frac{\psi}{\psi_{ref}}$
P	$K_P\psi$	$\frac{KK_P}{Ts^2+s+KK_P}$
PD	$K_P\psi + K_D\dot{e}$	$\frac{KK_R+KK_Ds}{Ts^2+(1+KK_D)s+KK_R}$
P–D	$K_Pe - K_D\dot{\psi}$	$\frac{KK_P}{Ts^2+KK_Ds+KK_P}$
PI	$K_Pe + K_I \int e$	$\frac{KK_I+KK_Ps}{Ts^3+s^2+KK_Ps+KK_I}$
I–P	$-K_P\psi + K_I \int e$	$\frac{KK_I}{Ts^3+s^2+KK_Ps+KK_I}$
PID	$K_Pe + K_D\dot{e} + K_I \int e$	$\frac{KK_Ds^2+KK_Ps+KK_I}{Ts^3+(1+KK_D)s^2+KK_Ps+KK_I}$
PI–D	$K_Pe + K_I \int e - K_D\dot{\psi}$	$\frac{KK_Ps+KK_I}{Ts^3+(1+KK_D)s^2+KK_Ps+KK_I}$
I–PD	$K_I \int e - K_P\psi - K_D\dot{\psi}$	$\frac{KK_I}{Ts^3+(1+KK_D)s^2+KK_Ps+KK_I}$

finite zero. The classic PID algorithm will be excluded from analysis due to the fact that leading the control difference directly through the derivation channel can seriously damage the actuator. In practice, PI–D controller is used instead, [61].

8.2 Distance Keeping Control System

Mathematical model of distance keeping scheme has been described in detail in Chapter 2.6. In the following part, a Kalman filter will be developed together with an angle and distance keeping controller. The angle controller is used to keep the vehicle at a specific angle with regard to the flat surface, and distance controller ensures the distance to the surface is kept at a desired value. The main sensor which is used in this control structure is the vision–based laser distance module which is described in Chapter 3.4.

8.2.1 Kalman Filter Design

Some motivation for the use of Kalman filtering has already been mentioned in Chapter 2.6. In fact, the motivation for the use of Kalman filter is dual:

1. estimation of unmeasurable yaw rate, r and surge speed u , which are needed for controller design.
2. estimation of the distance d from the surface when measurements are not available.

The latter motivation comes from the fact that the vision–based laser module works with frequency of 2Hz while control is performed at 10Hz and therefore estimation is

needed between two available measurements, see Fig. 8.10. Also, the vehicle might get too close or too far from the plane-like surface which leads to laser dots disappearing from the image – estimation in these cases is crucial for system operation.

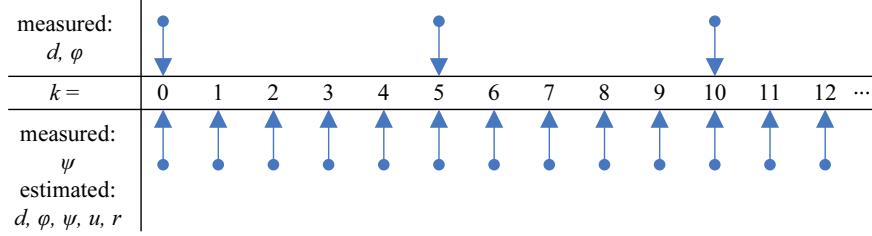


Figure 8.10. Timeline of measurements and estimations.

The signals that are measured in the distance keeping setup are compass heading, ψ , distance from obstacle, d , and angle with regard to the obstacle, φ , (two latter are obtained from the vision-based distance sensor). The estimates from the Kalman filter will be d , φ , heading ψ , surge speed u and yaw rate r .

The mathematical model that describes distance keeping is explained in detail in Chapter 2.6. That model is given in a general form. Since it has been shown in Chapters 7.3 and 7.6 that the dynamic model of VideoRay ROV is best described using a nonlinear model with constant drag parameters, i.e. $\beta(r) = \beta_{rr}|r|$ and $\beta(u) = \beta_{uu}|u|$, the distance keeping model for that vehicle is given with equations (8.31)–(8.37). Detailed description of model parameters can be found in Chapter 2.6.

$$\dot{u} = -\frac{\beta_{uu}}{\alpha_u}|u|u + \frac{1}{\alpha_u}X \quad (8.31)$$

$$\dot{r} = -\frac{\beta_{rr}}{\alpha_r}|r|r + \frac{1}{\alpha_r}N \quad (8.32)$$

$$\dot{\varphi} = r + v_\varphi \quad (8.33)$$

$$\dot{\psi} = r + v_\psi \quad (8.34)$$

$$\dot{d} = -u \cos \varphi + v_d \quad (8.35)$$

$$\dot{v}_\varphi = 0 \quad (8.36)$$

$$\dot{v}_d = 0 \quad (8.37)$$

Having this model in mind, an extended Kalman filter (EKF) in its discrete form can be designed, see [39] and [82]. If the state vector is

$$\mathbf{y}(k) = \left[u(k) \quad r(k) \quad \varphi(k) \quad \psi(k) \quad d(k) \quad v_\varphi(k) \quad v_d(k) \right]^T,$$

discrete-time EKF prediction and correction equations are derived from the mathematical model and are presented in Table 8.2. The minus sign in the superscript denotes the prediction. \mathbf{A} is the Jacobian matrix in the form given with (8.38). Covariance

matrices are determined based on a priori measurements as

$$\begin{aligned}\mathbf{Q}_{KF} &= 0.1\mathbf{I}_{7 \times 7} \\ \mathbf{P}_0 &= 1000\mathbf{I}_{7 \times 7} \\ \mathbf{R} &= \begin{bmatrix} 0.5 & 0 & 0 \\ 0 & 10 & 0 \\ 0 & 0 & 0.1 \end{bmatrix}.\end{aligned}$$

Table 8.2. Distance keeping Kalman filter equations

PREDICTION EQUATIONS:
$u^-(k) = u(k-1) - T\frac{\beta_{uu}}{\alpha_u} u(k-1) u(k-1) + T\frac{1}{\alpha_u}X(k)$
$r^-(k) = r(k-1) - T\frac{\beta_{rr}}{\alpha_r} r(k-1) r(k-1) + T\frac{1}{\alpha_r}N(k)$
$\varphi^-(k) = \varphi(k-1) + Tr(k-1) + Tv_\varphi(k)$
$\psi^-(k) = \psi(k-1) + Tr(k-1) + Tv_\psi(k)$
$d^-(k) = d(k-1) - Tu(k-1)\cos\varphi(k-1) + Tv_d(k-1)$
$v_\varphi^-(k) = v_\varphi(k-1)$
$v_d^-(k) = v_d(k-1)$
$\mathbf{P}^-(k) = \mathbf{A}(k)\mathbf{P}(k-1)\mathbf{A}(k)^T + \mathbf{Q}_{KF}$
CORRECTION EQUATIONS:
$\mathbf{K}(k) = \mathbf{P}^-(k)\mathbf{H}(k)^T [\mathbf{H}(k)\mathbf{P}^-(k)\mathbf{H}(k)^T + \mathbf{R}(k)]^{-1}$
$\hat{\mathbf{x}}(k) = \hat{\mathbf{x}}^-(k) + \mathbf{K}(k) [\mathbf{y}(k) - \mathbf{H}(k)\hat{\mathbf{x}}^-(k)]$
$\mathbf{P}(k) = [\mathbf{I} - \mathbf{K}(k)\mathbf{H}(k)] \mathbf{P}^-(k)$

$$\mathbf{A}(k) = \mathbf{I}_{7 \times 7} + T \begin{bmatrix} -2\frac{\beta_{uu}}{\alpha_u}|u(k)| & 0 & 0 & 0 & 0 & 0 & 0 \\ 0 & -2\frac{\beta_{rr}}{\alpha_r}|r(k)| & 0 & 0 & 0 & 0 & 0 \\ 0 & 1 & 0 & 0 & 0 & 1 & 0 \\ 0 & 1 & 0 & 0 & 0 & 1 & 0 \\ -\cos\varphi(k) & 0 & 0 & u(k)\sin\varphi(k) & 0 & 0 & 1 \\ 0 & 0 & 0 & 0 & 0 & 0 & 0 \\ 0 & 0 & 0 & 0 & 0 & 0 & 0 \end{bmatrix} \quad (8.38)$$

Measurement matrix, $\mathbf{H}(k)$, which appears in correction equations has a form $\mathbf{H}_1(k)$ given with (8.39) when measurements from the vision-based laser module are available, and $\mathbf{H}_2(k)$ given with (8.40) when measurements are not available (at times between two measurements, or when laser dots are not found).

$$\mathbf{H}_1(k) = \begin{bmatrix} 0 & 0 & 1 & 0 & 0 & 0 & 0 \\ 0 & 0 & 0 & 1 & 0 & 0 & 0 \\ 0 & 0 & 0 & 0 & 1 & 0 & 0 \end{bmatrix} \quad (8.39)$$

$$\mathbf{H}_2(k) = \begin{bmatrix} 0 & 0 & 0 & 0 & 0 & 0 & 0 \\ 0 & 0 & 0 & 0 & 0 & 0 & 0 \\ 0 & 0 & 0 & 1 & 0 & 0 & 0 \end{bmatrix} \quad (8.40)$$

The unknown dynamic model parameters which appear in Kalman equations will be identified using the procedure described in the following section.

8.2.2 Distance Keeping Controller

The control scheme is given in Fig. 8.11. Underwater vehicle is presented with a general dynamic and kinematic block while the sensors that are used are magnetic compass (giving ψ measurements) and laser based distance module (giving φ and d measurements). Kalman filter outputs are used in both angle and distance controllers. The

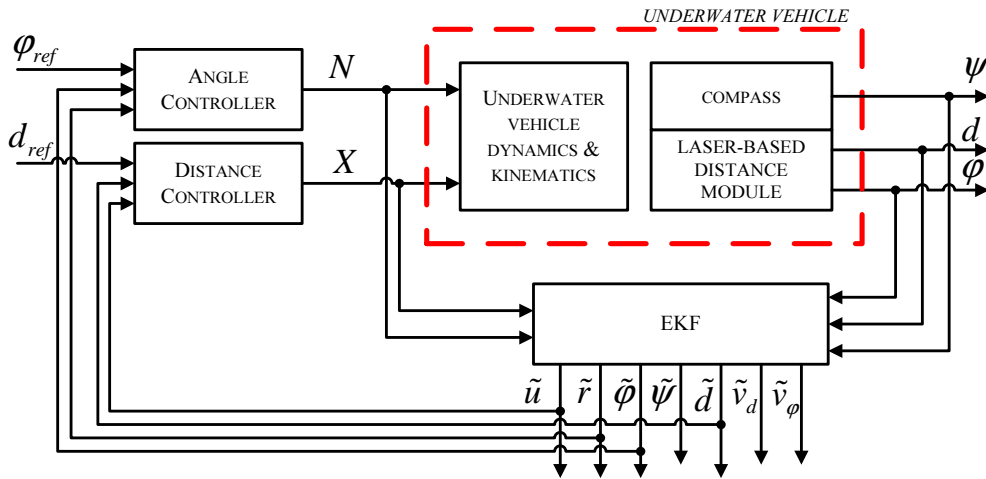


Figure 8.11. Distance keeping control scheme.

main objective of the distance keeping controller is to keep a desired distance from a flat surface. However, from (8.35) it is obvious that the angle relative to the surface and the distance are coupled. This coupling can be resolved if the vehicle is kept at a constant angle, which is chosen to be 0. This is the reason why an angle φ controller should be developed also. Setting $\varphi_{REF} = 0$ ensures that $\varphi \approx 0$. That is why, prior to

activating the distance d controller, angle φ controller is activated first.

Both angle and distance controllers which were implemented are of an I-PD form with a modification used for compensating the nonlinear term of the process, as it has already been described in Chapter 8.1.1. The angle controller is given with (8.41). It is worth noting that the derivative channel has estimated yaw rate \tilde{r} from the Kalman filter instead of $\dot{\tilde{\varphi}}$. The reference value is set to $\varphi_{ref} = 0$.

$$N(t) = K_{I\varphi} \int_0^t [\tilde{\varphi}_{REF}(t) - \tilde{\varphi}(t)] dt - K_{P\varphi} \tilde{\varphi}(t) - K_{D\varphi} \tilde{r}(t) \quad (8.41)$$

The distance controller is given with (8.42). It is worth noting that the derivative channel has $-\tilde{u}(t) \cos \tilde{\varphi}(t)$ instead of $\dot{\tilde{d}}$.

$$X(t) = K_{Id} \int_0^t [d_{REF}(t) - \tilde{d}(t)] dt - K_{Pd} \tilde{d}(t) - K_{Dd} [-\tilde{u}(t) \cos \tilde{\varphi}(t)] \quad (8.42)$$

Parameters of both controllers are set so that the closed loop transfer function for corresponding feedback loop ($x = \varphi$ for angle closed loop and $x = d$ for distance closed loop) is equal to the model function

$$G_m(s) = \frac{1}{a_{3x}s^3 + a_{2x}s^2 + a_{1x}s + 1}$$

which is stable. In that case, according to (8.5) the controller parameters for angle control are given with

$$\begin{aligned} K_{I\varphi} &= \frac{1}{a_{3\varphi}} \alpha_r \\ K_{P\varphi} &= \frac{a_{1\varphi}}{a_{3\varphi}} \alpha_r \\ K_{D\varphi} &= \frac{a_{2\varphi}}{a_{3\varphi}} \alpha_r - \beta_{rr} |\tilde{r}| \end{aligned} \quad (8.43)$$

and for distance control with

$$\begin{aligned} K_{Id} &= \frac{1}{a_{3d}} \alpha_u \\ K_{Pd} &= \frac{a_{1d}}{a_{3d}} \alpha_u \\ K_{Dd} &= \frac{a_{2d}}{a_{3d}} \alpha_u - \beta_{uu} |\tilde{u} \cos \tilde{\varphi}|. \end{aligned} \quad (8.44)$$

From (8.43) and (8.44) follows that controller parameters are time varying. A detailed stability analysis of the closed loop is given in Chapter 8.1.2 and the main result is that the structural and robust stability can be ensured by limiting the derivation

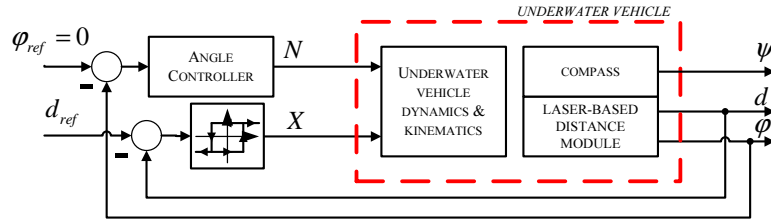


Figure 8.14. Distance keeping tuning algorithm: Step 3.

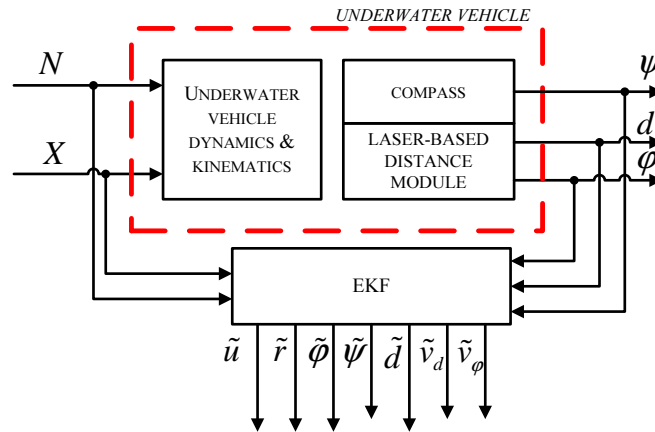


Figure 8.15. Distance keeping tuning algorithm: Step 4.

V. Use Kalman filter estimates as angle and distance controller inputs, as it is shown in Fig. 8.11.

■

Experimental result of IS–O method applied to the yaw DOF is analyzed in detail in Chapter 7.3, while the same method applied to surge DOF is shown in Fig. 7.32. Based on these experiments, unknown dynamic model parameters were calculated.

Fig. 8.16 demonstrates the responses of the complete closed loop distance keeping system to the ramp and step referent distance change and constant angle $\varphi_{REF} = 0$ with the previously described I–PD control algorithm. It can be seen that the Kalman filter estimates the distance value well in between the measurements. Also, surge (u_{EKF}) and yaw (r_{EKF}) speed estimates are smooth and show that the disturbance was significant during the experiments (mostly due to the influence of the tether). However, the controller performs well in transient as well as the steady state.

The case where measurements are not available for quite some time are shown in Fig. 8.17. At times $t = 435s$ and $t = 455s$ the laser dots from the laser–based distance module become unavailable due to an external disturbance and they appear back at $t = 440s$ and $t = 460s$, respectively. During this time, the Kalman filter estimated the behavior of the vehicle properly and control was not lost.

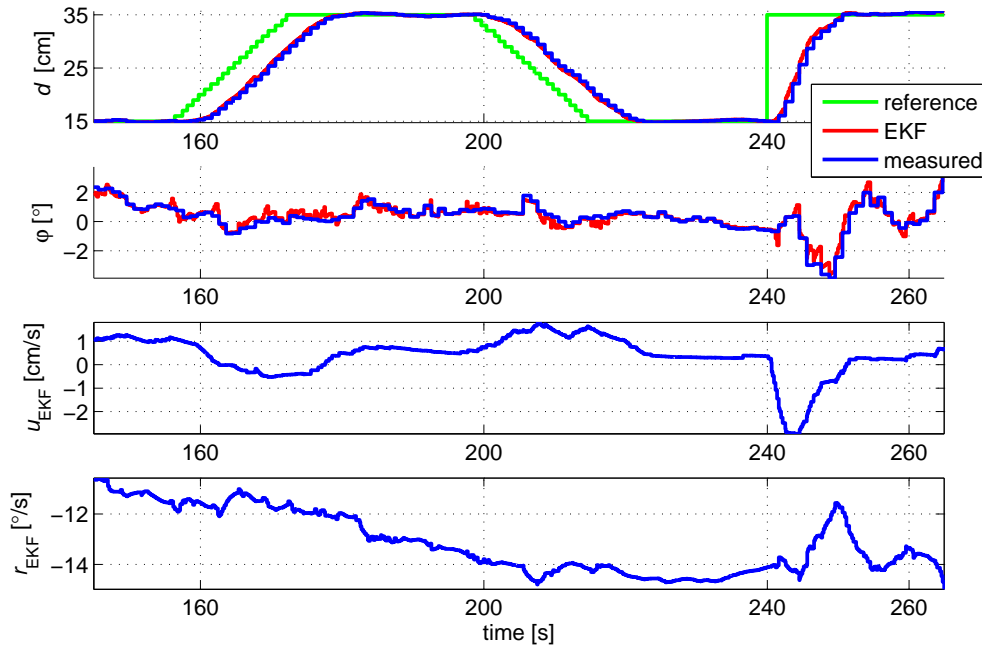


Figure 8.16. Responses of the closed loop system to the ramp and the step reference distance change and constant angle $\varphi_{REF} = 0$.

8.3 Line Following

The line following guidance goal is to set to zero the range d from the vessel and the target line, while maintaining the angle $\beta = \psi - \gamma$ between the desired line orientation γ and the vehicle heading ψ in $(-\frac{\pi}{2}, \frac{\pi}{2})$. Detailed equations for modelling the line following behaviour are given in Chapter 2.7.

Line following controllers can be implemented using two procedures, both of which will be described in the following part. Method 1 will be called *direct actuator control* since the line following controller will generate actuator command signals directly (rudder angle). Method 2 will be called *indirect actuator control* since the line following controller will generate commanded signals for the lower control level (heading control). Both methods have advantages and disadvantages and they will be referred to later.

8.3.1 Direct Actuator Control (Method 1)

Direct actuator control method generates actuator commands (rudder angle), which implies that the inner closed loop is yaw rate based as shown in Fig. 8.18 (Method 1). This method is advised if the vehicle control systems allows direct actuator commands, i.e. if inner closed loop controllers can be tuned, mostly because of its simplicity. The design procedure is based on a model function and is described in the following part.

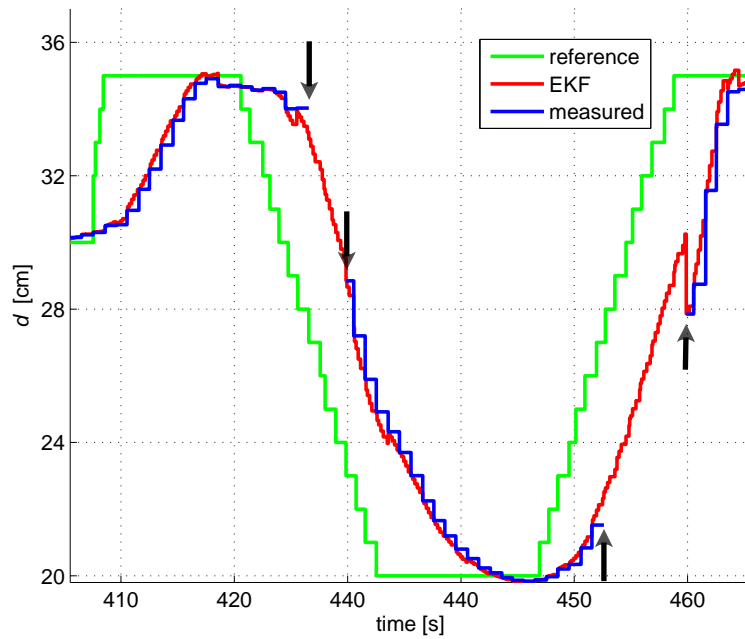


Figure 8.17. Responses of the closed loop system to distance change in case of missing measurements.

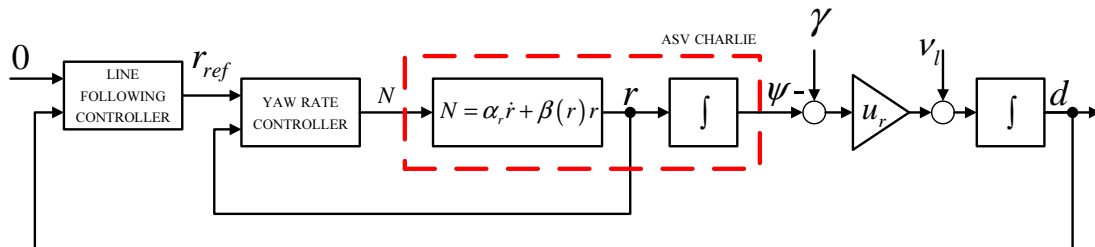


Figure 8.18. Line following control structure – Method 1

This method assumes that the low level controller is a yaw rate controller, i.e. the line following controller gives the reference yaw rate r_{ref} , as output. Firstly, the yaw rate closed loop transfer function design is presented, and then the line following controller design is given.

Yaw rate controller

The yaw rate controller is a P–D controller modified to compensate the process' non-linearity, if it exists, and it is given with (8.45).

$$N = K_{I_r} \int_0^t (r_{ref} - r) dt - K_{P_r} r + \tilde{\beta}(r)r \quad (8.45)$$

The inner closed loop transfer function is then

$$\frac{r}{r_{ref}} = \frac{1}{\underbrace{\frac{\tilde{\alpha}_r}{K_{I_r}}}_{a_{2r}} s^2 + \underbrace{\frac{K_{P_r}}{K_{I_r}}}_{a_{1r}} s + 1}$$

where a_{2r} and a_{1r} are the desired closed loop transfer function parameters. The controller parameters are then given with (8.46).

$$\begin{aligned} K_{P_r} &= \frac{a_{1r} \tilde{\alpha}_r}{a_{2r}} \\ K_{I_r} &= \frac{1}{a_{2r}} \tilde{\alpha}_r \end{aligned} \quad (8.46)$$

Line following controller

According to Fig. 8.18, the open loop transfer function is given with

$$\frac{d}{r_{ref}} = \frac{u_r}{s^2} \frac{r}{r_{ref}},$$

the line following controller is given with

$$r_{ref} = K_{P_d} (d_{ref} - d) + K_{D_d} \frac{d}{dt} (d_{ref} - d) \quad (8.47)$$

which yields the closed loop transfer function given with (8.48) where a_{4d} , a_{3d} , a_{2d} and a_{1d} are desired line following closed loop transfer function parameters.

$$\frac{d}{d_{ref}} = \frac{1 + \frac{K_{D_d} s}{K_{P_d}}}{\underbrace{\frac{a_{2r}}{u_r K_{P_d}}}_{a_{4d}} s^4 + \underbrace{\frac{a_{1r}}{u_r K_{P_d}}}_{a_{3d}} s^3 + \underbrace{\frac{1}{u_r K_{P_d}}}_{a_{2d}} s^2 + \underbrace{\frac{K_{P_d}}{K_{P_d}}}_{a_{1d}} s + 1} \quad (8.48)$$

Combining (8.46) and (8.48), the line following controller parameters can be calculated using (8.49).

$$\begin{aligned} K_{Ir} &= \frac{a_{2d}}{a_{4d}} \tilde{\alpha}_r \\ K_{Pr} &= \frac{a_{3d}}{a_{4d}} \tilde{\alpha}_r \\ K_{Pd} &= \frac{1}{u_r a_{2d}} \\ K_{Dd} &= \frac{a_{1d}}{u_r a_{2d}} \end{aligned} \quad (8.49)$$

Now it is evident that by setting the desired line following closed loop dynamics, the inner closed loop parameters are set automatically.

Algorithm 8.6. Direct actuator control (Method 1).

- I. Perform one self-oscillation experiment with the open loop steering system (6.33) and determine magnitude X_m and frequency ω of self-oscillations.
- II. Calculate $\tilde{\alpha}_r$ and $\tilde{\beta}(r)$ using expressions in Table 6.3.
- III. Define desired line following closed loop dynamics (a_{4d} , a_{3d} , a_{2d} and $a_{1\psi}$).
- IV. Calculate yaw rate and line following controller parameters using (8.49) and identified $\tilde{\alpha}_r$.
- V. Implement the yaw rate (8.45) and the line following (8.47) controllers.

■

8.3.2 Indirect Actuator Control (Method 2)

The second approach, indirect actuator control, is to generate referent heading as output from the line following controller (Method 2). This implies that there exists an inner heading based closed loop as shown in Fig. 8.19. If heading controller already exists and its structure or parameters cannot be changed, Method 2 is advised because the line following controller is tuned without changing the dynamics of the inner control loop. Design procedure for this method is also model based and will be described in the following part.

All classical closed loop transfer functions are listed in Table 8.1. As it has already been stated, all transfer functions have maximally three poles and one finite zero, apart from the case when PID controller is used and two zeros are generated. Since classical PID is not used for marine control purposes, the assumption is made that the low level heading closed loop can have three poles and one finite zero. This transfer function can be identified using the IS–O procedure as it is described in Chapter 6.6.4.

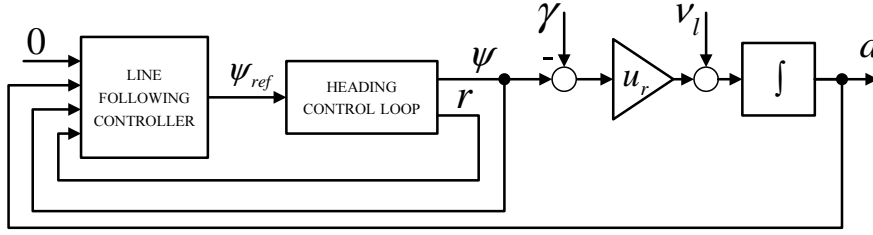


Figure 8.19. The line following control structure – Method 2

Let us suppose that the identified transfer function is given in a form (8.50).

$$\frac{\psi}{\psi_{ref}} = \frac{b_{1\psi}s + 1}{a_{3\psi}s^3 + a_{2\psi}s^2 + a_{1\psi}s + 1}. \quad (8.50)$$

The parameters in (8.50) are not known so two self-oscillation experiments have to be carried out as described in Chapter 6.6.4.

Measured variables that can be used in the line following controller tuning are heading ψ , yaw rate r and distance to the line d . These three states are not enough to position poles of the transfer function (8.50) using the pole placement method. That is why, for the purpose of controller design, the transfer function (8.50) is simplified using the Algorithm 8.7. The aim of this algorithm is to approximate the transfer function (8.50) with a second order transfer function with one finite zero, given with (8.51).

$$\frac{\psi}{\psi_{ref}} \approx \frac{\bar{b}_{1\psi}s + 1}{\bar{a}_{2\psi}s^2 + \bar{a}_{1\psi}s + 1} \quad (8.51)$$

Algorithm 8.7. Simplification of heading closed loop transfer function.

I. Calculate additional parameters Q , R , D , S and T .

$$\begin{aligned} Q &= \frac{1}{9a_{3\psi}^2}(3a_{1\psi}a_{3\psi} - a_{2\psi}^2) \\ R &= \frac{1}{54a_{3\psi}^3}(9a_{3\psi}a_{2\psi}a_{1\psi} - 27a_{3\psi}^2 - 2a_{2\psi}^3) \\ D &= Q^3 + R^2 \\ S &= \sqrt[3]{R + \sqrt{D}} \\ T &= \sqrt[3]{R - \sqrt{D}} \end{aligned}$$

II. Find the real pole

$$p = -\frac{1}{3} \frac{a_{2\psi}}{a_{3\psi}} + S + T$$

III. Find the two complex poles' parameters

$$\begin{aligned}\omega_n &= \sqrt{\frac{1}{-pa_{3\psi}}}, \\ \zeta &= \frac{\sqrt{-pa_{3\psi}}}{2} \left(\frac{a_{2\psi}}{a_{3\psi}} + p \right).\end{aligned}$$

IV. Calculate the new, simpler, transfer function (8.51) where

$$\begin{aligned}\bar{b}_{1\psi} &= b_{1\psi} + \frac{1}{p}, \\ \bar{a}_{1\psi} &= \frac{2\zeta}{\omega_n}, \\ \bar{a}_{2\psi} &= \frac{1}{\omega_n^2}.\end{aligned}$$

■

Line following controller

According to Fig. 8.19, open loop transfer function is given with

$$\frac{d}{\psi_{ref}} = -\frac{u_r}{s} \frac{\psi}{\psi_{ref}},$$

where $\frac{\psi}{\psi_{ref}}$ is described with (8.51). The line following controller is than given with

$$\psi_{ref} = -K_\psi \psi - K_r r - K_d d + K_{Id} \int_0^t (d_{ref} - d) dt \quad (8.52)$$

which yields the closed loop transfer function (8.53) with

$$\begin{aligned}a_0 &= \frac{u_r K_{Id}}{\bar{a}_{2\psi} + \bar{b}_{1\psi} K_r}, \\ a_1 &= \frac{u_r K_d + \bar{b}_{1\psi} K_{Id} u_r}{\bar{a}_{2\psi} + \bar{b}_{1\psi} K_r}, \\ a_2 &= \frac{1 + K_\psi + \bar{b}_{1\psi} K_d u_r}{\bar{a}_{2\psi} + \bar{b}_{1\psi} K_r}, \\ a_3 &= \frac{\bar{a}_{1\psi} + K_r + \bar{b}_{1\psi} K_\psi}{\bar{a}_{2\psi} + \bar{b}_{1\psi} K_r}.\end{aligned}$$

$$\frac{d}{d_{ref}} = \frac{(\bar{b}_{1\psi} s + 1) a_0}{s^4 + a_3 s^3 + a_2 s^2 + a_1 s + a_0} \quad (8.53)$$

From here, the controller parameter vector $\Theta_K = \begin{bmatrix} K_r & K_\psi & K_d & K_{Id} \end{bmatrix}$ can be calculated by solving the matrix equation (8.54).

$$\begin{bmatrix} 1 - a_3 \bar{b}_{1\psi} & \bar{b}_{1\psi} & 0 & 0 \\ -a_2 \bar{b}_{1\psi} & 1 & \bar{b}_{1\psi} u_r & 0 \\ -a_1 \bar{b}_{1\psi} & 0 & u_r & u_r b_{1\psi} \\ -a_0 \bar{b}_{1\psi} & 0 & 0 & u_r \end{bmatrix} \Theta_K = \begin{bmatrix} a_3 \bar{a}_{2\psi} - \bar{a}_{1\psi} \\ a_2 \bar{a}_{2\psi} - 1 \\ a_1 \bar{a}_{2\psi} \\ a_0 \bar{a}_{2\psi} \end{bmatrix} \quad (8.54)$$

The algorithm for designing line following controllers according to Method 2 is as follows.

Algorithm 8.8. Indirect actuator control (Method 2).

- I. Perform two self-oscillation experiments on a closed loop steering system (6.49) and determine magnitudes X_{m1} , X_{m2} and frequencies ω_1 , ω_2 of self-oscillations.
- II. Calculate $a_{3\psi}$, $a_{2\psi}$, $a_{1\psi}$ and $b_{1\psi}$ using (6.52).
- III. Use the Algorithm for simplification of heading closed loop transfer function to calculate $\bar{a}_{2\psi}$, $\bar{a}_{1\psi}$ and $\bar{b}_{1\psi}$.
- IV. Define desired line following closed loop dynamics (a_4 , a_3 , a_2 and a_1).
- V. Calculate line following controller parameters using (8.54).
- VI. Implement the line following controller using (8.52).

■

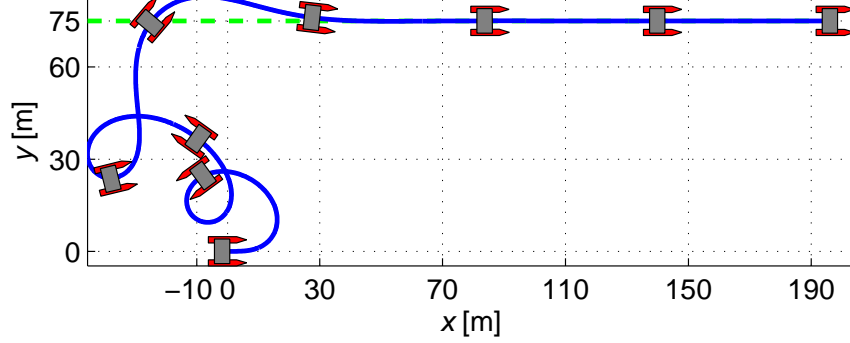
8.3.3 Monotonous Approach

If the line that the vehicle should approach is too far from the current vessel position, the vessel might start performing a spiral movement toward the line, or even worse it may start rotating at the smallest possible turn radius. This section will describe procedures which prevent this effect from happening in cases of direct and indirect actuator control.

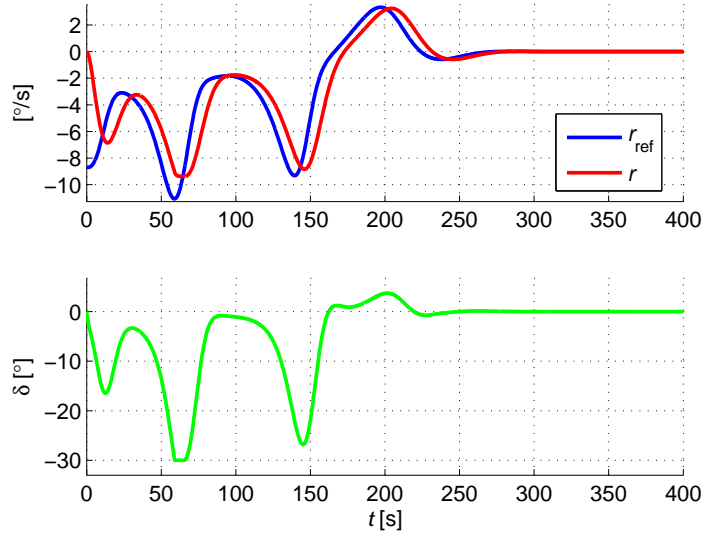
Direct actuator control

The line following controller in this method is given with (8.47) where the assumption is made that $d_{ref} = 0$. If d is large enough, the proportional part may result in r_{ref} so large that the vessel starts rotating or moving spirally towards the line as it is shown in Fig. 8.20(a). In this case the distance to the path is not monotonously decreasing and this presents an unacceptable behavior. The simulation was conducted with $\gamma = 90^\circ$, initial vessel heading $\psi(0) = 90^\circ$ and initial distance from the line $d(0) = 75\text{m}$.

The controller output r_{ref} (blue line) and vessel yaw rate r (red line) are given in Fig. 8.20(b), together with the rudder angle.



(a)



(b)

Figure 8.20. Spiral movement with Method 1: (a) line following, (b) responses.

This problem can be heuristically addressed if the reference heading is demanded to be zero, i.e. $r_{ref}(d, \beta) = 0$. If this is inserted into (8.47), expression (8.55) is obtained, where $\beta \in (-\frac{\pi}{2}, \frac{\pi}{2})$.

$$\sin(\beta) = -\left(\frac{K_{Pd}}{K_{Dd}u_r}d + \frac{\nu}{u_r}\right) \quad (8.55)$$

Equation (8.55) has a solution if and only if

$$\exists \bar{\beta} \in \left(-\frac{\pi}{2}, \frac{\pi}{2}\right) : \left|\frac{K_{Pd}}{K_{Dd}u_r}d + \frac{\nu}{u_r}\right| < \sin \bar{\beta}. \quad (8.56)$$

If maximum absolute value of the sea current ν is denoted with $\bar{\nu}$, and under the assumption that controller parameters and u_r are positive, (8.56) has a solution if

$$|d| < \frac{K_{Pd}}{K_{Dd}} (u_r \sin \bar{\beta} - \bar{\nu}) = \bar{d}. \quad (8.57)$$

Since $|d| > 0$ and $\sin \bar{\beta} < 1$, the trivial solution $\bar{\nu} < u_r$ is embedded. In other words, limiting the value d in (8.47), the heuristic line following control law is

$$r_{ref} = -K_{Pd} \text{sat}(d, -\bar{d}, \bar{d}) - K_{Dd} \dot{d} \quad (8.58)$$

which forces the vessel to approach the target line for large values of $|d|$ with approach angle β such that $r_{ref} = 0$, i.e.

$$\beta = \begin{cases} \arcsin \left(-\sin \bar{\beta} + \frac{\bar{\nu} + \nu}{u_r} \right), & d > \bar{d} \\ \arcsin \left(\sin \bar{\beta} - \frac{\bar{\nu} + \nu}{u_r} \right), & d < -\bar{d} \end{cases},$$

maintaining $\beta \in (-\frac{\pi}{2}, \frac{\pi}{2})$ also in the presence of the effects of measurement noise and underlying system dynamics. It is worth noting that for large values of $|d|$ applying the control law (8.58) is equivalent to requiring value of \dot{d} to be constant.

Using the saturated control law (8.58), path of the vessel shown in Fig. 8.20(a) is now shown in Fig. 8.21(a) from where it is obvious that the approach to the desired line is monotonous at a predefined approach angle $\bar{\beta} = 45^\circ$. The controller output r_{ref} (blue line) and vessel yaw rate r (red line) are given in Fig. 8.21(b), together with the rudder angle.

Indirect actuator control

For the direct actuator control, the proportional channel of the controller must be limited in order to ensure constant approach angle $\beta = \psi - \gamma$ to the line. In indirect actuator control the same has to be ensured in order to avoid paths toward the line as shown in Fig. 8.22(a), where the controller output (blue line), heading of the vessel (red line) and commanded rudder angle are given in 8.22(b). The line following controller for this method is given with (8.52). The simulation was conducted with $\gamma = 90^\circ$, initial vessel heading $\psi(0) = 90^\circ$ and initial distance from the line $d(0) = 70\text{m}$. From Fig. 8.22(b) it is obvious that the vehicle was circling before it converged to the desired path.

Ensuring constant approach angle in this method is much simpler since the controller itself gives commanded heading to the vehicle. In other words, if the maximum desired approach angle is $\bar{\beta}$, the controller output has to be limited so that

$$-\bar{\beta} - \gamma < \psi_{ref} < \bar{\beta} + \gamma.$$

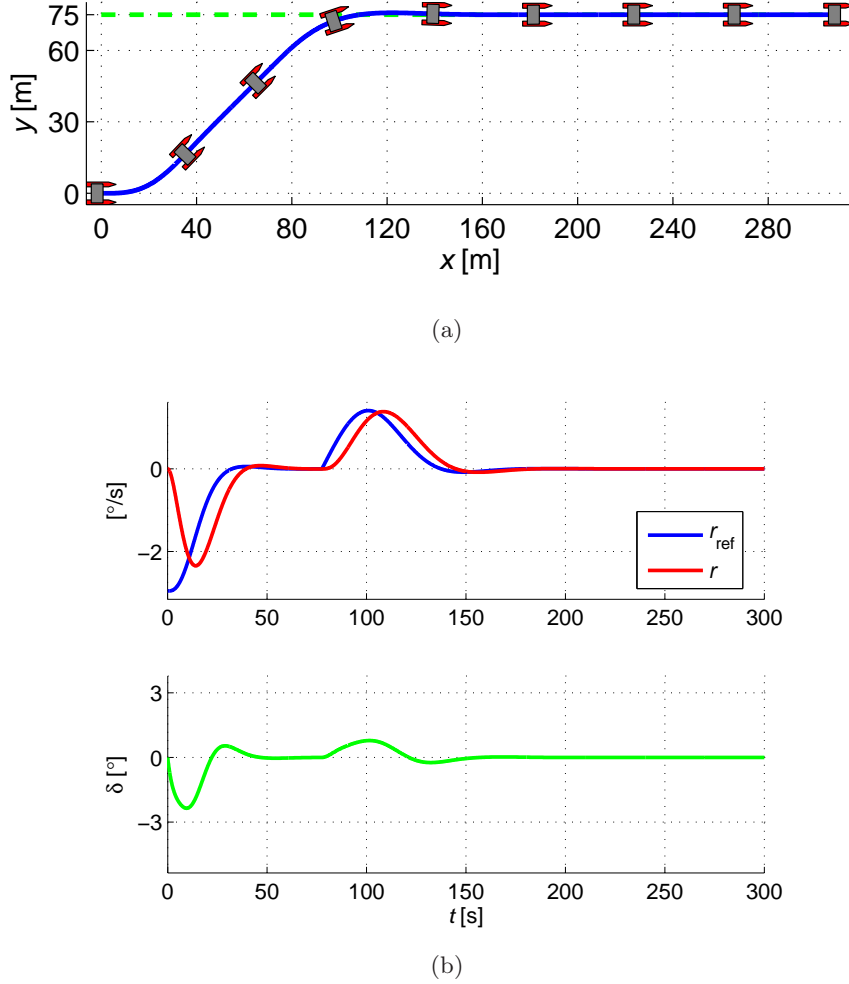
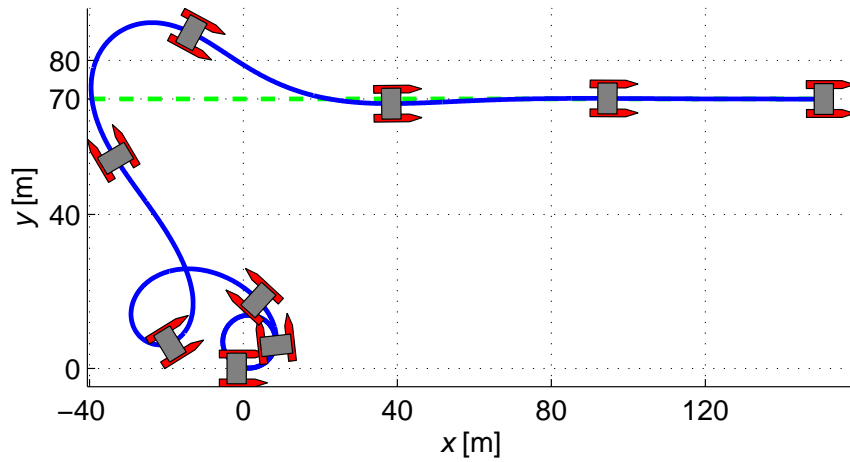


Figure 8.21. Method 1 with limited proportional channel: (a) line following, (b) responses.

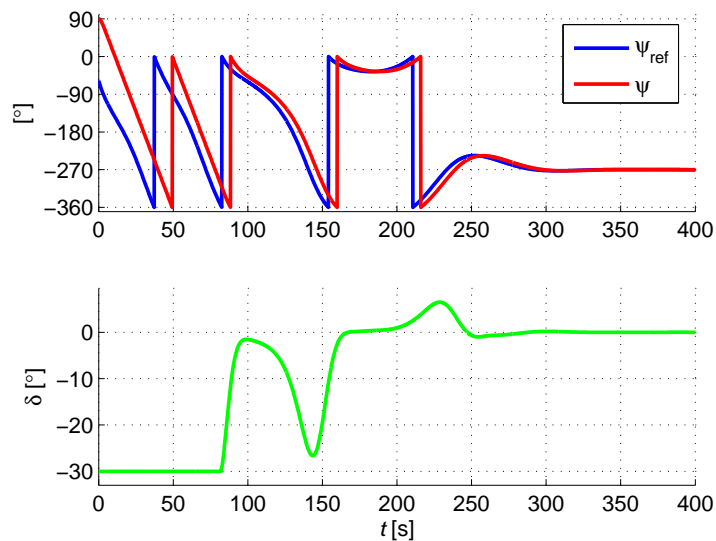
This means that the controller given with (8.52) is in fact

$$\psi_{ref} = sat \left(-K_{\psi}\psi - K_r r - K_d d - K_{Id} \int_0^t d dt, -\bar{\beta} - \gamma, \bar{\beta} + \gamma \right) \quad (8.59)$$

where it is assumed that $d_{ref} = 0$. Since the controller output is limited, it is crucial to perform antiwindup algorithm to the integrating channel as it is described in Chapter 8.1.3. The simulation results using the proposed algorithm for achieving monotonous approach to the path is given in Fig. 8.23(a). Fig. 8.23(b) shows commanded and vessel heading, and the commanded rudder angle.



(a)



(b)

Figure 8.22. Spiral movement with Method 2: (a) line following, (b) responses.

8.3.4 Experimental Results

The experimental results were obtained from autonomous catamaran Charlie. Forward speed was kept almost constant during the experiments by commanding $n^2 = 36[V^2]$. Both direct and indirect actuator control methods were applied and the results are given in the following part.

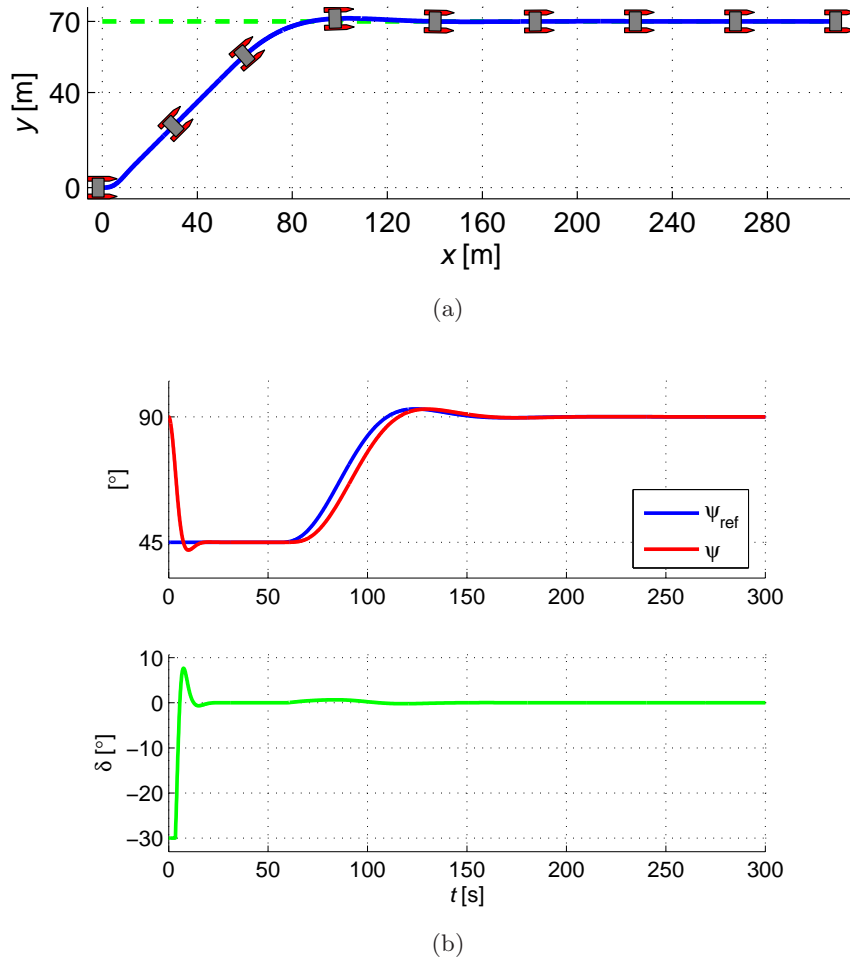


Figure 8.23. Method 2 with limited controller output: (a) line following, (b) responses.

Direct actuator control (Method 1)

The controller parameters for this method were tuned based on yaw degree of freedom model parameters which were identified using the IS–O method. Results of the experiment are given in Chapter 7.5 and the algorithm is given with Algorithm 8.6. The proportional channel of the algorithm was saturated as described in Chapter 8.3.3 so that the approach angle (with $\bar{v} = 0$) is $\bar{\beta} = 30^\circ$.

The obtained path is shown in Fig. 8.24(a) and responses during the path in Fig. 8.24(b).

Indirect actuator control (Method 2)

The controller parameters for this method were tuned using the heading closed loop model parameters which were identified using the IS–O method. As it was already

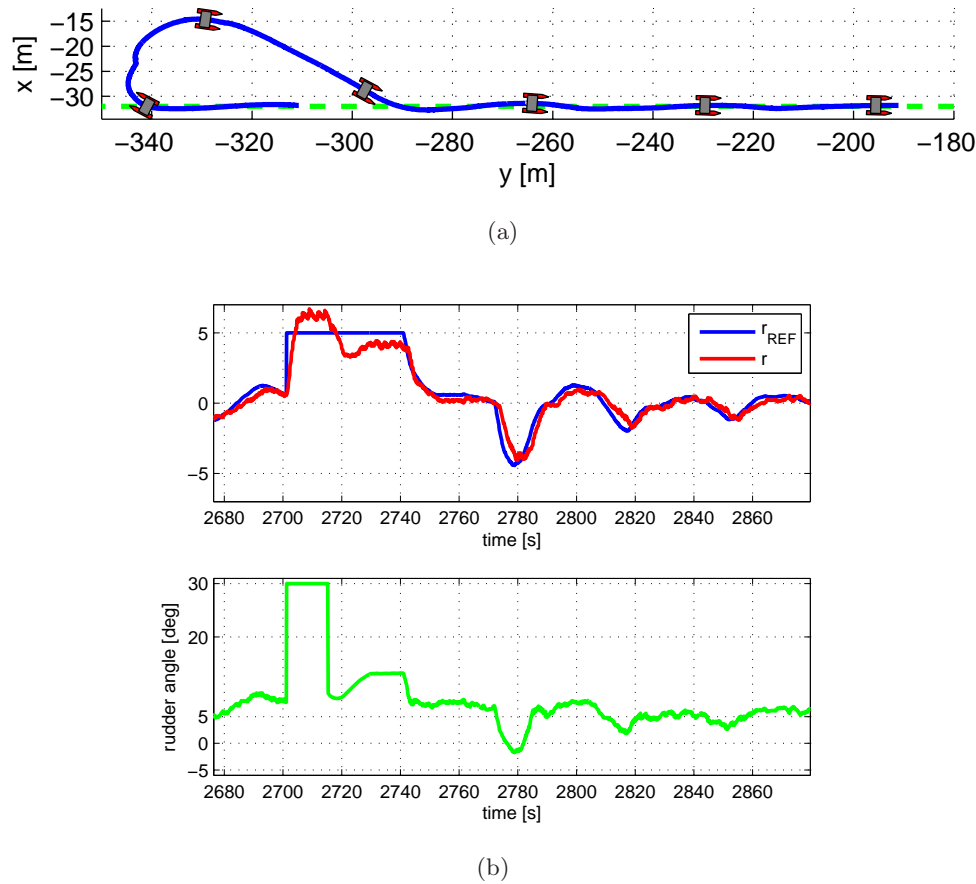


Figure 8.24. Direct actuator control (Method 1): (a) U-turn and line following, and (b) responses.

described in Chapter 7.7, two cases were observed so that Algorithm 8.8 would be tested on two different inner control loop structures:

- Case 1 includes a P-D heading controller and
- Case 2 an I-PD heading controller.

Results of the self-oscillation experiments for Case 1 are given in Fig. 7.7 and in Fig. 7.7 for Case 2. The controller output was saturated as described in Chapter 8.3.3 so that the approach angle is $\beta = 30^\circ$.

The paths for cases 1 and 2 are shown in Fig. 8.25(a) and Fig. 8.26(a), respectively. Corresponding responses are shown in Fig. 8.25(b) and Fig. 8.26(b), respectively. The results show that the rudder activity in the steady state is sufficiently low and that line following is performed without error. This proves that design procedure is valid and can be used regardless of the inner loop structure.

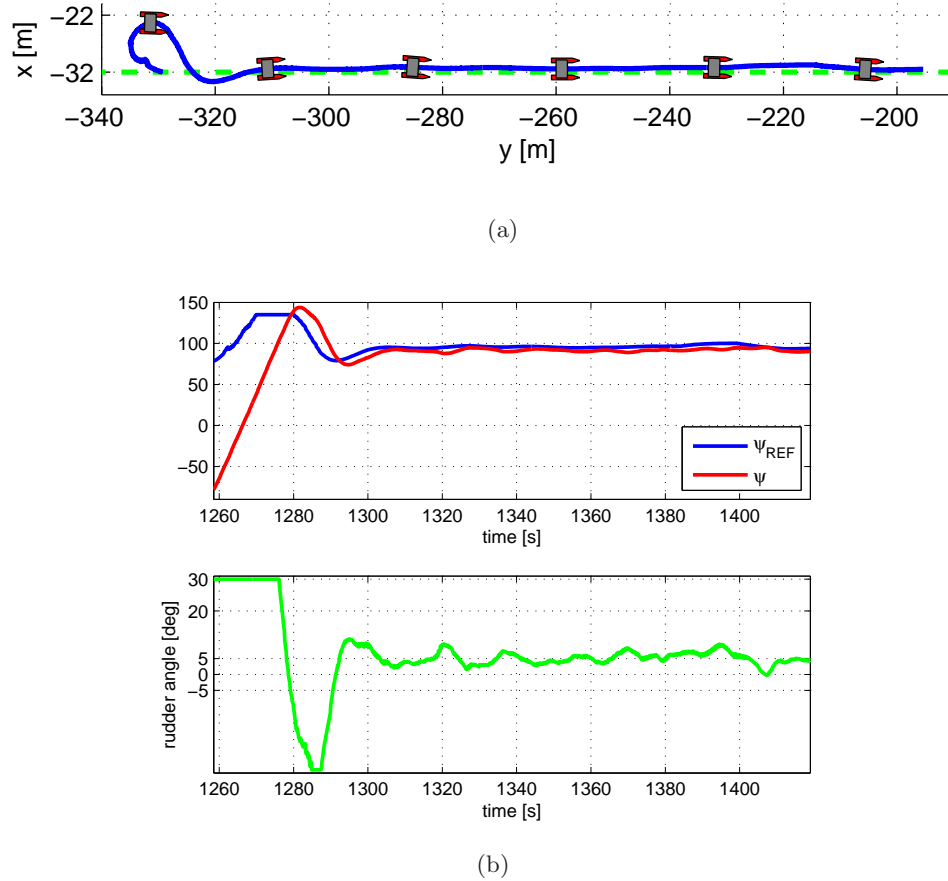
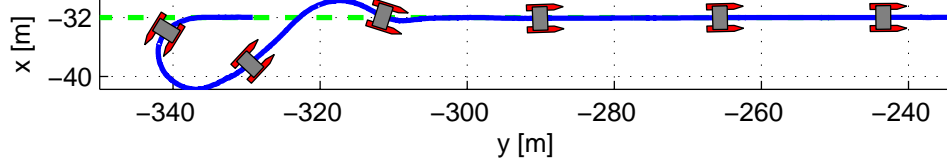


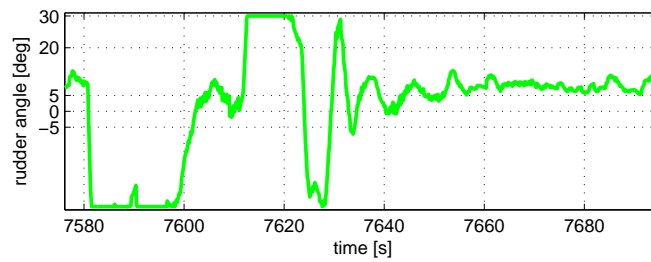
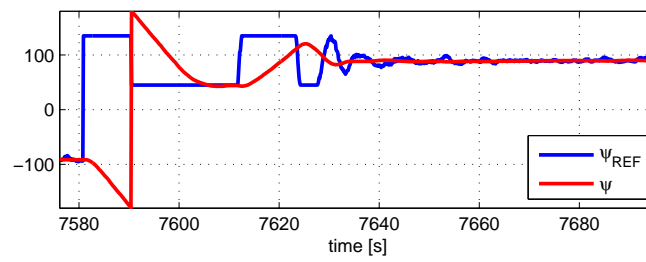
Figure 8.25. Method 2, Case 1: (a) U-turn and line following, (b) responses.

8.3.5 On Choosing the Model Transfer Function

A model transfer function used in controller design for both methods described before has to be chosen appropriately. Given the fact that during transient response rudder is almost always saturated (in order to achieve fast dynamics), the criterion for choosing the model transfer function is rudder activity during steady state. It is required that the rudder activity in steady state is low in order to minimize energy consumption and mechanical stress. Fig. 8.27 clearly demonstrates this issue. First 30s of the response is obtained with model function in Bessel form with characteristic frequency $\omega_c = 0.5\text{s}^{-1}$ ("faster" model). The following part of the response is obtained with model Bessel function with $\omega_c = 0.211\text{s}^{-1}$ ("slower model"). Since the model function describes only input-output behavior of the closed loop, internal signals have to be checked a posteriori. The results were obtained from Charlie USV.



(a)



(b)

Figure 8.26. Method 2, Case 2: (a) U-turn and line following, (b) responses.

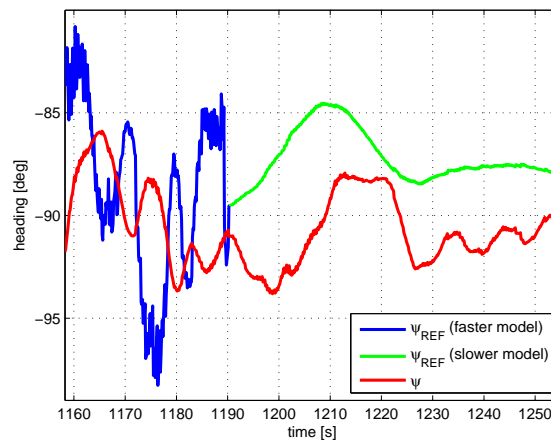


Figure 8.27. Rudder activity for two different model functions.

Conclusion

The area of marine robotics is characterized by complex mathematical modeling of hydrodynamic effects and highly unpredictable environmental influences. The problems of guidance and control of marine vessels in real life conditions has to address these issues. Prior to designing control structures, a reasonably accurate model of the vessel has to be known. Since the dynamics of the vessels may change during operation due to different payload suites, a need for quick identification method which is feasible in field conditions is needed. This thesis presents a method for identifying system parameters based on self-oscillations. The self-oscillations are in fact a usual procedure in the well known "zig-zag" experiment used to determine ships manoeuvring capabilities. However, the proposed methodology is used for identifying nonlinear drag and is applied to underwater vehicles.

The conclusions have been raised throughout the thesis at the end of each chapter, summarizing basic ideas which had been presented. The mathematical models for marine vehicles are given and their simplifications which are appropriate for control design are derived. These simplifications are given for small surface, rudder-actuated vehicles and unmanned underwater vehicles. In addition to that, mathematical modeling of distance keeping and line following for underactuated marine vehicles is presented.

The thesis' emphasis is on the application of the described algorithms on real vehicles, hence models and technical characteristics of three case study vehicles have been described: a micro remotely operated underwater vehicle (VideoRay), a small autonomous underwater vehicle (AutoMarine) and a small unmanned surface vehicle (Charlie). In addition to that, two vision-based sensor suites are presented: laser distance module and laboratory apparatus for mathematical model parameters identification.

In order to make a comparison between the proposed identification method based on self-oscillations (IS-O), three conventional methods for identification of marine vehicle's parameters have been presented with their advantages and disadvantages: the least-squares algorithm, open loop step response technique and the "zig-zag" manoeuvre.

The proposed IS-O method is based on self-oscillations, so the theory of harmonic

linearization is briefly presented. Three theorems and two lemmas which are relevant to application of the method on marine vehicles are given and proved. The IS–O method is described in detail, for a class of nonlinear systems, and a generalized matrix algorithm is given for static (Type 0) systems. The modifications of the proposed methodology for discrete–time systems, systems with delays and astatic (Type k) systems enable the use of the IS–O method on marine vehicles. This application is described on case studies of identifying yaw, surge and heave models, together with identifying closed loop heading systems.

The basis of the thesis are the experiments which have been performed on real vehicles in order to prove that the proposed methodology is applicable on real marine vehicles. Extensive experimental results are presented for

- identifying yaw DOF of VideoRay ROV (comparison with the least–squares method is given),
- identifying yaw DOF of AutoMarine AUV (comparison with the open loop step response method is given), and
- identifying yaw DOF of Charlie USV (comparison of two day trial results with the least–squares method is given).

These results have proven that the IS–O method gives sufficiently accurate identification results, with significantly lower experiment duration time. As a consequence, the method is advised to be used in situations where quick in the field identification is necessary. The experimental results which have been obtained solely for control design purposes are

- identifying surge DOF of VideoRay ROV (used for distance controller tuning) and
- identifying heading closed loop of Charlie USV (used for line following controller tuning).

Having said that, the reason for identification of mathematical model parameters lies in the necessity for tuning controllers. The thesis presents low level controllers which are tuned on the basis of the IS–O method. Stability analysis resulted in slight modifications to the conventional controllers, which ensure robust and structural stability of the closed loop systems. In the thesis, two methods for design and tuning of line following controllers is presented, based on the available actuation signals. To sum up, the IS–O method results have been used for:

- tuning of heading controllers (applied to Charlie USV),
- tuning of the Kalman filter parameters (applied to VideoRay ROV) which is used to estimate unmeasurable states or unavailable measurements,

- tuning of distance keeping controllers (applied to VideoRay ROV), and
- tuning of line following controllers in the cases when direct actuator control is available and when it is not (applied to Charlie USV).

The dissertation includes 10 descriptive examples which should help the interested reader in understanding the matter.

The original scientific contributions of the thesis are:

1. Identification of the hydrodynamic drag, mass and inertia of the nonlinear marine vessel mathematical model on the basis of transient response.
2. Matrix based algorithm for determining parameters of linear time invariant static (Type 0) and astatic (Type k) systems, discrete-time systems and systems with delays by the use of self-oscillations.
3. Experimentally verified procedure for parameter identification of a class of affine nonlinear models by the use of self-oscillations and its application on marine vehicles (surface and underwater).
4. Design of nonlinear autopilots by the use of self-oscillations and ensuring structural stability of marine vehicles' control system.
5. Design of the line following controllers by the use of self-oscillations.
6. Design of the distance-keeping controllers by the use of self-oscillations.
7. Experimental accuracy analysis of the identification method based on the use of self-oscillations.

-
- [1] 14th ITTC. Discussions and recommendations for an ittc 1975 maneuvering trial code. *14th International Towing Tank conference*, pages 248–365, 1975.
- [2] A. Abkowitz. Lectures on ship hydrodynamics steering and maneuverability. Technical Report Report No. Hy-5, Hydrodynamics Department Hydro-og Aerodynamics Laboratorium, Lyngby, Denmark, 1964.
- [3] S. Al-Hasan and G. Vachtsevanos. Intelligent route planning for fast autonomous vehicles operating in a large natural terrain. *Robotics and Autonomous Systems*, 40(1):1 – 24, 2002.
- [4] K.J. Åström and T. Hägglund. Automatic tuning of simple regulators with specifications on phase and amplitude margins. *Automatica*, 20(5):645 – 651, 1984.
- [5] M. Barbier and E. Chanthery. Autonomous mission management for unmanned aerial vehicles. *Aerospace Science and Technology*, 8(4):359 – 368, 2004.
- [6] M. Barisic, Z. Vukic, and N. Miskovic. Heuristic parameter tuning procedures for a virtual potential based AUV trajectory planner. *Proceedings of the 8th IFAC International Conference on Manoeuvring and Control of Marine Craft*, 2009.
- [7] M. Barisic, Z. Vukic, N. Miskovic, and S.P. Kragelund. A MOOS-based on-line trajectory re-planning system for AUVs. In *OCEANS 2009-EUROPE, 2009. OCEANS '09.*, pages 1 – 6, May 2009.
- [8] A. Besançon-Voda and H. Roux-Buisson. Another version of the relay feedback experiment. *Journal of Process Control*, 7(4):303 – 308, 1997.
- [9] M. Bibuli, M. Caccia, and L. Lapierre. Path-following algorithms and experiments for an autonomous surface vehicle. In *Proc. of IFAC Conference on Control Applications in Marine Systems*, Bol, Croatia, September 2007.
- [10] M. Caccia. Autonomous Surface Craft: prototypes and basic research issues. In *Proc. of IEEE 14th Mediterranean Conference on Control and Automation*, Lisbon, Portugal, September 2006.
- [11] M. Caccia. Laser-triangulation optical-correlation sensor for ROV slow motion estimation. *IEEE Journal of Oceanic Engineering*, 31(3):711–727, 2006.
- [12] M. Caccia, M. Bibuli, R. Bono, and G. Bruzzone. Basic navigation, guidance and control of an Unmanned Surface Vehicle. *Autonomous Robots*, 25(4):349–365, 2008.

-
- [13] M. Caccia, R. Bono, G. Bruzzone, G. Bruzzone, E. Spirandelli, G. Veruggio, A. Stortini, and G. Capodaglio. Sampling sea surface with SESAMO. *IEEE Robotics and Automation Magazine*, 12(3):95–105, 2005.
- [14] M. Caccia, G. Bruzzone, and R. Bono. Modelling and identification of the Charlie2005 ASC. *Proc. of IEEE 14th Mediterranean Conference on Control and Automation*, 2006.
- [15] M. Caccia, G. Bruzzone, and R. Bono. A practical approach to modeling and identification of small autonomous surface craft. *IEEE Journal of Oceanic Engineering*, 2008. DOI: 10.1109/JOE.2008.920157.
- [16] M. Caccia, G. Casalino, R. Cristi, and G. Veruggio. Acoustic motion estimation and control for an unmanned underwater vehicle in a structured environment. *Control Engineering Practice*, 6(5):661–670, 1998.
- [17] M. Caccia, G. Indiveri, and G. Veruggio. Modelling and identification of open-frame variable configuration unmanned underwater vehicles. *IEEE Journal of Oceanic Engineering*, 25(2):227–240, 2000.
- [18] M. Caccia and G. Veruggio. Guidance and control of a reconfigurable unmanned underwater vehicle. *Control Engineering Practice*, 8(1):21–37, 2000.
- [19] R.C. Chang, S.H. Shen, and C.C. Yu. Derivation of transfer function from relay feedback systems. *Industrial & Engineering Chemistry Research*, 31(3):855–860, 1992.
- [20] H.-H. Chen. Vision-based tracking with projective mapping for parameter identification of remotely operated vehicles. *Ocean Engineering*, 35(10):983 – 994, 2008.
- [21] M. Chyba, T. Haberkorn, R.N. Smith, and S.K. Choi. Design and implementation of time efficient trajectories for autonomous underwater vehicles. *Ocean Engineering*, 35(1):63 – 76, 2008.
- [22] D. Clarke. The foundations of steering and maneuvering. *Proc. of IFAC Conference on Maneuvering and control of marine crafts (MCMC'2003)*, pages 2 – 16, 2003.
- [23] J. Curcio, J. Leonard, and A. Patrikalakis. SCOUT - A low cost autonomous surface platform for research in cooperative autonomy. In *Proceedings of MTS/IEEE OCEANS, 2005.*, Washington D.C., USA, September 2005.
- [24] T. N. Delmer, T. C. Stephens, and J. M. Coe. Numerical simulation of towed cables. *Ocean Engineering*, 10(2):119 – 132, 1983.
- [25] T.I. Fossen. *Guidance and Control of Ocean Vehicles*. John Wiley & Sons, England, 1994.

-
- [26] R. Galeazzi and M. Blanke. On the feasibility of stabilizing parametric roll with active bifurcation control. In *Proc. 6th IFAC Conference on Control Applications in Marine Systems, CAMS'2007*, 2007.
- [27] R. Galeazzi, M. Blanke, and N. K. Poulsen. Parametric roll resonance detection using phase correlation and log-likelihood testing techniques. In *Proc. 8th IFAC International Conference on Manoeuvring and Control of Marine Craft, MCMC'2009*, pages 316–321, 2009.
- [28] C. C. Hang, Q. G. Wang, and L. S. Cao. Self-tuning Smith predictors for processes with long dead time. *International Journal of Adaptive Control and Signal Processing*, 9(3):255–270, 1995.
- [29] Y. il Lee, Y.-G. Kim, and L. J. Kohout. An intelligent collision avoidance system for AUVs using fuzzy relational products. *Information Sciences*, 158:209–232, 2004.
- [30] J. M. J. Journée. A simple method for determining the manoeuvring indices K and T from zigzag trial data. Technical Report 0267, Delft University of Technology, Ship Hydromechanics Laboratory, Delft, Netherlands, 2001.
- [31] G.C. Karras and K.J. Kyriakopoulos. Localization of an underwater vehicle using an imu and a laser-based vision system. In *Mediterranean Conference on Control Automation, 2007. MED '07.*, pages 1–6, June 2007.
- [32] G.C. Karras, D.J. Panagou, and K.J. Kyriakopoulos. Target-referenced localization of an underwater vehicle using a laser-based vision system. In *OCEANS 2006*, pages 1–6, Sept. 2006.
- [33] I. Kaya and D. P. Atherton. Parameter estimation from relay autotuning with asymmetric limit cycle data. *Journal of Process Control*, 11(4):429–439, 2001.
- [34] Y. H. Kim. PI controller tuning using modified relay feedback method. *Journal of Chemical Engineering of Japan*, 28(1):118–121, 1995.
- [35] R. Prasanth Kumar, A. Dasgupta, and C.S. Kumar. Real-time optimal motion planning for autonomous underwater vehicles. *Ocean Engineering*, 32(11–12):1431–1447, 2005.
- [36] H. J. Kwak, W. S. Sung, and I.-B. Lee. On-line process identification and autotuning for integrating processes. *Industrial & Engineering Chemistry Research*, 36(12):5329–5338, 1997.
- [37] L. Lapierre, D. Soetanto, and A. Pascoal. Nonlinear path following with the applications to the control of autonomous underwater vehicles. In *Proc. of 42nd IEEE Conference on Decision and Control*, pages 1256–1261, 2003.

-
- [38] E. V. Lewis. *Principles of Naval Architecture*, volume 3. The Society of Naval Architects and Marine Engineers, 2nd edition, 1989.
- [39] F.L. Lewis and V.L. Syrmos. *Optimal Control*. John Wiley & Sons, Inc., New York, NY, USA, 1995.
- [40] Jia-Wang LI, Bao-Wei SONG, and Cheng SHAO. Tracking control of autonomous underwater vehicles with internal moving mass. *Acta Automatica Sinica*, 34(10):1319–1323, 2008.
- [41] W. Li, E. Eskinat, and W. L. Luyben. An improved autotune identification method. *Industrial & Engineering Chemistry Research*, 30(7):1530–1541, 1991.
- [42] L. Ljung. *System Identification – Theory for the User*. Prentice Hall, 2nd edition, 1999.
- [43] E. López, F.J. Velasco, E. Moyano, and T.M. Rueda. Full-scale manoeuvring trials simulation. *Journal of Maritime Research*, 1(3):37–50, 2004.
- [44] W. L. Luyben. Derivation of transfer functions for highly nonlinear distillation columns. *Industrial & Engineering Chemical Research*, 26(12):2490–2495, 1987.
- [45] J. Majohr and T. Buch. *Advances in unmanned marine vehicles*, chapter Modelling, simulation and control of an autonomous surface marine vehicle for surveying applications Measuring Dolphin MESSIN, pages 329–352. IEE Control Series, 2006.
- [46] J. Manley. Development of the autonomous surface craft ACES. *Proceedings of MTS/IEEE Conference OCEANS’97*, 2:827–832, 1997.
- [47] J. Manley, A. Marsh, W. Cornforth, and C. Wiseman. Evolution of the autonomous surface craft AutoCat. *Proceedings of MTS/IEEE Conference and Exhibition OCEANS 2000*, 1:403–408, 2000.
- [48] A. Martins, J.M. Almeida, E.P. Silva, and F.L. Pereira. Vision-based autonomous surface vehicle docking manoeuvre. In *Proc. of 7th IFAC Conference on Manoeuvring and Control of Marine Craft*, Lisbon, Portugal, September 2006.
- [49] N. Minorski. Directional stability of automatic steered bodies. *Journal of the American Society for Naval Engineers*, 34(2):280–309, 1922.
- [50] N. Miskovic and Z. Vukic. Feedback linearization, 2009. Lecture notes.
- [51] N. Miskovic, Z. Vukic, and M. Barisic. Identification of coupled mathematical models for underwater vehicles. In *Proceedings of OCEANS 2007 - Europe*, pages 1–6, 2007.

-
- [52] N. Miskovic, Z. Vukic, and M. Barisic. Transfer function identification by using self-oscillations. *Proc. of the 15th Mediterranean Conference on Control and Applications*, 2007.
- [53] N. Miskovic, Z. Vukic, and M. Barisic. Identification of unmanned underwater vehicles by self-oscillation method. *AUTOMATIKA – Journal for control, measurement, electronics, computing and communications*, 3-4:167–183, 2009.
- [54] N. Miskovic, Z. Vukic, and M. Barisic. *Intelligent Underwater Vehicles*, chapter Identification of Underwater Vehicles for the Purpose of Autopilot Tuning, pages 327–346. InTech Education and Publishing, Vienna, 2009.
- [55] N. Miskovic, Z. Vukic, M. Barisic, and P.P. Soucacos. AUV identification by use of self-oscillations. Bol, Croatia, 2007.
- [56] N. Miskovic, Z. Vukic, M. Barisic, and B. Tovornik. Autotuning autopilots for micro-ROVs. In *Proc. of the 14th Mediterranean Conference on Control and Automation, 2006. MED '06.*, pages 1–6, 2006.
- [57] N. Miskovic, Z. Vukic, M. Bibuli, M. Caccia, and G. Bruzzone. Marine vehicles' line following controller tuning through self-oscillation experiments. In *Proc. of the 17th Mediterranean Conference on Control and Automation*, Thessaloniki, Greece, 2009.
- [58] N. Miskovic, Z. Vukic, and E. Omerdic. Control of UUVs based upon mathematical models obtained from self-oscillations experiments. *Proc. of the NGCUV'08 Conference*, 2(1), 2008.
- [59] N. Miskovic, Z. Vukic, I. Petrovic, and M. Barisic. Distance keeping for underwater vehicles - tuning Kalman filters using self-oscillations. In *Proc. of the OCEANS 2009-EUROPE*, pages 1–6, 2009.
- [60] N. Mišković, M. Bibuli, G. Bruzzone, M. Caccia, and Z. Vukić. Tuning marine vehicles' guidance controllers through self-oscillation experiments. *Proceedings of the MCMC'09 Conference*, 2009.
- [61] L. Moreira, T. I. Fossen, and C. Guedes Soares. Path following control system for a tanker ship model. *Ocean Engineering*, 34(14-15):2074–2085, 2007.
- [62] K. Nomoto. Analysis of Kempf's standard manoeuvre test and proposed steering quality indices. *First Symposium on Ship Manoeuvrability*, October 1960.
- [63] N. H. Norrbin. On the design and analysis of the zig-zag test on base of quasi linear frequency response. Technical Report B104–3, The Swedish State Shipbuilding Experimental Tank, Gothenberg, Sweden, 1963.

-
- [64] SNAME The Society of Naval Architects and Marine Engineers. Nomenclature for treating the motion of a submerged body through a fluid. *Technical and Research Bulletin*, 1-5, 1950.
- [65] E. Omerdic. *Thruster fault diagnosis and accommodation for overactuated open-frame underwater vehicles*. PhD thesis, University of Wales College, Newport, United Kingdom, 2002.
- [66] F. A. Papoulias. Guidance and control laws for vehicle pathkeeping along curved trajectories. *Applied Ocean Research*, 14(5):291–302, 1992.
- [67] T. Perez and M. Blanke. Mathematical ship modelling for marine applications. Technical report, Technical University of Denmark, 2002.
- [68] F. Repoulias and E. Papadopoulos. Planar trajectory planning and tracking control design for underactuated AUVs. *Ocean Engineering*, 34(11-12):1650–1667, 2007.
- [69] P. Ridaou, J. Batlle, and M. Carreras. Model identification of a low-speed UUV with on-board sensors. In *Proc. of IFAC conference Control applications in marine systems, CAMS 2001*, Glasgow, Scotland, United Kingdom, 2001.
- [70] P. Ridaou, A. Tiano, A. El-Fakdi, M. Carreras, and A. Zirilli. On the identification of non-linear models of unmanned underwater vehicles. *Control Engineering Practice*, 12:1483–1499, 2004.
- [71] G. N. Roberts and R. Sutton. *Advances in Unmanned Marine Vehicles*, chapter Editorial: Navigation, guidance and control of unmanned marine vehicles, pages 1–12. IEE Control Series, 2006.
- [72] E. A. Sperry. Automatic steering. *Transactions: Society of Naval architects and Marine Engineers*, pages 53–61, 1922.
- [73] M. Stipanov. Autonomization of the VideoRay Pro II remotely operated submersible. Diploma thesis, University of Zagreb, Faculty of Electrical Engineering and Computing, 2007. (in Croatian).
- [74] M. Stipanov, N. Miskovic, Z. Vukic, and M. Barisic. ROV autonomization – yaw identification and Automarine module architecture. *Proc. of the CAMS'07 Conference*, 2007.
- [75] K. K. Tan, T. H. Lee, and Q. G. Wang. An enhanced automatic tuning procedure for PI/PID controllers for process control. *American Institute of Chemical Engineers Journal*, 42(9):2555–2562, 1996.
- [76] Z. Vukic. A tutorial on adaptive control: The self-tuning approach. Lecture notes, 2000.

-
- [77] Z. Vukic and Lj. Kuljaca. *Automatic Control – Analysis of Linear Systems*. Kigen, Zagreb, 2005. (in Croatian).
- [78] Z. Vukic, Lj. Kuljaca, D. Donlagic, and S. Tesnjak. *Nonlinear Control Systems*. Marcel Dekker, New York, 2003.
- [79] L. Wang, M. L. Desarmo, and W. R. Cluett. Real-time estimation of process frequency response and step response from relay feedback experiments. *Automatica*, 35(8):1427–1436, 1999.
- [80] Q. G. Wang, C. C. Hang, and Q. Bi. Process frequency response estimation from relay feedback. *Control Engineering Practice*, 5(9):1293–1302, 1997.
- [81] Q. G. Wang, C. C. Hang, and B. Zou. Low order modeling from relay feedback. *Industrial & Engineering Chemistry Research*, 36(2):375–381, 1997.
- [82] G. Welch and G. Bishop. *An Introduction to the Kalman filter*. University of North Carolina, Chapell Hill, 2006.
- [83] T. Xu, J. Chudley, and R. Sutton. Soft computing design of a multi-sensor data fusion system for an unmanned surface vehicle navigation. In *Proc. of 7th IFAC Conference on Manoeuvring and Control of Marine Craft*, Lisbon, Portugal, September 2006.

-	logical negation or mean value
•	variables regarding some conventional identification method
\cdot_{calib}	calibration parameters for the vision-based laser distance module
◦	variables regarding the novel IS-O identification method
\sim	identified parameter or an estimate
\wedge	logical AND operator
\cdot_{ref}	reference value
$\hat{}$	the predicted value
$\mathbf{A}(\mathbf{k})$	the extended Kalman filter state matrix
B	buoyancy
$\{B\}$	body-fixed coordinate frame
C	output value of the relay
$\mathbf{C}_A(\mathbf{v})$	the added-mass Coriolis and centripetal matrix
\mathbf{C}_{RB}	rigid-body Coriolis and centripetal matrix
CG	center of gravity
CP	centre of pressure
C_T	constant parameter
D	forward distance of from the flat surface (in distance keeping applications)
$\mathbf{D}(\mathbf{v})$	total hydrodynamic damping matrix
$\hat{\mathbf{E}}$	the vector of prediction errors
$\{E\}$	Earth-fixed coordinate frame
$F(x)$	function describing a static nonlinear element
F_d	nonlinear characteristic acting on the falling input signal
F_u	nonlinear characteristic acting on the rising input signal
$G_L(p)$	transfer function of the linear part of the process
G_N	the describing function of the nonlinear element
$\mathbf{H}(\mathbf{k})$	the Kalman filter measurement matrix
\mathbf{I}_0	inertia tensor with respect to $\{B\}$
$\mathbf{I}_{n \times n}$	identity matrix of size n
I_i	moment of inertia about arbitrary axis i
I_{ij}	product of inertia
$\mathbf{J}, \mathbf{J}_1, \mathbf{J}_2$	matrices used in the kinematic model
$J(\hat{\theta})$	the least-squares criterion function
K	roll moment
K_I, K_P, K_D	integral, proportional and derivative controller gains
K_{ss}	the steady-state value
L	distance from the rudder to the center of mass

L_L, L_R	distances from the left and right laser beam to the flat surface
M	pitch moment
\mathbf{M}_A	the added-mass matrix
\mathbf{M}_{RB}	rigid-body inertia matrix
N	yaw moment
\mathbf{P}, \mathbf{Q}	vectors of real and imaginary parts of the describing function obtained during experiments
P_N	real part of the describing function
$\mathbf{Q}_{KF}, \mathbf{P}_0, \mathbf{R}$	the Kalman filter covariance matrices
Q_N	imaginary part of the describing function
$R(t)$	reference value
$S(t)$	step input (the Heaviside function)
T_L	linear system equivalent time constant
T_N	nonlinear system equivalent time constant
T_S	sampling time
T_d	time delay
U	absolute speed of the vessel
W	weight
X	surge force
X_m	magnitude of self-oscillations
Y	sway force
\mathbf{Y}	the vector of measurements
Y_0, Y_{Pk}, Y_{Qk}	Fourier series decomposition coefficients of the output of the nonlinear element
Z	heave force
Δ	disturbance acting at the input of the process (or constant signal at the output of the nonlinear element)
Φ	angle of the vessel with regard to the flat surface (in distance keeping applications)
Φ	the matrix of regressors
Θ	vectors of unknown parameters
$\theta(k)$	the vector of unknown parameters
Θ_K	vector containing controller parameters
α_ν	single degree of freedom generalized inertia parameter
$\beta(\nu(t))$	single degree of freedom generalized drag parameter
β_ν	single degree of freedom constant drag parameter
$\beta_{\nu\nu}$	single degree of freedom linear drag parameter
δ	rudder angle
δ_a	attack angle
δ_f	angle of the flow in the body-fixed reference frame
δ_s	stall angle

$\hat{\varepsilon}(k)$	prediction error
ε	number of experiments
ε_v	the velocity error
η	6-by-1 vector of positions and orientations
η_1	3-by-1 vector of positions
η_2	3-by-1 vector of orientations
$\eta(t)$	single degree of freedom position or orientation variable
γ	orientation of the straight line in the line following model
λ	robustness parameter in the model decision making process
v	6-by-1 vector of linear and angular velocities
v_1	3-by-1 vector of linear velocities
v_2	3-by-1 vector of angular velocities
$\nu(t)$	single degree of freedom velocity variable
ω	frequency of self-oscillations
ω	vector of frequencies of self-oscillations obtained during experiments
ϕ	roll angle
$\Phi(k)$	the regression vector
φ	angle with regard to a flat surface (in the distance keeping model) or with regard to a line (in the line following model)
ψ	yaw angle (heading)
ρ_A	the mass density of the body
$\sigma_{\%}$	standard deviation
τ_{RB}	the generalized vector of forces and moments
τ	6-by-1 vector of forces and moments acting on the rigid body
τ^i	vector consisting of commanded thrusts for each actuator
$\tau(t)$	single degree of freedom force or moment variable
τ^i	thrust generated by the i -th actuator
$\tau.E$	single degree of freedom external disturbance
τ_{min}, τ_{max}	upper and lower saturation limit of the input signal
θ	pitch angle
a_f, a_b, b_f, b_b	thruster coefficients
a_i, b_i	linear process transfer function parameters
$a_i.$	parameters of the model transfer function
$a_{i\psi}, b_{i\psi}$	heading closed loop transfer function parameters
$a_{thruster}, b_{thruster}$	thruster coefficients
$a_{u,n}, a_{d,n}$	Taylor series coefficients of the nonlinear function
c_F	rudder coefficient
d	distance from a flat surface (in the distance keeping model) or from a line (in the line following model)
d_{DM}	distance between the left and the right laser

$f(\cdot)$	general nonlinear process
$f_0(\cdot), f_R(\cdot), f_I(\cdot)$	coefficients of the general nonlinear process development into Fourier series
$\mathbf{g}(\boldsymbol{\eta})$	vector of restoring forces
k_{r1}, k_{r2}	constant parameters used for modeling the thrust exerted by the rudder
m	mass
\mathbf{n}^i	vector consisting of commanded inputs for each actuator
n^i	commanded input for the i -th actuator
p	roll speed and the differential operator
p_x	relative error between the real and the identified parameter x
q	pitch speed
q^i	moment generated by the i -th actuator
q^{-1}	backward discrete operator
r	yaw speed
\mathbf{r}_G	centre of gravity with respect to $\{B\}$
u	surge speed
\dot{u}^\diamond	integral of measured speed
u_a	ambient water velocity
u_r	constant surge speed in the line following model
u_{wake}	wake speed
v	sway speed
v_d, v_φ	disturbances in the distance keeping model
v_l	disturbance perpendicular to the line in the line following model
v_{av}	average flow passing through the rudder
w	heave speed
x	absolute position with regard to the N -axis of the $\{E\}$ frame
$x(t)$	signal at the input of the nonlinear element
x^*	monoharmonic component of the signal $x(t)$
x_0	biased component of the signal $x(t)$
x_L, x_R	distances of the left and the right laser dot from the central vertex within the acquired image
x_a	width of the hysteresis
x_a^*	modified hysteresis width
y	absolute position with regard to the E -axis of the $\{E\}$ frame
$y(t)$	process output
$y_N(t)$	output from the nonlinear element
z	depth
IS-O	identification by use of self-oscillations
L-S	least-squares
SR	step response

Use of Self-Oscillations in Guidance and Control of Marine Vessels

This dissertation presents an identification method based on self-oscillations (IS-O) used for the purpose of guidance and control of marine vessels (underwater and surface). The proposed method is described for a general class of nonlinear systems and a general, matrix based algorithm is given for static (Type 0) linear time invariant systems with its modification for discrete-time systems, astatic systems (Type k) and systems with delays. Special attention is devoted to a class of affine nonlinear system models which are used to describe the dynamics of marine vehicle. The main advantage of the proposed method is its applicability during in the field operation and time parsimony. The IS-O method is experimentally tested on two unmanned underwater vehicles and an unmanned surface marine vessel, and comparison to conventional identification methods is given, proving the accuracy of the proposed method on real marine vehicles operating in the field conditions. The identification results are used for the design of heading controllers, distance keeping controllers and line following controllers. Experimental results obtained from real marine vehicles are presented in the thesis.

Keywords: marine vessels, unmanned underwater vehicles, unmanned surface vehicles, nonlinear systems, identification, self-oscillations, control and guidance of marine vehicles, line following, distance keeping

Primjena vlastitih oscilacija u vođenju i upravljanju plovilima

Ova disertacija predstavlja identifikacijsku metodu temeljenu na vlastitim oscilacijama (IVO) koja se koristi u svrhu vođenja i upravljanja plovilima (podvodnim i površinskim). Predloženi postupak je opisan za opću klasu nelinearnih sustava i dan je opći algoritam, temeljen na matričnom zapisu, za statičke linearne vremenski nepromjenjive sustave uz modifikacije za diskretne sustave, astatičke sustave i sustave s transportnim kašnjenjem. Posebna je pažnja posvećena klasi afinih nelinearnih modela sustavâ koji se koriste za opis dinamike plovila. Glavna prednost predložene metode je primjenjivost tijekom rada na terenu i vremenska štedljivost. IVO postupak je eksperimentalno ispitan na dvije bespilotne ronilice i bespilotnom površinskom plovilu, i dana je usporedba sa konvencionalnim identifikacijskim postupcima, koja dokazuje točnost predloženog postupka na stvarnim plovilima koja rade u terenskim uvjetima. Rezultati identifikacije su iskorišteni za projektiranje regulatorâ kursa, regulatorâ udaljenosti i regulatorâ za praćenje linije. Eksperimentalni rezultati dobiveni na stvarnim plovilima su prezentirani u disertaciji.

Ključne riječi: plovila, bespilotne ronilice, bespilotna površinska plovila, nelinearni sustavi, identifikacija, vlastite oscilacije, vođenje i upravljanje plovilima, praćenje linije, držanje udaljenosti

I was born on 17 March 1982 in Zagreb where in 2000 I finished the V. natural science and mathematics high school. The same year, I enrolled the Faculty of Electrical Engineering and Computing (FER) at the University of Zagreb. In 2003 the Faculty council appointed me to finish the diploma studies with emphasis on scientific research. I obtained my diploma in February with a 4.87 average (out of 5) with the topic on fault tolerant control of unmanned underwater vehicles, under the supervision of Prof. Zoran Vukić. The same year in March I enrolled in postgraduate studies at FER where I am employed as a research and teaching assistant. I passed the qualifying doctoral exam and the public talk in July 2007 and March 2008, respectively.

From 2001 until 2003, I received a scholarship for especially gifted students by the Croatian Ministry of Science, Education and Sports, and from 2003 until 2005 a scholarship by the City of Zagreb. The Faculty council of FER awarded me with three recognitions Josip Lončar for the second, third and fourth year of my diploma studies. From January until April 2008, I was doing research at the Consiglio Nazionale delle Ricerche in Genoa, Italy funded by a scholarship by the Governments of the Republic of Italy and the Republic of Croatia. In 2008 I was awarded with the scholarship for excellent postgraduate students from the "prof. Zlata Bartl" foundation (founded by the "Podravka" company). In the Workshop on Navigation, Guidance and Control of Underwater Vehicles held in Limerick, Ireland in 2008 I was awarded with the best student paper presentation award. In March 2009 I received a grant for attending the HYCON-EECI Graduate School on Control in Paris, France.

During my doctoral studies, I was a teaching assistant in the following FER-I and FER-II courses: Nonlinear and Optimal Control Systems, Digital and Nonlinear Control Systems, Adaptive and Robust Control, Digital Control Systems, Automatic Control, Nonlinear Control Systems, Guidance and Control of Marine Vehicles, Laboratory and Skills – Matlab, Synthesis of Linear Control Systems, and Laboratory of Automatics 1 and 2.

I am a member of the Centre for Underwater Systems and Technologies (CUST), IEEE Oceanic Engineering Society (IEEE-OES), European Embedded Control Institute (EECI) and Amnesty International Croatia.

The main areas of my scientific interest are control theory, nonlinear systems, identification procedures, autonomous marine surface and underwater vehicles, navigation, guidance and control of marine vehicles.

Rođen sam 17. ožujka 1982. u Zagrebu gdje sam 2000. završio V. prirodoslovno-matematičku gimnaziju u Zagrebu. Iste sam godine upisao Fakultet elektrotehnike i računarstva (FER) na Sveučilištu u Zagrebu. Godine 2003. Fakultetsko vijeće odobrilo mi je završetak studija sa naglaskom na znanstveno-istraživačkom radu. Diplomirao sam u veljači 2005. s prosjekom ocjena 4.89 na temu upravljanja bespilotnim ronilicama koje je tolerantno na kvar, pod mentorstvom prof. dr. sc. Zorana Vukića. U ožujku iste godine upisujem poslijediplomski studij na FER-u gdje se zapošljavam kao asistent i znanstveni novak. Kvalifikacijski doktorski ispit sam položio u srpnju 2007. a javni razgovor održao u ožujku 2009.

U razdoblju od 2001. do 2003. primao sam državnu stipendiju za osobito nadarene studente, a od 2003. do 2005. stipendiju Grada Zagreba. Fakultetsko vijeće mi je dodijelilo tri priznanja Josip Lončar za osobit uspjeh na drugoj, trećoj i četvrtoj godini studija. U razdoblju od siječnja do travnja 2008. boravio sam na Consiglio Nazionale delle Ricerche (CNR) u Genovi, Italija radi znanstvenog usavršavanja, kao stipendist Vladâ Republike Italije i Republike Hrvatske. Godine 2008. primao sam stipendiju Zaklade "prof. Zlata Bartl" za odlične poslijediplomske studente. Na konferenciji Workshop on Navigation, Guidance and Control of Underwater Vehicles u Limericku, Irska 2008. mi je dodijeljena nagrada za najbolju prezentaciju studentskog rada. U ožujku 2009. sam nagrađen stipendijom za pohađanje HYCON-EECI Graduate School on Control u Parizu, Francuska.

Tijekom dokorskog studija sudjelujem u izvođenju nastave na kolegijima programâ FER-I i FER-II Nelinearni i optimalni sustavi upravljanja, Digitalni i nelinearni sustavi upravljanja, Adaptivno i robusno upravljanje, Digitalni sustavi upravljanja, Automatsko upravljanje, Nelinearni sustavi upravljanja, Vođenje i upravljanje plovilima, Laboratorij i vještine – Matlab, Sinteza linearnih sustava upravljanja, te Laboratorij automatike 1 i 2.

Član sam Centra za podvodne sustave i tehnologije (CePoST), IEEE Oceanic Engineering Society (IEEE-OES), European Embedded Control Institute (EECI) te Amnesty International Hrvatska.

Glavna područja mog znanstvenog interesa su teorija upravljanja, nelinearni sustavi, postupci identifikacije, autonomna površinska i podvodna plovila, te navigacija, vođenje i upravljanje plovilima.